Classification of the interactions of planetary bodies with stellar winds by hybrid simulation

Von der Fakultät für Elektrotechnik, Informationstechnik, Physik
der Technischen Universität Carolo-Wilhelmina
zu Braunschweig
zur Erlangung des Grades eines
Doktors der Naturwissenschaften
(Dr.rer.nat.)
genehmigte
Dissertation

von Yoann Edwin Vernisse
aus Corbeil-Essonnes, France

Bibliografische Information der Deutschen Nationalbibliothek

Die Deutsche Nationalbibliothek verzeichnet diese Publikation in der Deutschen Nationalbibliografie; detaillierte bibliografische Daten sind im Internet über `http://dnb.d-nb.de` abrufbar.

1. Referentin oder Referent: Prof. Dr. Karl-Heinz Glassmeier
2. Referentin oder Referent: Prof. Dr. Uwe Motschmann
eingereicht am: 05.06.2014
mündliche Prüfung (Disputation) am: 14.07.2014

ISBN 978-3-944072-06-7

uni-edition GmbH 2014
http://www.uni-edition.de

Printed in Germany

Vorveröffentlichungen der Dissertation

Teilergebnisse aus dieser Arbeit wurden mit Genehmigung der Fakultät für Elektrotechnik, Informationstechnik, Physik, vertreten durch den Mentor der Arbeit, in folgenden Beiträgen vorab veröffentlicht:

Publikationen

- **Vernisse, Y.**, Kriegel, H., Wiehle, S., Motschmann, U., Glassmeier, K.-H., (Aug. 2013), Stellar winds and planetary bodies simulations: Lunar type interaction in super-Alfvénic and sub-Alfvénic flows, *Planetary and Space Science*, *84*, 37 – 47 The author's contribution: Y.V. performed and analyzed the simulations, created the figures and wrote the manuscript of the article with the help of the co-authors.

Tagungsbeiträge

- **Vernisse, Y.**, Kriegel, H., Wiehle, S., Motschmann, U., Gleissmeier, K.-H. (Apr. 2013), Interaction of plasma flows with non-magnetized bodies: simulation from super-Alfvénic to sub-Alfvénic regime, *EGU General Assembly Conference Abstracts*, *15*, 5439

- **Vernisse, Y.**, Kriegel, H., Wiehle, S., Motschmann, U. M., Glassmeier, K.-H (Dec. 2013), Variation of the dipole strength in super and sub-Alfvenic regime: Dione-type to Ganymed-type interactions (Invited), *AGU Fall Meeting Abstracts*, D2

Contents

Abstract

Interactions of planetary obstacles with the interplanetary magnetic field have nearly exclusively been studied from the point of view of the planets in the solar system. In addition, the moons of Jupiter and Saturn are embedded in the magnetic field generated by their host planets, allowing to study moon-magnetosphere interactions. All these cases in the solar system represent points in a parameter space governed by plasma interaction physics. Up to now, very few studies have investigated the types of interactions that are absent from our solar system. Indeed, the abilities to extrapolate such interactions requires numerical tools that have only been available for a decade. In this work we use one of those numerical tools, the AIKEF code. The AIKEF code is a hybrid simulation code, which treats the plasma by simulating electrons as a fluid and ions as particles. In this thesis, the AIKEF code is used in a first part to simulate Lunar-Type and Rhea-Type interactions. Between those two points in the parameter space of the interactions regimes, other types are explored, separated by qualitative differences. In a second part, simulations are performed to study Mercury-Upward and Ganymede-Upward systems. Those two other points in the parameters space have been discussed in the literature and can be used as reference points. Subsequently, the configurations of the plasma interactions in between these two points are described through several characteristic systems. These systems are also investigated for different orientations of the planetary magnetic field. In the following chapter, the code is used to investigate a Venus-Type system and interpolate possible interaction types between this point in the plasma interaction parameter space and the Lunar-Type system. The purpose of this thesis is first to give an insight about possible interactions of extrasolar planets with their star, and to provide the keys to understand which mechanism is triggered in which regime of plasma interaction. The final point is to visualize the parameter space of the plasma interaction regime.

Zusammenfassung

Die Wechselwirkungen planetarer Körper mit dem interplanetaren Magnetfeld sind fast ausschließlich nur aus dem Blickwinkel der Planeten unseres Sonnensystems untersucht worden. Des Weiteren sind die Monde von Jupiter und Saturn in das vom jeweiligen Planeten erzeugte Magnetfeld eingebettet, was die Analyse von Mond-Magnetosphären-Wechselwirkungen ermöglicht. Alle diese Fälle im Sonnensystem stehen für Punkte in einem Parameterraum, der durch die Physik der Plasmawechselwirkungen aufgespannt wird. Bis jetzt haben nur äußerst wenige Studien die Wechselwirkungstypen untersucht, die nicht in unserem Sonnensystem vorkommen. Tatsächlich benötigt man für die Extrapolation von den bekannten Fällen zu diesen Wechselwirkungen numerische Werkzeuge, die erst seit einem Jahrzehnt verfügbar sind. In dieser Arbeit nutzen wir eines dieser numerischen Werkzeuge, den AIKEF-Code. Dieser ist ein Hybrid-Simulationscode, der das Plasma mittels der Beschreibung von Elektronen als Flüssigkeit und von Ionen als Teilchen behandelt. Im ersten Teil der vorliegenden Dissertation wird der AIKEF-Code genutzt um Lunar-Type- und Rhea-Type-Wechselwirkungen zu simulieren. Zwischen diesen beiden Punkten im Parameterraum der Wechselwirkungsregime werden auch andere Typen untersucht, die sich qualitativ unterscheiden von den bekannten unterscheiden. Im zweiten Teil werden Simulationen durchgeführt um Mercury-Upward- und Ganymede-Upward-Systeme zu untersuchen. Diese zwei Punkte im Parameterraum wurden bereits in der Literatur diskutiert und können als Referenzpunkte verwendet werden. Anschließend werden mittels mehrerer charakteristischer Systeme die Plasmastrukturen von Objekten untersucht, die zwischen diesen Punkten liegen. Diese Systeme werden zudem für verschiedene Orientierungen des interplanetaren Magnetfeldes untersucht. In anschließenden Kapitel wird der Code dazu genutzt um ein Venus-Type-System zu untersuchen und zwischen dem entsprechenden Punkt im Plasma-Wechselwirkungs-Parameterraum und dem Lunar-Type-System zu interpolieren. Das Ziel dieser Arbeit ist es, einen Einblick in mögliche Wechselwirkungen von extrasolaren Planeten mit ihrem Stern zu geben und die Schlüssel zum Verständnis der Mechanismen, die in den verschiedenen Regimen ausgelöst werden, bereit zu stellen. Der letzte Punkt ist die Visualisierung des Parameterraums der Plasma-Wechselwirkungs-Regime.

1 Introduction

Exoplanets have been studied since the middle of the 90's. The discoveries appending to this field are shredding a new light on the physics, which was mostly based on our observation of the solar System. Many domains are concerned by the study of exoplanets, but in this dissertation we focus on interplanetary plasma physics. This field was born in the 30's (Chapman and Ferraro 1930), and further developed with, for example, the introduction of magnetohydrodynamic waves (Alfvén 1942). The model of the propagation of the magnetic field via the solar wind used up to now has been developed by Parker (1965). The first missions which brought measurement to improve our understanding of the plasma physics were held at the early beginning of the space exploration. During these missions, the magnetic field around Earth was measured and the presence of a shock and a magnetosphere confirmed (Bryant et al. 1962). Subsequent missions to other bodies of the solar system led to the discoveries of new type of plasma interactions. Studies of the Moon have started with Luna 2 (Halekas et al. 2011). Venus was later explored by Mariner 2 and, despite of its lack of a dipole momentum, a strong plasma interaction was measured, which originates from the interaction between the interplanetary magnetic field and the Venus' ionosphere (Smith et al. 1963, Sonett 1963). Mariner 10, the first mission to Mercury (Ness et al. 1974, Ogilvie et al. 1974), revealed its particular magnetic dipole momentum. Mars was studied during the 60's starting with flyby by the missions Mariner 4, 6 and 7 (Haider et al. 2011). Jupiter has been studied starting the Pioneer 10 mission (Smith et al. 1974). The spacecraft Pioneer 11 was the first to approach Saturn (Opp 1980).

Therefore, up to now most of the investigations of space plasma interactions were made with those particular cases. What is lacking is a global understanding of how a particular plasma interaction evolves from one state to another. Only few studies about this problematic have been performed. Evolution of the magnetic moment was investigated through the case of an asteroid with different dipole momentum strength, by Omidi et al. (2004) and Simon et al. (2006). Also, the impact of different values of ionospheric production was investigated through the approaches of the sun of the comets Wirtanen by Bagdonat and Motschmann (2002b) and Churyumov-Gerasimenko by Gortsas et al. (2010). Similar study of the impact of the ionospheric production was also performed via the simulation of the time evolution of the Martian magnetic field by Boesswetter et al. (2004, 2007, 2010) and Kallio et al. (2008).

The theory of plasma physics is based on fluid and electromagnetism dynamic, and, due to the absence of analytical solutions to such equations, simulation codes are used to predict the results of a particular system. Therefore, simulations are therefore used to fit data from spacecrafts' instruments and to extrapolate the outcomes. Four major kinds of simulation are used to study interplanetary plasma. Put in order of computation expenses,

there is first the fluid simulation, also called magnetohydrodynamic code. Used to simulate large scale interactions, like the interaction between an exoplanet and its host star (Saur et al. 2013), the interaction of Earth with the solar wind during a strong interplanetary magnetic field (IMF) enhancement (Ridley 2007), the effect of the dipole tilt angle (Liu et al. 2012). In those codes, electrons and ions are treated as single fluid. Bi-fluid or multi-fluid simulations are based on the same approach, except that the fluid equations are applied separately to each ion species and electrons. Such simulations were run for example for Earth (Winglee 1998) or Mars (Riousset et al. 2013). Another type of model is the hybrid simulations which treat the electrons as a fluid and ions as particles. This thesis is based on such a code. Up to now, hybrid model have been applied to study intermediate sized plasma interactions like Mercury (Richer et al. 2012), Venus (Dyadechkin et al. 2013), Mars (Brecht and Ledvina 2006, Motschmann and Kührt 2006), or the moons of Saturn (Ledvina et al. 2004, Modolo and Chanteur 2008) and Jupiter (Lipatov and Combi 2006). Hybrid simulations for large scale interactions such as Earth are under development (Pokhotelov et al. 2013). The costliest models in terms of computational resources are the full particle models. Those simulations treat ions and electrons as independent particles. To date, full particle simulations have been used to study crustal field of the moon, or the interaction of a spacecraft with its surrounding plasma (Muranaka et al. 2009, Deca et al. 2013). In this dissertation, we use a hybrid simulation code, which is a good compromise between physical accuracy and computational performances. The code is called AIKEF for Adaptive Ion Kinetic Electron Fluid. All the numerical aspects concerning the code are developed in Chapter 2. The average calculation time for each simulation performed for this thesis is between one and two days running on one hundred and twenty-eight processors.

Our goal is to explore new plasma interactions which can be expected in extra solar systems using the AIKEF code. In the process, we expect to acquire a better understanding of the impact of each plasma parameter. The plasma structures described in this thesis are articulated around the electromagnetism currents. They are derived from Maxwell-Ampère equation, which gives $\nabla \times \boldsymbol{B} = \mu_0 \boldsymbol{j}$ after simplifications. Next, this equation leads to $\nabla \cdot \boldsymbol{j} = 0$. These equations state the direct link between the magnetic field and the currents, in addition to the divergence free property of the current. This means that, in the frame of our simulation, and in the applicability range of its simplifications, the currents form a system of closed loops. The advantages of describing the plasma structures in terms of currents is to relate each identified current to a specific physical process. The currents described in this thesis are all listed in Chapter 2. Consequently, when we establish a relationship between a current and its corresponding plasma structure, we relate the existence of a current to a certain set of plasma parameters.

In the framework of our study, the plasma parameters have to be though in terms of normalized quantities. A natural generalization of the results of our simulations is achieved through normalization with respect to the upstream stellar wind parameters as implemented by Bagdonat (2004). Indeed, as explained in Chapter 2, using such normalization decreases the total number of parameters that has to be explored. Considering the normalized quantities, the parameters playing a role in the plasma interactions are the stellar wind velocity and orientation relative to the IMF, the plasma β, the planetary radius, the planetary conductivity profile, the presence, strength and orientation of a magnetic field generated by the planet, and the presence and properties of an ionosphere. The direction

chosen to structure this thesis is to study the parameter space as far as possible following a predefined organization. We focus on cornerstone interaction types, which we describe the overall plasma interaction structures. Cornerstones are important if we want to consistently describe intermediate steps and the dynamics of the development of the different plasma structures. Thus, we define in Chapter 3 two cornerstones: the Lunar-Type and the Rhea-Type obstacles. The choice of a Lunar-Type obstacle as a starting point results from two conditions: (1) it is one of the simplest interactions known, and (2), is has already been extensively studied (Halekas et al. 2011). Thus, we start our study by investigating Earth's moon, or more generally, a "Lunar-Type obstacle". This object has already been studied with the AIKEF code by Wiehle et al. (2011) and Wang et al. (2011), using comparison with ARTEMIS data. Consequently, the study of Earth's moon gives a good starting point to explore the parameter space using our hybrid model. The choice of the second cornerstone is guided by the will to investigate the development of the plasma structure by stellar wind velocity modification. Therefore, decreasing the stellar wind velocity leads to a Rhea-Type interaction. Like Earth's moon, Rhea has been investigated using the AIKEF simulation code by Simon et al. (2012). In the following part, we focus on the intermediate steps between the Lunar-Type and the Rhea-Type bodies.
In the subsequent sections, we consider the interaction of a stellar wind with a magnetized obstacle. The plasma interactions between a magnetized planetary obstacle and the IMF involve a major point which is the angle of the magnetic moment, relative to the IMF and the incident upstream flow. In this thesis the IMF is always perpendicular to the upstream flow. For the magnetic moment, two cases are treated: parallel (in Chapter 4) and anti-parallel (in Chapter 5) to the IMF. In Chapter 4, we define four cornerstones: (1) the Lunar-Upward; (2) the Mercury-Upward; (3) the Rhea-Upward; and (4) the Ganymede-Upward interactions. From those points, we introduce qualitative intermediate steps which describe the successive evolutions of the plasma interactions by modifying the strength of the magnetization of the obstacle and the stellar wind velocity. In Chapter 5, we define two cornerstones: (1) the Lunar-Downward and (2) the Mercury-Downward interactions. From this point we define the intermediate states as the magnetization of the planetary obstacle is modified, on the basis of qualitative differences. In Chapter 6, we model the interaction between a stellar wind and a planetary obstacle possessing an ionosphere. The importance of an ionosphere is described by the production of ions due to the photoionization of the neutral atmosphere. In our simulation, we switch the production value from a Weak-Ions-Type to a Venus-Type interaction. Those two cases define the cornerstones of Chapter 6, establishing the boundaries of the intermediate states investigated in this last chapter. To conclude this dissertation, remarks and outcomes are brought in Chapter 7.

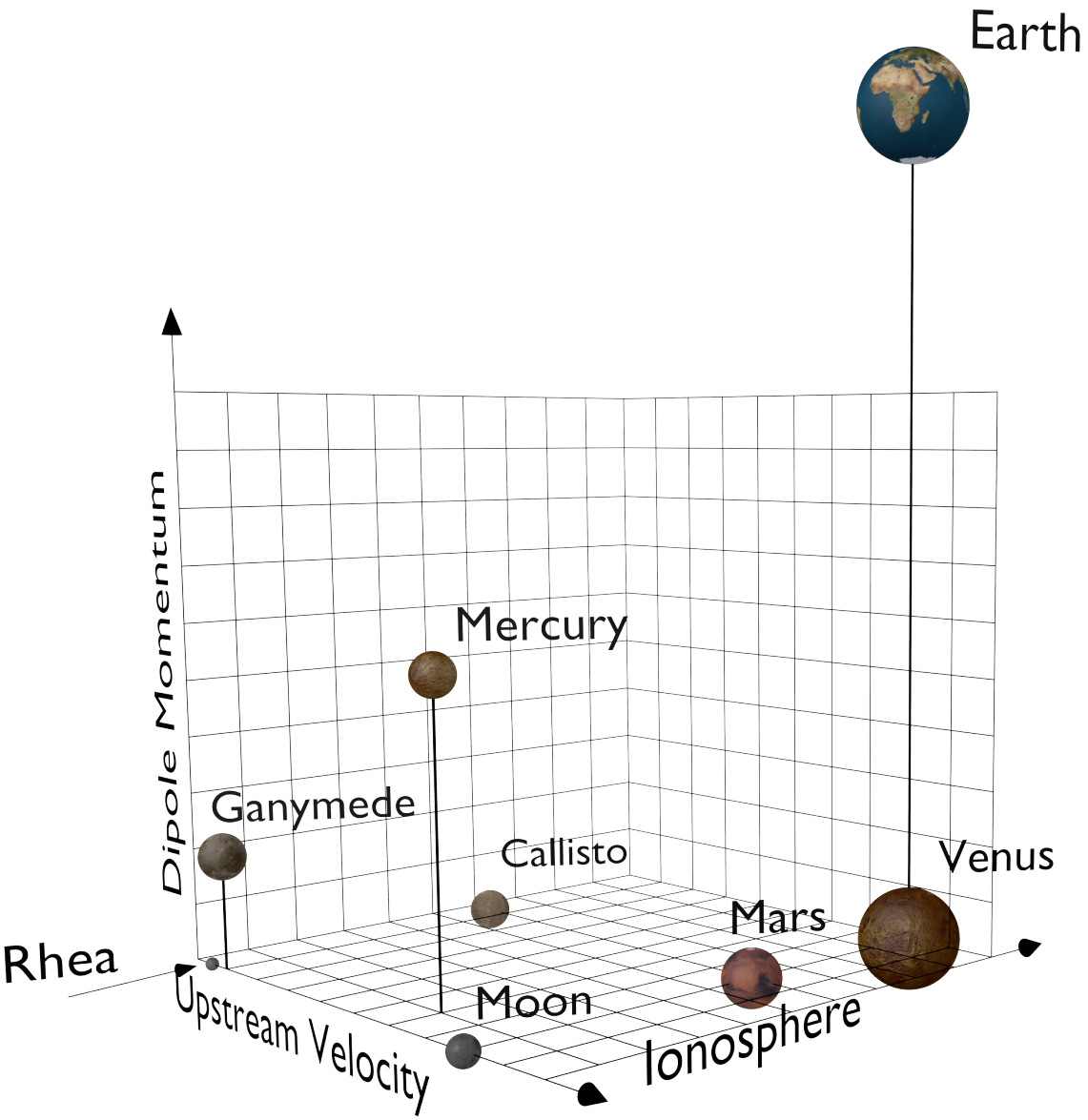

Figure 1.1: Example of the position of solar system objects in the plasma parameter space. The position of each object can vary along each axis depending on the upstream solar wind conditions.

2 Model formulation

2.1 Introduction

The work described in this thesis has been performed using a three dimensional hybrid model. This code is called AIKEF which stands for Adaptive Ion Kinetic Electron fluid. In this chapter we first explain the model and equations, which the AIKEF code and its properties are based on. We present a summary of the parameters used by the simulation in this dissertation.
The AIKEF code is based on the curvilinear code developed by Bagdonat and Motschmann (2002b); it has been further developed and described by Mueller et al. (2011). The AIKEF code has been quantitatively and qualitatively validated for numerous objects of the solar system. Data from the ARTEMIS mission have been compared to a simulation of the Moon (Wiehle et al. 2011, Wang et al. 2011). Simulations on Rhea (Roussos et al. 2008, Simon et al. 2012), Enceladus (Kriegel et al. 2009, 2011), Tethys (Simon et al. 2009) and Titan (Mueller et al. 2010, Simon et al. 2006) have been performed to study data from the Cassini spacecraft. Also data from the messenger mission have been correlated to simulations of Mercury (Mueller et al. 2012, Wang et al. 2010). Also, simulations of Mars and Venus were performed and compared to data from the Mars-Express (Boesswetter et al. 2007) and Venus-Express (Martinecz et al. 2009) missions, respectively. These applications of the AIKEF simulation code demonstrate its ability to treat different plasma interaction regimes. Therefore, we assume that the AIKEF code is also able to provide results for which in-situ measurements are not available at present. Such approach has been used in the frame of the mission Rosetta, which the AIKEF code has provided an estimation of the future in-situ measurements (Gortsas et al. 2009, 2010, Koenders et al. 2013), and in the study of exoplanets (Johansson et al. 2009, 2011).
This chapter is divided into two large sections. First we describe the simulation code focusing on the specific points pertinent to this thesis, then we give details on the currents in the plasma, which are the core points of this dissertation.

2.2 The hybrid simulation code AIKEF

The AIKEF code is based on the hybrid model which considers the electrons as a fluid and ions as particles. The advantage of this technique lies in the ability to resolve low frequency effects (related to ions) with limited resource needs. However high frequency effects (related to electrons) and charge separations are absent from the simulation. These properties have to be kept in mind for every investigated physical effect, and requires us

to verify that high frequency effects are limited to the lowest order of magnitude in the results. In this section we first develop the equations of the hybrid model then we discuss the technical parts of the code regarding stability and mesh.

2.2.1 Fundamental equations

The hybrid model has been thoroughly described, e.g. Matthews (1994), Bagdonat (2004), therefore only a short presentation of the basic equations is reported here. The hybrid model is a description of the interplanetary medium, made of collisionless plasma steeped in a magnetic field. Therefore it solely follows the laws of electromagnetism. Other effects like gravitational attraction or collisions are neglected. Electromagnetism is based on Maxwell equations:

$$\nabla \cdot \boldsymbol{B} = 0 \quad ; \tag{2.1}$$

$$\nabla \cdot \boldsymbol{E} = \frac{1}{\varepsilon_0}\rho_\mathrm{c} \quad ; \tag{2.2}$$

$$\nabla \times \boldsymbol{E} = -\frac{\partial \boldsymbol{B}}{\partial t} \quad ; \tag{2.3}$$

$$\nabla \times \boldsymbol{B} = \mu_0 \boldsymbol{j} + \frac{1}{c^2}\frac{\partial \boldsymbol{E}}{\partial t} \quad ; \tag{2.4}$$

where ρ_c is the charge density, ε_0 the vacuum permittivity, μ_0 the vacuum permeability and c the speed of light. The terms $\boldsymbol{B}$, $\boldsymbol{E}$, and $\boldsymbol{j}$ are the magnetic field, electric field, and current density, respectively. Next, the Vlasov equation is applied to the electrons:

$$m_e n_e d_t(\boldsymbol{u_\mathrm{e}}) = -e n_\mathrm{e}(\boldsymbol{E} + \boldsymbol{u_\mathrm{e}} \times \boldsymbol{B}) - \nabla P_\mathrm{e} + e n_\mathrm{e} \mathbf{R} \cdot \boldsymbol{j} \quad , \tag{2.5}$$

where u_e, n_e, m_e and P_e are the electron bulk velocity, density, mass and pressure tensor, respectively. The term e is the elementary charge. The resistivity tensor ($\mathbf{R}$) is manually defined in the simulation, for example to set up a resistivity profile to the simulated obstacle. The resistivity tensor can also be used to model collision in the plasma and ion-electron momentum exchange. In this work, the resistivity tensor is taken as being zero in the plasma and different from zero inside the obstacle. Details about resistivity inside the obstacle are developed in Appendix A.1.
Equation (2.5) is further simplified in the hybrid model by setting up of three approximations:

- The first approximation is in the name "hybrid model", where "hybrid" stands for the consideration of electrons as a massless fluid:

$$m_\mathrm{e} \sim 0 \quad . \tag{2.6}$$

  This approximation leads to a first simplification of Equation (2.5), which becomes:

$$\boldsymbol{E} = -\boldsymbol{u_\mathrm{e}} \times \boldsymbol{B} - \frac{\nabla P_\mathrm{e}}{e n_\mathrm{e}} + \mathbf{R} \cdot \boldsymbol{j} \quad . \tag{2.7}$$

- In addition, the total charge is considered to be neutral (quasi-neutrality), which means there is an equal density of positive and negative charges. If we write n_e the number density of electrons, q_α and n_α the charge and number density of each ion species, it yields:

$$en_e = \sum_\alpha q_\alpha n_\alpha = \rho_c \quad . \tag{2.8}$$

  The validity of this approximation is constrained by the possibility of separation of ions and electrons, defined by the Debye length:

$$\lambda_D = \sqrt{\frac{\varepsilon_0 k_B}{\frac{e^2 n_e}{T_e} + \sum_\alpha \frac{q_\alpha^2 n_\alpha}{T_\alpha}}} \quad . \tag{2.9}$$

  For the typical solar wind, the Debye length is about λ_D=10 m, however, in regions such as the Lunar wake, there is a quasi void with densities on the order of 10^{-3} cm^{-3} leading to Debye lengths about 50 km. In this case the separation between the ions and the electrons cannot be ignored and the quasi neutrality is not applicable. To apply the quasi-neutrality approximation, it is rewritten in terms of current and bulk velocity:

$$\boldsymbol{j} = \boldsymbol{j_e} + \boldsymbol{j_i} = \rho_c(-\boldsymbol{u_e} + \boldsymbol{u_i}) \quad \Longrightarrow \quad \boldsymbol{u_e} = \boldsymbol{u_i} - \boldsymbol{j}/\rho_c \quad , \tag{2.10}$$

  where $\boldsymbol{j_e}$ and $\boldsymbol{j_i}$ are the electron and ions current densities, respectively. The term $\boldsymbol{u_i}$ is the ions bulk velocity. Applied to Equation (2.5), the previous simplification leads to:

$$\boldsymbol{E} = -\boldsymbol{u_i} \times \boldsymbol{B} + \frac{\boldsymbol{j} \times \boldsymbol{B}}{\rho_c} - \frac{\nabla P_e}{\rho_c} + \mathbf{R} \cdot \boldsymbol{j} \quad . \tag{2.11}$$

- The third property is the Darwin approximation (Hewett 1985), which results in neglecting the term $\partial \boldsymbol{E}/\partial t$. Maxwell-Ampère's law becomes:

$$\nabla \times \boldsymbol{B} = \mu_0 \boldsymbol{j} \quad . \tag{2.12}$$

  Applying this simplification to Equation (2.5) leads to the final expression for the field:

$$\boldsymbol{E} = -\boldsymbol{u_i} \times \boldsymbol{B} + \frac{\nabla \times \boldsymbol{B}}{\mu_0 \rho_c} \times \boldsymbol{B} - \frac{\nabla P_e}{\rho_c} + \mathbf{R} \cdot \frac{\nabla \times \boldsymbol{B}}{\mu_0} \quad . \tag{2.13}$$

The ions are described kinetically, their motion is calculated for each particle following the Lorentz force:

$$\frac{d\boldsymbol{v_\alpha}}{dt} = \frac{q_\alpha}{m_\alpha}(\boldsymbol{E'} + \boldsymbol{v_\alpha} \times \boldsymbol{B}) \quad , \tag{2.14}$$

with $\boldsymbol{v}_\alpha$, q_α, m_α the velocity, charge, and mass of each particle, respectively. The expression of the electric field has to take into account the resistive term in order to satisfy the momentum conservation (Bagdonat 2004):

$$\boldsymbol{E}' = \boldsymbol{E} - \mathbf{R} \cdot \frac{\nabla \times \boldsymbol{B}}{\mu_0} \quad . \tag{2.15}$$

The last equation required to close the system is given by the expression of the electron pressure. It is assumed that it follows the adiabatic law:

$$P_\mathrm{e} = P_{\mathrm{e}0} \left(\frac{n_\mathrm{e}}{n_{\mathrm{e}0}} \right)^\kappa \tag{2.16}$$

where $n_{\mathrm{e}0}$ and $P_{\mathrm{e}0}$ are the initial number density and electron pressure. The term κ is the electron adiabatic coefficient. It is widely accepted (Bagdonat 2004, Meyer-Vernet and Issautier 1998) that the degree of freedom of an electron embedded in a magnetic field is equal to 2, consequently, the adiabatic coefficient is set to, with f the degree of freedom: $\kappa = 1 + 2/f = 2$.

2.2.2 Numerical aspects

The AIKEF code is based on the particle-in-cell approach. While the fields are derived at the nodes of each cell, the particles are evolving inside the cells. The evaluation of the field at the particle position is derived using a linear interpolation from the corners of the cell. Details about the adaptive mesh and the possibility to adjust the resolution in time and space, as well as the field discretization routine, particles merging and splitting, boundary conditions and parallelization are available in Mueller (2011).

2.2.2.1 Normalization and constant parameters

The importance of the normalization has been mentioned in Chapter 1. While performing our studies, the parameters in the simulation are directly set in normalized values. The normalization formulas are presented in Table 2.1, which relates each quantity to their corresponding normalization value. To derive the physical values from the normalized quantities provided by the simulation, one only needs to know the real stellar wind magnetic field, and number density, and the mass and charge distribution of the stellar wind particles. When studying interactions of the solar system objects, It is usual to set the mass and charge of particles being equal to the proton mass and charge. However one should note that, for example, inside the magnetosphere of Jupiter or Saturn, the mass of the upstream flow species is often equal to several time the proton mass, as well as the upstream species charge can be different from the elementary charge (Kivelson et al. 2004). Table 2.1 gives an example of normalized quantities for a stellar wind having a magnetic field of 5 nT, a number density of 5 cm^{-3}, and composed of ionized hydrogen. Those parameters correspond to values close to the composition of the solar wind around Earth. Switching between normalized parameters and real parameters in the framework of the results presented in this thesis is important to handle, in order to generalize the simulation outputs to different stellar wind conditions.

Quantity	*Variable*	*Normalized variable*[†]	*Normalization parameter*[†] *(symbol)*	*Normalization parameter (example)*
Magnetic field	B	$B^* = B/B_0$	B_0	5.0 nT
Number density	n	$n^* = n/n_0$	n_0	5.0 cm^{-3}
Mass	m_α	$m_\alpha^* = m_\alpha/m_0$	m_0	1.0 m_p
Charge	q_α	$q_\alpha^* = q_\alpha/q_0$	q_0	1.0 e
Time	t	$t^* = t/t_0$	$t_0 = m_0/(q_0 B_0)$	2.1 s
Length	x	$x^* = x/x_0$	$x_0 = (m_0/(\mu_0 q_0^2 n_0))^{1/2}$	$1.0 \cdot 10^2$ km
Velocity	u	$u^* = u/u_0$	$u_0 = x_0/t_0 = B_0/(\mu_0\rho_0)^{1/2} = v_{A,0}$	48 km/s
Gyrofrequency	Ω_α	$\Omega_\alpha^* = \Omega_\alpha/\Omega_0$	$\Omega_0 = 1/t_0$	0.48 Hz
Mass density	ρ	$\rho^* = \rho/\rho_0$	$\rho_0 = n_0 m_0$	$8.4 \cdot 10^{-21}$ kg/m^3
Charge density	ρ_c	${\rho_c}^* = \rho_c/\rho_{c,0}$	$\rho_{c,0} = n_0 q_0$	$8.0 \cdot 10^{-13}$ C/m^3
Current density	j	$j^* = j/j_0$	$j_0 = q_0 n_0 v_{A,0}$	3.9 nA/m^2
Electric field	E	$E^* = E/E_0$	$E_0 = v_{A,0} B_0$	$2.4 \cdot 10^{-4}$ V/m
Resistivity	η	$\eta^* = \eta/\eta_0$	$\eta_0 = E_0/j_0$	$6.2 \cdot 10^3$ Ω m
Conductivity	σ	$\sigma^* = \sigma/\sigma_0$	$\sigma_0 = 1/\eta_0$	$1.6 \cdot 10^{-4}$ S/m
Magnetic moment	M	$M^* = M/M_0$	$M_0 = 4\pi B_0 x_0^3/\mu_0$	$5.3 \cdot 10^{13}$ A m^2
Pressure	P	$P^* = P/P_0$	$P_0 = B_0^2/(2\mu_0)$	$9.9 \cdot 10^{-3}$ nPa
Ion production	Q_α	$Q_\alpha^* = Q_\alpha/Q_{\alpha,0}$	$Q_{\alpha,0} = n_0 x_0^3/t_0$	$2.9 \cdot 10^{21}$ s^{-1}

[†] With appropriate definition when necessary.

Table 2.1: Table of normalizations with an example of application at Earth. The terms m_p and e are the mass of the proton and the elementary charge, respectively. One should note that the expressions here are written without any simplification. For example, a common simplification is to consider: m_0=m_p and q_0=e. One should keep in mind that this is not always true. In this dissertation, one should always consider that B_0=B_{sw}, n_0=n_{sw}, q_0=q_{sw}, and m_0=m_{sw} (with B_{sw}, n_{sw}, q_{sw}, and m_{sw} are the upstream stellar wind magnetic field magnitude, number density, particle charge, and particle mass, respectively), i.e., the normalization is made using the upstream stellar wind parameters. The term $v_{A,0}$ stands for the Alfvén velocity.

In the work presented in this thesis, the initialization parameters that are studied are: the upstream velocity, the magnetization of the planet and the ionospheric properties of the planet. The other initialization parameters which are kept constant among the runs are: the planetary radius R_p, the stellar wind ion plasma beta (β_i), the stellar wind electron plasma beta (β_e), the orientation of the IMF, and the orientation of the stellar wind flow. The stellar wind is flowing along the X-axis, with $\boldsymbol{v_{sw}} = +|\boldsymbol{v_{sw}}|\, \boldsymbol{e_x}$. The IMF is taken along the Z-axis with $\boldsymbol{B_{sw}} = -|\boldsymbol{B_{sw}}|\, \boldsymbol{e_z}$. The electron and ion plasma beta are both set to $\beta_i = 0.5$ and $\beta_e = 0.5$. The planetary radius is set to $R_p = 20\ x_0$. One should note that, treating the radius in term of inertial length implies that, to compare the obstacle in the simulation to a real case, the variation of density in the stellar wind gives different values for the planetary radius. For example, a density of 5 cm^{-3}, with a planetary radius of 20 x_0, leads to a value 2000 km. With a density of 50 cm^{-3}, the radius becomes 650 km. These constant parameters are written in Table 2.2.

2.2.2.2 Stand-off distance

In this thesis, one parameter is often referred as the stand-off distance, noted L_{SO}. It is only used when the planet is magnetized and refers to the point of equilibrium between

Quantity	*Symbol*	*Value*
Ion plasma beta	β_i	0.5
Electron plasma beta	β_e	0.5
Planetary radius	R_p	$20x_0$
Electron adiabatic exponent	κ	2

Table 2.2: Initialization parameters which are common to all simulations in this dissertation. The electron plasma beta, planetary radius, and adiabatic exponent are constant through a simulation run.

the stellar wind and planetary magnetic fields. This parameter has been used for the study of Earth's magnetosphere in order to test models of pressure balance using data from THEMIS (Glassmeier et al. 2008). The expression is based on a simple pressure equilibrium between the planetary magnetic pressure and the stellar wind pressure. In the literature (Baumjohann and Treumann 1996), only the dynamic pressure of the stellar wind is taken into account, here the magnetic pressure is also used in the calculation. Introducing the magnetic pressure is required when studying stellar wind with a velocity $\lesssim 1\ v_{\mathrm{A},0}$. In this regime, the stellar wind magnetic pressure is greater or equal to its own dynamic pressure. The pressure equilibrium can be written as:

$$\frac{B_\mathrm{sw}^2}{2\mu_0} + \frac{\alpha}{2}\rho v_\mathrm{sw} = \frac{B_\mathrm{M}^2}{2\mu_0} \quad , \tag{2.17}$$

where α is a coefficient which represents the average momentum transferred by the particles to the magnetosphere. $\alpha/2$ is commonly said to be equal to 0.88 (Baumjohann and Treumann 1996) by considering an average value of the direction taken by the reflected particles at the magnetopause. The magnetic field magnitude at the subsolar point of the magnetopause (B_M) is usually defined with respect to the surface magnetic field by introducing the radius of the obstacle (R_p) and the distance between the magnetopause subsolar point (x_M) and the center of the obstacle:

$$B_\mathrm{M} = \lambda B_\mathrm{surf}\left(\frac{x_\mathrm{M}}{R_\mathrm{p}}\right)^3 = \lambda B_\mathrm{surf} L_\mathrm{SO}^3 \quad , \quad \text{where} \quad L_\mathrm{SO} = \frac{x_\mathrm{M}}{R_\mathrm{p}} \quad . \tag{2.18}$$

The term λ represents a coefficient defining the value of the magnetic field at the subsolar point also called the compression factor. Conventionally, this coefficient is set equal to 2 (Baumjohann and Treumann 1996), the reason being that the magnetic field at the magnetopause is equal to the sum of the planetary field and the field generated by the magnetopause current, which are assumed to be equal. The expression of the stand-off distance can finally be written as:

$$L_\mathrm{SO} = \left(\frac{\lambda^2 B_\mathrm{surf}^2}{B_0^2 + \frac{\alpha}{2}\mu_0\rho v_\mathrm{sw}^2}\right)^{1/6} \quad , \tag{2.19}$$

with the stand-off distance expressed in planetary radius. This expression can also be expressed in terms of normalized values:

$$L_{\mathrm{SO}} = \left(\frac{\lambda^2 B^{*2}}{1 + \frac{\alpha}{2} \rho^* {v^*_{\mathrm{sw}}}^2} \right)^{1/6} \quad . \tag{2.20}$$

The formulas is applied to each study of magnetized obstacle effected in thesis, and presented in the table introduced in Chapter 4 and 5.

2.2.2.3 Smoothing

For stability purposes, a numerical diffusion has been implemented through a smoothing procedure. By writing $F_{[i,j,k]}$ any field at the grid point $\{i, j, k\} \in \mathbb{Z}$, and setting the smoothing strength S_0 (arbitrarily input by the user), the smoothed field F' is expressed as (Bagdonat 2004):

$$F'_{[i,j,k]} = (1 - S_0) F_{[i,j,k]} + S_0 \langle F_{[i,j,k]} \rangle \quad , \tag{2.21}$$

with

$$\langle F_{[i,j,k]} \rangle = \sum_{q,r,s=-1}^{1} F_{[i+q,j+r,k+s]} \frac{1}{8} 2^{-(q^2+r^2+s^2)} \quad . \tag{2.22}$$

A common range of values of the arbitrary factor is from $S_0 = 0.005$ to $S_0 = 0.05$. This factor controls the importance of the neighboring cells in the calculation of the field. The smoothing is responsible for the numerical damping; it averages the field locally and generates a local merging of the field lines and vectors. Also, reconnection solely due to smoothing is present and field lines merging is likely to happen. This point is important to notice for the interpretation of the simulation results. In Chapter 1, we introduced the description of the plasma interactions using currents, i.e. each current can be described by a particular physical process. Therefore, the separation of the currents, related to their physical process, should be possible. However, due to the smoothing, there is a mixing between the different currents; it is thus not always possible to establish a clear distinction between the origins of the various currents. Furthermore, a direct consequence of the smoothing can be a possible inaccuracy in some of the quantities observed. It means that, in absence of data, the exact quantitative results from the data should be carefully considered. In this dissertation, the plots are presented with their quantitative values, therefore, we will limit ourselves to qualitative interpretations, whenever quantitative analysis is not supported by data. The use of quantitative results from the AIKEF code, without experimental data to compare, should only be used by taking into account the numerical diffusion process, and thus put in a range of possible values.

2.2.3 Ionosphere modeling

In order to form an ionosphere in our model, used in Chapter 6, a routine adding ionospheric ions is implemented and introduces ions into the simulation box following the Chapman profile (Baumjohann and Treumann 1996). We provide a description of the profile for the sake of completeness: this model starts with a neutral atmosphere defined by an exponential density profile $n_{\mathrm{n}}(r)$ (with $n_{\mathrm{n}}(0) = n_{\mathrm{n,surf}}$):

$$n_{\mathrm{n}}(r) = n_{\mathrm{n,surf}} \exp\left(\frac{-r}{H}\right) \quad , \quad \text{with} \quad H = \frac{k_{\mathrm{B}} T_{\mathrm{n}}}{m_{\mathrm{n}} g} \quad . \tag{2.23}$$

The term H is the scaleheight, k_{B}, the Boltzmann constant, T_{n}, the temperature of the neutrals, m_{n}, the mass of the neutral, and g, the gravity of the planet. The expression of the radiation intensity is written along a line of the ray defined by $dr/\cos\theta$ and given by:

$$dI = \sigma_\nu n_{\mathrm{n}} \frac{dr}{\cos\theta} I \quad , \tag{2.24}$$

where σ_ν is the absorption surface of the radiation (which depends on the photon frequency ν), and θ the angle to the subsolar point. The term $\sigma_\nu n_{\mathrm{n}}$ can be interpreted as the inverse of the optical depth of the atmosphere. Integrating expression (2.24) yields:

$$I(r,\theta) = I_\infty \exp\left(-\frac{\sigma_\nu n_{\mathrm{n,surf}} H}{\cos\theta} \exp\left(-\frac{r}{H}\right)\right) \quad , \tag{2.25}$$

with I_∞ the radiation intensity at the surface of the atmosphere. One introduces the photoionization $q_{\nu,\alpha}(r,\theta)$ as a function of the intensity I:

$$q_{\nu,\alpha}(r,\theta) = \kappa_\nu \cos\theta \frac{dI}{dr} \quad , \tag{2.26}$$

with κ_ν the efficiency of the photoionization, i.e. the number of ions produced per unit of energy absorbed. By replacing dI/dr using Equations (2.24) and (2.25), one obtains:

$$q_{\nu,\alpha}(r,\theta) = \kappa_\nu \sigma_\nu n_{\mathrm{n,surf}} I_\infty \exp\left(-\frac{r}{H} - \frac{\sigma_\nu n_{\mathrm{n,surf}} H}{\cos\theta} \exp\left(-\frac{r}{H}\right)\right) \quad . \tag{2.27}$$

Equation (2.27) is used as a probability function to evaluate the chances of an ionization event occurring at a given position. We see that the shape of an ionosphere following a Chapman profile is characterized by three parameters: the scale height (H), the surface absorption of the radiation (σ_ν) and the neutral density at the surface of the obstacle ($n_{\mathrm{n,surf}}$). The maximum of the profile is found at the height r_{max}:

$$r_{\max} = R_{\mathrm{p}} - H \ln \frac{1}{H \sigma_\nu n_{\mathrm{n,surf}}} \quad , \tag{2.28}$$

above the surface of the obstacle. In the code, the value of the Chapman profile at $r_{\max}$ is used to optimize the calculation generating the ions. The procedure to generate ions is as follow: a random point is generated inside a volume arbitrary set. A random value is assigned to this random point, and compared to the value of the profile at this point. For example, a random point is generated in the equatorial plane at (x=$-10x_0$, y=$30x_0$), corresponding to (r=$31.6x_0$, θ=$-71°$), resulting in a value of the function $q_{\nu,\alpha}(r,\theta)/q_{\nu,\alpha}(r_{\max},0) = 7.4 \cdot 10^{-2}$. A second random value (e.g. $\xi \in [0,1]$) is generated, if $\xi \leqslant 7.4 \cdot 10^{-2}$, the point is accepted, i.e. introduced in the simulation box, if $\xi \geqslant 7.4 \cdot 10^{-2}$, the point is rejected. One understands than since the number of generated ions is preset by the user, to optimize the number of points generated, the production has to be divided by its maximal value ($q_{\nu,\alpha}(r_{\max},0)$) in order to put its maximum equal to 1.
In the simulations ran for the results presented in this dissertation, the parameters used are as followed: the scaleheight is H=$2x_0$, the absorption surface and density are

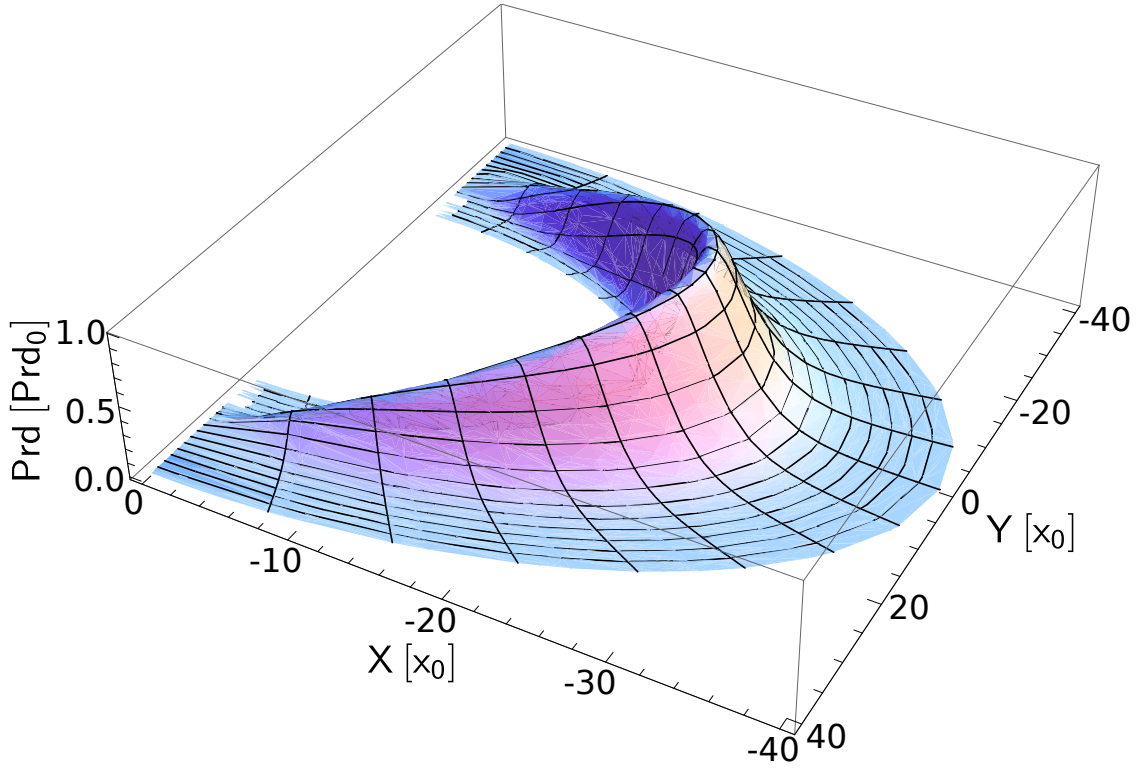

Figure 2.1: Representation of the Chapman profile in the equatorial plane using the expression $q_{\nu,\alpha}(r,\theta)/q_{\nu,\alpha}(r_{\max},0)$ (see Equation (2.27) and (2.28)) with $H = 2\ x_0$, $\sigma_\nu n_{\mathrm{n,surf}} = 5\ x_0^{-1}$, $r \in [20,40]\ x_0$ and $\theta \in \left[-\frac{\pi}{2},\frac{\pi}{2}\right]$. The amplitude represents the probability of generation of a random ion.

$\sigma_\nu n_{\mathrm{n,surf}}$=$5x_0^{-1}$. It is important to note that these values are set arbitrarily, by testing the profile and finding a good compromise for the physical modeling. A representation of the profile with those parameters is given in Figure 2.1.
The number of ions inserted in the simulation box each second during a simulation run is set by the parameter Q_α, its expression corresponds to:

$$Q_\alpha = \int_V q_{\nu,\alpha} dV \quad . \tag{2.29}$$

Where V represents the volume of integration, which is the volume where the ions are inserted in the simulation box. This value is normalized following the expression provided in Table 2.1.

2.3 Currents

The importance of the description of plasma interactions, using currents based formulations, has been emphasized in Chapter 1. An advantage of such a description is to be able to show in one plot the structure of the plasma and the physical processes that drive the electromagnetic structures. In order to explain the physical mechanisms, we detail several

currents that are typically encountered in our simulation results.

2.3.1 The polarization current j_{pol}

The polarization current reveals the importance of the MHD waves in the interaction region. In the literature, the polarization current refers to a time derivative of the electric field (Baumjohann and Treumann 1996). In this section we derive j_{pol} by developing the Lorentz force term in the Vlasov equation for the ions species α, in stationary state ($\partial_t = 0$):

$$(\boldsymbol{u}_\mathbf{i} \cdot \nabla)\, \boldsymbol{u}_\mathbf{i} = \frac{q_\alpha}{m_\alpha} (\boldsymbol{E} + \boldsymbol{u}_\mathbf{i} \times \boldsymbol{B}) + \frac{\nabla P_i}{m_\alpha n} \quad . \tag{2.30}$$

The term ∇P_i is the ion pressure gradient and is used to define the diamagnetic current. We only look at the Lorentz force term, to which we apply the cross product with $\boldsymbol{B}/B^2$:

$$(\boldsymbol{E} + \boldsymbol{u}_\mathbf{i} \times \boldsymbol{B}) \times \frac{\boldsymbol{B}}{B^2} = \frac{\boldsymbol{E} \times \boldsymbol{B}}{B^2} + \frac{(\boldsymbol{B} \cdot \boldsymbol{u}_\mathbf{i})\boldsymbol{B}}{B^2} - \frac{(\boldsymbol{B} \cdot \boldsymbol{B})\boldsymbol{u}_\mathbf{i}}{B^2} \quad . \tag{2.31}$$

In the r.h.s. of the last equation, one can recognize the $\boldsymbol{E} \times \boldsymbol{B}$ drift as the first term. The second term is equal to the bulk velocity parallel to the magnetic field:

$$\boldsymbol{u}_{\mathbf{i},\parallel} = \frac{(\boldsymbol{B} \cdot \boldsymbol{u}_\mathbf{i})\, \boldsymbol{B}}{B^2} \quad . \tag{2.32}$$

The third term of the r.h.s. of Equation (2.31) is simply the bulk velocity. The subtraction of the parallel velocity to the total velocity gives the perpendicular velocity. Therefore, by writing $\boldsymbol{u}_\mathbf{E}$, the $\boldsymbol{E} \times \boldsymbol{B}$ drift velocity and $\boldsymbol{u}_{\mathbf{i},\perp} = \boldsymbol{u}_\mathbf{i} - \boldsymbol{u}_{\mathbf{i},\parallel}$ the velocity perpendicular to the magnetic field, one obtains:

$$(\boldsymbol{E} + \boldsymbol{u}_\mathbf{i} \times \boldsymbol{B}) \times \frac{\boldsymbol{B}}{B^2} = -\boldsymbol{u}_{\mathbf{i},\perp} + \boldsymbol{u}_\mathbf{E} = -\boldsymbol{u}_\mathbf{pol} \quad . \tag{2.33}$$

Here, $\boldsymbol{u}_{\mathbf{i},\perp} - \boldsymbol{u}_{\mathbf{i},\mathbf{E}}$ represents the local drift of the fluid, it corresponds to the polarization drift $\boldsymbol{v}_\mathbf{pol}$. One takes the definition of the current: Multiplying by the number density and the particle charge gives the current density:

$$\boldsymbol{j}_\mathbf{pol} = -nq_\alpha\, (\boldsymbol{E} + \boldsymbol{u}_\mathbf{i} \times \boldsymbol{B}) \times \frac{\boldsymbol{B}}{B^2} \quad . \tag{2.34}$$

This expression can also be written in terms of normalized quantities. We can define, using the normalization from Bagdonat (2004) and summarized in Table 2.1:

$$\boldsymbol{u}^*_\mathbf{i} = \frac{\boldsymbol{u}_\mathbf{i}}{v_{\mathrm{A},0}} \quad ; \quad \boldsymbol{j}^*_\mathbf{pol} = \frac{\boldsymbol{j}_\mathbf{pol}}{j_0} \quad . \tag{2.35}$$

Using the Definitions 2.35 into Equation (2.34) gives:

$$\boldsymbol{j}^*_\mathbf{pol} = -n^* q^*_\alpha \left(\boldsymbol{E}^* + \boldsymbol{u}^*_\mathbf{i} \times \boldsymbol{B}^*\right) \times \frac{\boldsymbol{B}^*}{B^{*2}} \quad . \tag{2.36}$$

This last equation is mainly used to prove that the derivation of the polarization current can be directly calculated from the simulation output.

2.3.2 Ohmic field and inner obstacle diffusion

The obstacle is defined in the simulation as a spherical volume were particles are removed when they hit its surface. As mentioned in Section 2.2.1, a resistivity profile is applied inside the volume where the obstacle is defined. It should be noticed that, the field inside the obstacle is therefore only propagated via the resistive term. In this section we detail the relationship between the obstacle resistivity and the Ohmic current triggered. We emphasize that the resistivity profile of the obstacle define the velocity of propagation of the magnetic field inside the obstacle. This velocity is given by the magnetic Reynolds number which can be derived in the particular case of the frozen in conditions by:

$$-\boldsymbol{v}_{\mathbf{sw}} \times \boldsymbol{B}_{\mathbf{sw}} = \boldsymbol{E}_{\mathbf{ohm}} = \eta \boldsymbol{j}_{\mathbf{ohm}} \quad , \tag{2.37}$$

where $\boldsymbol{E}_{\mathbf{ohm}}$ is the electric field induced by the IMF flowing inside the obstacle. Assuming that $\boldsymbol{B}_{\mathbf{ohm}}$ and $\boldsymbol{j}_{\mathbf{ohm}}$ are constant along their area of integration we have from Ampère's law:

$$\nabla \times \boldsymbol{B}_{\mathbf{ohm}} = \mu_0 \boldsymbol{j}_{\mathbf{ohm}} \Rightarrow B_{\mathrm{ohm}} L = \mu_0 j_{\mathrm{ohm}} S \quad , \tag{2.38}$$

where L is the perimeter of the circle of integration of the magnetic field and S the surface of integration of the current. We define the characteristic length L_{char} as:

$$L_{\mathrm{char}} = S/L \quad . \tag{2.39}$$

The expression of the Ohmic current becomes:

$$j_{\mathrm{ohm}} = \frac{B_{\mathrm{ohm}}}{\mu_0 L_{\mathrm{char}}} \quad . \tag{2.40}$$

For a planet we can approximate the surface of integration of the current as the north-south pole disc, which is equal to πR_{p}^2. The length of integration of the magnetic field can also be approximated by the perimeter of the obstacle which is $2\pi R_{\mathrm{p}}$. This pictures the planet as a wire with a radius R_{p}. The induced field derived from this model can be written in the case of a stellar wind flowing perpendicularly to the IMF:

$$B_{\mathrm{ohm}} = \frac{L_{\mathrm{char}}\mu_0}{\eta} |\boldsymbol{v}_{\mathbf{sw}} \times \boldsymbol{B}_{\mathbf{sw}}| = \frac{L_{\mathrm{char}}\mu_0 v_{\mathrm{sw}}}{\eta} B_{\mathrm{sw}} = \mathcal{R}e B_{\mathrm{sw}} \quad , \tag{2.41}$$

where $\mathcal{R}e$ is the magnetic Reynolds number defined by $\mathcal{R}e = L_{\mathrm{char}}\mu_0 v_{\mathrm{sw}}/\eta$. Hereafter we show how to obtain an approximation of the magnetic field induced by the resistivity of the obstacle. Using the pressure balance equation, we can derive the minimal resistivity preventing the formation of plasma structures such as magnetospheres and bow-shocks. A bow-shock is triggered when:

$$\frac{1}{2}\rho v_{\mathrm{sw}}^2 \leqslant \frac{B_{\mathrm{ohm}}^2}{2\mu_0} \quad \Leftrightarrow \quad v_{\mathrm{sw}}^2 \leqslant \mathcal{R}e^2 v_{\mathrm{A},0}^2 \quad \Rightarrow \quad \frac{v_{\mathrm{sw}}}{v_{\mathrm{A},0}} \leqslant \mathcal{R}e \quad , \tag{2.42}$$

where $v_{\mathrm{A},0}$ is the Alfvén velocity defined in Table 2.1. This means that a magnetosphere and a bow-shock should develop if the magnetic Reynolds number is superior to the Alfvén Mach number of the stellar wind. In the case of the AIKEF code, we can use the normalized value of the resistivity (see also Table 2.1):

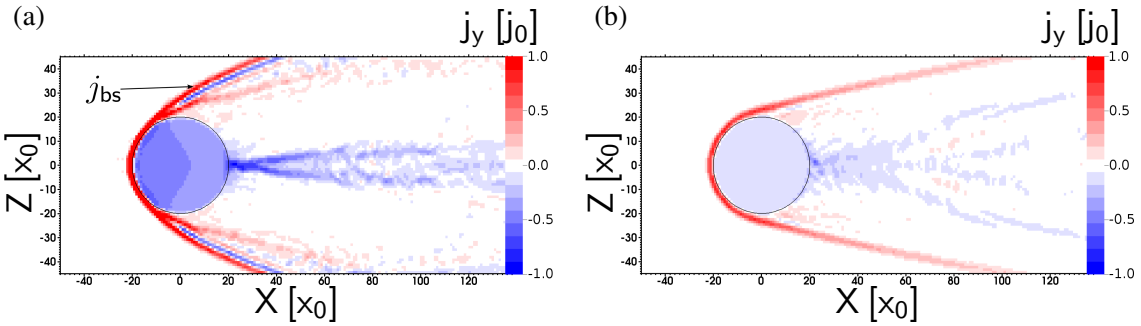

Figure 2.2: Y-component of the current density in the meridional plane. Panel (a) and (b) presents the results for a simulation where the resistivity of the obstacle is η^*=10 and η^*=50, respectively. The IMF is directed along $-Z$ and the flow is along $+X$. The upstream velocity is v_{sw}=8$v_{A,0}$, the planetary radius is R_p=20x_0. Details on the normalized values are provided in Table 2.1, and other simulation parameters are detailed in Table 2.2.

$$\eta^* = \frac{\eta}{\eta_0} \quad , \quad \text{with} \quad \eta_0 = \frac{m_0 B_0}{\rho_0 e} \quad . \tag{2.43}$$

This leads to:

$$\mathcal{R}e = \frac{L_{char}\mu_0 v_{sw}}{\eta^*}\frac{\rho_0 e}{B_0 m_0} = \frac{L_{char}}{x_0}\frac{v_{sw}}{v_{A,0}}\frac{1}{\eta^*} = \frac{L^*_{char} v^*_{sw}}{\eta^*} \quad . \tag{2.44}$$

Therefore a bow-shock should appear when the condition $\eta^* \leqslant L_{char}/x_0$. An application is shown in Figures 2.2a and 2.2b. The obstacle radius is R_p=20x_0 (see Table 2.2). A characteristic length 2.39 applied to Equation (2.44) gives a value L_{char}=10x_0. In the simulation presented in Figure 2.2a, a resistivity η^*=10 is applied to the obstacle and a bow-shock is triggered as it is shown by the strong Y-directed current in the meridional plane. The same simulation result is provided in Figure 2.2b, but with an obstacle resistivity η^*=50. We can see that for such resistivity no shock is triggered, the Ohmic field is not strong enough to balance the upstream dynamic pressure.

2.3.3 Ionospheric conductivity and Pedersen current j_{ped}

The purpose of this section is to estimate the magnetic Reynolds number in the ionosphere using the simulation outputs. First, we need to derive the effective collision frequency, in order to implement it in the expression of the Pedersen conductivity. Assuming that no collision occurs, the effective collision frequency reduces to the ion production function (Neubauer 1998):

$$\nu_{eff,\alpha} = \frac{q_{\nu,\alpha}}{n_\alpha} \quad . \tag{2.45}$$

The expression of the photoionization rate $q_{\nu,\alpha}$ is introduced in Section 2.2.3. In the AIKEF code, the photoionization is set by the user via the parameter Q_α described by Equation (2.29). In order to plot the photoionization rate, we need to retrieve the factor $\kappa_\nu \sigma_\nu n_{n,surf} I_\infty$ from the parameter Q_α. For the sake of clarity, we define:

$$A_0 = \kappa_\nu \sigma_\nu n_{\mathrm{n,surf}} I_\infty \quad , \tag{2.46}$$

and

$$f(r,\theta) = \exp\left(-\frac{r}{H} - \frac{\sigma_\nu n_{\mathrm{n,surf}} H}{\cos\theta} \exp\left(-\frac{r}{H}\right)\right) \quad . \tag{2.47}$$

Therefore, we can write:

$$q_{\nu,\alpha}(r,\theta) = A_0 f(r,\theta) \quad . \tag{2.48}$$

We integrate over the half-shell in which the dayside ionosphere is generated, i.e. $r \in \left[R_\mathrm{p}; 2R_\mathrm{p}\right]$ and $\theta \in \left[0; \frac{\pi}{2}\right]$. This yields:

$$Q_\alpha = \int_{R_\mathrm{p}}^{2R_\mathrm{p}} \int_0^{\frac{\pi}{2}} \int_0^{2\pi} A_0 f(r,\theta) r^2 \sin\theta dr d\theta d\varphi = A_0 V_{\mathrm{char}} \quad , \tag{2.49}$$

where we have defined:

$$V_{\mathrm{char}} = \int_{R_\mathrm{p}}^{2R_\mathrm{p}} \int_0^{\frac{\pi}{2}} \int_0^{2\pi} f(r,\theta) r^2 \sin\theta dr d\theta d\varphi \quad . \tag{2.50}$$

This integral is calculated with the parameters defined in section 2.2.3, i.e. H=2x_0 and $\sigma_\nu n_{\mathrm{n,surf}}$=5 x_0^{-1} (see Figure 2.1). This gives:

$$V_{\mathrm{char}} = 453 x_0^3 \quad . \tag{2.51}$$

This factor is then applied to the photoionization in order to retrieve a usable expression:

$$q_{\nu,\alpha}(r,\theta) = \frac{Q_\alpha}{V_{\mathrm{char}}} f(r,\theta) \quad . \tag{2.52}$$

The expression of the photoionization is implemented in the Pedersen conductivity (Baumjohann and Treumann 1996):

$$\sigma_{\mathrm{ped}} = \frac{\nu_{\mathrm{eff},\alpha}}{\nu_{\mathrm{eff},\alpha}^2 + \Omega_\alpha^2} \frac{n_\alpha q_\alpha^2}{m_\alpha} \quad , \tag{2.53}$$

replacing (2.52) in (2.53) yields:

$$\sigma_{\mathrm{ped}}(r,\theta) = \frac{\frac{\frac{Q_\alpha}{V_{\mathrm{char}}} f(r,\theta)}{n_\alpha}}{\left(\frac{\frac{Q_\alpha}{V_{\mathrm{char}}} f(r,\theta)}{n_\alpha}\right)^2 + \left(\frac{m_\alpha}{q_\alpha B}\right)^2} \frac{n_\alpha q_\alpha^2}{m_\alpha} \quad . \tag{2.54}$$

A more practical form of the above expression can be obtained using the normalization from Table 2.1:

$$\sigma^*_{\text{ped}}(r,\theta) = \frac{Q^*_\alpha f(r,\theta)}{V^*_{\text{char}}} \frac{q^2_\alpha}{m_\alpha} \frac{Q_{\alpha,0}\eta_0}{x_0^3\Omega_0^2} \frac{1}{\left(\dfrac{Q^*_\alpha f(r,\theta)}{n^*_\alpha V^*_{\text{char}}} \dfrac{Q_{\alpha,0}}{n_0 x_0^3 \Omega_0}\right)^2 + \Omega^{*2}_\alpha} \quad . \tag{2.55}$$

At this point it is useful to notice that:

$$\frac{Q_{\alpha,0}\eta_0}{x_0^3\Omega_0^2} = \frac{n_0 x_0^3 \Omega_0}{x_0^3\Omega_0^2} \frac{B_0}{q_0 n_0} = \frac{B_0}{q_0} \frac{m_0}{q_0 B_0} = \frac{m_0}{q_0^2} \quad , \tag{2.56}$$

and

$$\frac{Q_{\alpha,0}}{n_0 x_0^3 \Omega_0} = \frac{n_0 x_0^3 \Omega_0}{n_0 x_0^3 \Omega_0} = 1 \quad . \tag{2.57}$$

Therefore the normalized Pedersen conductivity becomes:

$$\sigma^*_{\text{ped}}(r,\theta) = \frac{Q^*_\alpha f(r,\theta)}{V^*_{\text{char}}} \frac{q^{*2}_\alpha}{m^*_\alpha} \frac{1}{\left(\dfrac{Q^*_\alpha f(r,\theta)}{n^*_\alpha V^*_{\text{char}}}\right)^2 + \Omega^{*2}_\alpha} \quad . \tag{2.58}$$

The analogy with the Ohmic current calculated in Section 2.3.2 to the Pedersen conductivity gives the Reynolds magnetic number associated with the ionosphere conductivity:

$$\mathcal{R}e = L^*_{\text{char}} v^*_{\text{sw}} \sigma^*_{\text{ped}} \quad . \tag{2.59}$$

Altogether (2.58) and (2.59) gives the magnetic Reynolds number associated to the Pedersen conductivity:

$$\mathcal{R}e(r,\theta) = \frac{L^*_{\text{char}} v^*_{\text{sw}} q^{*2}_\alpha}{V^*_{\text{char}} m^*_\alpha} \frac{Q^*_\alpha f(r,\theta)}{\left(\dfrac{Q^*_\alpha f(r,\theta)}{n^*_\alpha V^*_{\text{char}}}\right)^2 + \Omega^{*2}_\alpha} \quad . \tag{2.60}$$

With the same reasoning from Section 2.3.2, it leads to the same condition of triggering a bow-shock. Further details on the discontinuity in the case of ionospheric ions has been investigated by Motschmann et al. (1991). The Pedersen conductivity is also used to derive the Pedersen current following the expression (Baumjohann and Treumann 1996):

$$\boldsymbol{j}_{\text{ped}} = \sigma_{\text{ped}} \boldsymbol{E}_\perp \quad . \tag{2.61}$$

The Pedersen current is important in ionospheric processes, in this dissertation, this current is only present in the simulations ran in Chapter 6, where interactions between a stellar wind and a planetary obstacle with an ionosphere are investigated.

2.3.4 Alfvénic j_{alf}, and diamagnetic j_{dia} currents

The diamagnetic current refers to variations in the gradient of thermal pressure in the plasma as highlighted in Equation (2.30). The expression of the diamagnetic current is taken from Baumjohann and Treumann (1996):

Current	Definition	Color	Equation
j_{dia}	Diamagnetic current related to wake void	green	(2.62)
j_{pol}	Polarization current related to wake fast mode	blue	(2.34)
j_{alf}	Alfven wing currents	red	(2.63)
j_{cha}	Dayside Chapman-Ferraro current	orange	N/A
j_{ohm}	Ohmic current due to planet's conductivity	yellow	(2.40)
j_{bs}	Bow shock current	purple	N/A
j_{sho}	Shocklets current	cyan	N/A
j_{msph}	Tailside magnetospheric current	red	N/A
j_{ped}	Pedersen current	blue	(2.61)

Table 2.3: Summary of currents presented in this paper. To each current definition is attached a number drawn in the figures. When available, the current's formula is indicated.

$$\boldsymbol{j}_{\mathbf{dia}} = \frac{\boldsymbol{B} \times \boldsymbol{\nabla}_{\perp} P_{\perp}}{B^2} \quad . \tag{2.62}$$

The Alfvénic current is important to characterize the Alfvén wings, the details about deriving the expressions of the Alfvénic current and the Alfvén wings are written in Drell et al. (1965), Neubauer (1980), Kriegel (2014):

$$j_{\text{alf},\parallel} = \Sigma_{\text{A}} \boldsymbol{\nabla} \cdot \boldsymbol{E} \quad , \tag{2.63}$$

with:

$$\Sigma_{\text{A}} = \frac{1}{\mu_0 v_{\text{A}} \sqrt{1 + M_{\text{A}}^2}} \quad . \tag{2.64}$$

where M_{A} represents the velocity of the plasma in Alfvén Mach number, and v_{A} the Alfvén velocity. One should note that only the component parallel to the magnetic field of the Alfvénic current has a clear analytical expression. Although the parallel and perpendicular Alfvénic current are independent, i.e. $\nabla \cdot \boldsymbol{j}_{\mathbf{alf},\parallel} = \nabla \cdot \boldsymbol{j}_{\mathbf{alf},\perp} = 0$ (Kriegel 2014), it is not possible to distinguish the role of the parallel and perpendicular component in the simulation results (details are given in Section 2.2.2.3). Therefore, the Alfvénic current is always referenced as one current: j_{alf}.
The currents discussed so far only represent a fraction of the currents in the system. Other currents can also be present, but do not possess a clear analytical for associated with them. These as well as the polarization, Alfvénic, Pedersen, diamagnetic, and Ohmic currents are summarized in Table 2.3.

3 Inert obstacles in super- and sub-Alfvénic regime

This chapter contains large parts already published before the submission of this thesis. The copyright belongs to the publishing group Elsevier and the journal Planetary and Space Science. The reference of the publication is:
Y. Vernisse, H. Kriegel, S. Wiehle, U. Motschmann, and K.-H. Glassmeier (2013), Stellar winds and planetary bodies simulations: Lunar type interaction in super-Alfvénic and sub-Alfvénic flows, *Planetary and Space Science, 84, 37–47*, doi: 10.1016/j.pss.2013.04.004.

3.1 Introduction

A thin exosphere has been detected at the surface of the Moon (Tanaka et al. 2009) and its importance has been evaluated for the asymmetry in the Mach cone due to the mass loading (Lipatov et al. 2012). Yet, Earth's moon lacks both a global ionosphere and magnetic field. Therefore, as the particles carried by the solar wind hit the surface of the Moon, they are absorbed, leaving a wake in the plasma. The behavior of the plasma in the interaction between the solar wind and Earth's Moon has been described starting in the early time of space exploration with measurement by Lunar Explorer 35 (Ness et al. 1967) and is still going on. Several theoretical models were developed taking into account the magnetosonic mode triggered by the Moon and their interaction in the plasma (Whang 1968a,b, Catto 1974, Trávníček et al. 2005). The presence of sonic rarefaction modes has already been demonstrated (Samir et al. 1983), triggering a diamagnetic current in the center in the wake. In this chapter we emphasize the role of MHD modes as triggering polarization current around the wake. Parts of the currents system have been described by Owen et al. (1996). Zhang et al. (2012) have explored the existence of fast magnetosonic waves triggered by the Moon. The Moon has also been studied by means of simulation with drift-kinetic model (Lipatov et al. 2005), hybrid models (Kallio 2005) and full particle model (Birch and Chapman 2001). Presentation and overview of different models have been done by Lipatov (2002). Recent studies have involved investigations of the effects of the interplanetary magnetic field (IMF) angle (Wang et al. 2011), the current system and its evolution with the IMF angle (Fatemi et al. 2013), comparison with WIND data (Holmström et al. 2012) and ARTEMIS data (Wiehle et al. 2011). A summary of studies on the Moon is given by Halekas et al. (2011) who presents the most recent answers to investigations such as the effects triggered by the cavity behind the Moon and ions entering the wake.
Here, we expand these studies by deriving a more general current system that can be ap-

plied to any set of parameters and we study the effect of the upstream velocity on the wake structures. We construct such a model by using the currents to identify each interaction. The description of currents mentioned here is available in Section 2.3. Furthermore, we develop a model using magnetosonic modes triggered at the surface in the meridional plane of Moon and carried by the solar wind. Our purpose is to connect the magnetosonic modes and the currents in a self-consistent way. This method was investigated by Bale et al. (1997) and Wiehle et al. (2011). Since the magnetosonic modes can be derived from the parameters in a stationary situation, relying on the currents connected to the waves is helpful to derive a continuous variation between two arbitrary points of the parameter space: i.e. knowing how the waves propagation evolves with the modification of the upstream velocity allows us to derive the current system for any upstream velocity within the values which have been studied.
Once this starting point is established, we can choose several ways determined by the plasma or obstacle parameters to be varied. In this chapter, we modify the Lunar-Type plasma interaction configuration by decreasing the upstream velocity from the super-Alfvénic regime to a sub-Alfvénic regime. Sub-Alfvénic plasma interactions are present in our solar system for the case of the airless satellites of Jupiter and Saturn which are orbiting inside their respective magnetospheres. Differences between the sub-Alfvénic regime and the trans-Alfvénic regime have been studied for Rhea and Tethys (Khurana et al. 2008). But the transition of the structures between super- and sub-Alfvénic interactions has yet to be investigated before. Thus, we apply the description created from the Lunar-Type case study to the stellar wind velocity transition and confirm the evolution of current structures connected to the magnetosonic modes.
The configurations of the grid for the simulations ran for this chapter are detailed in Table 3.1. For the simulation of the Lunar-Type, a spatial domain focused on the obstacle and the wake is sufficient, due to absence of boundary effects. Thus, the mesh does not need to be locally refined. However, for the transition between the lunar type case to a sub-Alfvénic regime, the simulation domain had to be expanded due to boundary effects arising from Alfvén wings being reflected at the top and bottom of the domain boundaries. Two levels of refinement are used in the vicinity of the obstacle and the wake, each level multiplies the resolution by a factor of two. Further details concerning the configuration and in particular the obstacle are provided in Appendix A.1. The requirement of specific boundary for the treatment of the Rhea-Type is detailed in Appendix A.3. The obstacle is treated as a highly resistive object. For this particular simulation run, we set the global resistivity of the obstacle to $\eta = 1000\eta_0$. The relevance of this value is explained in Section 2.3.2. Such a value corresponds, for Moon (embedded in the solar wind with $B_{sw} = 5$ nT and $n_{sw} = 5$ cm^{-3}), to a value of $6 \cdot 10^6$ Ωm (see Table 2.1), which is close to the resistivity of the mantle of the Moon (Hood et al. (1982)). Another point that requires to be mentioned is the necessity of using ghost ions. This means inserting ions behind the obstacle, but with a density low enough that it does not have any impact on the general structure. This insertion is required in order to propagate the magnetic field behind the obstacle, which is not possible in complete vacuum in the hybrid model (Trávníček et al. 2005, Lipatov et al. 2005).
This chapter falls into two main parts, the simulations results are first introduced, providing the description of the Lunar-Type system and lower velocity regimes. Then we discuss the structure of the plasma interaction in a Lunar-Type system and its evolution

Simulation	*Axis*	*Box length*	*Cells*
Lunar-Type	X-axis	200 x_0	208
	Y-axis	100 x_0	96
	Z-axis	100 x_0	96
Rhea-Type and transitions	X-axis	600 x_0	144
	Y-axis	300 x_0	96
	Z-axis	400 x_0	96

Table 3.1: Configuration and size of the grid along each axis for the simulations presented in Chapter 3. The size are expressed in normalized length (see Table 2.1).

v_{sw} [$v_{A,0}$]	*Case*	*Alternative name*	*Figures*
8	Inert | $8v_{A,0}$	Lunar-Type	Fig. 3.1 and 3.2
7	Inert | $7v_{A,0}$		
4	Inert | $4v_{A,0}$		
2	Inert | $2v_{A,0}$		Fig. 3.3
1	Inert | $1v_{A,0}$		
0.5	Inert | $0.5v_{A,0}$	Rhea-Type	

Table 3.2: Physical parameters used in each simulation presented in Chapter 3. The figures related to the presented cases are referenced. The velocities are expressed in Alfvén Mach (see Table 2.1).

when decreasing the stellar wind velocity.

3.2 Results

This section is divided in two parts, we first present results for the Lunar-Type case and in the second part we show the transition from the Lunar-Type case to the Rhea-Type.

3.2.1 Lunar-Type case

We want to establish a systematized description of the interactions and a sketch of the complete current closure in the wake formed by a Lunar-Type obstacle. Results of the simulation are shown in Figure 3.1 and 3.2. Figure 3.1 shows the density, magnetic field and current of the interaction between the stellar wind and a Lunar-Type obstacle in the equatorial plane. The arrows indicate the direction of the currents on this plane. There are two regions that can be distinguished, the diamagnetic region (Colburn et al. 1967), labeled region ① and the fast mode region, labeled region ②. Figures 3.1a and 3.1b show that these regions are bounded by high density and magnetic field gradients. Region ① is characterized by an anticorrelation between the magnetic field magnitude and the density. While the total magnetic field increases, the density decreases. On the contrary, region ② is characterized by a correlation between the magnetic field magnitude and the density which both decrease. One can see in Figure 3.1c the X-component of the total current,

which exhibits an antisymmetry with respect to the plane Y=0. We identify the current flowing along those regions: by starting from Y=0, X=100 x_0 and going to Y=40 x_0, X=100 x_0, we see at first a current j_{dia} flowing in the $+X$ direction (and its opposite directed counterpart j'_{dia} flowing in $-X$ direction). This current is flowing at the boundary of region ①, the diamagnetic area.
In addition, there is a second current j_{pol1} flowing in the same direction as the previous one, and its opposite directed counterpart j'_{pol1}, also pointing in the same direction as j'_{dia}. We see that j_{dia} and j_{pol1} split at X=80 x_0. The current j_{pol1} can be seen in Figures 3.1a and 3.1b as flowing along one boundary of region ②. Furthermore, it is noticeable that the current j_{pol1} is obviously present in Figure 3.1d where the polarization current is shown. Next, we can see a third current j_{pol2} flowing anti-parallel to the stellar wind flow, and its opposite directed counterpart j'_{pol2}. The current j_{pol2} is more spread in space than the two currents described previously, and it can also be seen in Figures 3.1a and 3.1b as flowing along the outer part of region ②. Also, as for the current j_{pol1}, it is also clear that this current appear in 3.1d as a polarization current. Subsequently, a fourth current (j_{ohm}) is visible in Figure 3.1c, which flows in front of the obstacle, along the surface. The current j_{ohm} is related to an increase of the magnetic field in front of the obstacle as it is observable in Figure 3.1b. It corresponds to a pile up current due to the diffusion of the magnetic field into the obstacle which is slower than the convection velocity. More details can be found in Section 2.3.2.
As the purpose of this study is to sketch a full structure of the current closure we need a second point of view on the results. We plot the same quantities in a cross section through the wake by making a cut representing the plane X=100 x_0, which can be seen in Figure 3.2. The field aligned current, presented in Figure 3.2c, is derived by computing the scalar product between the total current and the magnetic field. In comparison to the observation in the plane Z=0 of Figure 3.1, we can see that the results are not only antisymmetric but also slightly asymmetric. However, this asymmetry is only clearly visible by the observation of the current in Figure 3.2c, where the currents j'_{dia}, j'_{pol1}, and j'_{pol2} are farther from the center of the wake than j_{dia}, j_{pol1}, and j_{pol2}. The reason for this asymmetry is the finite ion gyroradius. The arrows presented on each figure indicate the direction of the current within this plane. The currents previously described as j_{dia}, j_{pol1}, j_{pol2} in the Z cross-section are displayed at their respective positions in the X cross-section. The flow of the current can be followed in Figure 3.2c and one sees in Figure 3.2b that the current is flowing along the regions of high magnetic field magnitude gradient, also it is clearly observed in Figure 3.2a, that the current is flowing along the region of high density gradient. Thus, there is a clear correlation between the flow of the current and the configuration of the wake. We can recognize in Figure 3.2d that part of the current of Figure 3.2c is present on the left side of the figure, identifying it as a polarization current. Therefore, it is possible from the study of the plane X=100 x_0 to connect the observed feature to the one of the plane Z=0. We can then see that the currents of the part $Y \geqslant 0$ (j_{dia}, j_{pol1}, and j_{pol2}) are related to the currents flowing in the part $Y \leqslant 0$ (j'_{dia}, j'_{pol1}, and j'_{pol2}) by the current j_{alf} which forms a "bridge" in the X cross-section. A model of this description is drawn in Figure 3.6. The currents described here are annotated. The fast mode polarization currents (j_{pol1}, j'_{pol1}, j_{pol2}, and j'_{pol2}) are in blue, the diamagnetic currents (j_{dia}, j'_{dia}, and j_{dia2}) are in green, the Alfvénic current (j_{alf}) is in red and the pile-up current (j_{ohm}) is in yellow.

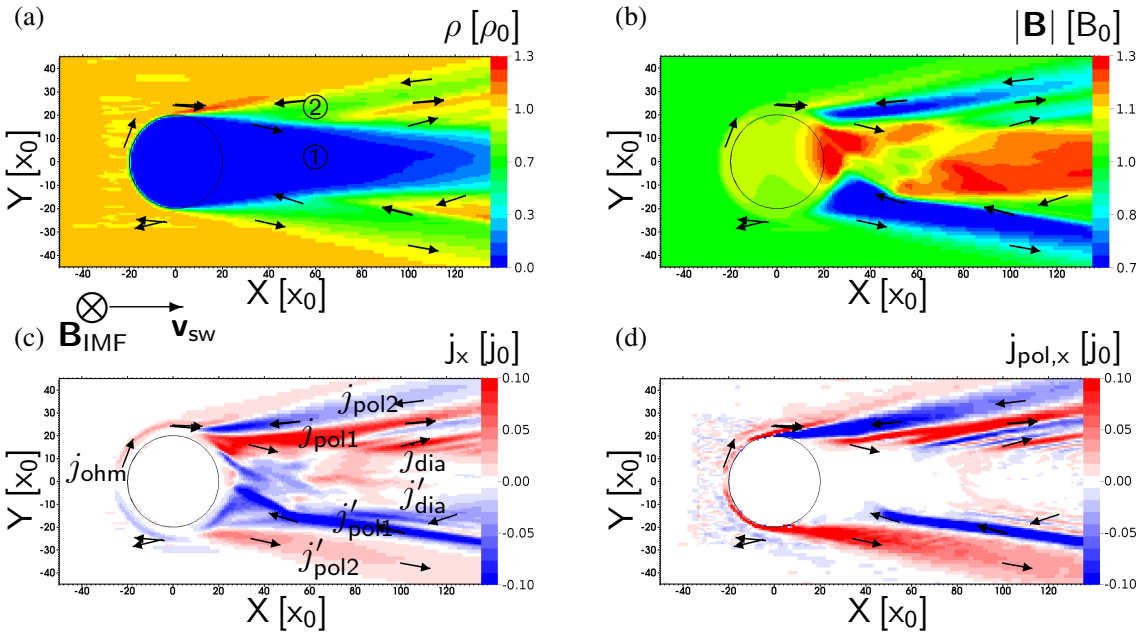

Figure 3.1: Simulation results in the plane Z=0. The stellar wind flow is directed to the right and the IMF is pointing into the plane. The arrows presented on each figure are the currents in this plane. Panel (a), (b), (c), and (d) show the density, the magnitude of the magnetic field, the X-component of the total current, and the X-component of the polarization current, respectively (see section 3.3.1).

3.2.2 Stellar wind velocity transitions

The goal of this section is to explore the parameter space in terms of stellar wind velocities; simulations are performed starting from the Lunar-Type case previously described with a stellar wind velocity v_{sw}=8 $v_{A,0}$ and extending to simulations with decreasing the stellar wind velocity step by step: the results presented are for simulations with stellar wind velocities v_{sw}=7 $v_{A,0}$, 4 $v_{A,0}$, 2 $v_{A,0}$, 1 $v_{A,0}$ and 0.5 $v_{A,0}$. Figure 3.3, rows a and b, gives the evolution of density and magnetic field structures, respectively. Two regions previously described for the Lunar-Type system can be identified, and their evolution with decreasing stellar wind velocity illustrated. While the region ① refills faster with decreasing velocity, the region ② expands away from the wake. When the trans-Alfvénic regime is reached (v_{sw}=1 $v_{A,0}$) and switches to a sub-Alfvénic regime (v_{sw}=0.5 $v_{A,0}$), the region ② completely disappears. The field depression which still appears for v_{sw}=1 $v_{A,0}$ and 0.5 $v_{A,0}$ at Y=±40 x_0 is due to the diamagnetic current. The asymmetry discussed in the previous section disappears as the upstream velocity decreases, due to the finite ion gyroradius which is proportional to the bulk velocity and which decreases from 8 x_0 at v_{sw}=8 $v_{A,0}$ to 0.5 x_0 at v_{sw}=0.5 $v_{A,0}$ (see Table 2.1 for the normalization units).
While decreasing upstream velocity, the magnetic Reynolds number decreases from $\mathcal{Re}$ = $8 \cdot 10^{-2}$ at v_{sw}=8 $v_{A,0}$ to $5 \cdot 10^{-3}$ at v_{sw}=0.5$v_{A,0}$. Therefore, at low upstream velocities, the obstacle acts like a perfect insulator and the magnetic field can freely penetrate the obstacle. This is presented in Figure 3.3 row b, where the magnetic field is not able to penetrate the obstacle for v_{sw}=7 $v_{A,0}$ and forms a small magnetic pile-up region in front of the ob-

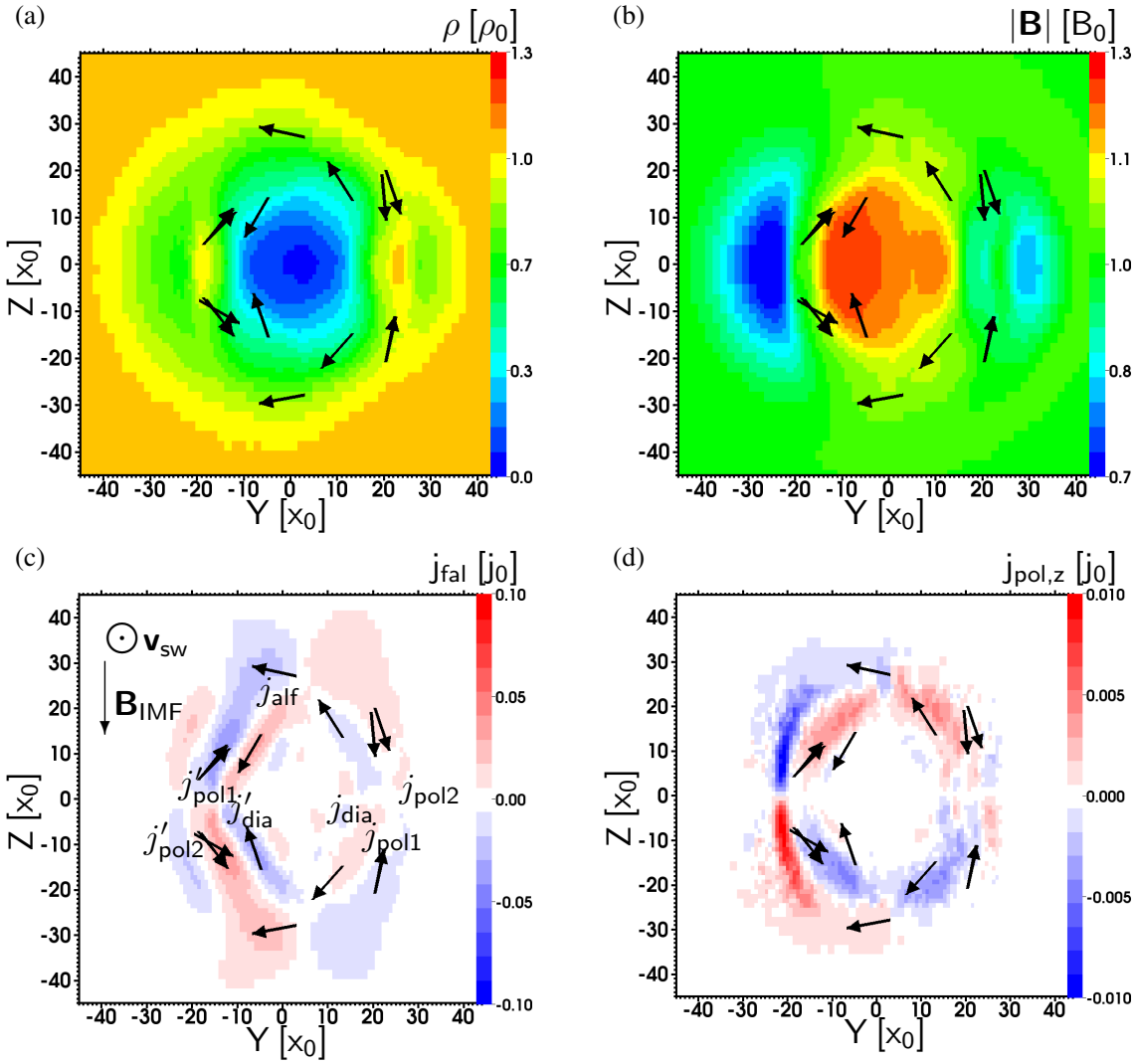

Figure 3.2: Simulation results in the plane X=100 x_0. The stellar wind flow is directed out of the plane and the IMF is directed southward. The arrows presented on each figure are the currents in this plane. The Panel (a) shows the density, Panel (b) shows the magnitude of the magnetic field, Panel (c) shows the field aligned current computed by deriving the scalar product between the magnetic field and the current, and Panel (d) shows the Z-component of the polarization current (see section 3.3.1).

stacle, the obstacle acts like a weakly conducting object. On the contrary for v_{sw}=1 $v_{A,0}$ the magnetic field can penetrate the obstacle and we observe a magnetic field gradient between the nightside and the dayside of the obstacle, which acts like a good insulating object. The magnetic field surrounding the obstacle at v_{sw}=0.5 $v_{A,0}$ may be due to the presence of slow magnetosonic waves. In Figure 3.3 row c, we can see the X-component of the current, where the currents j_{dia}, j_{pol1}, and j_{pol2} identified in Section 3.2.1 are recognizable. We can notice that the current in the obstacle seen in Figure 3.3 row f, is parallel to $\boldsymbol{E}$. This corresponds to the property of an Ohmic current. Figure 3.3e shows the draping of the magnetic field which follows the structure of an Alfvén wing. We see that the

magnitude of the variation of B_x decreases with the upstream velocity. This is consistent with the property of the Alfvén wing to have a maximum B_x variation proportional to the Alfvén Mach number multiplied by the magnetic field magnitude. Figure 3.3d presents the density in the meridional plane. We can see that the density signature widens while the stellar wind velocity decreases, which can be interpreted by means of the propagation of the slow magnetosonic waves triggered by the obstacle (this point is further discussed in Section 3.3). Figure 3.3f gives an overview of how the current flows around these wings: it flows into the plane in the outer part of the wings and flows out of the plane in the inner parts, and corresponds to the current labeled as j_{alf}. Another noticeable feature is the Y-component of the current represented in row f of Figure 3.3 flowing in front and inside of the obstacle and presented as current j_{ohm} in section 3.2.1. We can notice that, as the stellar wind velocity decreases, the magnetic Reynolds number decreases, thus the j_{ohm} current vanishes, as explained in section 2.3.2. The current appearing in front of the obstacle for v_{sw}=0.5 $v_{\mathrm{A,0}}$ is an Alfvén wing current.

3.3 Discussion

This section is divided in two parts. In the first part we explain the complete current and mode propagation structure of the Moon case. In the second part one extends the description of the structures to slower stellar wind velocities, in order to reach the sub-Alfvénic regime.

3.3.1 Lunar-Type case

The Moon is perturbing the plasma environment in two ways: (1) by absorbing particles and thus creating a density depletion, and (2) by propagating the magnetic field by diffusion through a weakly conducting medium, as explained in section 3.1. Most of the effects have been described in the literature (Halekas et al. 2011), here we provide a general description taking into account the magnetohydrodynamic waves triggered at the surface of the Moon. The absorption of plasma by the Moon leads to a density gradient between the wake and the undisturbed solar wind. This gradient leads to a diamagnetic current (Whang 1968a, Sonett and Colburn 1967) given by Equation (2.62), which are reproduced in our simulation and labeled j_{dia} and j'_{dia}, circumscribing the inner wake. However, the diamagnetic current alone is not sufficient to build a closed current system. One needs the addition of the polarization current, which is found in Figure 3.1d and Figure 3.2d. We show in section 3.2.1 that the current flowing along each region in the plane Z=0 closes by going out of this plane, following the outer shape of the magnetic field magnitude gradient ($\nabla|\boldsymbol{B}|$) region. Studies of current loops through the wake of the Moon can also be emphasized by means of magnetosonic waves soundings. Such studies have been carried out by Wiehle et al. (2011). It was shown that the variation of the magnetic field parallel and perpendicular to the interplanetary magnetic field (IMF), shows structures corresponding to the magnetosonic modes. However, this study used the phase velocity of waves carried by the solar wind. It would be more accurate to use the group velocity of the magnetosonic waves, which transports the energy. This creates grounds to obtain the detailed structure of the Moon's wake from the mode propagation. We can

then connect the current flowing around the wake as describing those structures. As seen in Figure 3.1, the currents j_{pol1}, j'_{pol1}, j_{pol2}, j'_{pol2}, and j_{alf} are flowing along the regions of high magnetic field gradient. In order to draw the propagated mode into the wake, we perform a calculation using the known solution of magnetosonic modes for the group velocity (Baumjohann and Treumann 1996). The complete detail of the calculation is given in Appendix B. To write these solutions we need to define the wave vector:

$$\boldsymbol{k} = \begin{pmatrix} k_\perp \\ k_\parallel \end{pmatrix} \quad , \tag{3.1}$$

with $k_\perp$ being the component of the wave vector perpendicular to the magnetic field and $k_\parallel$ the component parallel to the magnetic field. The solutions are written in the same base:

$$\boldsymbol{v}_{\mathbf{gr,A}} = \pm \begin{pmatrix} 0 \\ v_{\mathrm{A}} \end{pmatrix} \quad , \tag{3.2}$$

where $\boldsymbol{v}_{\mathbf{gr,A}}$ is the group velocity of the Alfvén mode. In order to write the group velocity, the magnetosonic phase velocity $v_{\mathrm{ph,ms}}$ needs to be defined:

$$v^2_{\mathrm{ph,ms}} = \frac{1}{2}\left(v^2_{\mathrm{A}} + c^2_{\mathrm{s}} \pm \sqrt{\left(v^2_{\mathrm{A}} - c^2_{\mathrm{s}}\right)^2 + 4c^2_{\mathrm{s}} v^2_{\mathrm{A}} \frac{k^2_\perp}{k^2}}\right) \quad , \tag{3.3}$$

the expression of the magnetosonic group velocity $v_{\mathrm{gr,ms}}$ of these modes is then:

$$\boldsymbol{v}_{\mathbf{gr,ms}} = \begin{pmatrix} \dfrac{k_\perp}{|\boldsymbol{k}|}\dfrac{1}{v_{\mathrm{ph,ms}}}\left(v^2_{\mathrm{ph,ms}} - \dfrac{k^2_\parallel}{k^2}\dfrac{c^2_{\mathrm{s}} v^2_{\mathrm{A}}}{c^2_{\mathrm{s}} + v^2_{\mathrm{A}} - 2v^2_{\mathrm{ph,ms}}}\right) \\ \dfrac{k_\parallel}{|\boldsymbol{k}|}\dfrac{1}{v_{\mathrm{ph,ms}}}\left(v^2_{\mathrm{ph,ms}} + \dfrac{k^2_\perp}{k^2}\dfrac{c^2_{\mathrm{s}} v^2_{\mathrm{A}}}{c^2_{\mathrm{s}} + v^2_{\mathrm{A}} - 2v^2_{\mathrm{ph,ms}}}\right) \end{pmatrix} \quad . \tag{3.4}$$

The maximum angle of the magnetic field in relation to the IMF is of the order of 5° which represents the maximum ratio $\delta B/B$. Thus, one can approximates the parallel component to the Z-component and the perpendicular component to the Y-component.
Wiehle et al. (2011) show that the outer structure of the wake follows a Friedrichs diagram-like configuration, but only the furthest positions of the propagated modes are plotted. Here we calculate the sum of the modes generated at the surface of the Moon and present the regions where this sum reaches a peak. Figure 3.4 presents the patterns of the propagated modes triggered at the surface of the Lunar-Type obstacle for a stellar wind v_{sw}=8$v_{\mathrm{A,0}}$ and v_{sw}=2$v_{\mathrm{A,0}}$. This matches the patterns defined by the magnetic field magnitude and the density. We can see in Figures 3.4a and 3.4c the levels of magnetic field and the levels of densities in the X-cross-section, respectively. By looking at the center of the wake, one can see that the slow mode is extending in a vertical way as the magnetic field increases and density decreases. The slow magnetosonic waves, which are dominant in the center of the wake, have a group velocity mainly directed along the field lines as seen in the structure of the density and magnetic field. The fast magnetosonic waves propagate in every direction and in particular perpendicular to the field. This is evinced by the local magnetic field and density decreases on each side of the wake. Although this modeling works well for weak disturbances of the plasma, it became necessary to take into account the bulk velocity field of the structure when disturbance

reach the same order of magnitude than the background. Furthermore, for disturbance stronger than the background, the density distribution and the magnetic field distribution must be taken into account in order to derive the Alfvén and sound velocities at each point of the grid, which remains to be implemented.
Examples of current streamlines are shown in Figure 3.5. Three different trajectories can be distinguished, starting in the $-Y$-part of the diamagnetic current, which corresponds to the j'_{dia} current previously described in section 3.2.1, and flowing towards the obstacle. These current streamlines flow in the equatorial plane, and slowly leave this plane. One can see that one current goes to the $+Y$ part by following a path in the X cross-section, described as j_{alf} current, and joins the diamagnetic current flowing away from the obstacle, described as j_{dia} current. A second current is also joining the $+Y$-part by passing by the X cross-section, but merges with the inner fast mode polarization current j_{pol1}. A last current is staying in the $-Y$-half plane and joins the outer fast mode polarization current j'_{pol2}.
From the descriptions detailed above, we obtain a consistent description of the interaction with a stellar in a Lunar-Type system and the evolution by changing the stellar wind velocity. This description is illustrated in Figure 3.6 which provides a thee dimensional diagram of the configuration of currents flowing in the Lunar-Type system, which uses a stellar wind velocity v_{sw}=8 $v_{\mathrm{A,0}}$. The different triggered currents are annotated, the path of the currents in the plasma structure is represented with their possibility of closing. As we have showed, there is a diamagnetic current flowing in the inner part of the wake due to the pressure gradient (see Equation (2.62)) directed outward of the wake (j_{dia}). The current j_{pol1} flows next to the current j_{dia} flows. It is a polarization current flowing around the outer fast mode represented by the wings of the wake, noted region ②. The outer part of the fast mode zone is bounded by the current j_{pol2}, which also appears to be a polarization current. A way to reach the current closure, is the current flowing in front of the obstacle (j_{ohm}), which is similar to a pile-up current. The existence of this pile-up current is highly dependent on the conductivity of the obstacle. In the case of Earth's moon, the diffusion velocity of the magnetic field is high enough to avoid any noticeable pile-up. However when studying a body of different composition, this aspect should not be neglected. Another current closure exists by means of a current flowing from the half plane $Y\geqslant 0$, Z=0 to the half plane $Y\leqslant 0$, Z=0 between the diamagnetic current. This current labeled j_{dia2} has been presented for Rhea by Simon et al. (2012); its existence is explained by the ion pressure gradient $\nabla \mathbf{P}_{\mathrm{i}}$ in the direction of the flow in the center of the wake. Such a pressure gradient leads to a diamagnetic current, which creates a draping of the magnetic field. The draping of the magnetic field follows an Alfvénic structure and thus a Alfvénic current (j_{alf}) is flowing around this structure, connecting the diamagnetic current (j_{dia}) on both side of the wake. The strength of the diamagnetic current j_{dia2} strongly depends on the ratio between the thermal velocity and the bulk velocity, which determine the expansion of the wake refilling, thus it is easily seen at Rhea than at the Moon.

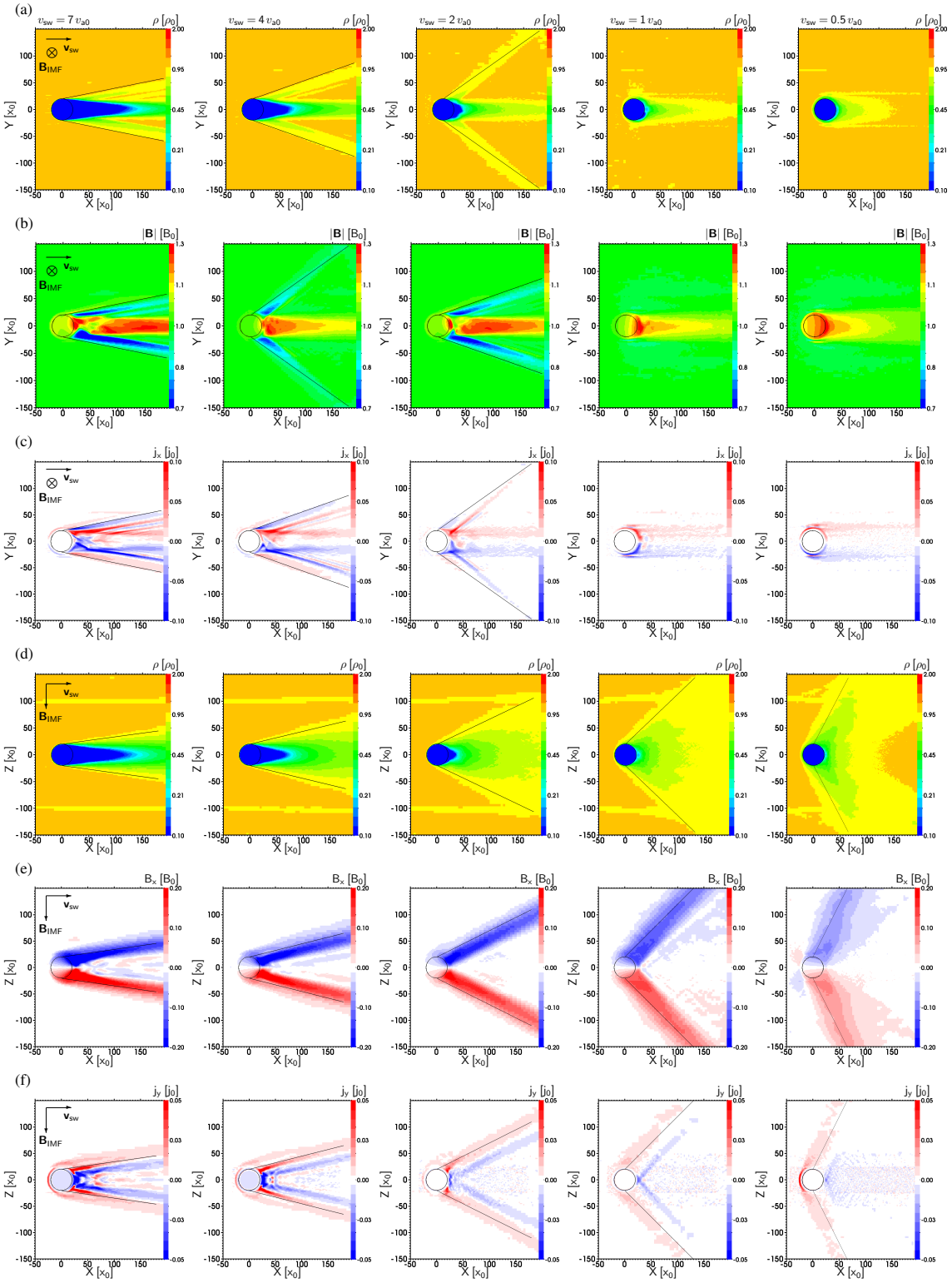

Figure 3.3: Simulation results for different stellar wind velocities. Each column is 7 $v_{A,0}$, 4 $v_{A,0}$, 2 $v_{A,0}$, 1 $v_{A,0}$ and 0.5 $v_{A,0}$, respectively. Rows (a), (b), (c) are the density, magnetic field magnitude, and X-component of the current density in the plane Z=0, respectively. Rows (d), (e), (f) are the density, X-component of the magnetic field, and Y-component of the current density in the plane Y=0, respectively. Black lines are boundaries derived from the group velocity of MHD modes with respect to each plane (see section 3.3.2).

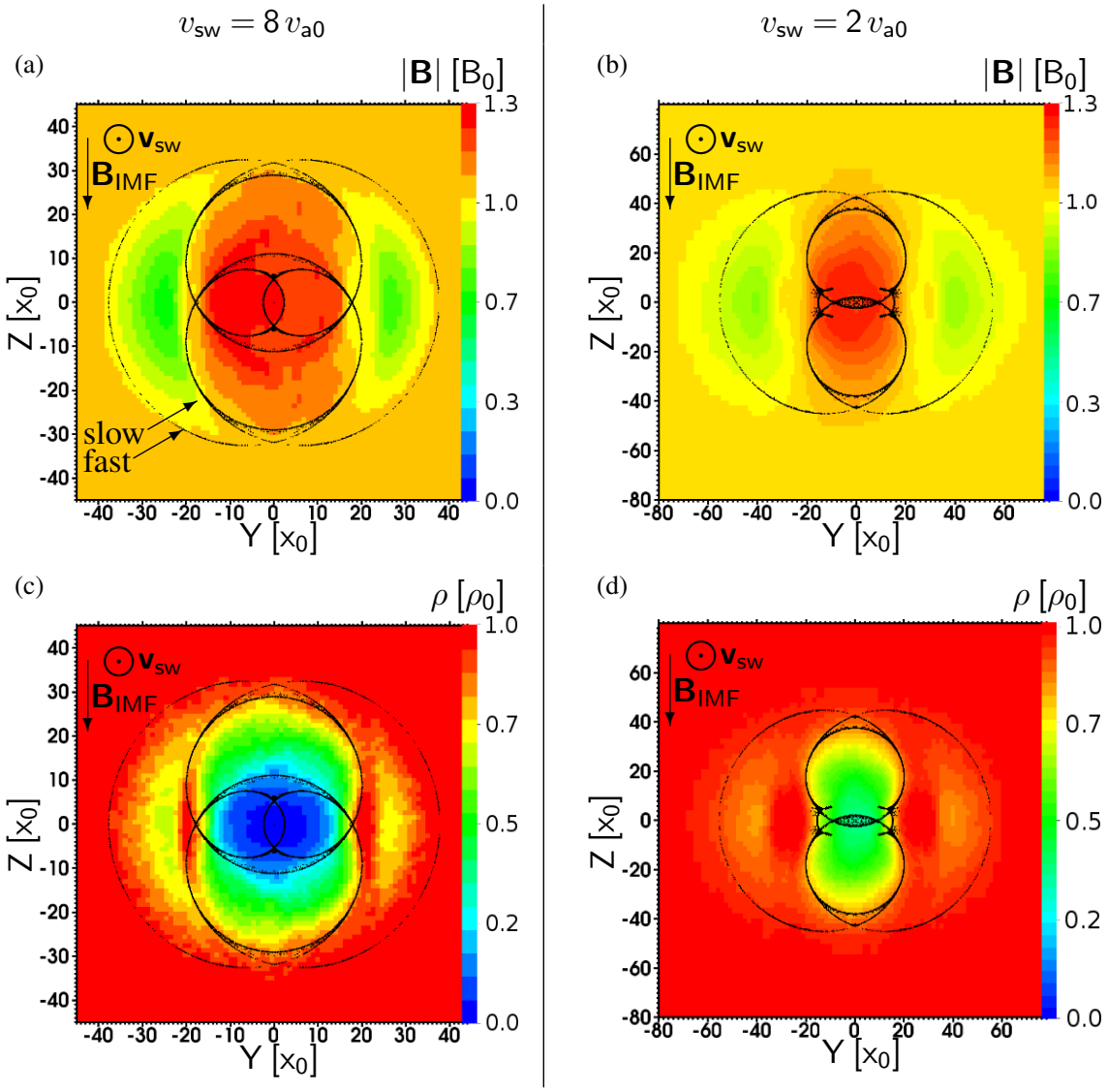

Figure 3.4: Configuration and comparison of the MHD waves triggered at the surface of the moon. On the left, Panels (a) and (c) show the magnetic field magnitude and the density, respectively, in the plane X=100 x_0 for a stellar wind velocity v_{sw}=8 $v_{A,0}$. On the right, Panels (b) and (d) are the magnetic field magnitude and the density, respectively, in the plane X=50x_0 for a stellar wind velocity v_{sw}=2$v_{A,0}$. We compute the waves by deriving the velocity of each wave at the surface of the Moon and propagating it by the stellar wind velocity. The waves are over-plotted to each figure. The annotation "slow" and "fast" refer to the slow and fast magnetosonic wave boundaries. Details on the normalized parameters are given in Table 2.1. The simulation geometry is detailed in Section 2.2.2.1.

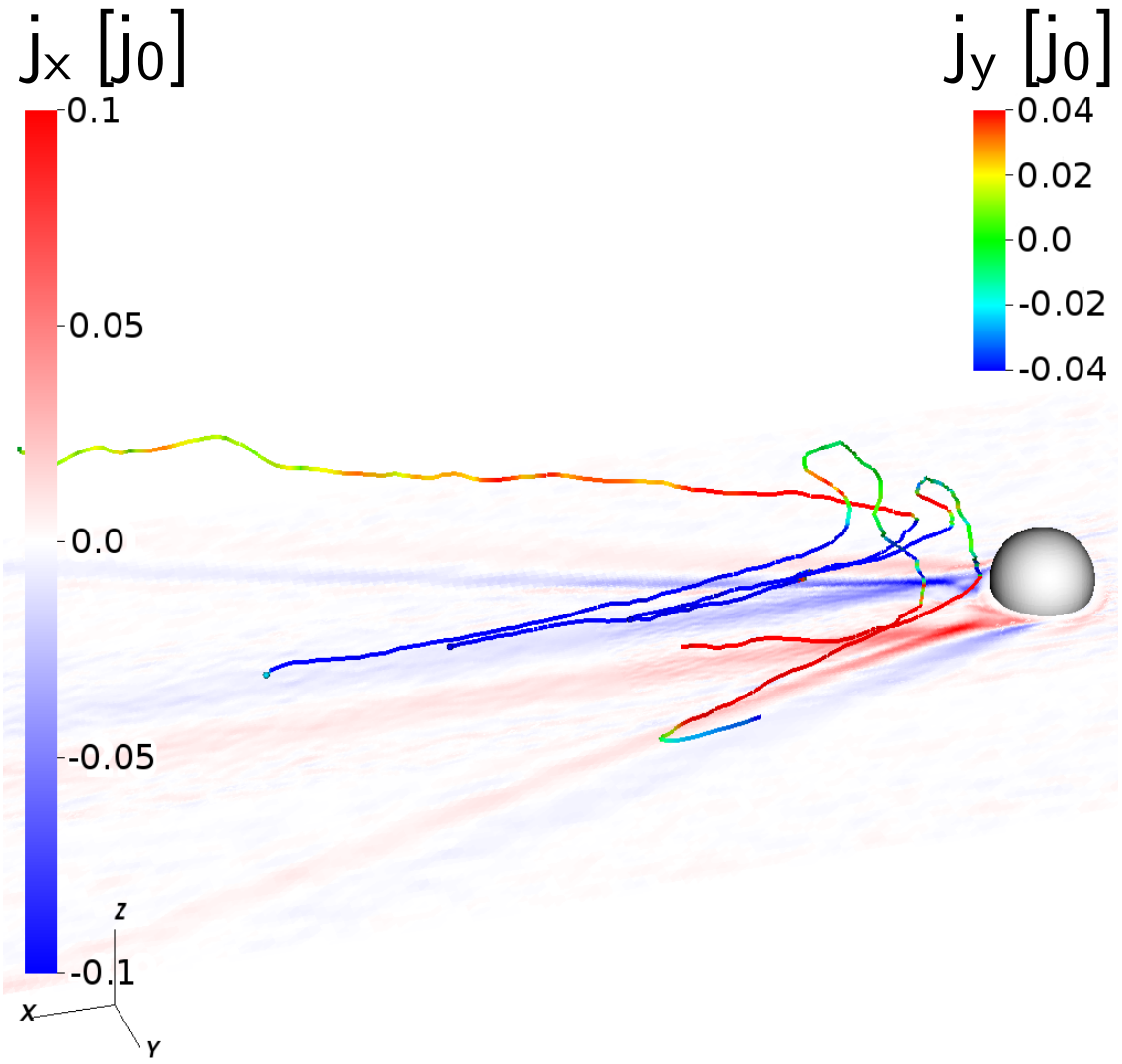

Figure 3.5: X-component of the current density is represented in the plane Z=−5x_0), its colorbar is on the left part. Three examples of current streamlines are presented with their colorbar on the right part. The streamlines start in the same current region and reach three different current regions.

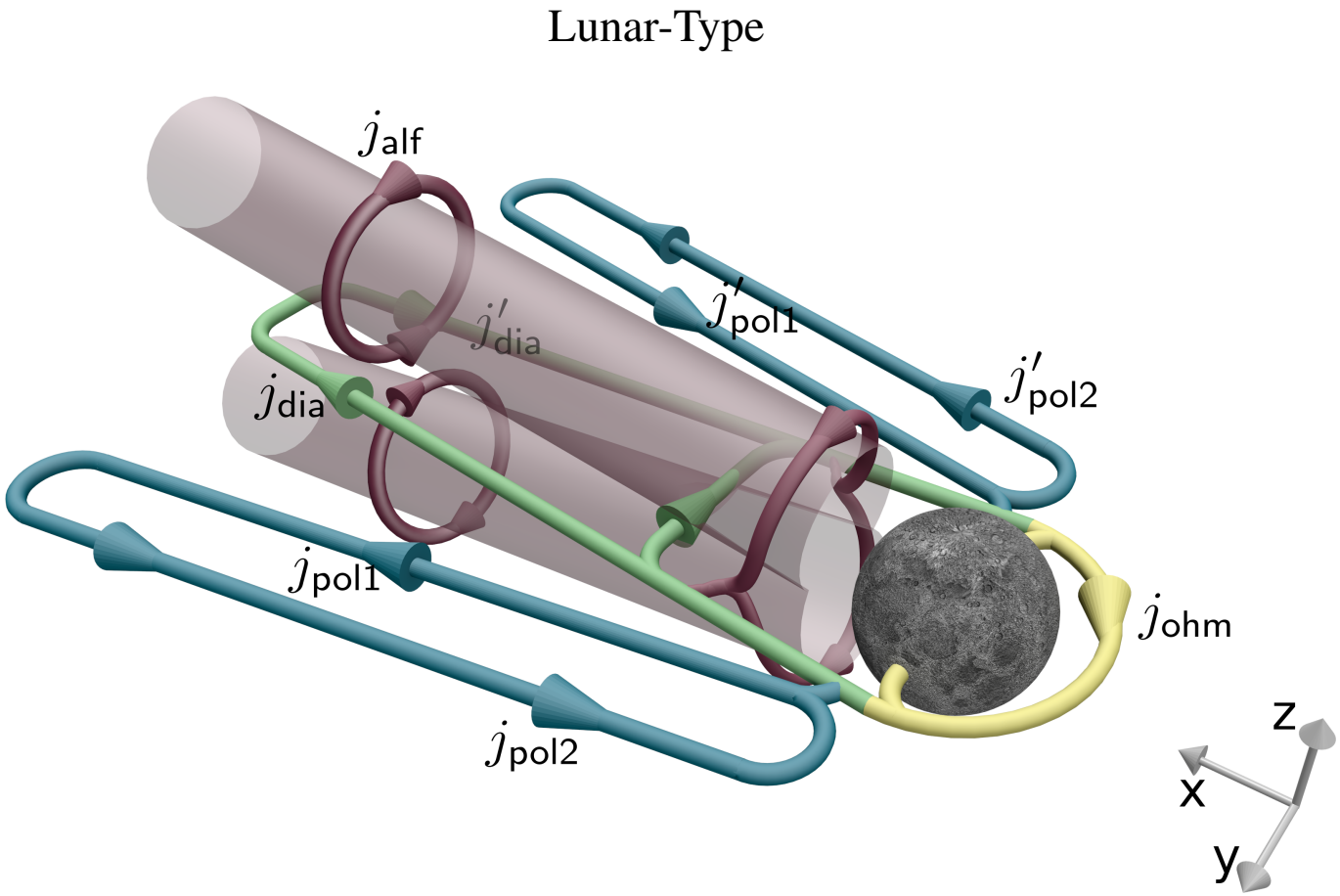

Figure 3.6: Three-dimensional representation of the Lunar-Type current system. Blue currents display fast fast waves polarization currents, Alfvénic currents are represented in red, green currents are diamagnetic currents and yellow currents are related to pile-up currents (see section 3.3 and Table 2.3). The stellar wind flows along $+X$, the IMF is directed along $-Z$. The semi-transparent layer represents the Alfvén wings. The radius of the obstacle is $20x_0$ (see Tables 2.2 and 2.1). The stellar wind velocity is $8v_{A,0}$ (see Table 3.2).

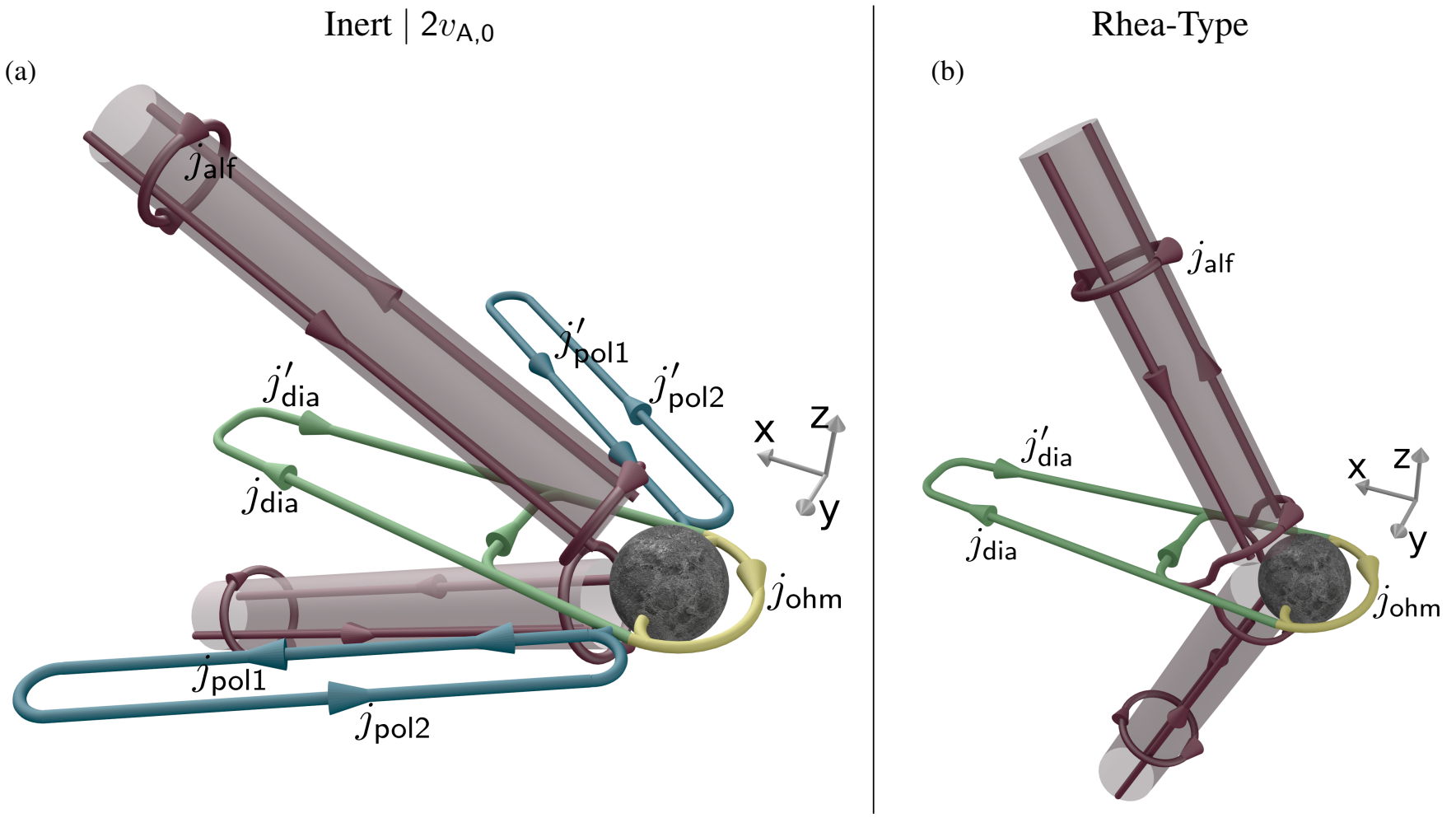

Figure 3.7: Three-dimensional representations of the current system: (a) Inert | $2v_{A,0}$ with $v_{sw} = 2\ v_{A,0}$; (b) Rhea-Type with $v_{sw} = 0.5\ v_{A,0}$ (see Table 3.2). Notations same as Figure 3.6.

3.3.2 Stellar wind velocity transitions

At this point, we have established the structure of the current loops for the Lunar-Type and Rhea-Type systems. The next step deals with the transition between the super-Alfvénic and the sub-Alfvénic regime. The mode description that we have presented in the previous section provides solid grounds to study this transition. We extend this mode description to different stellar wind velocities. The propagation of modes described by Equations (3.2) and (3.4) is shown in each plane in Figure 3.3. The fast mode boundaries are drawn in Figure 3.3d, their expression in the equatorial plane is $Y(X)=\pm X\left(\sqrt{v_A^2+c_s^2}\right)/v_{sw} \pm R_p$. The angle made by the fast mode boundaries to the X-axis is changing from 11° at $v_{sw}=7\,v_{A,0}$ to 35° at $v_{sw}=2v_{A,0}$. The function $Y(X)=\pm X v_A/v_{sw}\pm R_p$ is presented in Figures 3.3e and f, and represents the Alfvén waves boundaries in the longitudinal plane. The angle made by the Alfvén wing to the X-axis is changing from 8.1° at $v_{sw}=7\ v_{A,0}$ to 63° at $v_{sw}=0.5\ v_{A,0}$. The function $Y(X)=\pm X\,c_s/v_{sw}\pm R_p$, which represents the magnetosonic slow wave boundaries, is shown in row d. The angle made by the slow mode boundaries with the Y-axis is changing from 7.7° at $v_{sw}=7\ v_{A,0}$ to 62° at $v_{sw}=0.5\ v_{A,0}$. These results show that in the equatorial plane, the wings enclosed by currents j_{pol1} and j_{pol2} are signatures of the propagation of a fast magnetosonic waves generated at the surface of the Moon. Also, in the longitudinal plane, the current j_{alf}, which follows the draping of the magnetic field shown in row e of Figure 3.3, is linked to an Alfvén mode triggered by a diamagnetic current flowing at the center of the wake (Simon et al. 2012). Also the shape of the density depletion in the longitudinal plane follows the configuration of a slow magnetosonic waves triggered by the Moon. The results presented in Section 3.2.2 in Figure 3.3 show that, when the stellar wind velocity is decreased, the different current structures linked to Alfvén, slow and fast modes are spreading in space, whereas the diamagnetic current, directly related to the wake refilling, remain closer to the surface of the obstacle. Then, we can picture the current system from the prospect of the propagated modes. This is shown in Figure 3.4, where one sees the different propagated modes depending on the stellar wind velocity.

A summary of the evolution of the current structures is presented in Figure 3.7. Figure 3.7a presents the current structures for a stellar wind velocity $v_{sw}=2\ v_{A,0}$, and Figure 3.7b shows how the structures expand with a stellar wind velocity $v_{sw}=0.5\ v_{A,0}$. The Alfvénic structure is expending from the center of the wake to an angle determined by the ratio between the solar wind velocity and the Alfvén speed. This Alfvénic structure evolves from a state where it is merged with the center of the wake to a distinct structure. From a more general point of view, one can say that by decreasing the stellar wind velocity, the global structure switches from a horizontal structure to a vertical structure. The proportion of the diamagnetic current decreases, as the proportion of field aligned current increases. Another noteworthy point is that, a fast mode does not have a stationary solution in a trans- or sub-magnetosonic regime and thus is absent from our results (Neubauer 1998). This leads to the removal of the currents j_{pol1} and j_{pol2} (also j'_{pol1} and j'_{pol2}), which represent the polarization current of the fast mode, looping on both the outer edges of the wake. Figure 3.3 shows that the fast mode signature and thus the current loops disappear when we reach a stellar wind velocity $v_{sw}=1\ v_{A,0}$ and for a sub-Alfvénic regime, as shown in the three dimensional sketch in Figure 3.7b where the structures are drawn for an upstream velocity $v_{sw}=0.5\ v_{A,0}$.

3.4 Conclusions

We have investigated a generalization of the lunar type interaction, to establish a fully self-consistent model of the interaction between a lunar type obstacle and a stellar wind. We describe this interaction by magnetohydrodynamics waves triggered by the density depletion at the day-night boundary. This is a generalization of the wave propagation calculations by Wiehle et al. (2011). In this chapter, we have investigated the different types of lunar related currents flowing around the wake and the surface of a Lunar-Type obstacle, and identified three major types of current: (1) the diamagnetic current flowing on the both side of the wake; (2) the pile-up current which existence is dependent of the inner conductivity of the obstacle and the stellar wind velocity (both being summed up in the magnetic Reynolds number $\mathcal{R}e$); (3) the polarization current flowing around each mode structure propagated through the wake. The dominant current is the fast mode polarization current flowing along the wings of the plasma structure in the plane perpendicular to the IMF. This current disappears at trans-Alfvénic and sub-Alfvénic regimes due to the non-existence of the fast mode in these regime. The Alfvén polarization current can be observed mostly in the plane parallel to the IMF. Although the density depletion in the longitudinal plane follows the structure of the slow mode, no distinct current can be inferred. The systematization that we have established can thus be applied to any inert obstacle, and provides a good angle for a more complete generalization taking into account dipole fields and ionospheres.

4 Northward magnetized obstacles in super- and sub-Alfvénic regime

4.1 Introduction

In this chapter, we study a Moon-size obstacle lacking an ionosphere, but having an intrinsic magnetic dipole and a small core. Specifically, we treat the case of a planetary obstacle having a magnetic moment anti-parallel to the local interplanetary magnetic field (IMF). This configuration is usually referred to as "northward IMF" or "closed magnetosphere" in the literature. This particular state has been mostly studied in the framework of Earth's magnetosphere for time period ranging from several hours to a few days. A model of closed magnetosphere was proposed by Piddington (1979), taking into account the shearing of the magnetopause by the solar wind and assuming that no reconnection occurs. Several properties have been described such as the sunward convection at the polar cap due to reconnection (Russell 1972), two-cell convection patterns in the tail (Maezawa 1976). Confirmations and improvement of the description of these effects were done using magnetohydrodynamics (MHD) simulations (Ogino and Walker 1984, Wu 1985). They described the convection system through viscosity and reconnection. The reconnection process at high latitude associated with a northward IMF was first measured for Earth by Kessel et al. (1996). Besides, in the case of Earth, field aligned currents connected to the ionosphere were highlighted (Iijima et al. 1984). The entry of solar wind ions into the magnetosphere forming the cold dense plasma sheet has been described by Li et al. (2005), through Kelvin-Helmholtz diffusion processes.

In our simulation, we vary the strength of the magnetic moment from zero until a fully developed bow-shock arises for an Earth-like upstream velocity. We divide the evolution of the plasma structure in several qualitative steps and identify the currents out of the magnetic field configuration. We carry on this study for upstream velocities from Earth-like upstream velocity to sub-Alfvénic velocities. The case of a magnetic dipole in a sub-Alfvénic regime is only known in our solar system for the particular case of Ganymede (Kivelson et al. 1996). However the magnetic field of Ganymede is anti-parallel to the Jovian magnetic field. This configuration was described by Ridley (2007) in a sub-Alfvénic regime for Earth. He also introduces the particular case of Alfvén wing associated to a northward IMF.

The magnetic moments treated in this chapter are from M=100M_0 to M=80 $\cdot 10^3 M_0$. These values can be compared from obstacle of the solar system. For example, at Mercury, measurements give n_{sw}=30 cm^{-3}, B_{sw}=20 nT for the upstream conditions, and the magnetic moment of Mercury is M=1.4 $\cdot 10^{13}$ Am^2 (Mueller et al. 2012). Although a weak

Simulation regime	*Axis*	*Box length*	*Cells*
super-Alfvénic	*X*-axis	600 x_0	144
	Y-axis	300 x_0	96
	Z-axis	400 x_0	96
sub-Alfvénic	*X*-axis	400 x_0	128
	Y-axis	300 x_0	96
	Z-axis	800 x_0	256

Table 4.1: Configuration and size of the grid along each axis of the simulations presented in Chapter 4. The length are expressed in normalized values, detailed in Table 2.1.

ionosphere impact the field dynamic at Mercury (Glassmeier 1997), it should be noted that we do not take this point into consideration in this chapter. These upstream parameters correspond to a normalized magnetic moment M=130 $\cdot 10^3 M_0$ (according to Table 2.1). Measurements at Ganymede give (Kivelson et al. 2004): n_{sw}=8 cm^{-3}, B_{sw}=65 nT, and the magnetic moment of Ganymede is M=4.8 $\cdot 10^{15}$ Am^2. These upstream parameters correspond to a normalized magnetic moment M=35 $\cdot 10^3 M_0$. One notices that, though the absolute magnetic moment of Ganymede is higher than the moment of Mercury, once expressed in normalized units, we understand that the interaction system of Ganymede is weaker than Mercury.

The grid configurations of the simulations ran for this chapter are detailed in Table 4.1. The geometry of the simulations, the obstacle size, and the plasma beta are given in Section 2.2.2.1 and Table 2.2. Details about the boundary conditions, the resistivity profile of the obstacle, and the numerical limitation are explained in Appendix A.1, A.2, and A.3. The parameters of the various situations treated in this chapter are summarized in Table 4.2. The stellar wind velocities are provided as well as the normalized magnetic moments (see Table 2.1 for the normalization formulas), and the stand-off distances, related to Equation (2.19).

This chapter falls into three sections. Section 4.2 is devoted to the results for four plasma parameter grid points and develops the current structures of these interaction regimes. In Section 4.3 we study the transition regime between the four grid points aforementioned. Our results are summarized in Section 4.4.

4.2 Cornerstones in the parameter space

We study the interaction types depending on the flow velocity and the magnetization of the planetary obstacle. We define four cornerstones in this two-dimensional parameter space spanned just by the flow velocity and the planetary magnetization: (1) Lunar-Upward; (2) Mercury-Upward; (3) Rhea-Upward; and (4) Ganymede-Upward. The phrase "weak dipole" refers to a planetary obstacle which has a magnetic moment not strong enough to balance the stellar wind dynamic pressure, pushing the magnetopause below the obstacle surface.

v_{sw} [$v_{A,0}$]	M [M_0]	L_{SO} [R_p]	*Case name*	*Alternative name*	*Figure*
8	100	0.15	$+100M_0\hat{z} \mid 8v_{A,0}$	Lunar-Upward	Fig. 4.1
	$80 \cdot 10^3$	1.38	$+80\text{E}3M_0\hat{z} \mid 8v_{A,0}$	Mercury-Upward	
0,5	$5 \cdot 10^3$	1.04	$+5\text{E}3M_0\hat{z} \mid 0.5v_{A,0}$	Rhea-Upward	Fig. 4.3
	$40 \cdot 10^3$	2.08	$+40\text{E}3M_0\hat{z} \mid 0.5v_{A,0}$	Ganymede-Upward	
8	$5 \cdot 10^3$	0.55	$+5\text{E}3M_0\hat{z} \mid 8v_{A,0}$		
	$10 \cdot 10^3$	0.69	$+10\text{E}3M_0\hat{z} \mid 8v_{A,0}$		Fig. 4.5
	$20 \cdot 10^3$	0.87	$+20\text{E}3M_0\hat{z} \mid 8v_{A,0}$		Fig. 4.6
	$40 \cdot 10^3$	1.10	$+40\text{E}3M_0\hat{z} \mid 8v_{A,0}$		Fig. 4.7
	$50 \cdot 10^3$	1.18	$+50\text{E}3M_0\hat{z} \mid 8v_{A,0}$		
2	$5 \cdot 10^3$	0.84	$+5\text{E}3M_0\hat{z} \mid 2v_{A,0}$		Fig. 4.11
	$40 \cdot 10^3$	1.68	$+40\text{E}3M_0\hat{z} \mid 2v_{A,0}$		
1	500	0.45	$+500M_0\hat{z} \mid 1v_{A,0}$		Fig. 4.14
	$5 \cdot 10^3$	0.97	$+5\text{E}3M_0\hat{z} \mid 1v_{A,0}$		Fig. 4.15
	$40 \cdot 10^3$	1.94	$+40\text{E}3M_0\hat{z} \mid 1v_{A,0}$		Fig. 4.16

Table 4.2: Parameters for simulations presented in this chapter. The magnetic moment is given in normalized value (see Table 2.1). The term L_{SO} refers to the stand-off distance which expression is detailed in Section 2.2.2.2 and given by Equation (2.19). The name of each case gives the orientation ($-\hat{z}$) and the magnitude of the magnetic moment of the obstacle, and the upstream velocity of the stellar wind. The alternative names gives the reader an analogy to specific interaction systems found in the solar system. The figures associated with the presented cases are referenced in the last column.

4.2.1 Planetary obstacle in super-Alfvénic regime: Lunar-Upward versus Mercury-Upward

Figure 4.1 presents the simulation results for a Lunar-Upward case and a Mercury-Upward case. For these simulations, the upstream velocity is: v_{sw}=8 $v_{A,0}$. Figures 4.1a and 4.1b show the current loops for the Lunar-Upward obstacle. For this case, the stand-off distance (see Section 2.2.2.2) is L_{SO}=0.15 R_p, and the surface magnetic field is well beyond the IMF which therefore dominates the interior of the obstacle (see Table 4.2 for specific simulation parameters). The current identified as j_{ohm} in Figure 4.1a refers to the Ohmic current due the non-perfect dielectric nature of the obstacle. The Ohmic current is flowing along the obstacle on the dayside, anti-parallel to the electric field in the meridian plane, and parallel to the electric field inside the obstacle. The nightside of the interaction region is shown in Figure 4.1b. The current j_{alf} appears to flow in a closed loop. In the northern side of the wake, the current flows anti-parallel to the electric field in the top part and parallel to the electric field in the bottom part of the loop. The current j_{alf} is identified as an Alfvénic current in Chapter 3.

The current system of the Lunar-Upward system is comparable to the Lunar-Type interaction type. Therefore, the schematic of this interaction types refers to Figures 3.6. The currents j_{dia}, j_{pol}, j_{alf} and j_{ohm} have been fully described in Section 3.3, but a short summary is provided for the sake of clarity. The current j_{dia} (green) is a diamagnetic current

created by the pressure gradient between the void region (in the center of the wake) and the intermediate boundaries. The currents j_{pol} and j'_{pol} are fast mode polarization currents due to the rarefaction waves triggered by the obstacle. The current j_{alf} is an Alfvénic current generated by the draping of the magnetic field in the wake. This draping follows from a perpendicular diamagnetic current at the center of the wake (Simon et al. 2012). The current j_{ohm} is an Ohmic current, which existence depends on the conductive properties of the obstacle (see Section 2.3.2). One has to notice that, on the dayside of the obstacle, shown in Figure 4.1a, the compression of the planetary field leads to the creation of a Chapman-Ferraro current (further detail are given in Section 4.3.1). Due to the northward orientation of the planetary magnetic moment, the Chapman-Ferraro current merges with the Ohmic current in the equatorial plane, but competes with j_{ohm} at the north and south poles. However, The Chapman-Ferraro current is clearly noticeable when the strength of the planetary magnetic field at the surface of the obstacle reaches the order of magnitude of the IMF, which is not the case for the parameters used in the Lunar-Upward system. Therefore, although the Chapman-Ferraro current should be present in a Lunar-Upward system, we do not represent it, since its magnitude is inferior to the magnitude of the Ohmic current in this specific interaction type.

Figures 4.1c and 4.1d present the simulation results for the Mercury-Upward interaction. The surface magnetic field is stronger than the IMF with B_{surf}=10 B_0 and the stand-off distance for this case is L_{SO}=1.38 R_p. The Mercury-Upward presented here is a magnetized obstacle, which magnetic pressure at the surface is higher than the stellar wind dynamic pressure. In this situation, a bow-shock is triggered ahead of the obstacle and the magnetopause is well defined. The current j_{bs} is identified in Figure 4.1c. This current is flowing anti-parallel to the electric field at the subsolar point. Also the currents j_{cha} and j'_{cha} are identified on the same plot. The current j_{cha} is flowing in the equatorial plane in the direction anti-parallel to the electric field, which means parallel to the current j_{bs}. At the poles, j_{cha} is flowing parallel to the electric field, which also corresponds to the reconnection current in this region. The current j'_{cha} is flowing in the nightside of the obstacle in the equatorial plane in the direction anti-parallel to the electric field. At the poles, j'_{cha} is parallel to the electric field. Therefore on the dawn side, the currents j_{cha} and j'_{cha} are flowing parallel to the planetary magnetic dipole field. On the dusk side however, the currents j_{cha} and j'_{cha} are flowing anti-parallel to the planetary magnetic dipole field. The currents j_{sho}, j_{bs}, and j_{msph} are indicated in Figure 4.1d, and represent the shocklet current, the bow-shock current, and the magnetopause current, respectively. The current j_{sho} flows parallel to the equatorial plane, following the curve of the bow-shock, and in alternate directions. The current j_{msph} flows in a θ-like configuration (Eastman et al. 1984). In the equatorial plane, j_{msph} flows parallel to the electric field and in the northern and southern edges of the magnetosphere, anti-parallel to the electric field. On the flanks, j_{msph} flows anti-parallel to the magnetic field on the dawn side and parallel to the magnetic field on the dusk side.

A schematic version of the Mercury-Upward interaction is presented in Figure 4.2. The view is focused on the dayside plasma interaction region for more clarity. Each current previously indicated are reproduced in the schematic. Comparing to the Lunar-Upward, in the Mercury-Upward system, the diamagnetic current j_{dia} does not appear anymore. However, the fast mode polarization current j_{pol} is still present but with a qualitatively different structure, spread in space between the boundaries of the wake, (defined in Chap-

ter 3) and the shocklets currents. The current j_{pol}, associated to the propagation of fast-waves, also propagates along the Z-axis, due to the spatial propagation property of the fast waves (see Equation (3.4)). This can be interpreted in the way that the polarization current j_{pol} flows parallel to the one represented in the equatorial plane and translated along the boundaries of the propagation front. This is sketched by the semi-transparent cone-like structure bounding the wake in Figure 4.2. The bow-shock current j_{bs} also develops along the Z-axis. For a Mercury-Upward case, the bow-shock is fully developed; the formation of the bow-shock is detailed in Section 4.3.2. The multiple currents noted j_{sho} seen in the magnetosheath region is a new important structure appearing in this regime. The mechanism linking the bow-shock and the shocklets has been emphasized by Bagdonat and Motschmann (2002a). However, it should be noticed that unlike Bagdonat and Motschmann (2002a), the shocklets are symmetric in our results. This can be explained by the fact that they were studying comets. In that case, the shocklets are generated by an ionospheric ion pick-up process, which is asymmetric by definition, whilst we are focusing on an axisymmetrical dipole field.

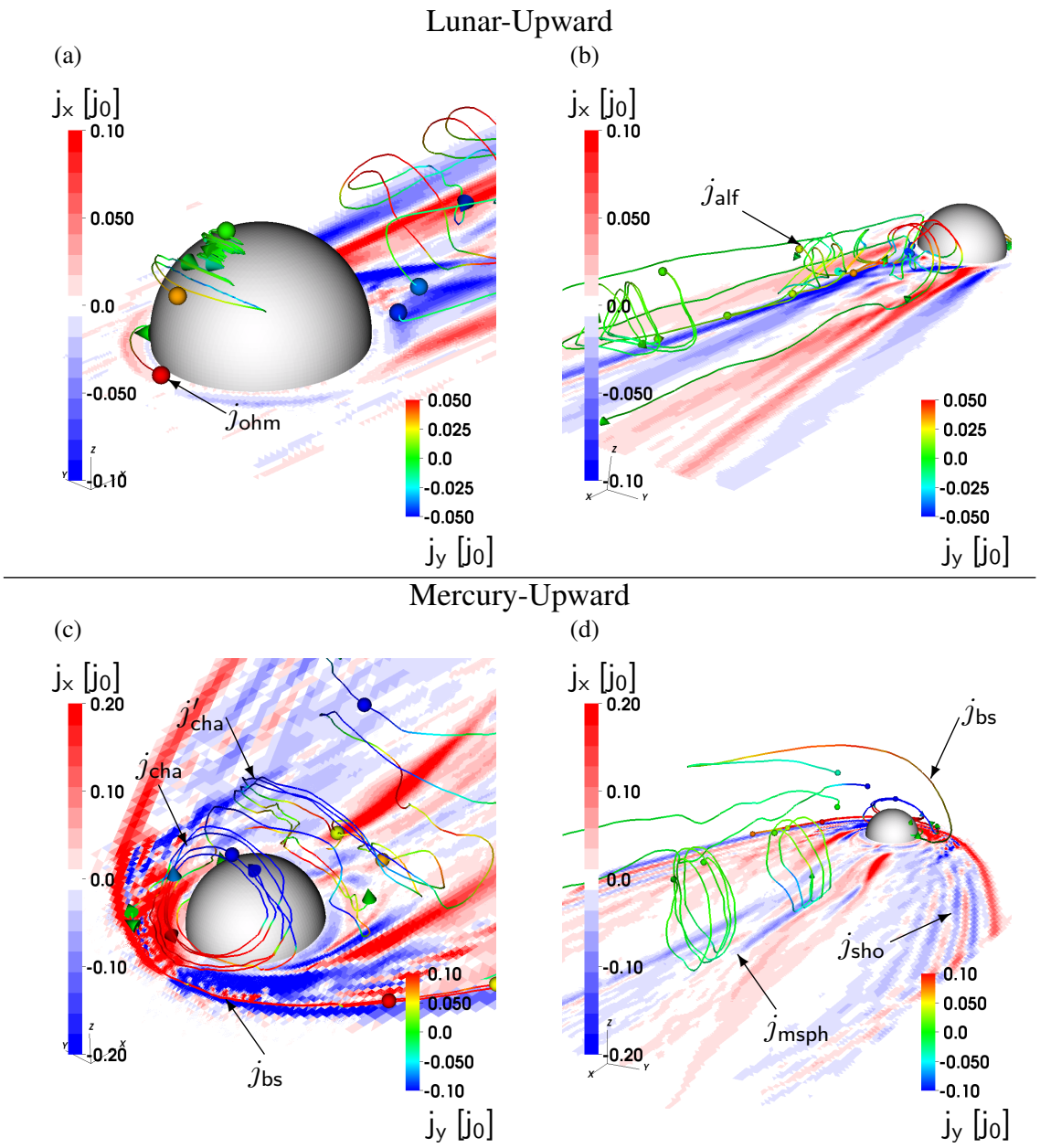

Figure 4.1: X-component of the current density in the equatorial plane for the front (a) and back (b) views of a Lunar-Upward obstacle and the front (c) and back (d) views of a Mercury-Upward obstacle. Blue segments are currents directed sunward and red segments are currents directed anti-sunward. The current density is given in normalized values (see Table 2.1). Current density streamlines are generated in several arbitrary points, and colored following the value of their Y-component (right bottom side colorbar) in order to give the reader a clear view of the streamlines directions. The descriptions of each labeled current are available in Table 2.3. The parameters common to the simulation are provided in Table 2.2, while parameters specific to each simulation type are given in Table 4.2.

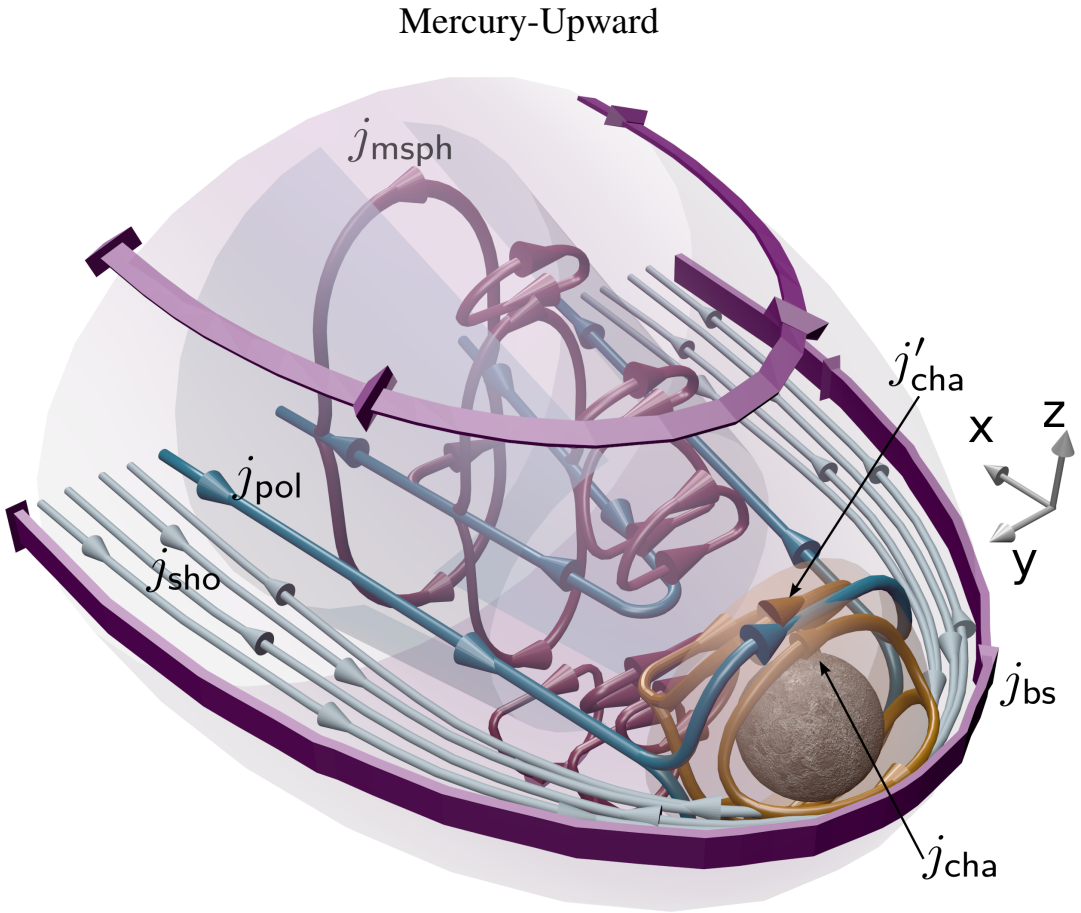

Figure 4.2: Three dimensional schematic representation of the structure of the currents for a Mercury-Upward obstacle (see Table 4.2 for parameters). The current j_{pol} is represented in blue, j_{msph} in red, j_{sho} in cyan, j_{cha} and j'_{cha} in orange, and j_{bs} in purple (see Table 2.3). The blue inner semi-transparent layer represents the nightside magnetopause, and the orange inner semi-transparent layer represents the dayside magnetopause. The outer purple semi-transparent layer represents the bow-shock.

4.2.2 Planetary obstacle in sub-Alfvénic regime: Rhea-Upward versus Ganymede-Upward

This section discusses the plasma interactions in sub-Alfvénic regime for weak and strong planetary dipole fields. The sub-Alfvénic velocity regime is present in our solar system for most of the satellites orbiting inside the magnetospheres of Jupiter and Saturn. The weak dipole case refers to a Rhea-Upward plasma interaction and the strong dipole refers to a Ganymede-Upward situation. The simulations presented here have an upstream velocity of 0.5 $v_{A,0}$.

The X-component of the current density in the equatorial plane and the current streamlines, colored following their Y-component are presented in Figure 4.3. The results for a Rhea-Upward obstacle with a magnetic moment of $M = 5 \cdot 10^3\ M_0$ are presented in Figures 4.3a and 4.3b. Such a magnetic moment leads to a theoretical stand-off distance $L_{SO} = 1.04\ R_p$ (see Equation 2.19). Figure 4.3a identifies and shows how the current j_{alf} forms a closed loop perpendicular to the magnetic field. A current flowing clockwise around the obstacle can also be observed in the equatorial plane. In the nightside of the plasma interaction region, a weak current, denoted j_{dia}, can be observed. Figures 4.3c and 4.3d show the simulation results for an obstacle with a planetary dipole field of $M = 40 \cdot 10^3\ M_0$. This configuration leads to an interaction regime similar to a Ganymede-Upward obstacle. The currents j_{cha}, j_{alf} and j_{dia} are such interaction indicators. The current j_{cha} flows in front of the obstacle in the direction anti-parallel to the electric field in the equatorial plane and parallel to the electric field at the poles of the obstacle. The Alfvén current, which appears at this location, merges with the field-parallel current and the field-perpendicular current due to numerical diffusion in the simulation domain. In the nightside of the interaction region, the current j_{dia} is clearly distinguishable and is flowing sunward on the dusk side and anti-sunward on the dawn side. A ring-shaped current flowing between the surface of the obstacle and the current identified as j_{cha} is also observed in Figure 4.3c.

A summary of the structure of the currents presented for Ganymede-Upward case is shown in Figure 4.4. The Rhea-Upward obstacle is similar to the Rhea-Type obstacle presented in Figure 3.7b (Chapter 3). Therefore, only a short summary is given here. In this regime, the interaction region is described by two major structures: (1) the Alfvén wing structure around the current j_{alf}, and (2) the diamagnetic current j_{dia} on the nightside of the obstacle. We develop further details about the appearance of the first structure. The triggering of the Alfvén wings in this interaction regime is subject to three effects. The first effect pertains to the ion pressure gradient $\nabla \mathbf{P}_i$ directed anti-sunward in the wake of the obstacle. As described by Simon et al. (2012) for the case of Rhea, the pressure gradient due to the refilling process along the X-axis can trigger Alfvén wings. This process is stronger for hot plasma where the wake refilling is faster and therefore the pressure gradient steeper. This is the case for Rhea where a plasma beta $\beta_i = 1.1$ for the ions is common. In our simulation the ion plasma beta is $\beta_i = 0.5$ (see Table 2.2) which trigger a weaker Alfvénic perturbation. The presence of a planetary dipole field (also linked to the presence of a core) and the resistivity of the obstacle can also trigger an Alfvén wing in our simulation. When the planetary dipole field is weaker than the IMF at the planetary surface, it stays confined within the obstacle. Therefore the IMF propagates into the mantle of the planet and the feedback to the plasma depends on the diffusion velocity of

the magnetic field in the planetary mantle. For a perfectly dielectric mantle, the magnetic field can move freely inside the obstacle, therefore the IMF does not undergo any lag during its propagation in the planet. However, as mentioned in Section 2.3.2 (and detailed in Appendix A.1), the obstacle in the simulation is not perfectly dielectric, therefore the magnetic field suffer a lag from the propagation into the obstacle. This effect can trigger a draping causing an Alfvén wing to appear. However, it is moderated by the extremely low convection velocity of the sub-Alfvénic case treated here ($v_{sw} = 0.5 v_{A,0}$). Indeed as shown in Chapter 3, the draping due to the conductivity of the obstacle depends exclusively on the value of the magnetic Reynolds number $\mathcal{Re}$, which is a function of the convection velocity (see Equation (2.44)). A study deriving the amplitude of the Alfvénic perturbation as a function of the configuration of the interior of the obstacle and the pressure gradient in the wake is required to give a more detailed answer about this problem. The second point to describe the structure of the interaction is the diamagnetic current (j_{dia}) in the nightside of the obstacle. This presence is triggered by the refilling process in the void, due to the particle absorption at the surface of the obstacle. In this regime, one observes an interaction articulated around two major currents j_{dia} and j_{cha}.
The essence of the plasma interaction region for a Ganymede-Upward interaction is presented in Figure 4.4. The planetary magnetic field at the surface of the obstacle is about $B_{surf} = 5\ B_0$. Yet, a dipole field stronger than the IMF, triggers a magnetopause, thus a Chapman-Ferraro current j_{cha}, indicated in this figure. In order to describe the size of the magnetopause in this regime, it is important to take into account the IMF pressure in the pressure balance equation (2.19). Indeed for an upstream velocity $v_{sw} = 0.5\ v_{A,0}$, the dynamic pressure is equal to the background magnetic field pressure. In this case, only a weak friction, which is proportional to the stellar wind velocity (Chodura and Schlueter 1981), is applied to the magnetosphere. This explains why the nightside of the interaction region is not developed. We summarize this interaction regime through three major currents. First as described before is the Alfvénic current. Here the Alfvén wings are triggered by the draping of the IMF by the encounter of the upstream plasma with the magnetopause. The second major current is the magnetopause (or Chapman-Ferraro) current, which is triggered by the interaction between the dipole field and the stellar wind pressure. The third important current is the diamagnetic current (j_{dia}) in the wake. As the magnetopause is deflecting the upstream ions, a void region is formed in the nightside of the interaction region. Also as the magnetosphere is weakly developed in the nightside due to low friction effect, the dominating effect is the void refilling process which is illustrated by the diamagnetic current (j_{dia}). A minor current, which is indicated here as j_{ring}, has the shape of a ring current. However this current is a diamagnetic current. Indeed there is a density depletion in the vicinity of the obstacle. This leads to a pressure gradient directed radially outward of the obstacle. Conjugated to a northward dipole, this leads to a diamagnetic current flowing parallel to the Chapman-Ferraro current on the dayside and anti-parallel to the Chapman-Ferraro current on the nightside.

4.3 Intermediate situations between the cornerstones

We now investigate the cases of three different velocity regimes for various obstacle, namely: $+10\text{E}3 M_0\hat{z} \mid 8 v_{A,0}$, $+20\text{E}3 M_0\hat{z} \mid 8 v_{A,0}$, $+40\text{E}3 M_0\hat{z} \mid 8 v_{A,0}$ (with v_{sw}=$8 v_{A,0}$),

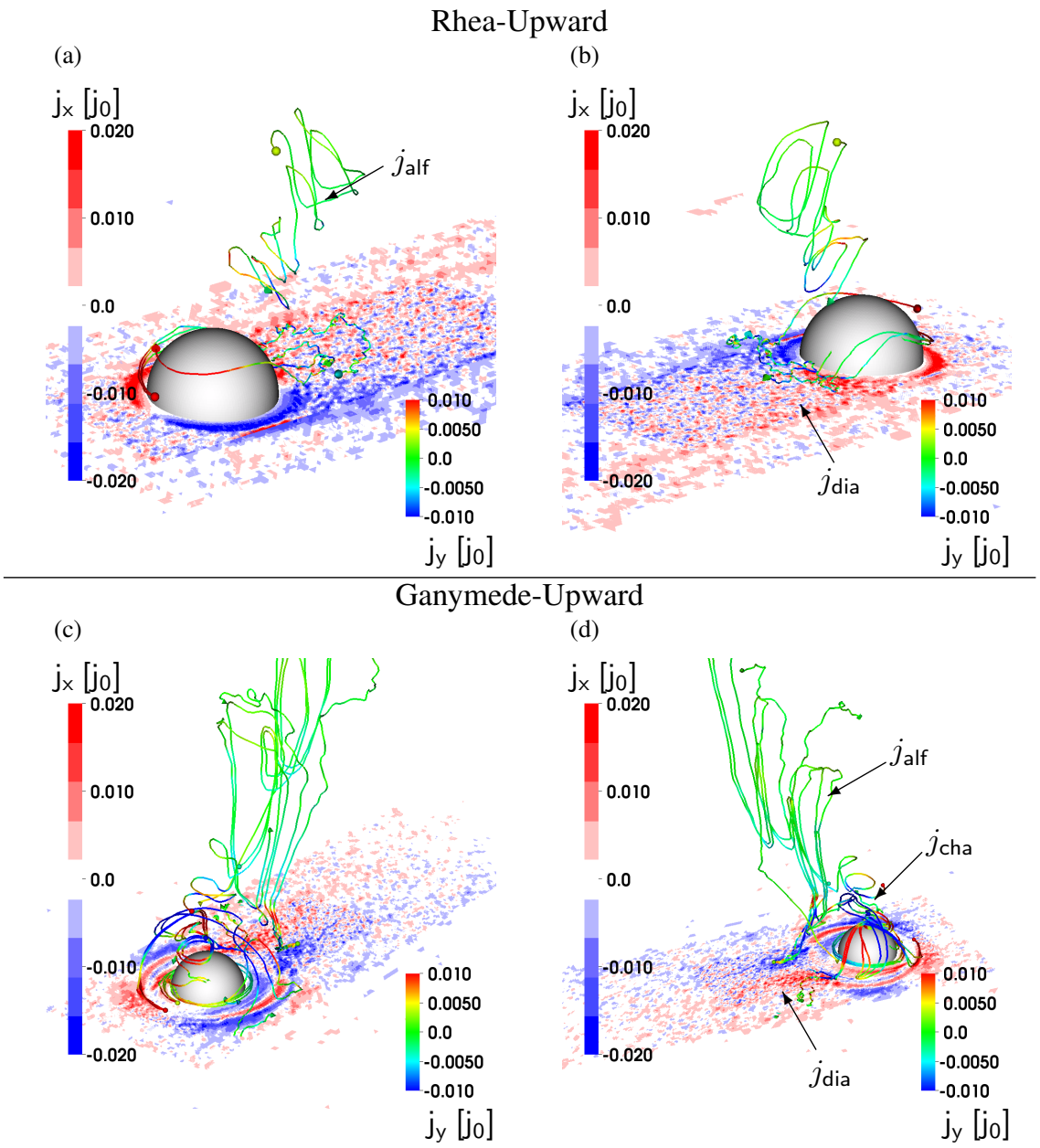

Figure 4.3: X-component of the current density in the equatorial plane and examples of current density streamlines. Front (a) and back (b) views of a Rhea-Upward obstacle. Front (c) and back (d) views of a Ganymede-Upward obstacle. Current description same as Figure 4.1.

$+5\text{E}3M_0\hat{z}$ | $2v_{A,0}$, $+40\text{E}3M_0\hat{z}$ | $2v_{A,0}$ (with v_{sw}=$2v_{A,0}$), and $+500M_0\hat{z}$ | $1v_{A,0}$, $+5\text{E}3M_0\hat{z}$ | $1v_{A,0}$, $+40\text{E}3M_0\hat{z}$ | $1v_{A,0}$ (with v_{sw}=$1v_{A,0}$).

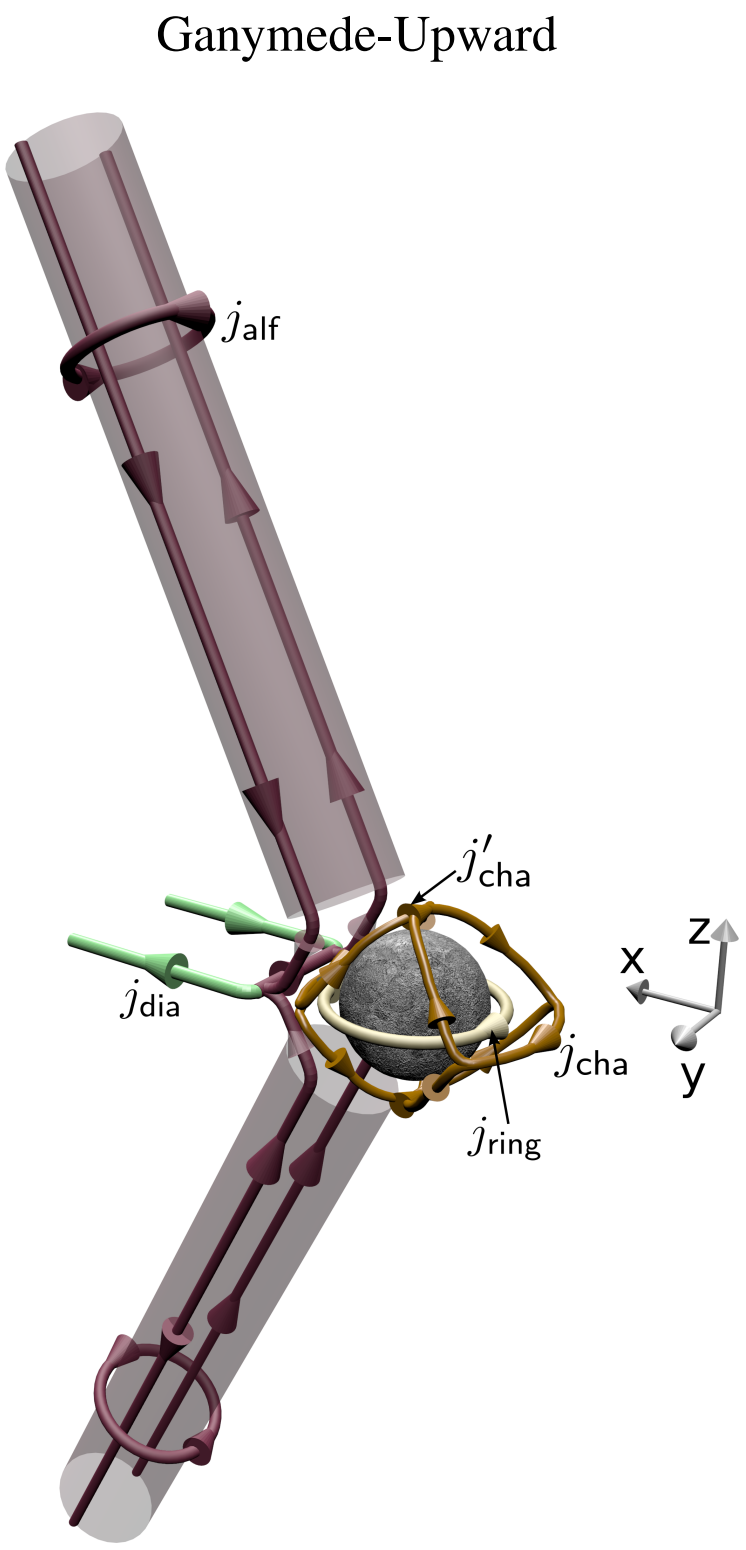

Figure 4.4: Three-dimensional diagram of the currents structures for a Ganymede-Upward obstacle (see Table 4.2 for parameters). Currents details and obstacle details same as Figure 4.2. The stellar wind velocity is $0,5\ v_{A,0}$.

4.3.1 From weak to strong magnetization

Our simulation results for a dipole strength varying between a Lunar-Upward situation and a Mercury-Upward system are presented in Figures 4.5, 4.6, and 4.7. The cases introduce are $+10\text{E}3M_0\hat{z} \mid 8v_{A,0}$, $+20\text{E}3M_0\hat{z} \mid 8v_{A,0}$, and $+40\text{E}3M_0\hat{z} \mid 8v_{A,0}$ in Figures 4.5, 4.6, and 4.7, respectively. The simulations are ordered by the normalized magnetic moment M_0 (see Table 2.1 and Table 4.2 for details on these parameters and Section 2.2.2.1 about the normalization).

The front and back views of the plasma interaction region of the $+10\text{E}3M_0\hat{z} \mid 8v_{A,0}$ simulation are presented in Figure 4.5a and 4.5b. The magnetization of this obstacle corresponds to a magnetic moment of $M = 10 \cdot 10^3\ M_0$, leading to a theoretical stand-off distance $L_{SO} = 0.69\ R_p$ (see Section 2.2.2.1) and a surface magnetic field $B_{surf} = 1.25\ B_0$. Figure 4.5a shows that the current along the polar cap regions starts to switch to a magnetosphere type current. However, the current displayed in Figure 4.5b is still noted j_{alf}. For every loop represented, one should note that it denotes two different currents, generated by two different magnetic field structures, via one common mechanism.

The results of the simulation of the $+20\text{E}3M_0\hat{z} \mid 8v_{A,0}$ system are presented in Figures 4.6a and 4.6b. The magnetization of the obstacle in this simulation is $M = 20 \cdot 10^3\ M_0$, the theoretical stand-off distance is $L_{SO} = 0.87\ R_p$, and the surface magnetic field is $B_{surf} = 2.5\ B_0$. These parameters produce a field that remains concentrated at the dayside surface of the obstacle. This generates a step in the magnetic field magnitude when crossing this surface. This jump is related to the Chapman-Ferraro current (noted j_{cha} in Figure 4.6a), and to the bow-shock current j_{bs}. One should note that in the particular case of the northward dipole, one cannot distinguish the Chapman-Ferraro current from the bow-shock current at the subsolar point. In this configuration, both currents are flowing in the same direction in the equatorial plane.

The structures appearing in the intermediate situations named the $+10\text{E}3M_0\hat{z} \mid 8v_{A,0}$ case and the $+20\text{E}3M_0\hat{z} \mid 8v_{A,0}$ case are displayed in Figure 4.8. This sketch should be regarded as a schematic of the intermediate steps between the cases presented in Figure 4.2. It is important to note that the whole process of the evolution of the plasma structures is continuous. No sudden appearance of structures has been observed. The magnetic field magnitude jumps, which are characteristic of discontinuities such as the magnetopause and the bow-shock, increase continuously and monotonically.

First we describe the evolution of the Chapman-Ferraro current. This current is identified as j_{cha} in Figures 4.2 and 4.8. It appears when the planetary magnetic field at the surface of the obstacle reaches the IMF strength. The Chapman-Ferraro current on the dayside is triggered by the compression of the planetary dipole field by the total stellar wind pressure. In a super-Alfvénic regime, the stellar wind dynamic pressure is higher than the IMF pressure. Therefore, one has a situation where the planetary dipole field is high enough to prevent the IMF from entering the interior of the obstacle, but not high enough to balance the stellar wind pressure. One then observes a situation where the planetary field is confined inside the obstacle. This leads to a particular discontinuity, which remains to be studied (more details are given in Appendix A.1). There is therefore a magnetic discontinuity, but also a conductivity, density and temperature discontinuity. Obviously, if the planetary magnetic pressure cannot counter the stellar wind dynamic pressure, one expects that the density above the surface is equal to the background density, which would

then drop to zero after being "absorbed" by the obstacle. Yet, we note that there is no sharp variation of the magnetic field magnitude between the plasma and the obstacle surface, but a continuous evolution instead. Therefore the magnetic field magnitude is increasing slightly above the surface, which triggers a local heating and pressure gradient. Assuming that the magnetic field follows a smoothed profile (see Section 2.2.2.3 for details on the smoothing procedure) at the interface between the plasma and the planetary surface, we conclude on the existence of a Chapman-Ferraro current flowing at the surface as it is depicted in Figure 4.8.

A second type of current, is the bow-shock current (denoted j_{bs}). It is a fast magnetosonic mode polarization current. When the magnetization of the obstacle is increased, one observes that this current grows in intensity, as the Chapman-Ferraro current does. The formation of this current follows the shape of the fast mode propagation diagram as shown in Chapter 3. When the surface magnetic field is close to the IMF, the amplitude of the bow-shock current approaches the order of magnitude of the normalized current in the equatorial plane. Then as the dipole strength is increased, the current spreads in a cone-like structure. The bow-shock current evolves in a parallel way to the fast mode current (identified as j_{pol}). These behaviors of the currents distribution are represented in Figure 4.8, by the conic semi-transparent layer. The outer partial conic structure linked to the bow-shock becomes complete when the planetary dipole field is strong enough to counter the stellar wind total pressure.

The evolution of the Chapman-Ferraro and the bow-shock currents is depicted in Figure 4.9. The curves related to the $+5\mathrm{E}3M_0\hat{z} \mid 8v_{\mathrm{A},0}$, $+20\mathrm{E}3M_0\hat{z} \mid 8v_{\mathrm{A},0}$, $+40\mathrm{E}3M_0\hat{z} \mid 8v_{\mathrm{A},0}$, $+50\mathrm{E}3M_0\hat{z} \mid 8v_{\mathrm{A},0}$, and $+80\mathrm{E}3M_0\hat{z} \mid 8v_{\mathrm{A},0}$ (also named Mercury-Upward) simulation types correspond to planetary magnetic moments of $5 \cdot 10^3\ M_0$, $20 \cdot 10^3\ M_0$, $40 \cdot 10^3\ M_0$, $50 \cdot 10^3\ M_0$, and $80 \cdot 10^3\ M_0$, respectively. For the $+5\mathrm{E}3M_0\hat{z} \mid 8v_{\mathrm{A},0}$, $+20\mathrm{E}3M_0\hat{z} \mid 8v_{\mathrm{A},0}$, and $+40\mathrm{E}3M_0\hat{z} \mid 8v_{\mathrm{A},0}$ simulation results, we observe a peak in the current density at $x = 24\ x_0$, with $|\boldsymbol{j}| = 0.3\ j_0$, $|\boldsymbol{j}| = 1.0\ j_0$, and $|\boldsymbol{j}| = 2.2\ j_0$, respectively. We also observe two peaks in each case, at $x = 24\ x_0$ and $x = 27\ x_0$ for the $+50\mathrm{E}3M_0\hat{z} \mid 8v_{\mathrm{A},0}$, and $x = 26\ x_0$ and $x = 33\ x_0$ for the $+80\mathrm{E}3M_0\hat{z} \mid 8v_{\mathrm{A},0}$. We conclude that the Chapman-Ferraro and bow-shock currents merges in the $+5\mathrm{E}3M_0\hat{z} \mid 8v_{\mathrm{A},0}$, $+20\mathrm{E}3M_0\hat{z} \mid 8v_{\mathrm{A},0}$, and $+40\mathrm{E}3M_0\hat{z} \mid 8v_{\mathrm{A},0}$ cases, start to separate at the $+50\mathrm{E}3M_0\hat{z} \mid 8v_{\mathrm{A},0}$ interaction, and are clearly distinct for the $+80\mathrm{E}3M_0\hat{z} \mid 8v_{\mathrm{A},0}$(or Mercury-Upward) system. The transition from the $+40\mathrm{E}3M_0\hat{z} \mid 8v_{\mathrm{A},0}$ to the Mercury-Upward simulations presented in Figure 4.9 corresponds to the transition around the stand-off distance $L_{\mathrm{SO}} = 1\ R_{\mathrm{p}}$. The process observed in this figure can be interpreted as a separation of the bow-shock current and the Chapman-Ferraro current through the increase of the planetary magnetization.

Another point pertaining to the Alfvénic current flowing in the wake is that a double draping pattern appears in the nightside when increasing the magnetization strength of the obstacle, due to the anti-parallel configuration between the IMF and the planetary magnetic moment. The superposition of the draping of the IMF and the stretching of the planetary magnetic field lines, leads to a succession of positive and negative B_x. This pattern is presented in Figure 4.10b. This field distortion in the nightside is partly due to the reconnection happening at the north and south poles of the obstacle. Figure 4.10a illustrates the reconnection process; the black lines represent the magnetic field lines. We notice that a reconnection takes place at the south and north poles of the obstacle, yielding an acceleration of the flow. As seen Figure 4.10a, the bulk ion velocity is higher

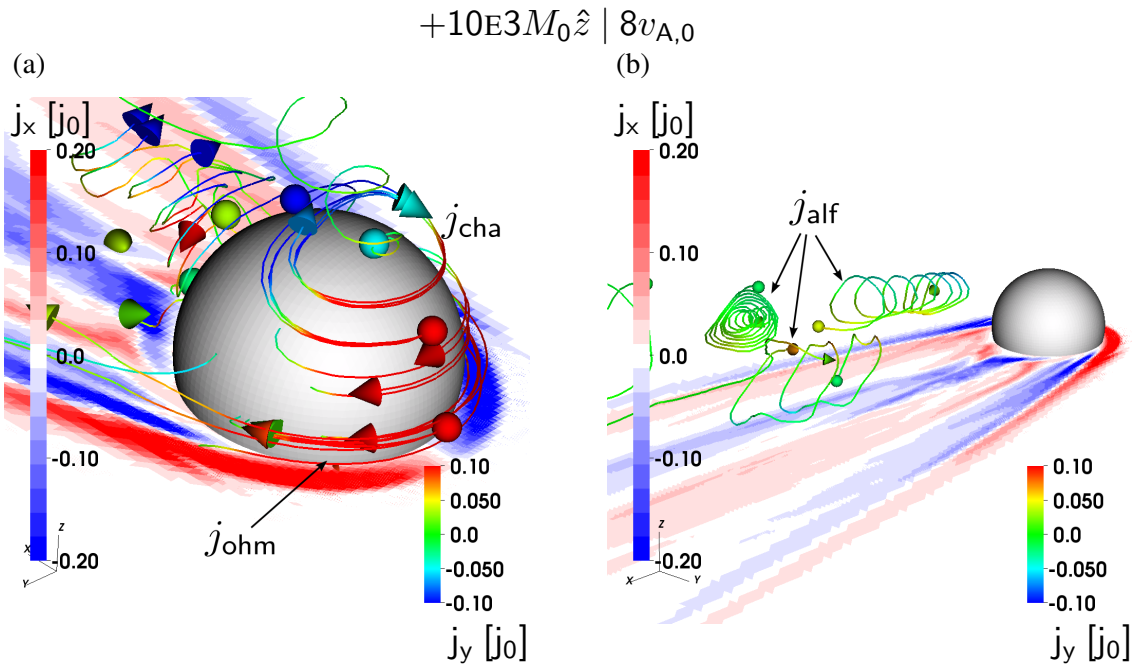

Figure 4.5: X-component of the normalized current density in the equatorial plane and examples of current density streamlines. Front (a) and back (b) views of a +10E3$M_0\hat{z}$ | 8$v_{A,0}$ obstacle. Current description same as Figure 4.1.

after the reconnection area, and reaches a value of $v_{sw} + v_{A,0}$ at the south and north parts of the nightside region. This explains the shape of the current j_{alf} in Figure 4.6b, and schematically represented in Figure 4.8.

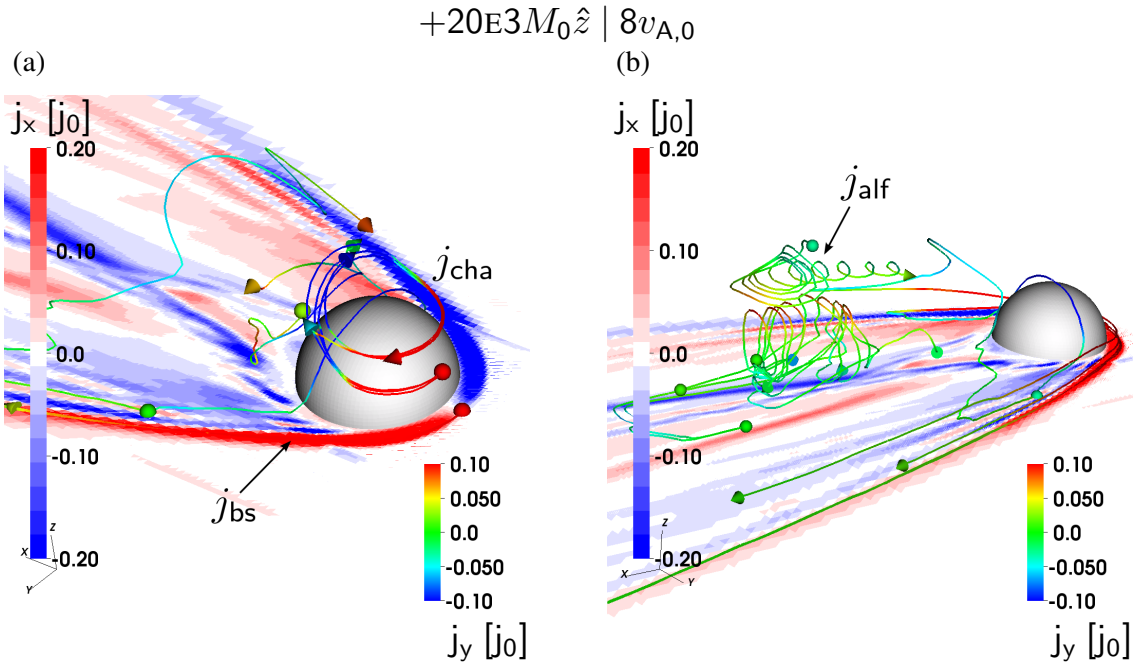

Figure 4.6: X-component of the normalized current density in the equatorial plane and examples of current density streamlines. Front (a) and back (b) views of a +20E3$M_0\hat{z}$ | 8$v_{A,0}$ obstacle. Current description same as Figure 4.1.

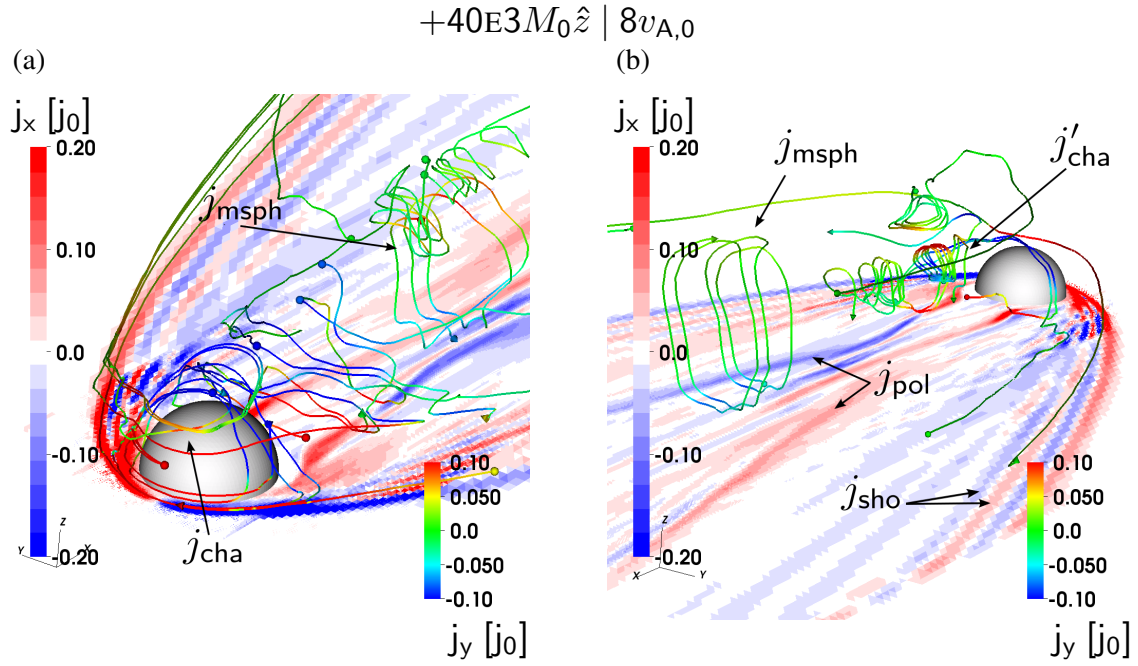

Figure 4.7: X-component of the normalized current density in the equatorial plane and examples of current density streamlines. Front (a) and back (b) views of a +40E3$M_0\hat{z}$ | 8$v_{A,0}$ obstacle. Current description same as Figure 4.1.

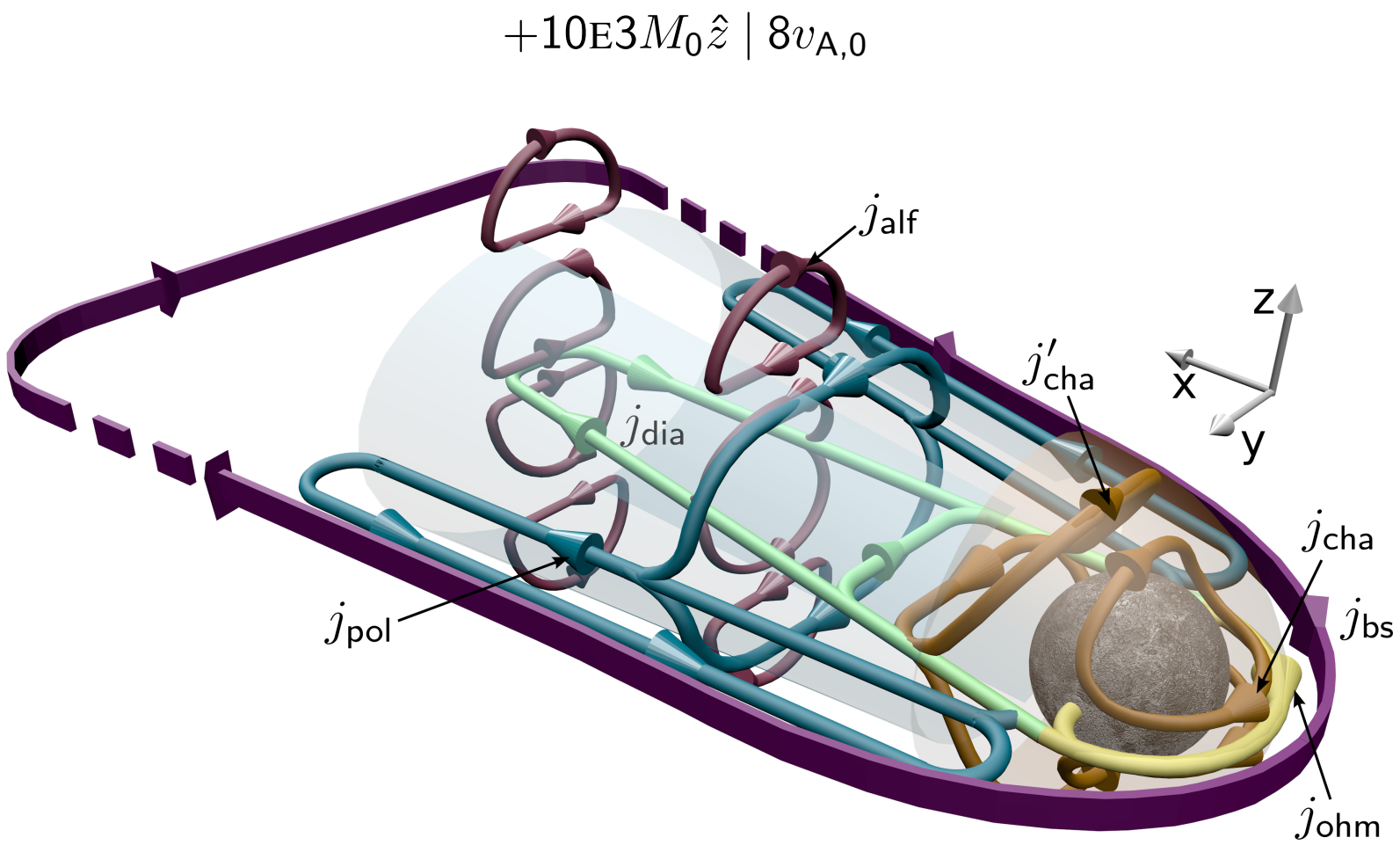

Figure 4.8: Schematic representation in three-dimension of the structure of the currents for the transition step between Lunar-Upward and Mercury-Upward objects, here called $+20\text{E}3M_0\hat{z} \mid 8v_{\text{A},0}$. Description of the currents same as Figure 4.2. The simulation parameters are given in Tables 2.2 and 4.2.

A different situation is presented in Figures 4.7a and 4.7b. It corresponds to the $+40\text{E}3M_0\hat{z} \mid 8v_{\text{A},0}$ interaction. One can find the previously described features, namely the bow-shock current and the Chapman-Ferraro current. However, the diamagnetic current j_{dia} has totally disappeared. One observes that the current j_{dia} is pushed away from the obstacle during the transition from $+10\text{E}3M_0\hat{z} \mid 8v_{\text{A},0}$ to $+40\text{E}3M_0\hat{z} \mid 8v_{\text{A},0}$. (see Table 4.2 for parameters). A less pronounced feature is the succession of currents along the bow-shock, with alternate directions. They are called shocklet current and denoted j_{sho} in Figure 4.7b. In the $+40\text{E}3M_0\hat{z} \mid 8v_{\text{A},0}$ regime, the double Alfvén wing structure, also observed for the $+10\text{E}3M_0\hat{z} \mid 8v_{\text{A},0}$ and $+20\text{E}3M_0\hat{z} \mid 8v_{\text{A},0}$ regimes, has vanished. As evidenced in Figure 4.7a, there is a major current loop j_{msph} between the equatorial plane and the magnetopause. On the nightside, the dipole field has stretched in the vicinity of the obstacle, and generates a 1 R_{p}-wide "shielded" region. In the equatorial plane, the interior boundaries of the wake are delimited by the fast mode polarization current (j_{pol}, described in Section 4.2.1). However these boundaries get wider as the strength of the dipole field increases. While the inner boundaries stay confined to the center of the wake, the outer boundaries are spread between the magnetopause and the shocklet current j_{sho}. Additionally, the stretching of the dipole field leads to a nightside Chapman-Ferraro current j'_{cha} in the vicinity of the obstacle. The complete loop is flowing anti-parallel to the electric field in the equatorial plane, field-aligned on the dawn and dusk sides, and parallel to the electric field at the poles. It should be noted that, a merging can be observed between the reconnection current, the dayside and nightside Chapman-Ferraro current at the poles.

4.3.2 Intermediate situations in super- and sub-Alfvénic regimes

Figures 4.11a and 4.11b show the current loops for the $+5\text{E}3M_0\hat{z} \mid 2v_{\text{A},0}$ interaction, which has an upstream velocity $v_{\text{sw}} = 2\ v_{\text{A},0}$, a surface field $B_{\text{surf}} = 0.62\ B_0$, and a stand-off distance of $L_{\text{SO}} = 0.84\ R_{\text{p}}$ (see Table 4.2 for details about the parameters). We observe for the $+5\text{E}3M_0\hat{z} \mid 2v_{\text{A},0}$ interaction, properties similar to the Mercury-Upward. The currents on the nightside of the plasma interaction region are presented in Figure 4.11a. The current denoted j_{alf} is related to the upper part double loop structure explained in Section 4.3.1. The diamagnetic current (j_{dia}) and the fast mode polarization current (j_{pol}) are also indicated. Their descriptions are provided in Section 4.2.1. The salient changes concern the angle of the fast mode current j_{pol} with the center of the wake, which increases as the velocity decreases (see Section 3 for further details). The dayside of the plasma interaction region is presented in Figure 4.11b. The Chapman-Ferraro current j_{cha} is observed in front of the obstacle as well as a bow-shock current j_{bs}.
Figures 4.11c and 4.11d present simulation results for the $+40\text{E}3M_0\hat{z} \mid 2v_{\text{A},0}$ interaction. The currents j_{dia}, j_{pol}, j_{alf}, and j_{msph} (see Table 2.3 for more details) are indicated in the nightside of the interaction region in Figure 4.11c. Compared to the Mercury-Upward, the diamagnetic and polarization currents are pushed away from the obstacle in the $+40\text{E}3M_0\hat{z} \mid 2v_{\text{A},0}$. The translations along the X-axis of those two currents are comparable to the expansion of the magnetospheric current (j_{msph}) on the nightside of the obstacle. On the dayside of the obstacle, shown in Figure 4.11d, one has identified the currents j_{cha}, j'_{cha} and j_{bs}. Compared to case $+5\text{E}3M_0\hat{z} \mid 2v_{\text{A},0}$, we note that the nightside Chapman-Ferraro current (j'_{cha}) extends farther in the wake, and that the dayside Chapman-Ferraro current (j_{cha}) is clearly distinct from the bow-shock current (j_{bs}).

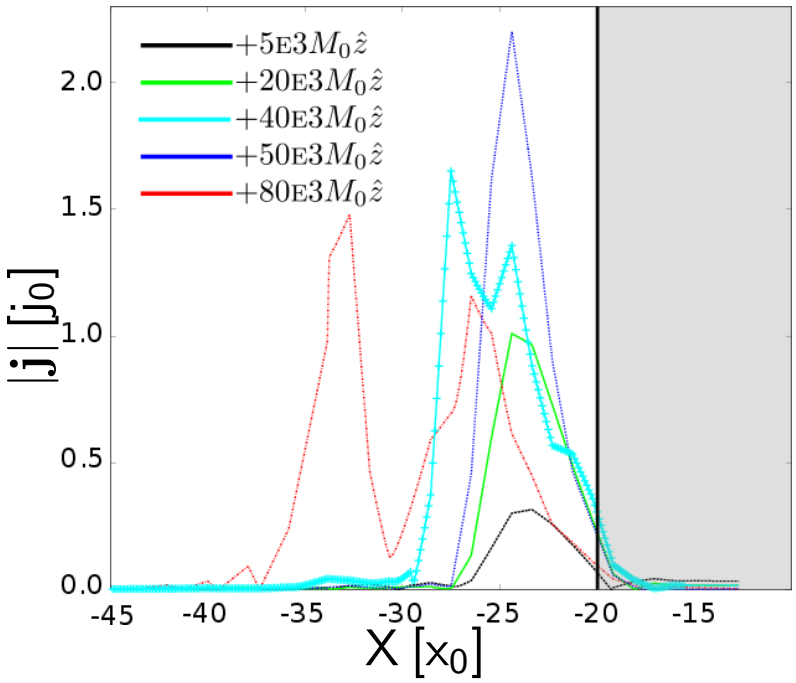

Figure 4.9: Four simulation results of the magnitude of the current density in normalized units (see Table 2.1), along the axis (Y=0, Z=0). The obstacle is represented by the shaded zone, which surface is the vertical black line at $x = 20\ x_0$. The parameters related to the $+5\text{E}3M_0\hat{z}$ | $8v_{A,0}$, $+20\text{E}3M_0\hat{z}$ | $8v_{A,0}$, $+40\text{E}3M_0\hat{z}$ | $8v_{A,0}$, $+50\text{E}3M_0\hat{z}$ | $8v_{A,0}$, and $+80\text{E}3M_0\hat{z}$ | $8v_{A,0}$ (Mercury-Upward) are summarized in Table 4.2. The stellar wind velocity is 8 $v_{A,0}$ (but not indicated in the simulation name legend for clarity)

A schematic representation of the simulation results from Figure 4.11 is provided in Figures 4.12 and 4.13. Figure 4.12 refers to case $+5\text{E}3M_0\hat{z}$ | $2v_{A,0}$, while Figure 4.13 represents the $+40\text{E}3M_0\hat{z}$ | $2v_{A,0}$ case. The structure of the $+5\text{E}3M_0\hat{z}$ | $2v_{A,0}$ interaction is essentially composed of the double loop structure, due to the current j_{alf}, and which mechanism is explained in section 4.3.1. In addition, we observe a fast mode polarization current, which angle to the meridional plane is given by the ratio between the fast mode group velocity and the upstream plasma velocity. Given the explanation on the non-homogeneous propagation of the fast mode (see Section 3.3.1), this angle triggers a cone-like structure. One can notice that the bow-shock follows the same mechanism as the fast mode wake waves. The configuration of the $+40\text{E}3M_0\hat{z}$ | $2v_{A,0}$ system displayed in Figures 4.13 is similar to the $+5\text{E}3M_0\hat{z}$ | $2v_{A,0}$ system. An interesting aspect is the displacement of the diamagnetic and polarization currents with respect to the $+5\text{E}3M_0\hat{z}$ | $2v_{A,0}$ and the $+40\text{E}3M_0\hat{z}$ | $2v_{A,0}$ configuration. Here we show that the magnetosphere acts like a cavity triggering magnetohydrodynamics modes at its boundaries.

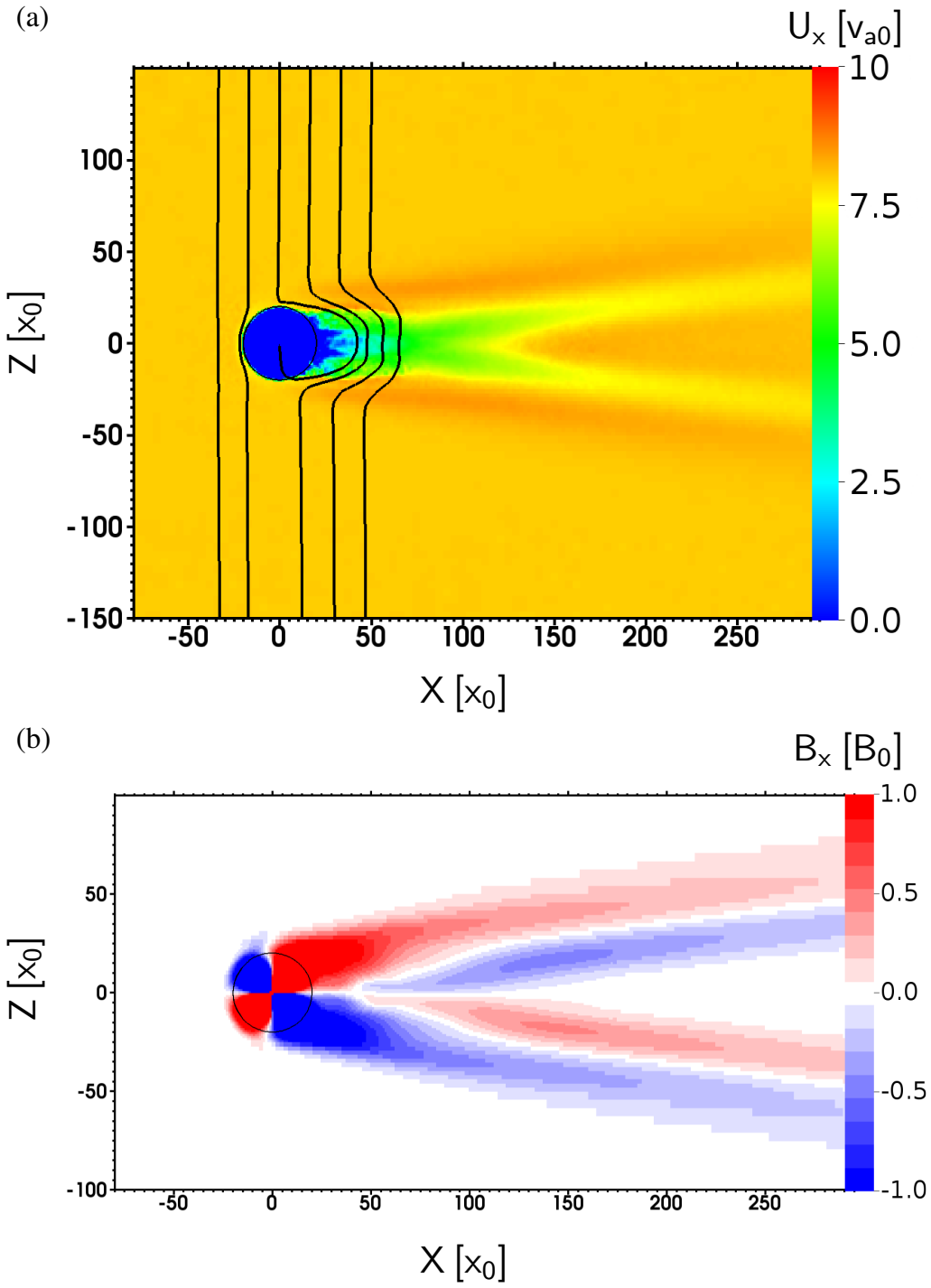

Figure 4.10: Panel (a) shows the X-component of the normalized bulk velocity and magnetic field lines (in black) generated between X=−50x_0 and X=+50x_0. Panel (b) presents the X-component of the normalized magnetic field (see Table 2.1 for the normalization). Both panels are plotted in the Y-cross-section of the simulation domain. The system simulated is a $+10\text{E}3M_0\hat{z} \mid 8v_{A,0}$ interaction system (parameters are given in Table 4.2). The obstacle is identified by a black circle centered at $(0, 0)$. The plasma beta and obstacle radius are given in Table 2.2.

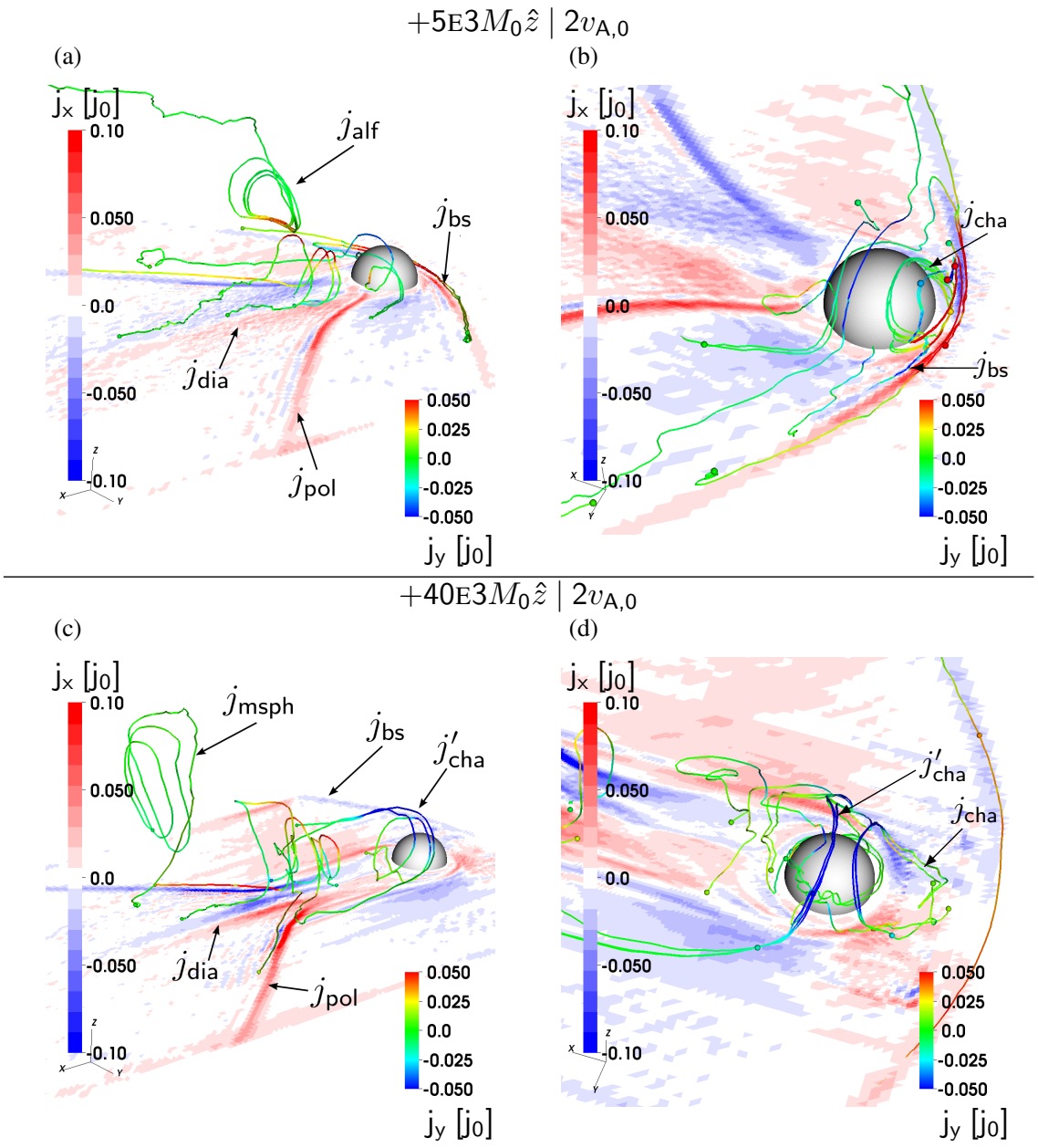

Figure 4.11: X-component of the current density in the equatorial plane and examples of current density streamlines. Front (a) and back views (b) of a +5E3$M_0\hat{z}$ | 2$v_{A,0}$ obstacle. Front (c) and back views (d) of a +40E3$M_0\hat{z}$ | 2$v_{A,0}$ obstacle (the parameters details are in Table 4.2). Current description same as Figure 4.1.

Figure 4.12: Three-dimensional representation of the current structures for a +5E3$M_0\hat{z}$ | 2$v_{A,0}$ obstacle (see Table 4.2 for parameters). Current description same as Figure 4.2. The upstream stellar wind velocity is v_{sw}=2 $v_{A,0}$.

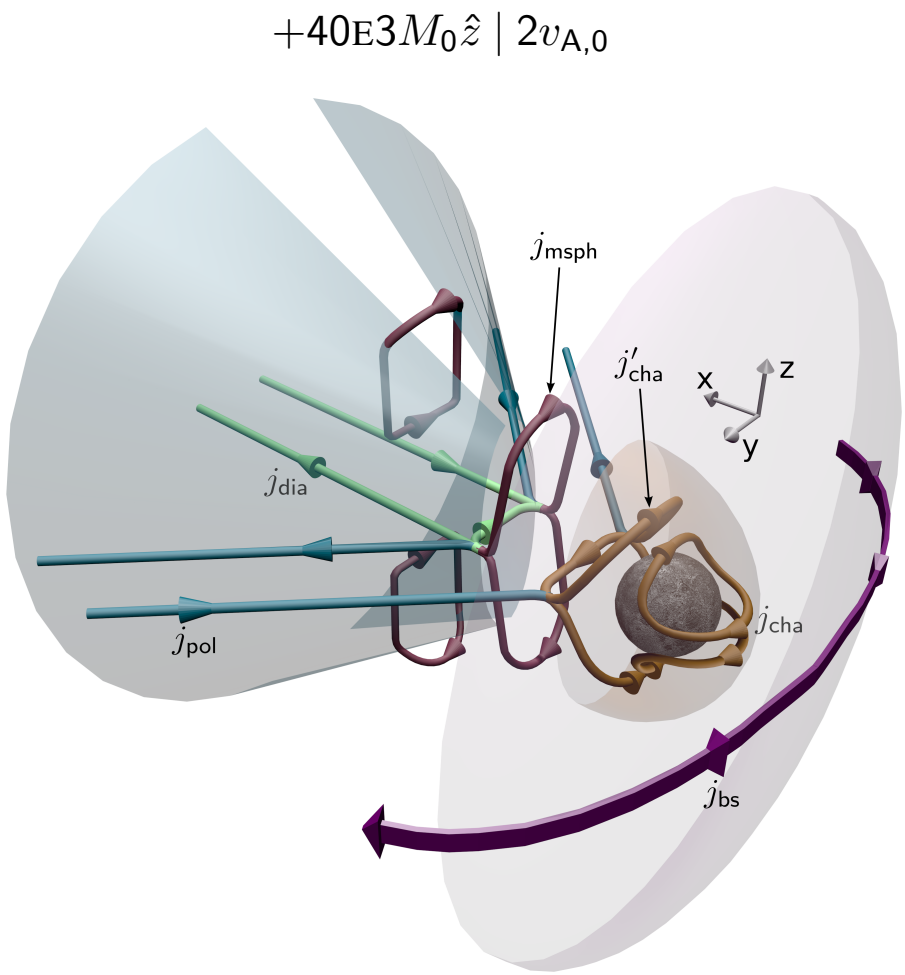

Figure 4.13: Three-dimensional representation of the current structures for a +40E3$M_0\hat{z}$ | 2$v_{A,0}$ obstacle (see Table 4.2 for parameters). Current description same as Figure 4.2. The upstream stellar wind velocity is v_{sw}=2 $v_{A,0}$.

The various current loops appearing for a stellar wind velocity $v_{sw} = 1\,v_{A,0}$ are represented in Figures 4.14, 4.15, and 4.16. These correspond to simulations of cases $+500M_0\hat{z} \mid 1v_{A,0}$, $+5\text{E}3M_0\hat{z} \mid 1v_{A,0}$ and $+40\text{E}3M_0\hat{z} \mid 1v_{A,0}$, respectively (see Table 4.2). The simulation results of the $+500M_0\hat{z} \mid 1v_{A,0}$ interaction show a diamagnetic current in the center of the wake (related to j_{dia} in Table 2.3). Also the current related to the Alfvén wings, j_{alf}, is present. Compared to higher velocities, the currents j_{pol} and j_{bs} have disappeared. This case is close to the Rhea-Upward obstacle discussed in Section 4.2. Figures 4.15a and 4.15b illustrate the output of Case $+5\text{E}3M_0\hat{z} \mid 1v_{A,0}$, where the surface magnetic field is on the order of magnitude of the IMF. The behavior of the plasma in this transition regime is quite similar to the one discussed in Section 4.3.1. This means that as the planetary magnetic field increases, the magnitude of the Chapman-Ferraro current also continuously increases on the dayside. Case $+40\text{E}3M_0\hat{z} \mid 1v_{A,0}$ is presented in Figures 4.16a and 4.16b. In this case, all magnetosphere related currents j_{cha}, j'_{cha} and j_{msph} are present. Since the upstream velocity is sub-fast-magnetosonic, there is no bow-shock and shocklets.

Schematic representations of the $+5\text{E}3M_0\hat{z} \mid 1v_{A,0}$ and $+40\text{E}3M_0\hat{z} \mid 1v_{A,0}$ current systems are provided in Figures 4.17a and 4.17b, respectively. Conversely to higher upstream velocities, a fully developed magnetosphere appears. For stellar wind velocity of 1 $v_{A,0}$, the dynamic pressure is about the same as the IMF pressure. Therefore, with such low pressure, the magnetization of the planet is only required to develop a surface magnetic field equivalent to the IMF in order to produce a shielded region. Another aspect deals with the Ohmic current: as shown in Section 2.3.2, when the velocity decreases, the planet does not produce a strong Ohmic current, since this current is proportional to the upstream velocity. Therefore for sub-Alfvénic upstream velocities, the Ohmic current related to the resistivity used in the simulation is negligible. Also, as the angle of the Alfvén wings is wider for lower velocities, they become clearly distinguishable from any other effect present in the nightside region of the obstacle. The Alfvén wings are represented bounded by the current j_{alf} in Figure 4.17. This current has two distinct components, a circular current perpendicular to the wing and a current parallel to the wing. In the Rhea-Upward obstacle shown in Figure 4.3a (introduced in Section 4.2.2), the closing of the Alfvénic current is made possible by a current related to the dipole compression, and flowing at the equator of the obstacle. Schematic Figures 4.17a and 4.17b illustrate how this dipole compression current evolves to a Chapman-Ferraro current.

The fundamental transition stages between the super- and sub-Alfvénic cases for limited planetary dipole field are presented in Figures 4.12, 4.13 and 4.17. Similarly to the transition for different planetary dipole magnitudes, it is noticeable that the transition between several velocity regimes is a continuous effect. For velocities higher than 2 $v_{A,0}$ (which corresponds to the fastest group velocity of the fast wave in the upstream plasma in our simulation), the fast waves can be stationary. The continuous nature of the transition between higher and lower velocities can be explained by the inhomogeneous property of the fast waves. The group velocity of the fast waves is slower along the field lines and faster perpendicular to the field. Therefore the stationary structure appears first along the field lines, and is complete when the upstream velocity is higher than the propagation velocity perpendicular to the field. In our simulation, the plasma beta ($\beta_i + \beta_e$) is equal to 1 (see Table 2.2), therefore the Alfvén and sound velocities are equal (Simon 2007). In this regime, the fast mode propagation velocity along the field line is close to the Alfvén velocity. Although with $\beta = 1$ there is a singularity at 90°, this does not affect the discus-

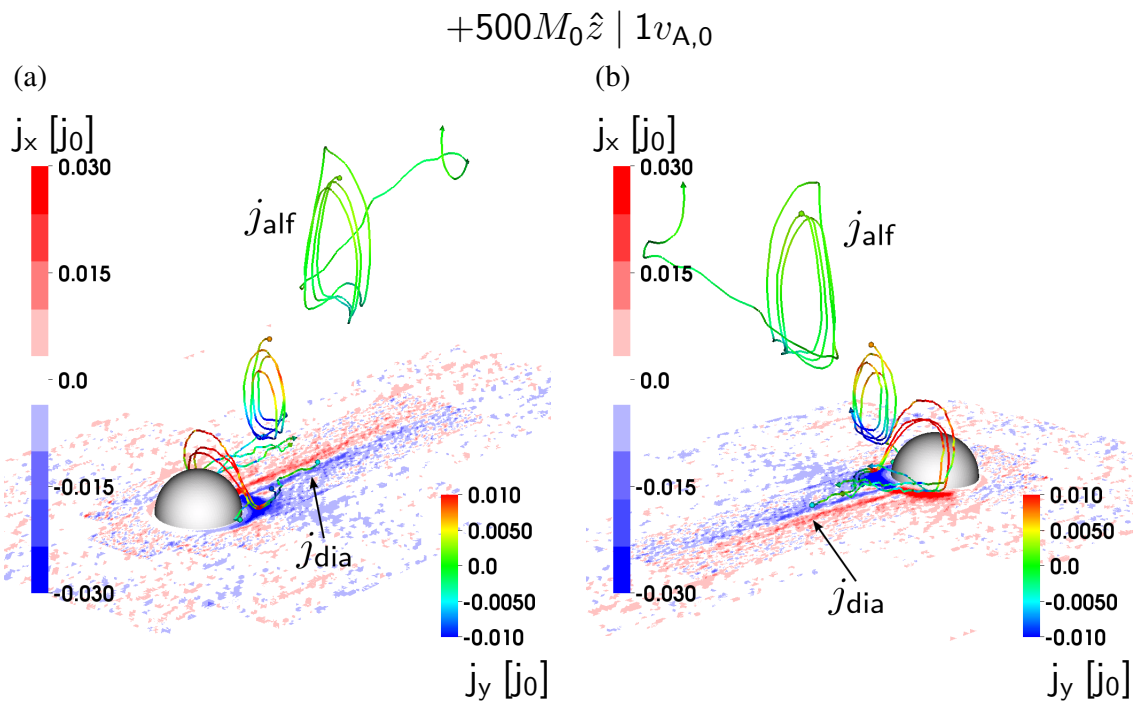

Figure 4.14: X-component of the current density in the equatorial plane and examples of current density streamlines. Front (a) and back (b) views of a +500$M_0\hat{z}$ | 1$v_{A,0}$ obstacle. Current description same as Figure 4.1.

sion here. Therefore the current triggered by the stationary fast mode along the field line interweaves with the current generated by the Alfvénic interaction. It is not completely clear how the fast mode develop between 1 $v_{A,0}$ and 2 $v_{A,0}$. This requires running a set of simulation with a plasma $\beta > 1$ in order to distinguish between the fast waves and the Alfvén wave along the field lines, which falls beyond the scopes of this work.

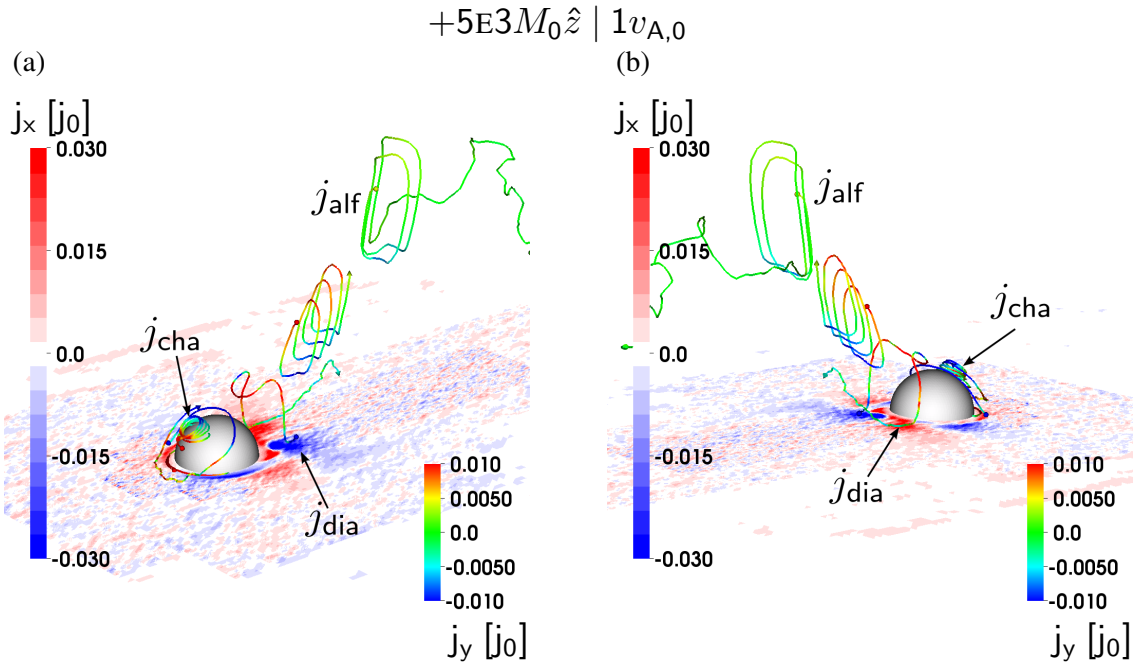

Figure 4.15: X-component of the current density in the equatorial plane and examples of current density streamlines. Front (a) and back (b) views of a +5E3$M_0\hat{z}$ | 1$v_{A,0}$ obstacle. Current description same as Figure 4.1.

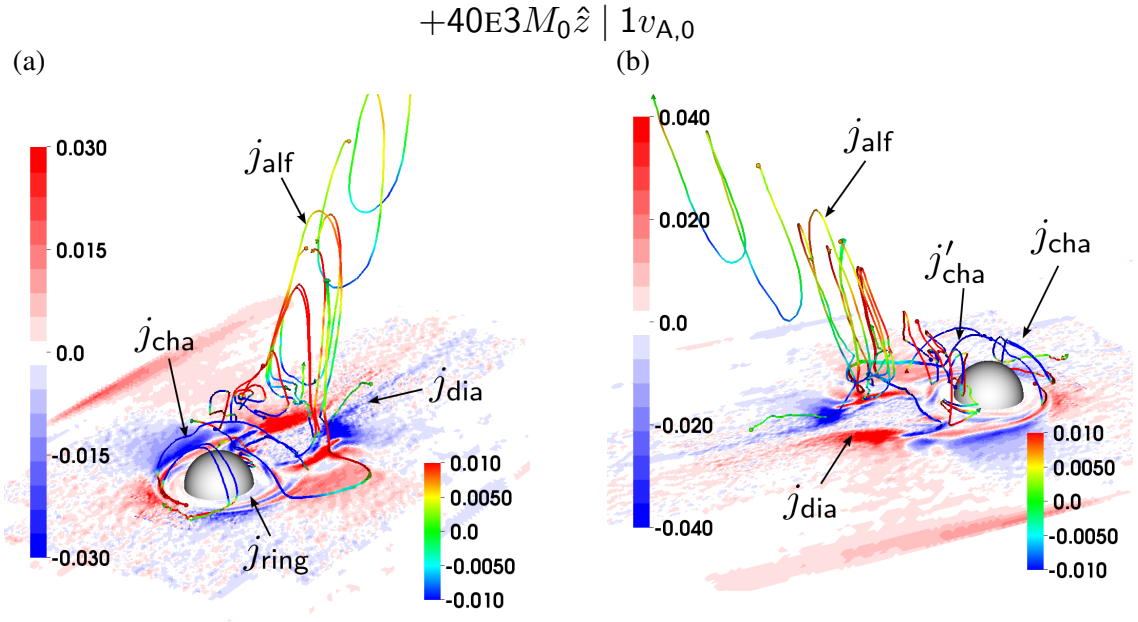

Figure 4.16: X-component of the current density in the equatorial plane and examples of current density streamlines. Front (a) and back (b) views of a +40E3$M_0\hat{z}$ | 1$v_{A,0}$ obstacle. Current description same as Figure 4.1.

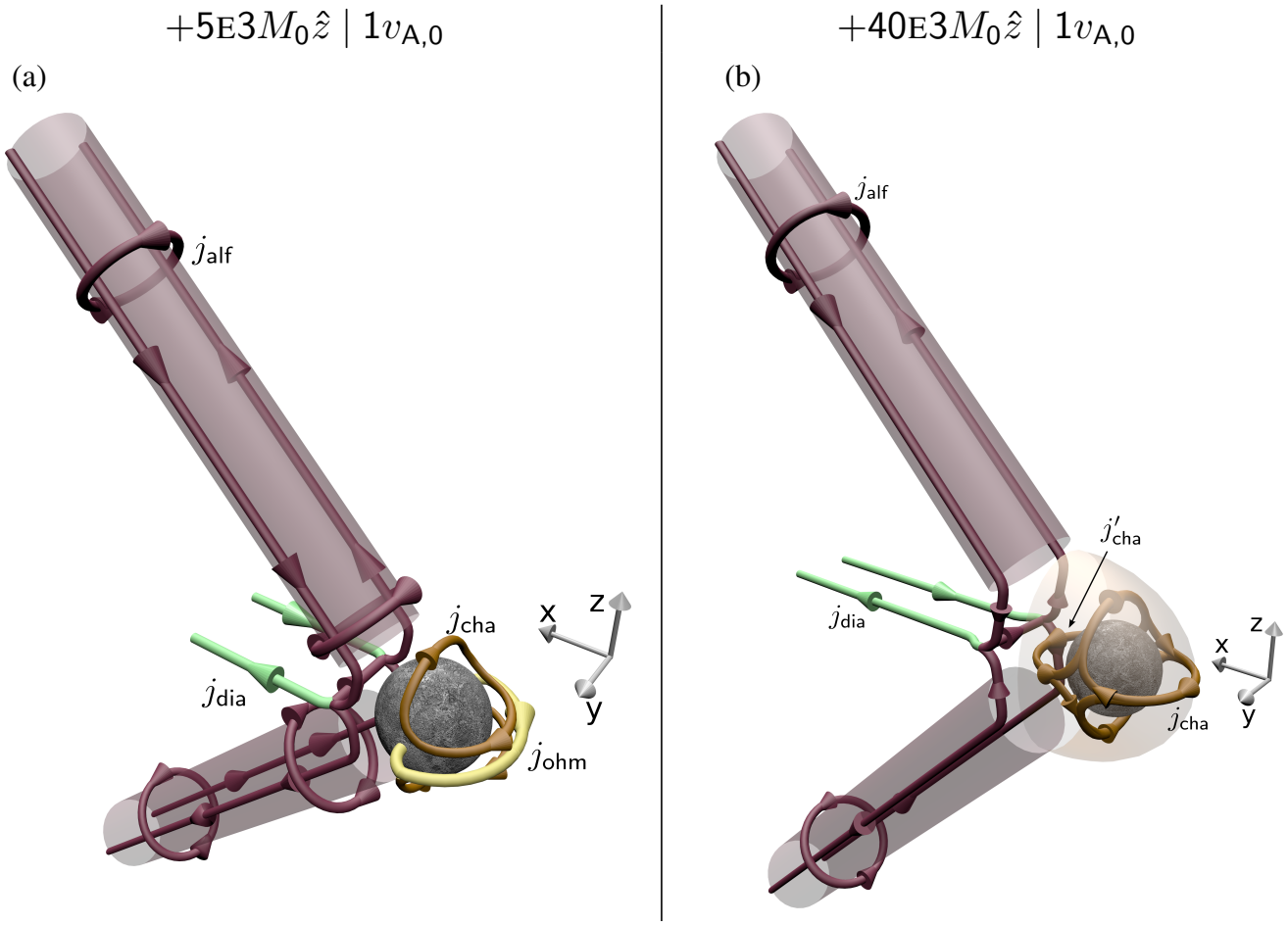

Figure 4.17: Three-dimensional representation of the current structures of the (a) +5E3$M_0\hat{z}$ | 1$v_{A,0}$ and (b) +40E3$M_0\hat{z}$ | 1$v_{A,0}$ systems (see Tables 2.2 and 4.2 for simulation parameters). Description of the currents same as Figure 4.2, except the red semi-transparent layer, which here represents the Alfvén wings. The stellar wind velocity is v_{sw}=1 $v_{A,0}$.

4.4 Conclusions

In this chapter we develop the configuration studied in Chapter 3. Starting from a Lunar-type obstacle we implement a dipole magnetic moment in the core of the obstacle and observe the evolution of plasma structures depending on two parameters: the magnitude of the magnetic moment and the stellar wind velocity. We mainly focus on northward magnetic moment. First, we set the cornerstones in the parameter space, and then we develop the intermediate situations between the cornerstones. The transition from a Lunar-Upward obstacle to a Mercury-Upward obstacle shows that the Chapman-Ferraro current initially appears on the dayside of the obstacle. Even if the magnetosphere is not developed outside of the obstacle, the Chapman-Ferraro current flows on the surface in order to confine the magnetic field within the planet. The Alfvénic current identified in the nightside region of the Lunar-Upward obstacle is divided into two distinct loops due to reconnection processes happening at the southern and northern poles of the obstacle. This reconnection processes generate an acceleration of the stellar wind in the reconnection region and causes a bending of the field lines downstream the wake. For stronger magnetic moments able to balance the stellar wind dynamic pressure, the bow-shock becomes detached. The deceleration of the flow around the obstacle (due to the existence of the bow-shock) decreases the impact of the reconnection process at the poles and therefore also decreases the twisting of the field lines in the wake. Also, the fast mode polarization current j_{pol} seen in the equatorial plane for super-Alfvénic simulations is translated downstream the wake due to the development of a shielded region in the vicinity of the obstacle. At this point we make an analogy with the case of the Lunar-type obstacle: while the perturbing object in the case of the Lunar-type is an inert obstacle, for the case of a developed magnetopause, one expects that the perturbing object is the region where the planetary magnetic field is dominant, also called the shielded region. When one looks at the transition regime between a Rhea-Upward obstacle and a Ganymede-Upward obstacle, we observe that, for upstream velocities $v_{\mathrm{sw}} \geqslant 2\, v_{\mathrm{A},0}$ (or super-fast-magnetosonic), the general current configurations are similar. The differences lay in the ratio between the stellar wind velocity and the MHD modes group velocity (see (3.4)) $v_{\mathrm{sw}}/v_{\mathrm{gr,ms}}$, which define how the plasma structures spread in space. For upstream velocities $v_{\mathrm{sw}} \leqslant 2\, v_{\mathrm{A},0}$ (or sub-fast-magnetosonic), we note the disappearance of the fast mode current, and therefore a structure centered on Alfvén wings for weak magnetic fields. For planetary dipole field stronger than the IMF, we observe the development of a complete magnetosphere.

5 Southward magnetized obstacles in super-Alfvénic regime

5.1 Introduction

In this chapter we study the plasma interactions between a stellar wind and a magnetized planetary obstacle, which magnetic moment is directed southward, i.e. anti-parallel to the cases discussed in Chapter 4. In this magnetic field configuration, reconnection processes occurs on the day- and nightsides of the obstacle. When the planetary dipole field is sufficiently strong, the dipole field line reconnects with the IMF following the process described by Dungey (1961). Studies regarding such configuration have been held for special cases as Earth (Potemra 1979) with detailed descriptions of the current structures. The major current appearing for Earth are the magnetopause current, the ring current, the plasma sheet current, the partial ring current, the neutral sheet current, the magnetotail current, and the Birkeland current (Kivelson and Russell 1995). In this chapter, the obstacle lacks an ionosphere, therefore Birkeland currents (Ogino 1986) are not expected to appear. This chapter focuses on the evolution of the magnetopause, Chapman-Ferraro j_{cha}, magnetotail j_{msph}, plasma sheet, neutral sheet, and more recently discovered, "banana" (Liemohn et al. 2013) currents. The southward IMF field configuration is also present in our solar system at Ganymede (Kivelson et al. 1996). The major differences compared to Earth concern the upstream velocity, which is mostly sub-Alfvénic at Ganymede. This chapter focuses on the plasma interactions in a super-Alfvénic regime, the upstream velocity in all simulations is equal to eight Alfvén Mach number ($8v_{\mathrm{A},0}$). We observe that the condition for triggering a specific current depends on the magnetic moment magnitude in the super-Alfvénic velocity regime. The magnetospheric currents are triggered once the planetary magnetic field at the surface is comparable to the IMF. As long as the magnetic moment is not high enough to fulfill this condition, the structure of the interaction region is similar to the Lunar-type obstacle. However, reaching the IMF magnitude at the surface triggers a Chapman-Ferraro current but is insufficient to trigger a fully developed bow-shock current. We see that only when the dynamic pressure of the stellar wind is fully balanced by the planetary dipole magnetic pressure, the bow-shock is clearly defined. In addition, we also show that every process happening during those transition regime is a continuous and monotonic process.

The grid configurations of the simulations ran for this chapter are detailed in Table 5.1. The geometry of the simulations, the obstacle size, and the plasma beta are given in Section 2.2.2.1 and Table 2.2. Details about the boundary conditions, the resistivity profile of the obstacle, and the numerical limitation are explained in Appendix A.1, A.2, and

Axis	*Box length*	*Cells*
X-axis	600 x_0	144
Y-axis	300 x_0	96
Z-axis	400 x_0	96

Table 5.1: Configuration and size of the grid along each axis of the simulations presented in Chapter 5. The length are expressed in normalized values, detailed in Table 2.1.

M [M_0]	L_{SO} [R_p]	*Case*	*Alternative name*	*Figure*
100	0.15	$-100M_0\hat{z}$	Lunar-Downward	Fig. 5.1
$80 \cdot 10^3$	1.38	$-80\text{E}3M_0\hat{z}$	Mercury-Downward	
$10 \cdot 10^3$	0.69	$-10\text{E}3M_0\hat{z}$		Fig. 5.3
$20 \cdot 10^3$	0.87	$-20\text{E}3M_0\hat{z}$		Fig. 5.5
$40 \cdot 10^3$	1.10	$-40\text{E}3M_0\hat{z}$		Fig. 5.6
$60 \cdot 10^3$	1.26	$-60\text{E}3M_0\hat{z}$		
$65 \cdot 10^3$	1.29	$-65\text{E}3M_0\hat{z}$		
$70 \cdot 10^3$	1.32	$-70\text{E}3M_0\hat{z}$		
$500 \cdot 10^3$	2.55	$-500\text{E}3M_0\hat{z}$		Fig. 5.10

Table 5.2: Parameters for simulations presented in this chapter. The stellar wind velocity is v_{sw}=8$v_{A,0}$ for every simulation, therefore it is not mentioned in the simulation name. The magnetic moment is given in normalized value (see Table 2.1). The term L_{SO} refers to the stand-off distance which expression is detailed in Section 2.2.2.2 and given by Equation (2.19). The name of each case gives the orientation ($-\hat{z}$) and the magnitude of the magnetic moment (M) of the obstacle. The alternative names gives the reader an analogy to specific interaction systems found in the solar system. The figures associated with the presented cases are referenced in the last column.

A.3. The parameters of the various situations treated in this chapter are summarized in Table 5.2, which provides the normalized magnetic moments (see Table 2.1 for the normalization formulas), and the stand-off distances, related to Equation (2.19).
This chapter falls into three parts. We start by introducing two parameter space points: (1) the Lunar-Downward and (2) the Mercury-Downward obstacles. In the following section, we study the transition between those two parameter space points. In the last section, we open the study on higher planetary field strength and introduce the development of the magnetospheric cavity after that the bow-shock has been triggered.

5.2 Two cornerstones in the parameter space: the Lunar-Downward and Mercury-Downward obstacles

In this section we describe and discuss the results obtained for simulation of a Lunar-Downward and a Mercury-Downward obstacles. For more detail about the parameters of the simulations in this section, the reader is referred to Table 5.2. The simulation results

and illustration of current loops of the Lunar-Downward are presented in Figures 5.1a and 5.1b. Such case is related to a stand-off distance of $L_{SO} = 0.15\ R_p$. The magnetic moment used in this simulation is $M = 100\ M_0$, which leads to a surface magnetic field $B_{surf} = 0.012\, B_0$. One notes the presence of the current j_{ohm} in Figure 5.1a. This current is flowing inside the obstacle, in the $-Y$-direction which is parallel to the electric field, and in front of the obstacle, anti-parallel to the electric field. In Figure 5.1b, one sees that the diamagnetic current noted j_{dia} closes via the Alfvénic current noted j_{alf}.

Figures 5.1c and 5.1d show the simulation results for a Mercury-Downward obstacle. This simulation uses a planetary dipole field with a magnetic moment $M = 80 \cdot 10^3\ M_0$, which leads to a surface magnetic field $B_{surf} = 10\ B_0$ and a stand-off distance $L_{SO} = 1.38\ R_p$. In this regime, the pressure from the planetary dipole field is high enough above the surface to balance the stellar wind total pressure. This produces a bow-shock, a magnetosphere, and their associated currents. Figure 5.1c provides the front view of the interaction regions; the dayside Chapman-Ferraro current noted j_{cha} is particularly noticeable, so are the nightside Chapman-Ferraro current j'_{cha}, and bow-shock current j_{bs}. The magnetospheric current j_{msph} is visible in the back view of the interaction region of the Mercury-Downward system, reported in Figure 5.1d. The magnetospheric current flows anti-parallel to the electric field in the north and south polar regions, and parallel to the electric field in the equatorial plane. On the flanks, this current is flowing along the magnetic field. The magnetosheath current, which is similar to the shocklet current, is flagged j_{sho}. From the simulation results, we infer that this current is mostly flowing along the direction of the flow in the $-Y$-section, and anti-parallel to the flow in the $+Y$-section. However, one should note that in the vicinity of the bow-shock, the shocklet current alternate between parallel and anti-parallel directions to the flow.

The Lunar-Downward is similar to the Lunar-type obstacle presented in Chapter 3. The reader is referred to Figure 3.6 for the description of the structures of the plasma interaction. As shown in Chapter 3, the current j_{ohm} is present due to the non perfect dielectric property of the obstacle (see Section 2.3.2). This current is flowing inside the obstacle parallel to the electric field and is closing in the plasma, flowing along the surface of the obstacle. More detail about this current have already been developed in Sections 3.3 and 2.3.2. The wake side of the plasma structure for Case Lunar-Downward is also similar to the lunar type obstacle with a diamagnetic current (j_{dia}) in the center of the wake, a fast mode polarization current (j_{pol}) on the sides of the wake and an Alfvénic current (j_{alf}) in the northern and southern hemisphere of the nightside region.

A schematic of the Mercury-Downward body is presented in Figures 5.2. In this regime, the bow-shock and the magnetosphere are fully developed. The currents j_{cha}, j'_{cha}, j_{msph}, j_{bs}, and j_{sho} are represented. The center of the tail-side is dominated by reconnection effect (first pictured by the "Dungey Cycle" (Dungey 1961)). Due to the reconnection processes, there is a differential velocity existing between the wake center and the surrounding of the reconnection area. This particular configuration leads to Kelvin-Helmholtz instabilities (Belmont and Chanteur 1989, Fermo et al. 2012). The details of the processes happening in this part of the interaction region are beyond the scope of this work, therefore this region is represented as a black box. However, the various currents present in this region follow a global direction, parallel to the electric field. Nonetheless, one must not forget the existence of strong X-components of the current density in the wake center. The nightside region of the equatorial plane is divided into two parts, the shielded region,

where the planetary field is dominant, at the vicinity of the obstacle, and the reconnection region. Since the currents of these regions are parallel, their differentiations can only be done by a specific study of the magnetic field distribution. In this study, we point out the differences between the region dominated by the planetary magnetic field and the region dominated by the IMF. The region dominated by the planetary magnetic field is identified as the shielded region and its currents are assimilated to Chapman-Ferraro current. The downstream part of the wake, dominated by the IMF is therefore assimilated to the reconnection region. In the particular case of an open magnetosphere, one must keep in mind that there is a continuous exchange of material between those two regions and that the "separation line" is a dynamic boundary. On the dayside, the Chapman-Ferraro current and the reconnection current are merged. This situation is similar to the "northward IMF" situation where the Chapman-Ferraro current also merges with the reconnection current at the poles. On the other hand, the bow-shock current does not merge with the Chapman-Ferraro current; this particularity is used in the description of the transition in Section 5.3 to emphasize the development of the bow-shock.

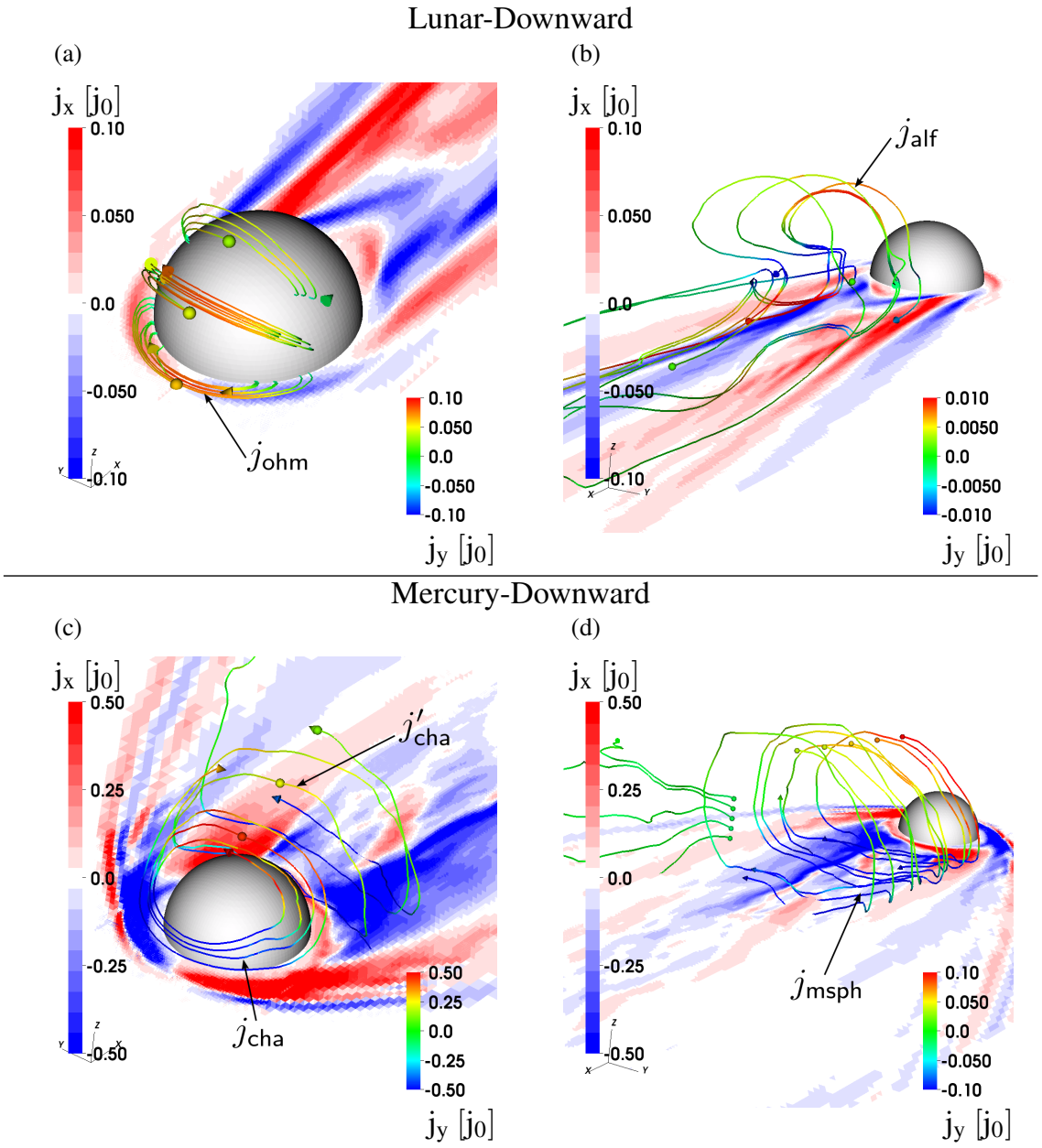

Figure 5.1: X-component of the current density in normalized value (see Table 2.1), in the equatorial plane, for the front (a) and back (b) views of a Lunar-Downward obstacle and the front (c) and back (d) views of a Mercury-Downward obstacle. Blue segments are currents directed sunward and red segments are currents directed anti-sunward. Examples of streamlines of current are represented with their colorbar is on the right bottom of each panel, which gives the Y-component of the current density in order to give the reader a clear view of the streamlines directions. The descriptions of each labeled current are available in Table 2.3. The parameters common to the simulation are provided in Table 2.2, while parameters specific to each simulation type are given in Table 5.2.

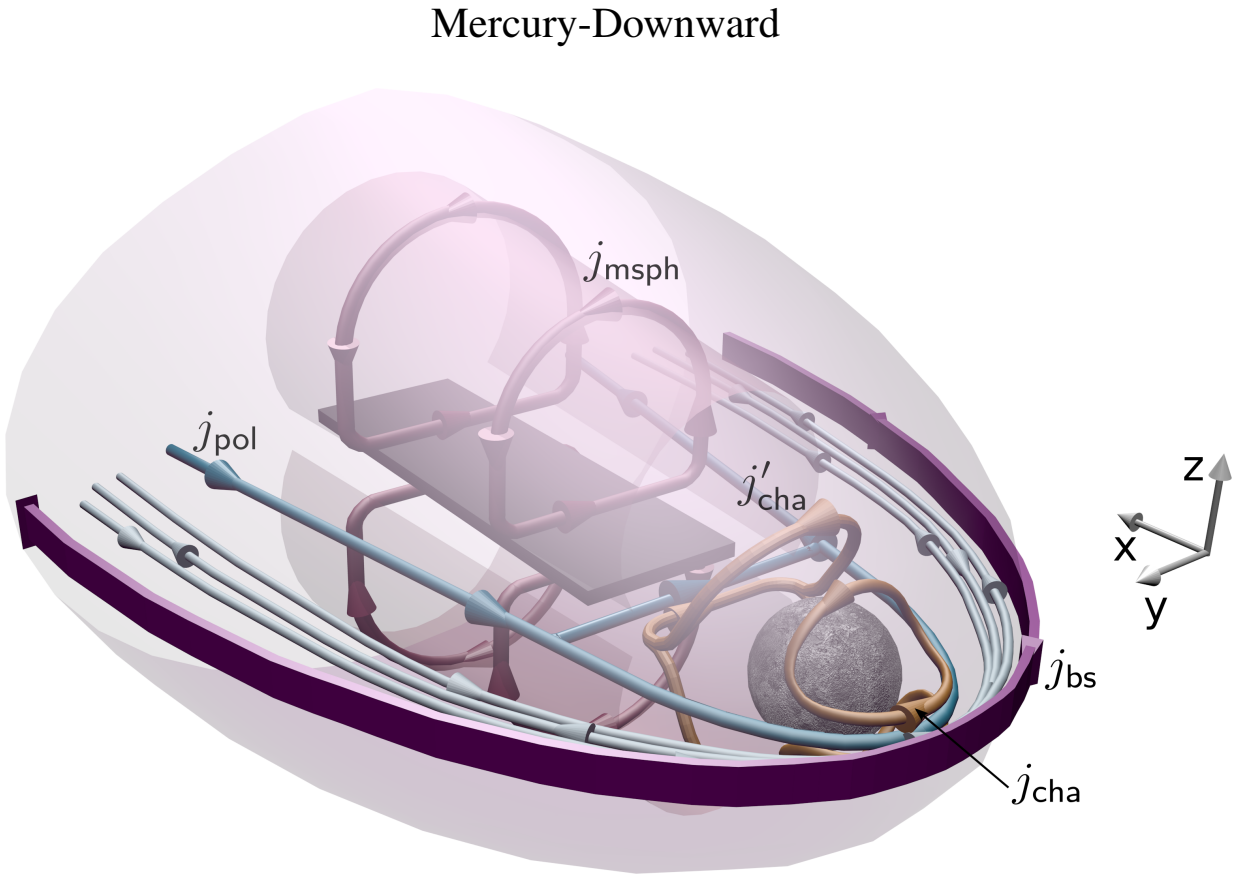

Figure 5.2: Three dimensional schematic representation of the structure of the currents for a Mercury-Downward obstacle (see Tables 2.2 and 5.2 for parameters, and Section 2.2.2.1 about the simulation geometry). The current j_{pol} is represented in blue, j_{msph} in red, j_{sho} in cyan, j_{cha} and j'_{cha} in orange, and j_{bs} in purple (see Table 2.3). The red inner semi-transparent layer represents the nightside magnetopause, and the orange inner semi-transparent layer represents the dayside magnetopause. The outer purple semi-transparent layer represents the bow-shock. The back box at the center of the wake represent a highly perturbed area (see Section 5.2).

5.3 Transition scenarios between the cornerstones

In this section we describe the results obtained for the transition cases where the planetary magnetic field pressure, initially stronger than the IMF pressure at the surface of the obstacle, evolves from weaker than the dynamic pressure to stronger than the dynamic pressure. This evolution is useful to observe how the bow-shock is rising, when the planetary magnetic moment is increased. We then switch from a pure magnetospheric current configuration to a configuration with magnetospheric and bow-shock currents. The parameters related to this section are those of cases $-10\text{E}3M_0\hat{z}$, $-20\text{E}3M_0\hat{z}$, and $-40\text{E}3M_0\hat{z}$ detailed in Table 5.2.

5.3.1 The first intermediate system

The results of the simulation for the $-10\text{E}3M_0\hat{z}$ obstacle are introduced in Figures 5.3a and 5.3b. This simulation corresponds to plasma parameters of $M = 10 \cdot 10^3\ M_0$ for the magnetic moment, leading to a stand-off distance $L_{\text{SO}} = 0.69\ R_{\text{p}}$. The front view of the plasma interaction is shown in Figure 5.3a. The current no longer flows through the obstacle as in the Lunar-Downward case. We have instead a Chapman-Ferraro current (j_{cha}) loop flowing in the $-Y$-direction, parallel to electric field, in front of the obstacle. At the dawn-dusk limit, this front current is merging with the wake currents (usually j_{pol} and j_{dia}). The back view of the plasma interaction is displayed in Figure 5.3b. We can see that in this region, there are no major differences between the Lunar-Downward and the $-10\text{E}3M_0\hat{z}$ cases. The same Alfvénic (j_{alf}) current is present, and consists in large loops flowing perpendicular to the magnetic field in the equatorial plane and in the polar part of the wake, and field aligned on the nightside.
The first stage in the evolution of the plasma interaction region is pictured in Figure 5.4. This is realized through the $-10\text{E}3M_0\hat{z}$ system, where the surface magnetic field is about $B_{\text{surf}} = 1.25\ B_0$, i.e. close to the IMF. In this case, the planetary magnetic moment can push the IMF away from the obstacle, but the stellar wind dynamic pressure confines the dipole field near the surface of the obstacle. This results into two effects: (1) a compression of the planetary dipole field on the dayside, and (2) a stretching of the planetary dipole field lines on the nightside by friction. When this particular regime is achieved, a reconnection process is triggered. The consequences of this reconnection process are an increase of the bending of the field line in the nightside region, leading to differential velocities downstream as seen in Figure 5.7a.
The Chapman-Ferraro current (j_{cha}) develops on both the day- and the nightside. With the configuration of a southward magnetic moment and a southward IMF, the Chapman-Ferraro current at the poles and the Ohmic current (j_{ohm}) are merged. Also, due to this particular configuration between the IMF and planetary magnetic moment orientation, the outer part of the fast wave polarization current in the wake in the equatorial plane, is consistent with the direction of the Chapman-Ferraro current in the equatorial plane on the dayside. This means that, unlike in the case of the planetary northward magnetic moment studied in Chapter 4, the currents which are merging in the front side are the fast mode polarization current and the Chapman-Ferraro current. On the nightside, there is a double draping configuration due the competition between two effects. The first effect is the draping due to the encounter of the interplanetary magnetic field lines and the planetary

dipole. The IMF is deviated when encountering the obstacle and therefore slowed down in the region of the obstacle. The consequence of this stellar wind velocity reduction leads to the appearance of the outer current loops noted j_{alf}. In the configuration of a southward directed planetary moment and southward IMF, the outer Alfvénic current due to the IMF lines draping is parallel at the poles to the Chapman-Ferraro current and the Ohmic current. This implies that in order to get a precise understanding of the role of each current in the area of the poles, several measurements should be used and compared to a theoretical derivation of each effect. The second field line draping in the nightside is due to the reconnection happening on the dayside and in the wake of the obstacle. At the limit of the dipole shielded region observable in Figure 5.7b, the field lines attached to the obstacle after the dayside reconnection get stretched while traveling further downstream of the stellar wind. The sequence of Figures 5.7a, b, c, and d illustrates the differences in field line bending with respect to the strength of the planetary magnetic field.
Regarding the polar part of the Alfvénic current, we emphasize that in this regime, the polar Alfvénic current is interwoven with the fast mode polarization current. One way to study both current separately would be to use a plasma beta $\beta_{\mathrm{i}} + \beta_{\mathrm{e}} > 1$. In this case, the propagation velocity of the fast mode along the field line is equal to the sound velocity, and can therefore be separated from the Alfvén waves which propagate at the Alfvén velocity. Another approach is to derive the energy transported by the fast waves and the Alfvén waves separately. Compared to a Lunar-type obstacle, the flow is more asymmetric, in the equatorial plane. In the $Y \leqslant 0$-region, the equatorial plane current configuration is similar to Case Lunar-Downward while in the $Y \geqslant 0$-region, there is a succession of currents triggered in the same area located at the dawn-side terminator. This is represented by the current j'_{pol} in Figure 5.4. The salient differences between this case and the "northward IMF" simulations presented in Chapter 4 lies in the presence of a reconnection process in the wake. Indeed, the velocity of the plasma in the wake is faster in a "southward IMF" configuration than in a "northward IMF".

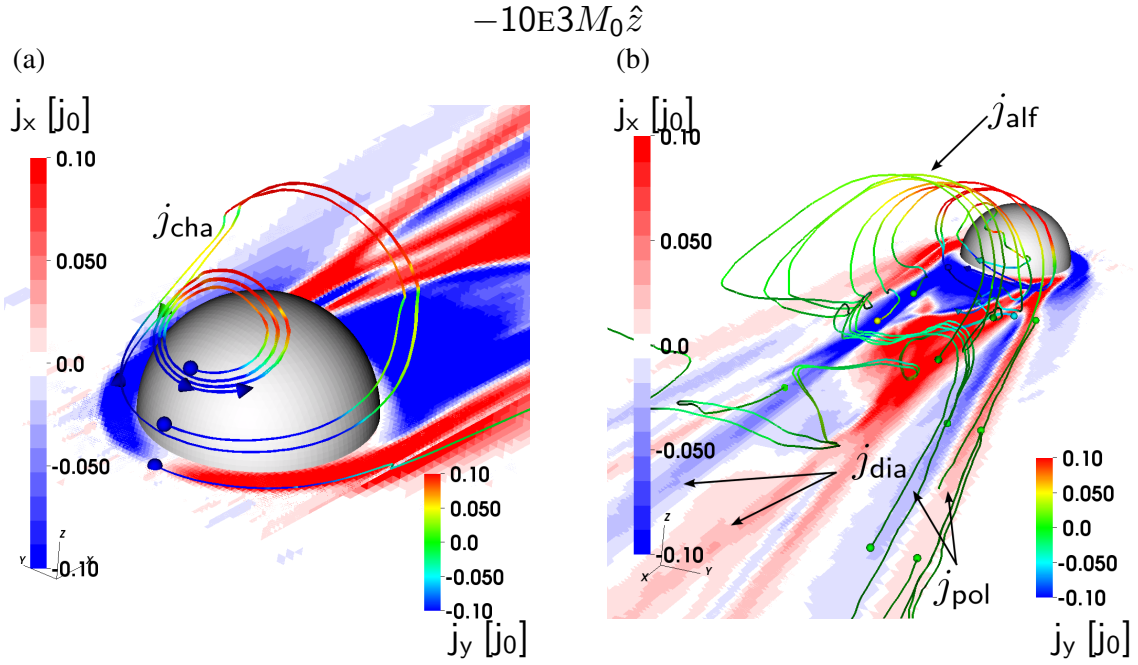

Figure 5.3: X-component of the current density in the equatorial plane for the front (a) and back (b) views of the $-10\text{E}3M_0\hat{z}$ interaction (see parameters in Table 5.2). Current description same as Figure 5.1.

Figure 5.4: Three-dimensional schematic representation of the first stage of the transition between the Lunar-Downward and Mercury-Downward systems, named the $-10\text{E}3M_0\hat{z}$ interaction (parameters in Table 5.2). Description of the currents same as Figure 5.2.

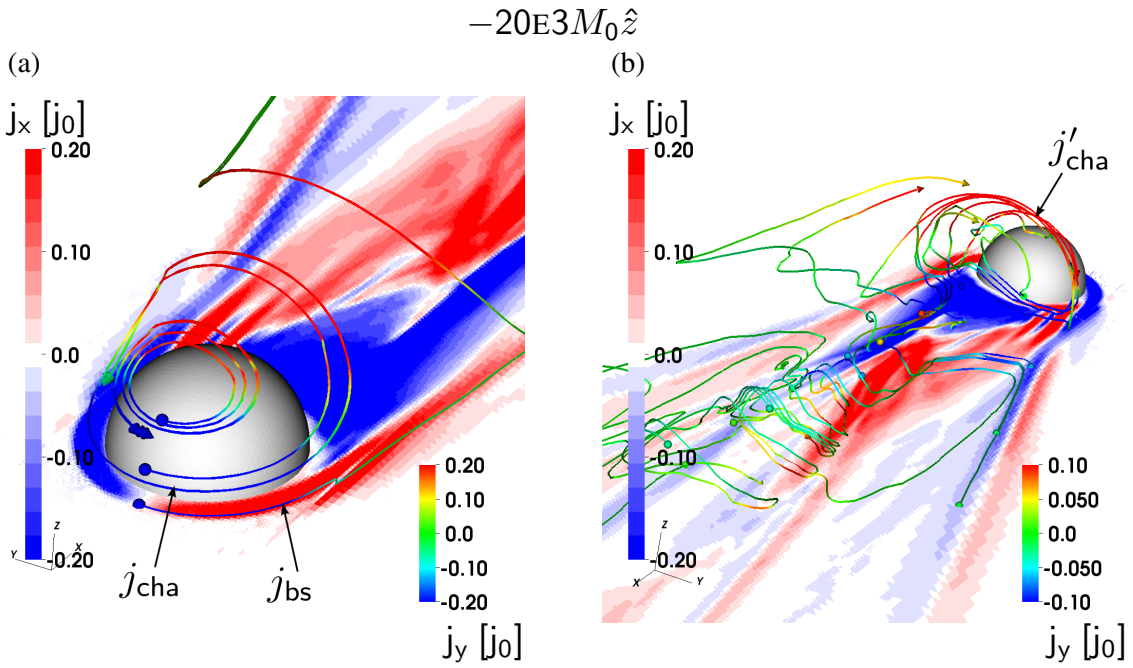

Figure 5.5: Front (a) and back (b) views of the X-component of the current density in the equatorial plane of a $-20\text{E}3M_0\hat{z}$ interaction (see parameters in Table 5.2). Description of current same as Figure 5.1.

5.3.2 The second intermediate system

Figures 5.5a and 5.5b display the configuration of the currents in the $-20\text{E}3M_0\hat{z}$ system. Such an obstacle possesses an internal magnetic moment of $M = 20 \cdot 10^3\ M_0$ and a stand-off distance $L_{SO} = 0.87\ R_p$. In this regime, the planetary dipole field is still confined into the obstacle due to the dynamic pressure of the stellar wind. However, at the surface, the planetary field is equal to $B_{surf} = 2.5\ B_0$. This means that the magnetic pressure of the planetary dipole field is stronger than the IMF pressure and can therefore extend in the nightside of the obstacle, where the dynamic pressure of the stellar wind does not play a role. Figure 5.5a shows the front view of the obstacle. The current configuration is the same as the $-10\text{E}3M_0\hat{z}$ system, the Chapman-Ferraro current (j_{cha}) flows parallel to the electric field in front of the obstacle and anti-parallel to the electric field on the south and north poles of the obstacle. Figure 5.5b presents the nightside view of the interaction region. We can see that, compared to $-10\text{E}3M_0\hat{z}$, the different currents are hardly distinguishable. We observe the development of a nightside Chapman-Ferraro current (j'_{cha}), but the presence of an Alfvénic current (j_{alf}) is no longer noticeable. A strong asymmetry is rising in the tail-side of the interaction region, as Figure 5.5b shows. Also, this region fills up with different velocity regimes, which triggers instabilities.

The results of the simulation of the $-40\text{E}3M_0\hat{z}$ body are shown in Figures 5.6a and 5.6b. For this simulation, the dipole moment is $M = 40 \cdot 10^3\ M_0$. This yields a stand-off distance $L_{SO} = 1.10\ R_p$. This situation represents the limit before the magnetosphere can extend in the dayside. In Figure 5.6a we can observe the front side of the plasma interaction area. This shows that the Chapman-Ferraro current (j_{cha}) on the front side is fully developed

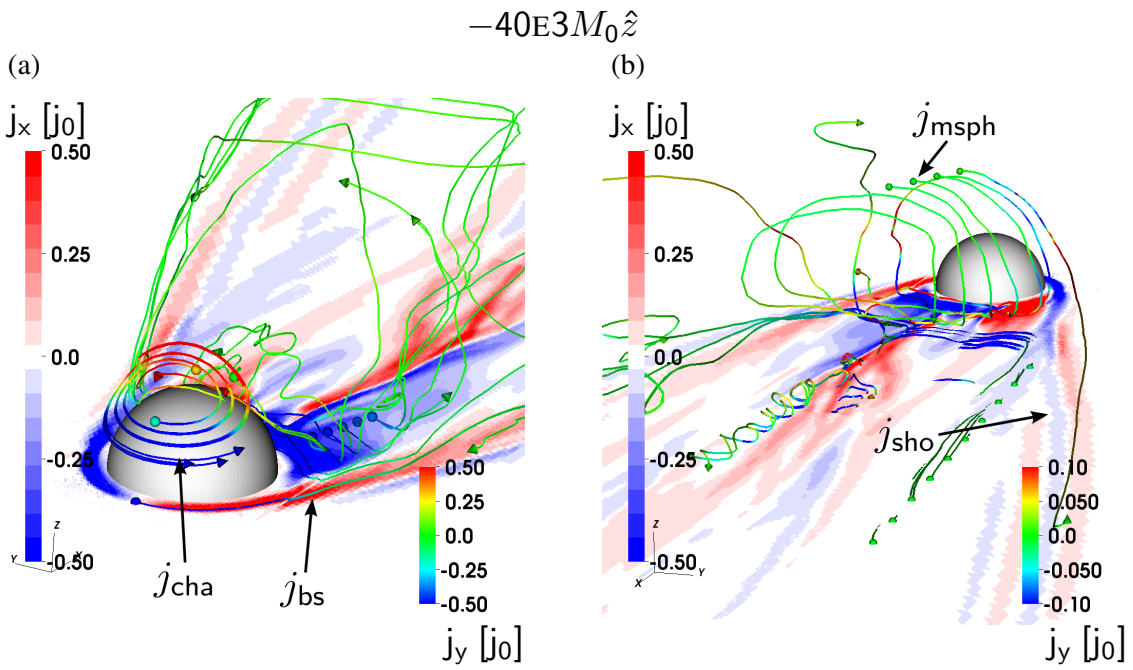

Figure 5.6: Front (a) and back (b) views of the X-component of the current density in the equatorial plane of a $-40\text{E}3M_0\hat{z}$ interaction (see parameters in Table 5.2). Description of current same as Figure 5.1.

and clearly flows in the direction opposite to the bow-shock in the equatorial plane. The back view of the $-40\text{E}3M_0\hat{z}$ case is presented in Figure 5.6b. The dominant current is the magnetospheric current j_{msph}, which flows along the boundaries of the magnetosphere. In the magnetosheath, one notes that the field-perpendicular current j_{sho}, flows in the $+X$-direction in the $Y \leqslant 0$-section and in $-X$-direction in the $Y \geqslant 0$-section.
The evolution of the reconnection process with respect to the magnetization of the planet is shown in Figure 5.7. The displayed simulations are $-10\text{E}3M_0\hat{z}$, $-20\text{E}3M_0\hat{z}$, $-40\text{E}3M_0\hat{z}$, and Mercury-Downward, in Figure 5.7a, 5.7b, 5.7c, and 5.7d, respectively. These four cases are plotted to emphasize the modification of the bending of the field lines between the various regimes presented in this chapter. Looking at the night-side reconnection region, the first inferred property is the position of the reconnection region with respect to the planetary magnetization. Indeed, as the planetary magnetic moment is increased, the position of the nightside reconnection region moves downstream the wake. This effect is easily explainable by the requirement of the reconnection process. Reconnection can happen when the frozen-in condition is broken, which happens when the magnetic field magnitude reaches zero. Therefore, as the planetary magnetic moment increases, the region of zero magnetic field magnitude moves downstream the wake. We note that the bending of the field lines does not play role in the position of the reconnection region, due to the symmetry of the problem in the Y cross-section in regards to the line (Y=0, Z=0). The major difference lies in the magnitude of B_x away from the reconnection point. Figure 5.7 shows that for higher planetary field strength, the IMF line bending in the nightside is more pronounced. This effect is due to the differences in bulk velocities surrounding the reconnection region for each plasma interaction regime. Following the reconnection pro-

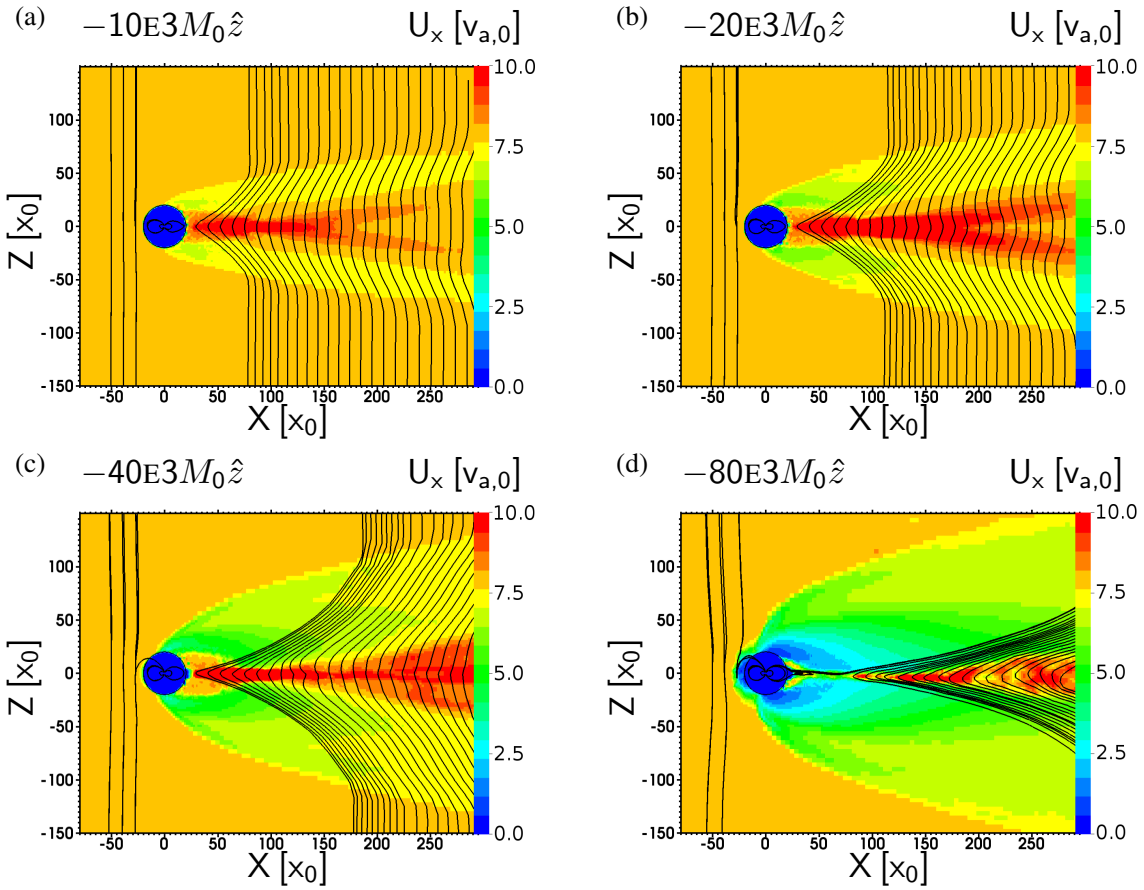

Figure 5.7: X-component of the bulk velocity in the meridional plane (Y-cross section) in normalized values (see Table 2.1). Examples of magnetic field lines are generated from X=−50x_0 to X=300x_0 and represented in black lines. The obstacle is delimited by a black circle with a radius R_p = 20 x_0, which center is at (X=0, Y=0). The simulation presented are the (a) −10E3$M_0\hat{z}$, (b) −20E3$M_0\hat{z}$, (c) −40E3$M_0\hat{z}$, and (d) −80E3$M_0\hat{z}$ (also named Mercury-Downward) interaction types. The parameters of each simulation are available in Table 2.2 and 5.2. The simulation geometry is detailed in Section 2.2.2.1.

cess on the nightside of the interaction region, the inner center of the wake is accelerated sunward ahead of the reconnection point and anti-sunward downstream the reconnection point. This pattern leads to an inner wake current, which is marked j_{alf} in Figure 5.4.

The next step of the topological evolution of the plasma interactions with a planetary obstacle is presented in Figure 5.9, which refers to the case −40E3$M_0\hat{z}$. In this regime, the bow-shock is in a transitory configuration, as presented in Figure 5.8. One should notice that the outer current is triggered by the draping of the field lines by the dipole. It flows parallel to the magnetospheric current. This is represented in Figure 5.9, where the polar part of the outer current loops, noted j_{alf}, is drawn parallel to the bow-shock current noted j_{bs}. In the magnetosheath region, there is a dominant fast mode polarization current j_{pol} flowing perpendicular to the magnetic field and aligned with the flow. Between the current j_{pol} and the bow-shock current, we observe a succession of shocklet currents (j_{sho}). Figure 5.8 depicts the evolution of the currents related to the bow-shock. The simulation results

plotted in each figure refer to parameters close to the bow-shock triggering point. The chosen cases are $-60\text{E}3M_0\hat{z}$, $-65\text{E}3M_0\hat{z}$, $-70\text{E}3M_0\hat{z}$, and Mercury-Downward in Figures 5.8a, 5.8b, 5.8c, and 5.8d, respectively. The associated magnetic moments are increased from $60 \cdot 10^3\ M_0$ to $80 \cdot 10^3\ M_0$, leading to a surface field varying from $7.5\,B_0$ to $10\,B_0$ and a stand-off distance ranging from $L_{\text{SO}} = 1.26\,R_\text{p}$ to $L_{\text{SO}} = 1.38\,R_\text{p}$ (see Table 5.2 for details on the parameters and Table 2.1 for the normalization formulas). In this configuration where the IMF is directed southward, the bow-shock is easily identified by a current directed along the $+Y$-direction. Also, the Chapman-Ferraro current (which is parallel to the reconnection current) and the bow-shock current are anti-parallel in the specific region of the subsolar point. However, at the poles, the Chapman-Ferraro current is parallel to the bow-shock current and no distinction can be made in this region in this regime. One should note that when the configuration is reversed (e.g. in Chapter 4, where the IMF is southward and the magnetic moment is northward), the problematic is also reversed. For the $-60\text{E}3M_0\hat{z}$ system, we notice that the bow-shock current is negligible compared to the Chapman-Ferraro current in front of the obstacle, yet, the bow-shock currents is well-defined on the sides of the interaction region. This indicates the early development of the bow-shock which is fully develop in the Mercury-Downward system. Then, for Cases $-65\text{E}3M_0\hat{z}$ in Figure 5.8b and $-70\text{E}3M_0\hat{z}$ in Figure 5.8c, we see that the current (red area) rises slowly in front of the obstacle. Once the Mercury-Downward interaction reached (Figure 5.8d), the bow-shock current is fully defined. Looking at the results presented in Figure 5.8, we note that there is a displacement of the reconnection point in the wake introduced by Figure 5.7. The reconnection point is moving downstream the wake. Looking at the Y-component of the current in Figure 5.8, we can see that the area behind the reconnection point can be identified by a turbulent area. This starting point of the turbulence can therefore be seen as a separation between the shielded region and the region dominated by the IMF.

On the nightside of the obstacle depicted in Figure 5.9, we have represented the double draping structure explained for the $-20\text{E}3M_0\hat{z}$ system, caused by the planetary field draping for the outer part and the reconnection process for the inner part. The most important difference lies in the equatorial plane in the wake. The magnetosphere being fully developed on the nightside, there is no more refilling process at the center of the wake. The wake is dominated by the reconnection process, which accelerates the flow along the X-axis. The flow acceleration due to the reconnection associated with the wake asymmetry leads to a Kelvin-Helmholtz instability in the wake. The instabilities complicate the current structure in this part of the simulation domain. Their study falls beyond the scope of this dissertation. The general shape of the current flowing in the black box region is a direct current flowing parallel to the electric field (in the $-Y$-direction), which is the property represented in Figures 5.9 by the current j_{msph}.

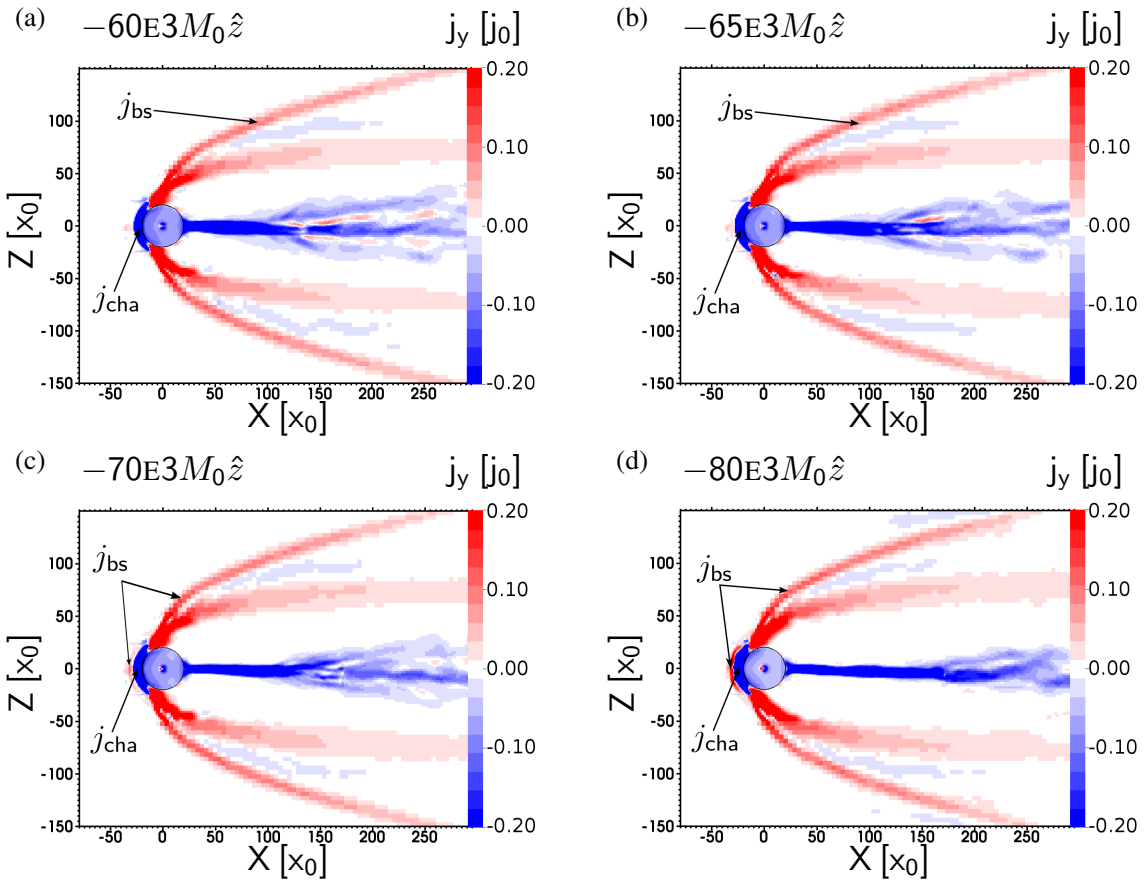

Figure 5.8: Y-component of the current density in the meridional plane (Y cross-section) in normalized values (see Table 2.1). Panels (a), (b), (c), and (d), present results for $-60\text{E}3M_0\hat{z}$, $-65\text{E}3M_0\hat{z}$, $-70\text{E}3M_0\hat{z}$, and $-80\text{E}3M_0\hat{z}$ (Mercury-Downward), respectively. The parameters related to each simulation are given in Table 5.2. The parameters common to the simulation are provided in Table 2.2, while the geometry is detailed in Section 2.2.2.1. The obstacle is represented by a black circle at ($X = 0, Z = 0$). The currents j_{bs} and j_{cha} represent the bow-shock and the Chapman-Ferraro currents, respectively. The description of the annotated currents is given in Table 2.3.

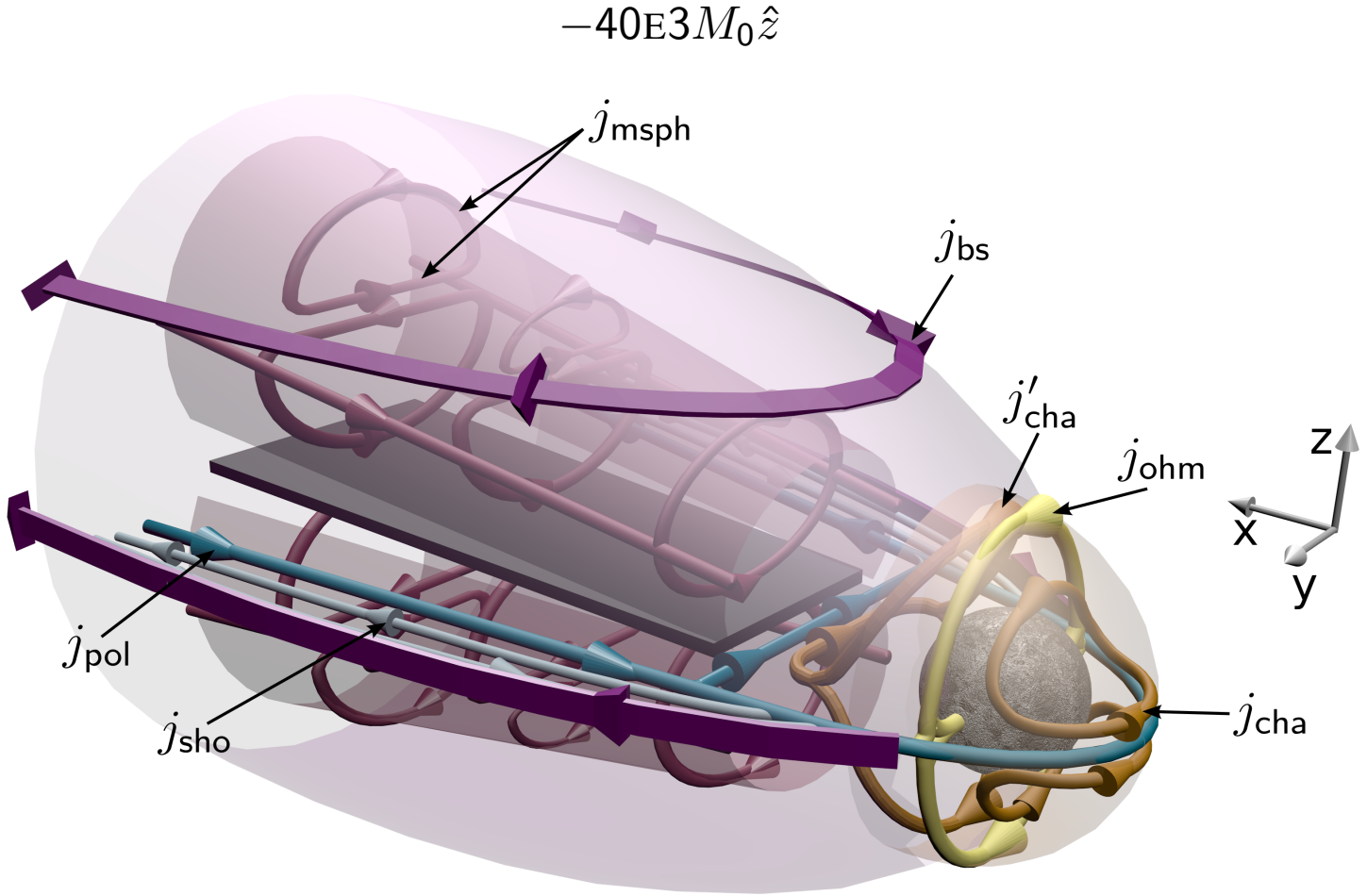

Figure 5.9: Three-dimensional schematic representation of the second intermediate stage between the Lunar-Downward and the Mercury-Downward systems, so-called the $-40\text{E}3M_0\hat{z}$ interaction. The specific simulation parameters are given in Table 5.2. Description of the currents same as Figure 5.2.

5.4 Extension to stronger planetary fields

In this section we describe a dipole field which magnetic pressure is able to counter the stellar wind dynamic pressure above the surface of the obstacle. Referring to Equation (2.19), this means magnetic pressure above $B_{\text{surf}} = 8\ B_0$. Also due to the super-Alfvénic nature of the results presented in this chapter, this means that every planetary magnetic field pressure at the surface presented in this section is stronger than the IMF pressure.
The simulation results for case of the $-500\text{E}3M_0\hat{z}$ obstacle are shown in Figure 5.10. Such an obstacle has a magnetic moment of $M = 500 \cdot 10^3\ M_0$, which leads to a surface magnetic field of $B_{\text{surf}} = 62.5\ B_0$ and a stand-off distance of $L_{\text{SO}} = 2.55\ R_{\text{p}}$ (see Table 5.2 for parameter details). Figure 5.10a displays the front view of the plasma interaction region, a clear distinction between the Chapman-Ferraro current (j_{cha}) and the bow-shock current (j_{bs}) is observable. Figure 5.10b shows examples of current lines for the nightside magnetospheric current. We see that this current flows in the direction of the electric field in the equatorial plane, but anti-parallel to the electric field at the poles. The overall tail displayed in this figure is dominated by this magnetospheric current, which defines the magnetopause.
The general structures of the plasma interactions in Case $-500\text{E}3M_0\hat{z}$ are drawn in Figure 5.11. Compared to the Mercury-Downward system presented in Figures 5.2c and 5.2d, a first distinction can be inferred when looking at the nightside of the interaction region. The double draping loop structure presented for Case $-40\text{E}3M_0\hat{z}$ in Figures 5.9c and 5.9d evolves to a single magnetospheric current loop (j_{msph}) seen for the Mercury-Downward in Figure 5.2c and 5.2d after increasing the planetary dipole field. This evolution is due to the translation of the reconnection region. As shown in Section 5.3, when the magnetic moment is increased, the reconnection region moves downward the wake. Therefore, for stronger magnetic moment, the vicinity of the nightside of the obstacle is dominated by the current of the shielded region, which consists in a simple loop between the center of the wake and the magnetopause (Potemra 1979). This configuration is also referred to as the θ-configuration. The existence of double loop structure seen for weaker magnetized obstacle in the nightside are expected to be seen for a $-500\text{E}3M_0\hat{z}$ obstacle, but further downstream. To show this effect in our results, this would require using a larger simulation domain, which is not currently possible due to computational requirements. The center of the inner wake of the interaction region is subject to reconnection. As explained in Section 5.3, the reconnection triggers a differential acceleration in the flow inside the wake, leading to a difficult interpretation of the current structure in this particular region. Therefore, this region is represented by a black box to clearly indicate the complexity of the currents in this region. Among the currents represented in Figure 5.11, one is the current j_{ring}. The existence of this current in this regime is subject to particular caution. Indeed, the first problem concerns the orientation. In the literature, this current is discussed as flowing in a way that it increases the strength of the planetary dipole field. In our results, this current is shown as weakening the magnetic moment. This question remains open at present.

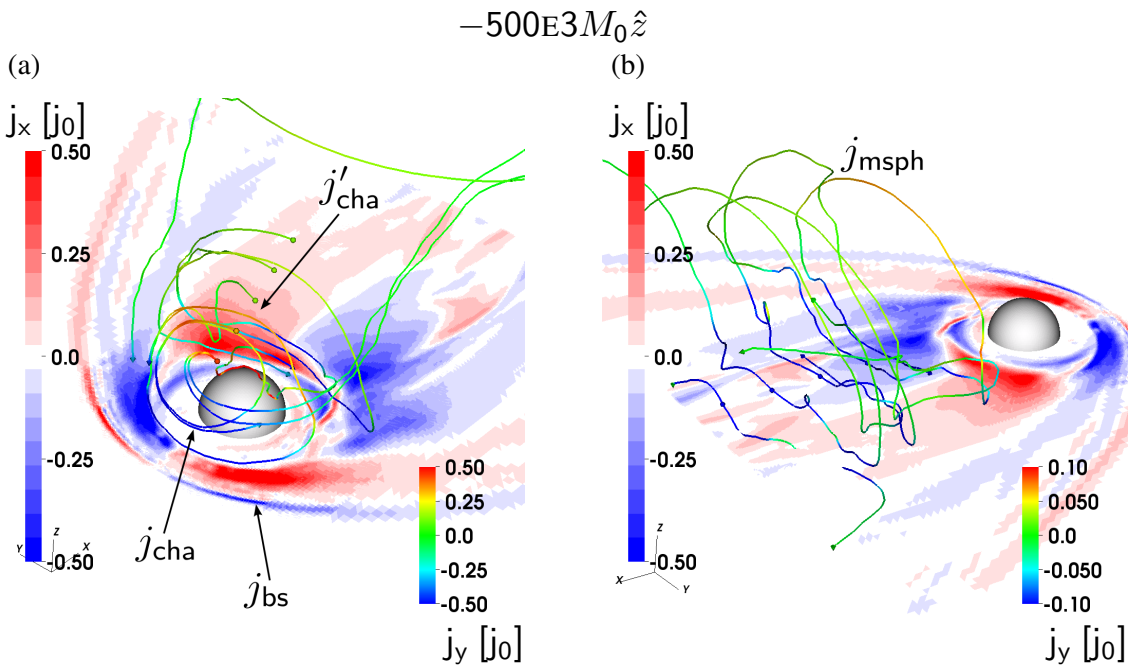

Figure 5.10: Front (a) and back (b) views of the X-component of the current density in the equatorial plane of a $-500\text{E}3M_0\hat{z}$ interaction (see parameters in Table 5.2). Description of current same as Figure 5.1.

5.5 Conclusions

The results presented in this chapter show how the various interaction regimes interact in the case of a southward planetary magnetic moment conjugated with a southward IMF. We set two boundary points, which we call the Lunar-Downward obstacle and the Mercury-Downward system. Those two points are defined by qualitative interaction regime defined by a Lunar-type interaction studied in Chapter 3 for the first case and a shock triggering interaction for the second regime. Between those two points, we define two qualitative interaction regimes. The first stage appears when the surface magnetic field reaches the magnitude of the IMF, and consists in a growing magnetosphere and a double draping pattern in the wake due to the reconnection process. The second stage appears in the regime where the surface planetary magnetic pressure is one order of magnitude larger than the IMF but less than the stellar wind dynamic pressure, and sees an interaction region dominated by the bow-shock current. Those steps are illustrated by two processes: reconnection and bow-shock formation. We show that the reconnection point moves downward the wake as the planetary dipole magnitude increases. The particular configuration between the IMF and the planetary field allows distinguishing between the bow-shock current and the Chapman-Ferraro current. Therefore we observe that the bow-shock current appears after the Chapman-Ferraro current, when the theoretical stand-off distance reaches a value of $L_{SO} = 1.38\,R_p$. In the last section, we present results of interactions of planetary fields having a stand-off distance $L_{SO} > 1\,R_p$. When such a regime is simulated, the magnetospheric cavity becomes more developed.

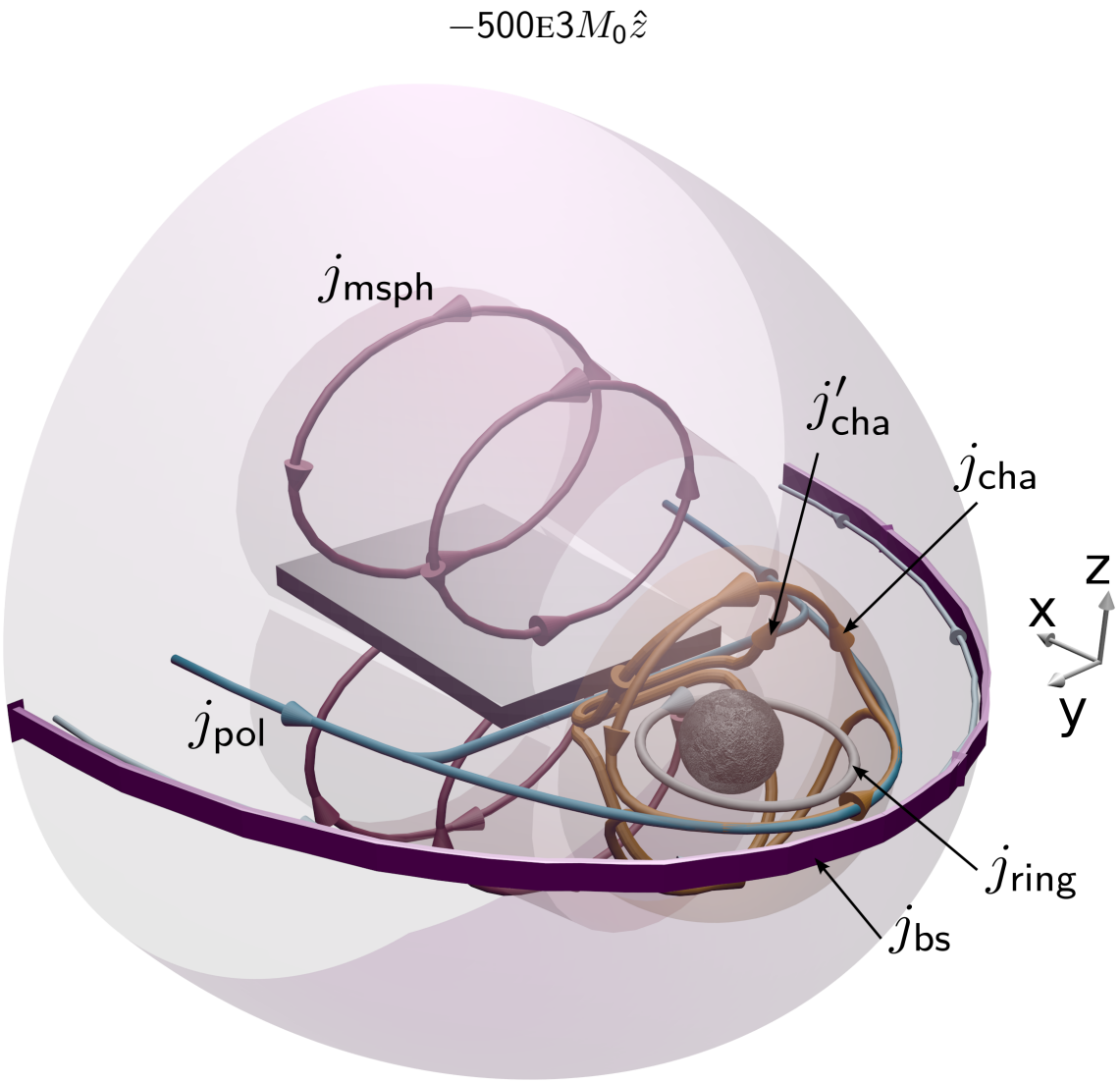

Figure 5.11: Three-dimensional schematic representation of the $-500\text{E}3M_0\hat{z}$ interaction. The specific simulation parameters are given in Table 5.2. Description of the currents same as Figure 5.2.

6 Ionospheres in super-Alfvénic regime

6.1 Introduction

The ionospheric density at the dayside of an obstacle can vary from few particles per cubic centimeters, which is the case for Earth's moon where weak sputtering of particles has been observed (Wurz et al. 2007), to values like 10^5 cm^{-3} for example at Venus (Luhmann and Cravens 1991). In this chapter, we focus on the investigation of those two cornerstones and the interaction systems in between by varying the production rate of the ionosphere. The plasma interactions are only treated in a super-Alfvénic regime, with a stellar wind velocity $v_{sw} = 8v_{A,0}$ (consistent with the choice of the stellar wind velocity used in the Lunar-Type interaction). Plasma interactions in sub-Alfvénic regime are present in the solar system with for example the outer moons like Titan or Callisto, which are embedded in the magnetospheres of Saturn and Jupiter, respectively. The study of Callisto-type interaction and the transition between Callisto-type and Venus-type will be addressed in future work. Therefore the results presented in this chapter are only compared to Venus and Mars simulations.

Various mechanisms occur within an ionosphere such as ionization (photoionization, particle impact ionization), dynamo effect (neutral-ion collision), recombination, chemical reactions, precipitation (Kivelson and Russell 1995, Schunk and Nagy 2004). Two major ionization mechanisms are usually taken into account to produce ions in the case of a planetary obstacle: photoionization and collisions with high energy particles. The dynamo process taking place into an ionosphere is identified through various names for the same mechanism, in this dissertation we call it ionospheric conductivity. The general idea is to express the current generated by the mechanisms within an ionosphere via a conductivity tensor, which components are the Pedersen and Hall conductivities. The equilibrium between ions and neutrals is commonly set up by the ratio between the ionization processes, the recombination, and the pick-up. The recombination is commonly described by three processes: radiative recombination, dissociative recombination and attachment (Baumjohann and Treumann 1996). The major interaction between the ionosphere and the stellar wind is driven by mass-loading and ionospheric conductivity. At the interface between the ionosphere and the stellar wind, those processes drive a magnetic pile-up boundary (Brain et al. 2003).

In our simulations, we focus on the production function. An equilibrium is reached when the number of produced ions is equal to the number of ionospheric ions moving out of the simulation domain. We also do not implement any chemical reaction or collision and

charge exchange. A consistent study of ionospheric interactions should implement every process. However, our purpose in this chapter is to introduce a general description of the interaction of a stellar wind with an inert body possessing an ionosphere. For this, we use generation of ions based on the Chapman profile (Baumjohann and Treumann 1996). Details about the generation profile is given in Section 2.2.3. As it was mentioned, the parameters used to generate the profile should be different for two different ionospheric species. In this chapter our investigation focuses on the ionospheric production and the impact of the mass of the ionospheric ions. We therefore generate ionosphere using H^+, with a mass $m_\alpha = 1m_0$, and O^+, with $m_\alpha = 16m_0$.

The configuration of the grid for the simulation run in this chapter is provided in Table 6.1, while the constant simulation parameters as the obstacle radius and the stellar wind plasma beta at initialization are given in Table 2.2. The parameters of the simulation ran for this chapter are detailed in Table 6.2. The production input in the simulation, based on Equation (2.29) is varied from $Q_\alpha = 100Q_{\alpha,0}$ to $Q_\alpha = 50 \cdot 10^3 Q_{\alpha,0}$ (see Table 2.1 for the definition of $Q_{\alpha,0}$). Compared to the solar system obstacle, the range of production values presented in the table contains productions of Venus and Mars. At Venus, typical production are e.g. given by Martinecz et al. (2009): $B_0 = 5$ nT, $n_0 = 5$ cm^{-3}, and the total production is $Q_\alpha = 1.04 \cdot 10^{26}$ s^{-1}, which in normalized units gives: $Q_\alpha = 36300Q_{\alpha,0}$. Other values at Venus are given by Jarvinen et al. (2010), which provides another set of parameters: $B_0 = 10$ nT, $n_0 = 14$ cm^{-3}, $Q_\alpha = 4.09 \cdot 10^{24}$ s^{-1} for the production of O^+, and $Q_\alpha = 6.42 \cdot 10^{24}$ s^{-1} for H^+. This corresponds in our table of parameters to $Q_\alpha = 1200Q_{\alpha,0}$ and $Q_\alpha = 1880Q_{\alpha,0}$, for H^+ and O^+, respectively. At Mars, an example of the ionospheric production is furnished by Boesswetter et al. (2004), with $B_0 = 3$ nT, $n_0 = 4$ cm^{-3}, $Q_\alpha = 5.37 \cdot 10^{25}$ s^{-1} for a production of O^+. This corresponds in our normalized units to $Q_\alpha = 28000Q_{\alpha,0}$. However, those values are specific production at specific time, one expects to observe a wide range of production values for those specific cases, depending on the brightness of the sun (Brace and Kliore 1991, Moore et al. 1991, Zhang et al. 1993). Also, the total ionization frequency of a planetary ionospheres, has to take into account the various mechanism occurring in it. The derivation of the total ionization rate of an ionosphere is usually made by first determining the neutral profile of the atmosphere and calculating the ionization rate of the neutral atmosphere (Najib et al. 2011, Riousset et al. 2014). In this chapter, collisions and recombination are not taken into account for simplicity, therefore the neutral profile is only expressed through the values used in the Chapman profile, and is the same for every simulation.

The range of production values presented in this chapter goes across both Venus and Mars, and tend to present possibilities of plasma structure configuration depending on the importance of the ionization processes. Table 6.2 also provides the species used in each simulation. We separately study the plasma and current structures for an ionosphere first only composed of H^+ (with $m_\alpha = 1m_0$) and then composed of O^+ (with $m_\alpha = 16m_0$). The charge of both species is $q_\alpha = 1q_0$. The plasma beta for each ionospheric species is set at the start of the simulation to 0. Setting the ionospheric beta to 0 implies lowering thermal effects at the interface between the ionosphere and the stellar wind. Thus, the observed effects in the simulation are mostly due to the mass-loading. Albeit two different species are used, the same set of parameters is used, detailed in Section 2.2.3. A full treatment would require adapting the scale height and the cross-section for each ion species used. In this dissertation, we keep the number of parameters modified for each new step at

Axis	*Box length*	*Cells*
X-axis	400 x_0	96
Y-axis	400 x_0	96
Z-axis	400 x_0	96

Table 6.1: Configuration and size of the grid along each axis of the simulations presented in Chapter 6. The length are expressed in normalized values, detailed in Table 2.1.

his lowest, therefore we do not change the fundamental parameters of the ionospheric generation profile. The Chapman profile in the equatorial plane related to such values is plotted in Figure 2.1.
Studies of the various plasma interaction under different ionospheric production conditions have been held by Jarvinen et al. (2009) for Venus, where they performed a range of test for production rates from $Q_\alpha = 10^{21}$ s^{-1} to $Q_\alpha = 10^{27}$ s^{-1}. Boesswetter et al. (2010) studied the evolution of the ionosphere of Mars, through various production parameters. Similar investigations were done on comets approaching the sun (Biver et al. 1997).
This chapter is divided in three major sections. The first and second parts discuss the results of the simulations with two kinds of ionospheres, hydrogen-generated and oxygen-generated ionospheres. Each of these two major parts is divided in subsection ordered as in the previous chapter, beginning with a description of the cornerstones of the parameter space, and followed by a discussion of the transition states. In the last section we bring up concluding remarks.

6.2 H^+ generated ionospheres

In this section, ionized hydrogen is used to generate the ionosphere. The section is divided in two parts: first the two cornerstones in the parameter space, which are the Weak-H^+ and the Venus-H^+ obstacles, are described. In the second part, the transition between those two points are studied.

6.2.1 Cornerstones in the parameter space: the Weak-H^+ and the Venus-H^+ cases

Figures 6.2a and 6.2b display the plasma interaction of the Weak-H^+ system. The production rate used for this simulation is $Q_\alpha = 100\ Q_{\alpha,0}$ (see Table 2.1). As shown by Figure 6.1a, after reaching the stationary state, the surface density of the ionospheric ions on the dayside reaches about $n_{\alpha,\mathrm{surf}} = 0.01\ n_0$. Although in this regime the ionospheric ion density is well beyond the background density, its impact on the IMF is observable as shown by Figures 6.2a and 6.2b. Qualitatively, the description of the overall structure is similar to a Lunar-type system described in Chapter 3. The currents j_{dia}, j_{alf}, j_{pol}, and j_{ohm} are also identified in this regime.
A schematic representation of the Weak-H^+ system is provided as Figure 6.3a. The presence of the ionospheric ions once the stationary state is reached is illustrated through the semi-transparent white area, as it is presented by the results in Figure 6.1a. The inter-

Species	Q_α [$Q_{\alpha,0}$]	$n_{\alpha,\text{surf}}$ [n_0]	*Case*	*Alternative name*	*Figure*
H^+	100	0.01	$100Q_{\alpha,0}$ | H^+	Weak-H^+	Fig. 6.2
	$50 \cdot 10^3$	10	$50\text{E}3Q_{\alpha,0}$ | H^+	Venus-H^+	
	$1 \cdot 10^3$	0.1	$1\text{E}3Q_{\alpha,0}$ | H^+		Fig. 6.4
	$10 \cdot 10^3$	1	$10\text{E}3Q_{\alpha,0}$ | H^+		Fig. 6.5
	$25 \cdot 10^3$	5	$25\text{E}3Q_{\alpha,0}$ | H^+		Fig. 6.6
O^+	100	0.05	$100Q_{\alpha,0}$ | O^+	Weak-O^+	Fig. 6.9
	$50 \cdot 10^3$	200	$50\text{E}3Q_{\alpha,0}$ | O^+	Venus-O^+	
	$1 \cdot 10^3$	0.5	$1\text{E}3Q_{\alpha,0}$ | O^+		Fig. 6.12
	$10 \cdot 10^3$	10	$10\text{E}3Q_{\alpha,0}$ | O^+		Fig. 6.13
	$25 \cdot 10^3$	50	$25\text{E}3Q_{\alpha,0}$ | O^+		Fig. 6.13

Table 6.2: Simulation parameters used in this chapter. First column gives the species used to generated the ionosphere in the simulations. the second column gives the values of the production Q_α (see Equation (2.29)) in normalized values (see Table 2.1), generating the ionosphere. For more detail about how the production is calculated, see Section 2.2.3. The third column gives an overall estimation of the dayside density at stationary state in normalized values. The fourth column gives the name of the simulation, which provides the production and the species. The fifth column presents an alternative name for specific cases chosen as cornerstones in the parameter space. The last column gives the related figures where the simulation results are presented. For every simulation, the upstream stellar wind is v_{sw}=8$v_{\text{A},0}$, and the ionospheric ion beta is zero at the initialization. Other simulation parameters (stellar wind beta and planetary radius) are detailed in Table 2.2.

action region in the Weak-H^+ system is more asymmetric that of a Lunar-type obstacle, which results from the presence of ionospheric ions. This means that, even for an ionospheric density of 0.01 ρ_0, the magnetic perturbations in the interaction region, i.e. in the nightside of the obstacle, are of the order of magnitude of the Lunar-type perturbations. The bow-shock current here noted j_{bs} is partly represented in Figure 6.3a, in order to show its asymmetric property in this particular regime. However, as shown by Figures 6.2a and 6.2b, its magnitude is one order lower than the diamagnetic current and the polarization current. One illustration of this regime can be obtained by comparing our obstacle with a cometary obstacle. The study by Bagdonat and Motschmann (2002a) (Figure 8), showed that, while the pick-up ion process is holding in the $-Y$-plane, (i.e. in the electric field direction), the shocklets, or fast mode cones are developing in the $+Y$-plane. However, the asymmetric property of the interaction region is only noticeable in the outer regions. In the center of the wake, for such a weak ionospheric density, the interaction regime is similar to the Lunar-type interaction, which means that the particle void generates a pressure gradient boundary and consequently, a diamagnetic current bounds this region. Also the draping initiated by the mass-loading of the stellar wind generates an Alfvénic current on the top and down sides of the interaction region.

Figures 6.2c and 6.2d present the simulation results for the Venus-H^+ interaction. This regime is generated by a production rate $Q_\alpha = 50 \cdot 10^3$ $Q_{\alpha,0}$. As observed in Figure 6.1b, the average ionospheric density on the dayside close to the surface at steady state is

$n_{\alpha,\mathrm{surf}} = 10\ \mathrm{n}_0$. Few currents have been identified in this regime. The overall interaction structure is articulated around the bow-shock current (j_{bs}), the magnetospheric current (j_{msph}), and the shocklet current (j_{sho}). Conversely to the interaction of a stellar wind with a planetary dipole, one does not see any Chapman-Ferraro, reconnection, or ring currents. Indeed those currents are related to planetary magnetic field distortions, which are absent in this regime. Compared to the Weak-H^+ system, the interaction region is mostly symmetric, the absence of asymmetry is discussed in detail in the next section.
A schematic interpretation of the simulation of a Venus-H^+ body is provided in Figure 6.3b. The currents present in this interaction regime are the bow-shock current (j_{bs}), the magnetospheric current (j_{msph}), the Pedersen current (j_{ped}), and the shocklet current (j_{sho}). The description of the Pedersen current depends on the interpretation of the phenomena. One point of view describes the ionospheric current as a current generated by the mass-loading of the stellar wind. This mass-loading creates a slow down of the stellar wind ions and therefore a draping of the IMF lines. Consequently to this field line bending, the mass-loading, or Pedersen current (in this chapter annotated as j_{ped}) appears. Another point of view is to explain that the Pedersen current is generated by the Pedersen conductivity. This conductivity is inherent to an ionosphere, and, in this work, is derived from the ionospheric ions production. Subsequently to this conductivity, the electric field generates the Pedersen current, and therefore a draping is observed in the results. The common idea is to explain the physical process by the transfer of momentum between the stellar wind and the ionosphere, however, an easy way of modeling this interaction is done by introducing the Pedersen conductivity created by the production rate. In this dissertation, we use the production rate to derive the conductivity of the ionosphere. Therefore, in order to not mix the two points of view, we focus on the Pedersen conductivity generated by the ionospheric production rate for the rest of this chapter. This is represented by the Pedersen current (j_{ped}) in Figure 6.3.
The overall current system of the Venus-H^+ interaction regime is due to the draping of the IMF generated by the ionosphere. The magnetic field which piles-up at the dayside of the obstacle generates a shielding which triggers a magnetopause around the interaction regions. Consequently to this magnetopause, a bow-shock is also triggered. The detailed configuration of the overall system is, however, quite complex and requires further investigations.

6.2.2 Transition states between the Weak-H^+ and the Venus-H^+ obstacles

The simulation of the $1\mathrm{E}3Q_{\alpha,0}\,|\,H^+$ system, which results are presented in Figure 6.4, uses a production rate of $Q_\alpha = 1 \cdot 10^3 Q_{\alpha,0}$. This leads to an average density on the dayside at the stationary state of $n_{\alpha,\mathrm{surf}} = 0.1 n_0$, observable in Figure 6.7a. On the nightside, the mean ionospheric density is about $n_\alpha = 0.1 n_0$. The currents j_{pol}, j_{alf}, and j_{ohm} are visible. The $10\mathrm{E}3Q_{\alpha,0}\,|\,H^+$, presented in Figure 6.5 focus on a simulation with a production rate $Q_\alpha = 10 \cdot 10^3 Q_{\alpha,0}$. Once the stationary state is reached, the density on the dayside of the obstacle is $n_{\alpha,\mathrm{surf}} = 1 n_0$ and $n_\alpha = 0.5 n_0$ in the wake, as shown by Figure 6.7b. One still observes the Pedersen current (j_{ped}) and the bow-shock current (j_{bs}) in the equatorial plane. In the nightside, the Alfvénic perturbation evolves into a magnetopause current (j_{msph}).

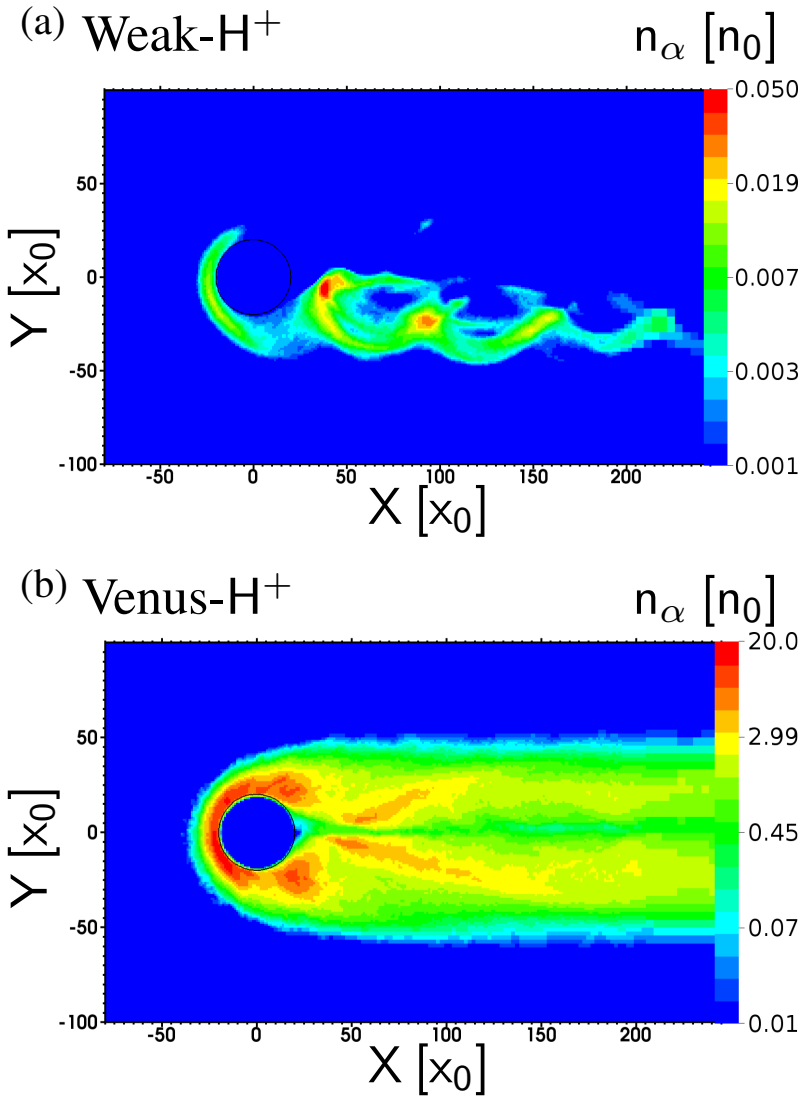

Figure 6.1: Number density of the ionospheric ions in the equatorial plane in normalized units (see Table 2.1). Panels (a) and (b) present the results for the Weak-H^+ and the Venus-H^+ interaction systems, respectively (see details of the parameters in Table 6.2). The colorbar uses a logarithmic scale. The IMF is directed along the $-Z$-axis, the stellar wind flows in the $+X$-direction. The geometry is detailed in Section 2.2.2.1. The configuration of the grid is given in Table 6.1. The obstacle is represented by a black circle centered at (X=0, Y=0), the obstacle radius and plasma beta are given in Table 2.2. The ionospheric plasma beta is set to zero at the initialization.

Figures 6.6a and 6.6b present the front and back views of the simulation results of $25\text{E}3Q_{\alpha,0}$ | H^+ system, which simulates an obstacle having an ionosphere with a production parameter $Q_\alpha = 25 \cdot 10^3 Q_{\alpha,0}$. The simulation results of the $25\text{E}3Q_{\alpha,0}$ | H^+ emphasize the Pedersen current j_{ped} in the entire ionosphere region. In this regime, Figure 6.7c shows that at steady state, the dayside density reaches values about $n_{\alpha,\text{surf}} = 5n_0$. One observes that the currents in the wake are dominated by the magnetospheric current

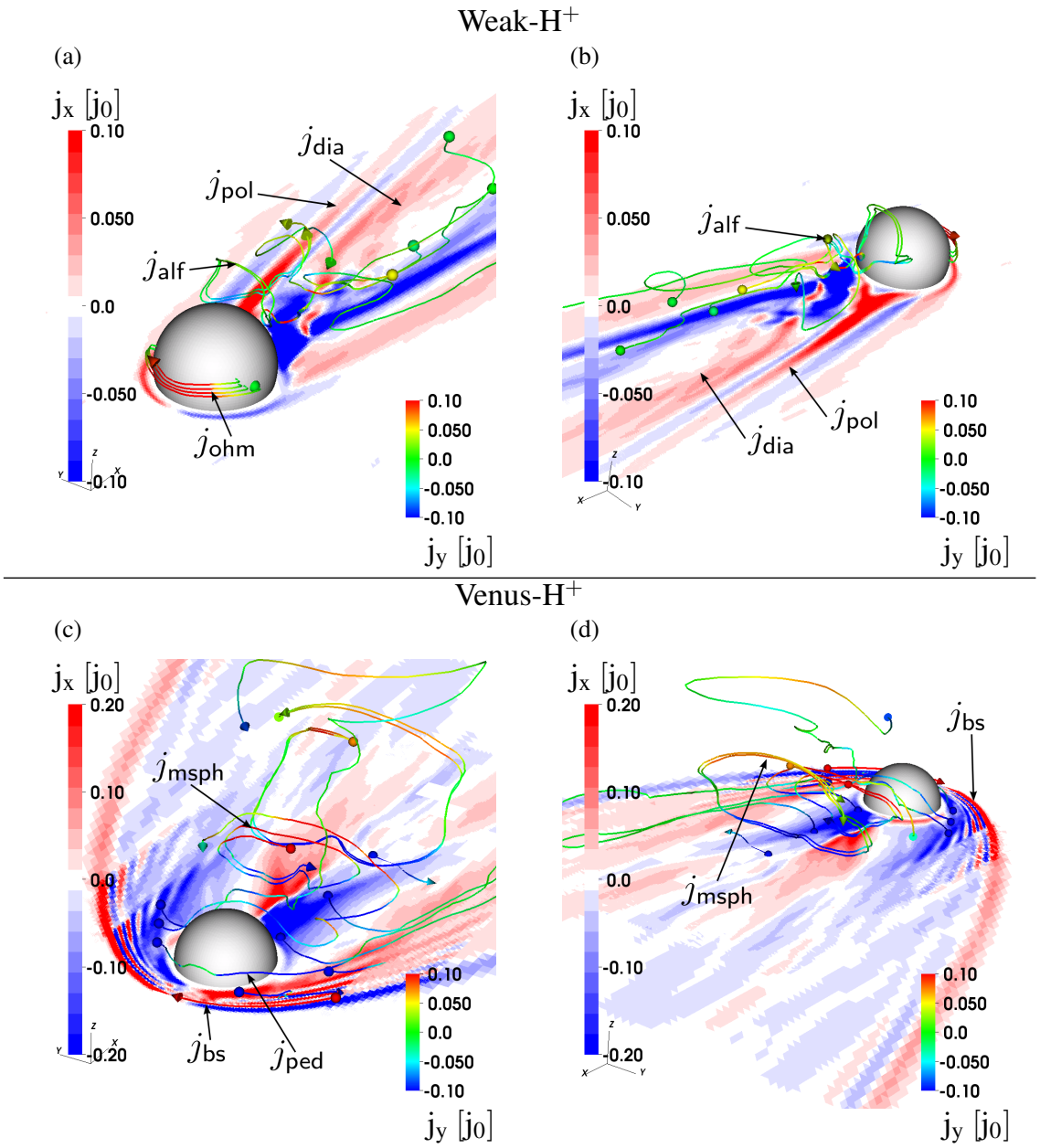

Figure 6.2: X-component of the current density in the equatorial plane in normalized units (see Table 2.1). Examples of streamlines of currents are generated in several points. The streamlines are colored following the Y-component of the current density for the sake of clarity (the colorbar is in the bottom right corner of each panel). Panels (a) and (b) provide the front and back views of the Weak-H^+ system. Panels (c) and (d) provide the front and back views of the Venus-H^+ system. The parameters of the simulations are provided in Table 6.2. The identified currents (j_{alf}, j_{pol}, j_{dia}, j_{msph}, j_{bs}, and j_{ped}) are detailed in Table 2.3. The geometry of the simulation is explained in Section 2.2.2.1. The radius of the obstacle and the plasma beta are given in Table 2.2. The ionospheric plasma beta is set to zero at the initialization.

(j_{msph}).
The transitions between the three steps presented here are distinguished by the importance taken by the Pedersen conductivity in the total current. This property is illustrated by Figure 6.8. The Pedersen conductivity (σ_{ped}) has been represented in Figure 6.8a, while the Reynolds number ($\mathcal{R}e$) is plotted in Figure 6.8b. The Pedersen conductivity is derived using Equation (2.53). One sees that the Pedersen conductivity reaches values up to $\sigma_{ped} = 4.5\sigma_0$ for the Venus-H^+. According to Table 2.1, such conductivity leads to values as $\sigma_{ped} = 7 \cdot 10^{-4}$ S/m. Typical ionospheric profile available for example for Earth gives Pedersen conductivity values of $\sigma_{ped} = 10^{-4}$ S/m (Takeda and Araki 1985). The Reynolds number is here represented to give an example of the necessary production rate to trigger a magnetopause and a bow-shock. We make an analogy between the Pedersen current and the Ohmic current, as developed in Section 2.3.2. We consider the ionosphere as a wire with a cross-section equal to the planetary diameter. Applying this estimation shows that triggering a bow-shock requires the magnetic Reynolds number to be higher than the stellar wind Alfvén mach number (which is equal to 8 in this chapter). Figure 6.8b shows that the pressure equilibrium is reached between the $1\text{E}3Q_{\alpha,0}$ | H^+ and the $10\text{E}3Q_{\alpha,0}$ | H^+, which is confirmed by Figures 6.4 and 6.5.
The evolution of the interaction region as a function of the parameters studied here is performed in two steps. There is an initial development on the nightside region, due to frictions, as developed in Chapters 4 and 5. In particular this means that the stellar wind does not play a direct role in the nightside region, therefore the first modifications of the plasma region are observable there, as shown in Figures 6.4 and 6.5. The second step is the development of the dayside region, which appears when the conductivity of the ionosphere increases, proportionally to the production. Therefore, Figure 6.6 shows that the Pedersen current is completely dominant in the dayside region. This increasing conductivity of the ionosphere through the production leads to the development of a magnetopause and bow-shock, which is observed for the $25\text{E}3Q_{\alpha,0}$ | H^+ and Venus-H^+.

6.3 O^+ generated ionospheres

This section is divided in two subsections. Two particular cases are first investigated: the Weak-O^+ and the Venus-O^+ systems. In a second time, the transition steps between those two parameter space cornerstones are studied. The parameters of the simulations performed for this section are given in Table 6.2.

6.3.1 Cornerstones in the parameters space: the Weak-O^+ and Venus-O^+ obstacles

The simulation results of the Weak-O^+ system are displayed in Figures 6.9a and 6.9b. The ionospheric production in this simulation is $Q_\alpha = 100Q_{\alpha,0}$. Figure 6.15a shows that such a production leads to an ionospheric density $n_\alpha = 0.05n_0$ once the stationary state is reached. The current j_{ohm} is observable in Figure 6.9a. In the back view in Figure 6.9b, one can notice the existence of the Pedersen current (j_{ped}), which dominates the electric field side of the nightside interaction region. Furthermore, in the same shadowed region,

the diamagnetic current (j_{dia}) and the polarization current (j_{pol}) are interweaving with the Pedersen current (j_{ped}).
A schematic representation of the Weak-O^+ system is given in Figure 6.11a. The plasma structures are articulated around the currents discussed above. The stellar wind is slowed down by the encounter with the ionospheric ions. As explained in Section 6.2, the bending of the magnetic field lines is due to the mass-loading of the stellar wind, which we represent by the current j_{ped}, derived with the ionospheric Pedersen conductivity. This current is shown to flow in the direction of the electric field and passing by the dayside of the obstacle. One should notice that, in this regime, with an ionospheric density in the stationary state of $n_\alpha = 0.01 n_0$, the general patterns of the disturbed magnetic field, inferred from Figure 3.1 compared to Figure 6.9, is close to the Lunar-type of interaction. Although the magnetic field is only weakly perturbed in the electric field plane, the total current density in the wake is modified, and due to the diffusion inherent to the simulation, the distinction cannot be made between the mass-loading current and the polarization current.
The results of the Venus-O^+ system are displayed in Figures 6.9c and 6.9d. The production of ions is $Q_\alpha = 50 \cdot 10^3 Q_{\alpha,0}$, which leads in steady-state, as shown by Figure 6.10b, to an ion density at the surface of the obstacle of $n_\alpha = 200 n_0$. The Pedersen current (j_{ped}), and the bow-shock current (j_{bs}) are visible in the front view. The nightside of the magnetosphere, shown in Figure 6.9d, is dominated by one magnetospheric current identified (j_{msph}).
The schematic diagram of the Venus-O^+ displayed in Figure 6.11b presents the characteristics and positions of the bow-shock current (j_{bs}), the Pedersen current (j_{ped}), and the magnetospheric current (j_{msph}). In this regime, the magnetospheric cavity and more generally the bow-shock are symmetric with respect to the meridional plane. The two diagrams presented in Figure 6.11 illustrate that the system switches from a complete asymmetric configuration to a symmetric configuration, the intermediate steps and the switching process are detailed in the next section. On can note by comparing Figures 6.3a and 6.11a the role of the ionospheric ion mass in the global structure. While a hydrogen ionosphere produces a weak asymmetry in the system, using oxygen as ionospheric ions creates a clearly distinguishable wing on the electric field side of the interaction region. One can safely extrapolates that an ionosphere composed of several species would generates mass-loading currents particular to each species and directly depending on their gyration radii, i.e. the mass of each particle.

6.3.2 Transition states between the Weak-O^+ and the Venus-O^+ obstacles

The production function is increased progressively (see parameters in Table 6.2) from the value used in the Weak-O^+ to that of the Venus-O^+ interaction systems. The front and back views of the simulation results for the $1\text{E}3 Q_{\alpha,0}$ | O^+ are shown in Figures 6.12a and 6.12b. The production function value for this simulation has been set to $Q_\alpha = 1 \cdot 10^3 Q_{\alpha,0}$. Figure 6.15a shows that such a production rate leads to an ionospheric density on the dayside at the stationary state of $n_{\alpha,surf} = 0.5 n_0$. One also observes that the average density of particles into the wake is about $n_\alpha = 0.1 n_0$. We notice the presence of the current j_{ped} in the front view panel, and the current j_{alf} in the back view panel.
For the simulation of the $10\text{E}3 Q_{\alpha,0}$ | O^+ case, which results are presented in Figures 6.13a

and 6.13b, we can see in the front view that the Pedersen current j_{ped} is dominating the dayside region. On the nightside, we can see that the overall region is dominated by the magnetospheric current j_{msph}. The simulation parameters of the $10\mathrm{E}3Q_{\alpha,0} \mid \mathrm{O}^+$ obstacle are $Q_\alpha = 10 \cdot 10^3 Q_{\alpha,0}$ for the ionospheric production, yielding $n_{\alpha,\mathrm{surf}} = 10n_0$ for the average ionospheric density at the stationary state, as evinced by Figure 6.15b.
Figures 6.14a and 6.14b provide the front and back views of the simulation results for the $25\mathrm{E}3Q_{\alpha,0} \mid \mathrm{O}^+$. The production rate is $Q_\alpha = 25 \cdot 10^3 Q_{\alpha,0}$. Figure 6.15c shows that such a ionization rate produces an ionospheric density of $n_{\alpha,\mathrm{surf}} = 50n_0$ in stationary state. In this regime, the bow-shock current (j_{bs}), the Pedersen current (j_{ped}) are visible on the dayside, while on the nightside, the currents j_{msph} and j_{sho} are dominant.
A schematic representation of the simulation results presented in the previous section are displayed in Figure 6.17. The currents identified in the simulation results are represented. The wake center is governed by the diamagnetic current (j_{dia}) and the Alfvénic current (j_{alf}). The polarization current (j_{pol}) is highly perturbed in the electric field plane by the pick-up process which brings ionospheric ions into the nightside region. There are two competing currents along the ion pick-up trajectory. A fast mode polarization current which becomes a bow-shock current with higher density, and the Pedersen current. Both of them are anti-parallel to each other.
Estimations of the Pedersen conductivities σ_{ped} for the interaction systems introduced in Section 6.3 are provided in Figure 6.16a. One observes that the Pedersen conductivity increases with the production rate until a maximum value at $\sigma_{\mathrm{ped}} = 55\sigma_0$. However, we did not perform yet a specific study on the stagnation of the Pedersen conductivity following this result. Therefore we can unfortunately not draw any conclusion. Further work on this subject will enlighten this point, but fall beyond the scope of this thesis. An important point is the triggering of a bow-shock, which follows the same reasoning as detailed in Sections 2.3.2 and 6.2. We see that, as confirmed by the results presented in Figures 6.12 and 6.13, the pressure equilibrium is reached between the Weak-O^+ and $1\mathrm{E}3Q_{\alpha,0} \mid \mathrm{O}^+$ systems.

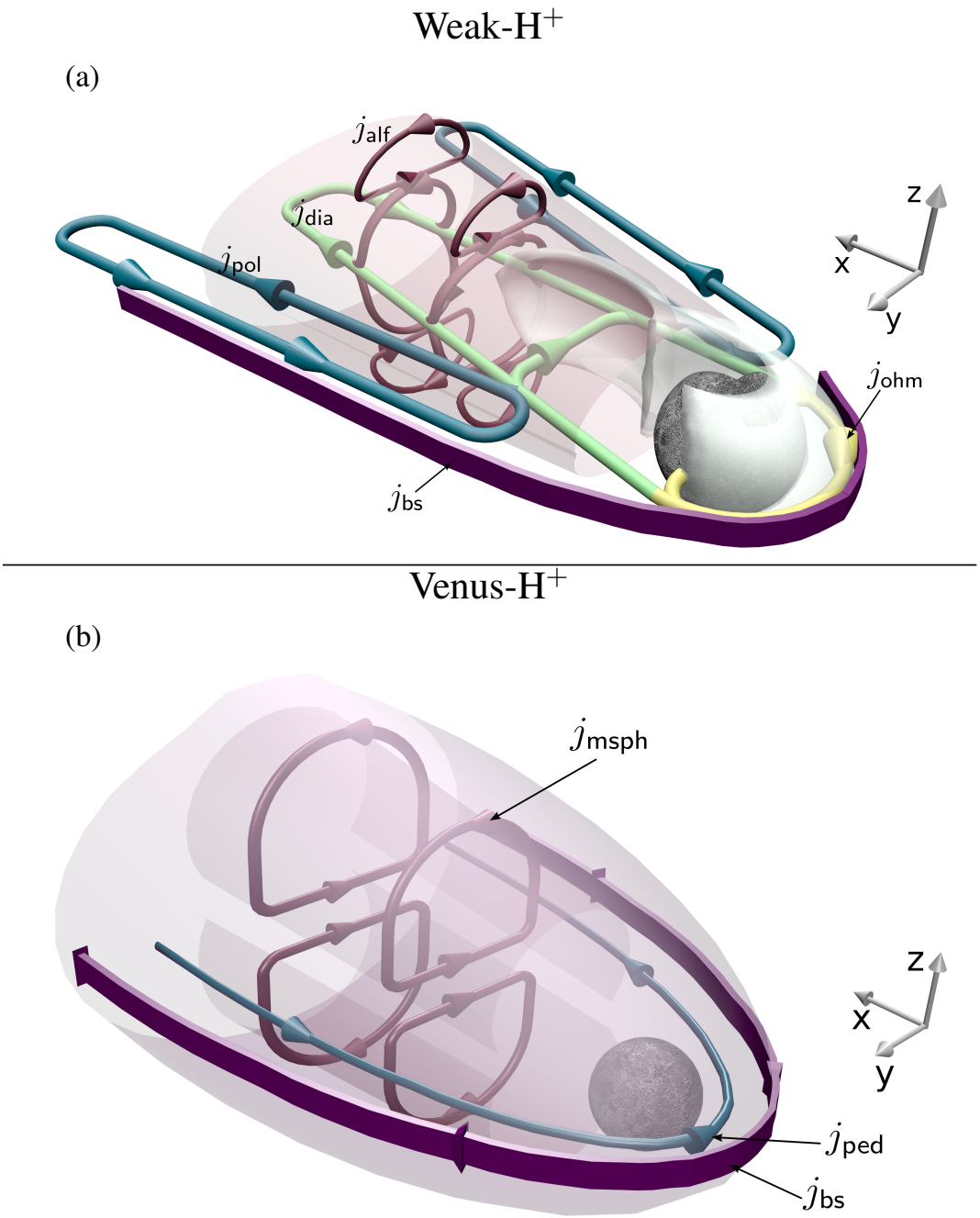

Figure 6.3: Three dimensional diagram of the (a) Weak-H^+ and (b) Venus-H^+ systems (see parameters in Tables 2.2 and 6.2). The IMF is along $-Z$, the stellar wind flows along $+X$ (see Section 2.2.2.1). The trajectory of the ionospheric ions is represented in the diagram of Panel (a) by a semi-transparent white trail. The ionospheric ions in the Venus-H^+ are not present at a particular location of the interaction region and therefore not represented. The diamagnetic (j_{dia}), Ohmic (j_{ohm}), polarization (j_{pol}), Alfvénic (j_{alf}), bow-shock (j_{bs}), magnetopause (j_{msph}), and Pedersen (j_{ped}) are colored in green, yellow, blue, red, purple, red, and blue, respectively. The description of each current is provided in Table 2.3. The magnetopause is represented with the red semi-transparent inner layer, while the bow-shock is shown by the semi-transparent outer layer.

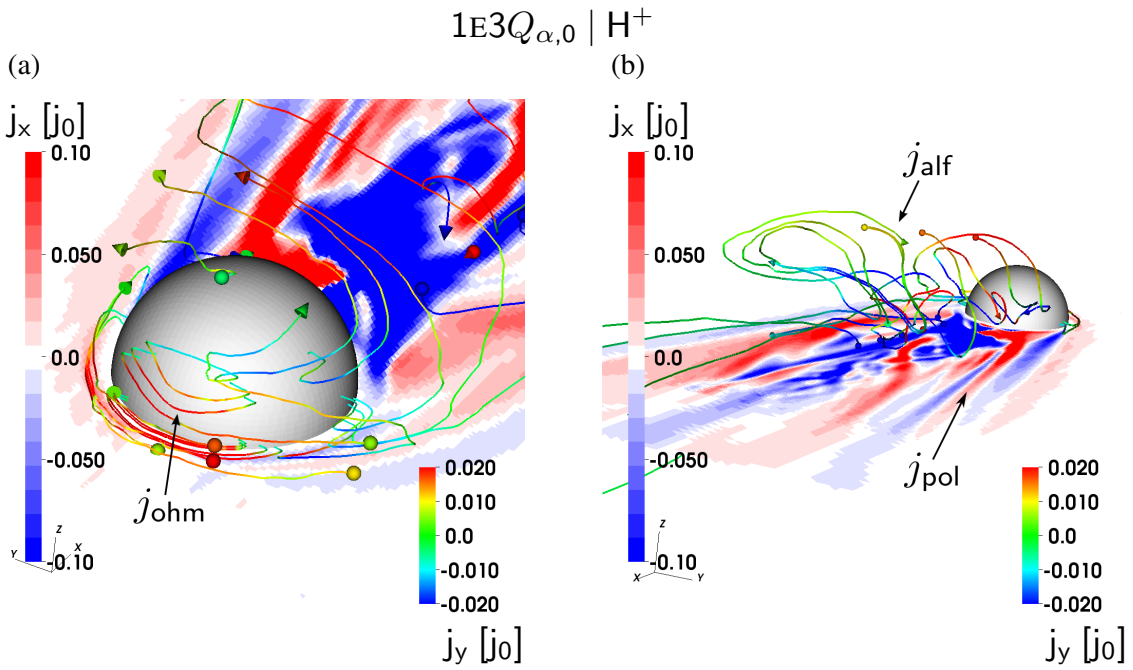

Figure 6.4: Front (a) and back (b) views of the 1E3$Q_{\alpha,0}$ | H+ interaction system (see Table 6.2). Description same as Figure 6.2.

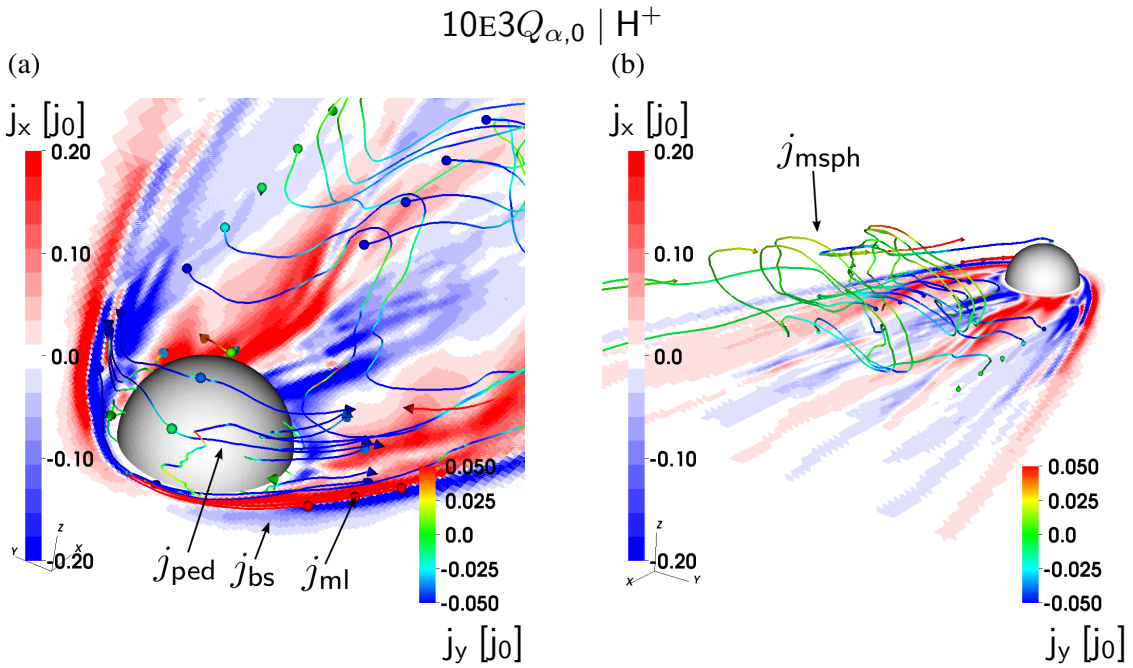

Figure 6.5: Front (a) and back (b) views of the 10E3$Q_{\alpha,0}$ | H+ interaction system (see Table 6.2). Description same as Figure 6.2.

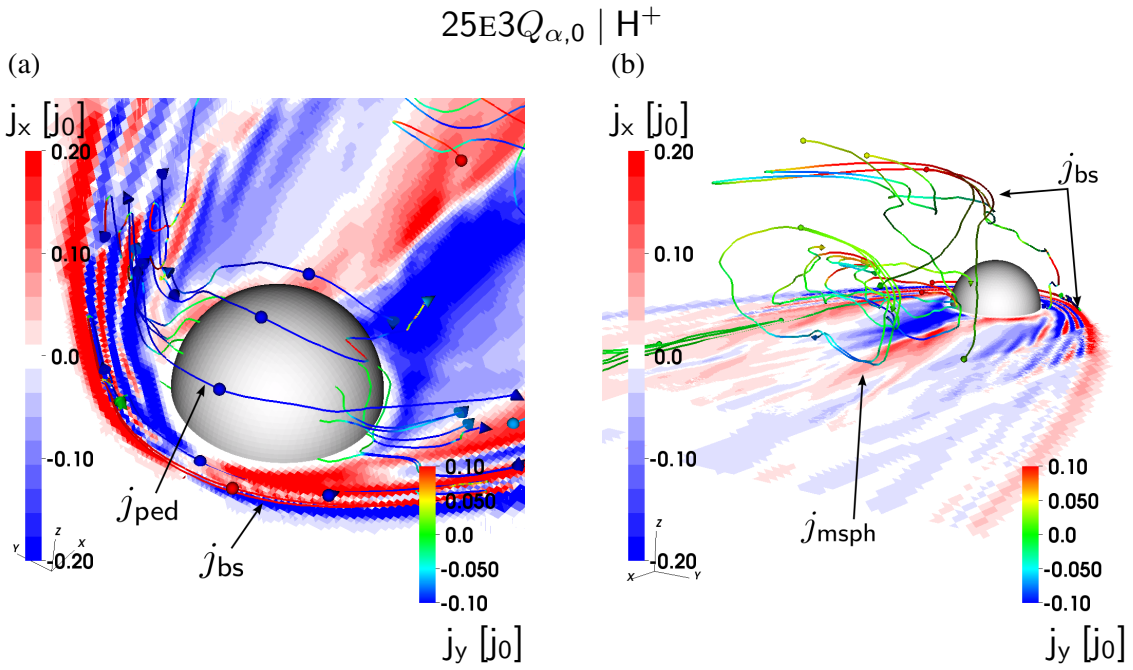

Figure 6.6: Front (a) and back (b) views of the 25E3$Q_{\alpha,0}$ | H^+ interaction system (see Table 6.2). Description same as Figure 6.2.

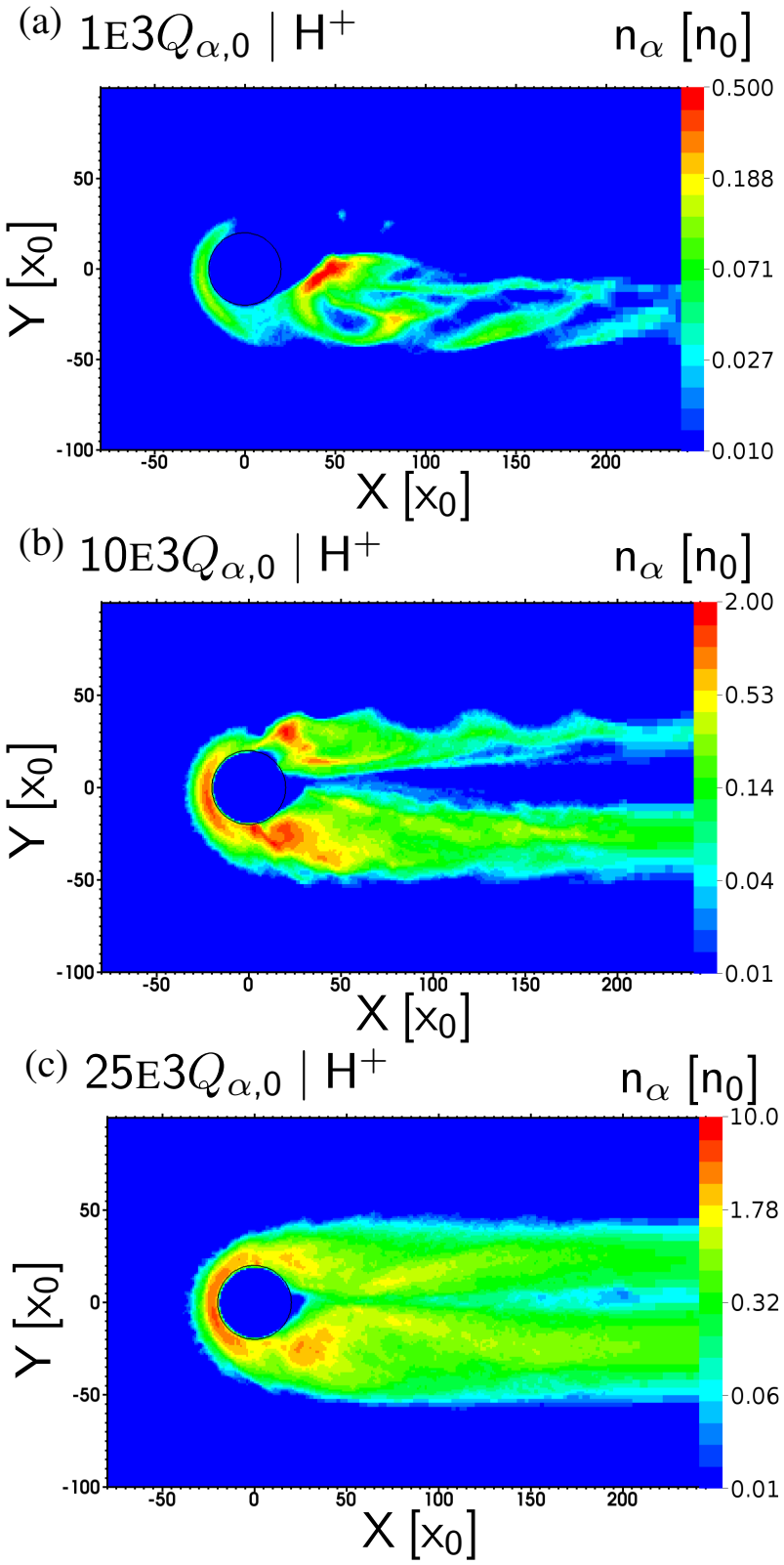

Figure 6.7: Ionospheric density in the equatorial plane for the 1E3$Q_{\alpha,0}$ | H^+, 10E3$Q_{\alpha,0}$ | H^+, and 25E3$Q_{\alpha,0}$ | H^+ systems in Panels (a), (b), and (c), respectively. Description same as Figure 6.1.

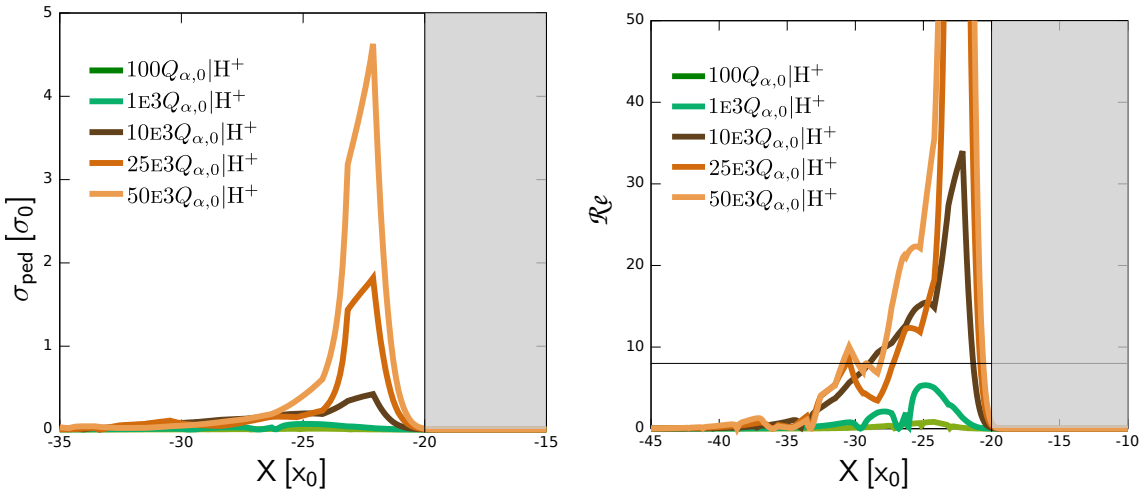

Figure 6.8: (a) Pedersen conductivity and (b) Reynolds magnetic number along the X-axis. The Pedersen conductivity is expressed in normalized units (see Table 2.1), its expression is given by Equation (2.53). The expression of the magnetic Reynolds is written in Equation (2.59). A limit at $\mathcal{R}e$=8 is drawn to show the pressure equilibrium condition (see Section 2.3.2). The cases represented are all treated in Section 6.2 (see Table 6.2). The obstacle is represented by the gray shadowed region. The simulation geometry and parameters are provided in Section 2.2.2.1 and Table 2.2.

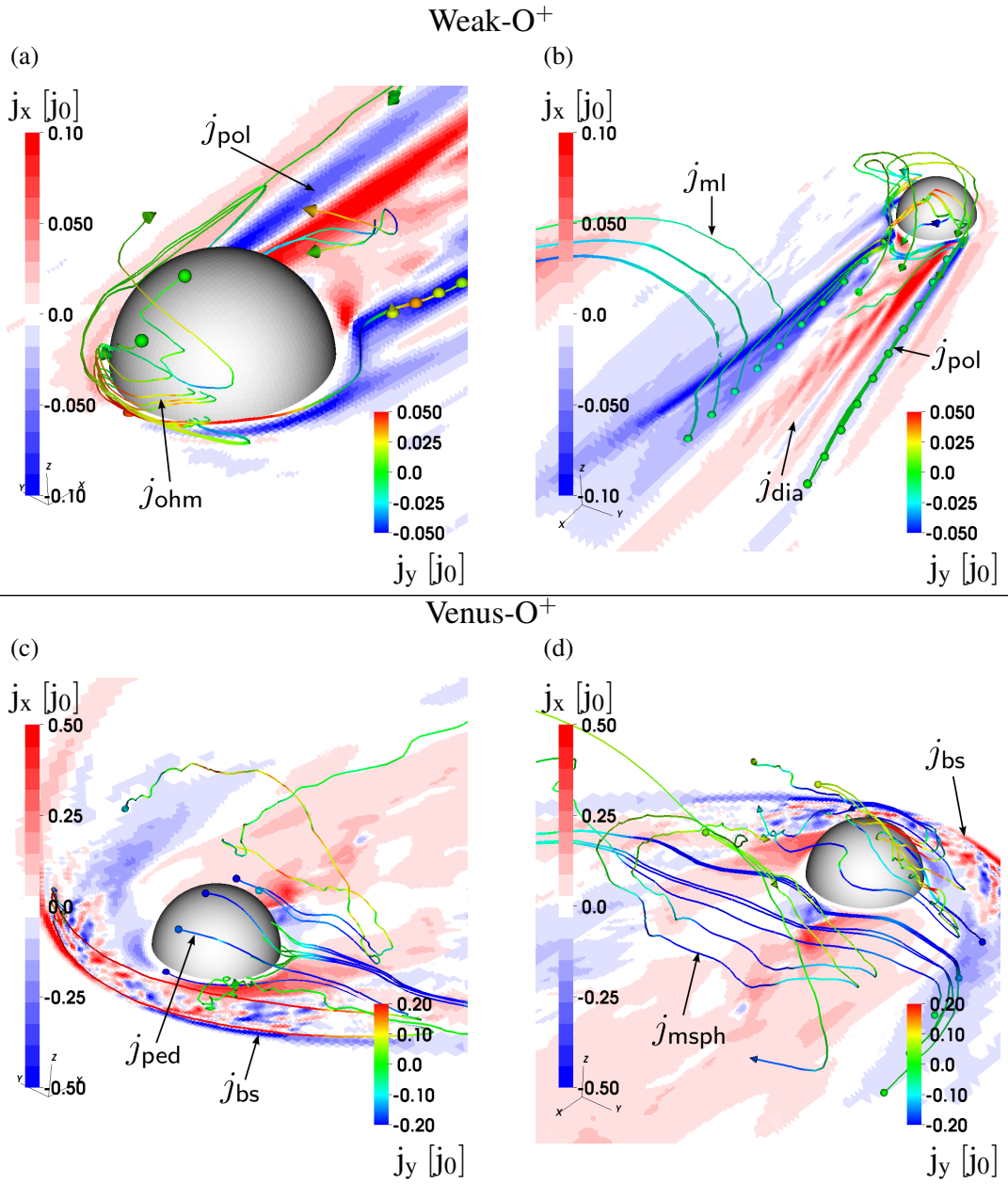

Figure 6.9: Front (a) and back (b) views of the Weak-O^+ system and front (c) and back (d) views of the Venus-O^+ interaction (see Table 6.2). Description same as Figure 6.2.

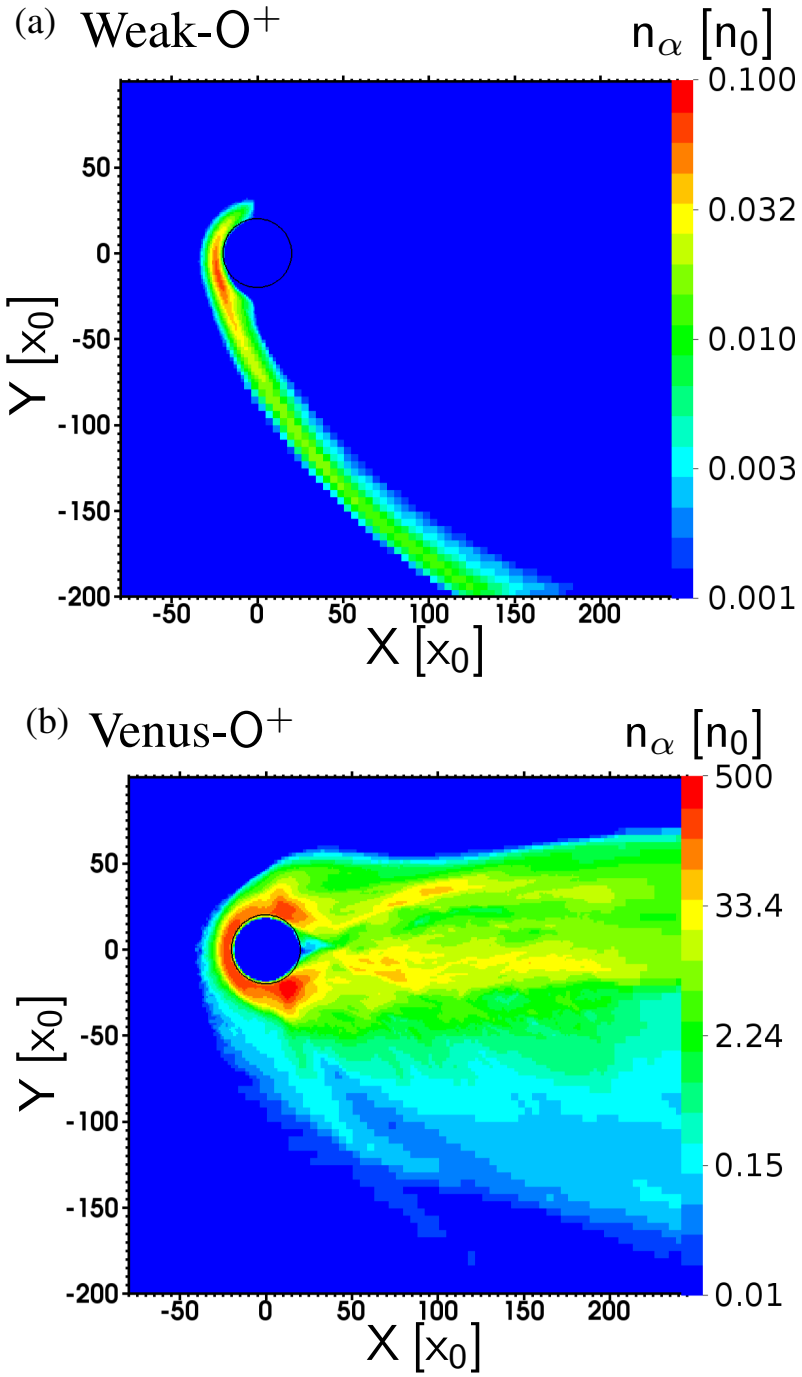

Figure 6.10: Ionospheric density of the (a) Weak-O^+ and (b) Venus-O^+ systems in the equatorial plane (see Table 6.2). Description same as Figure 6.1.

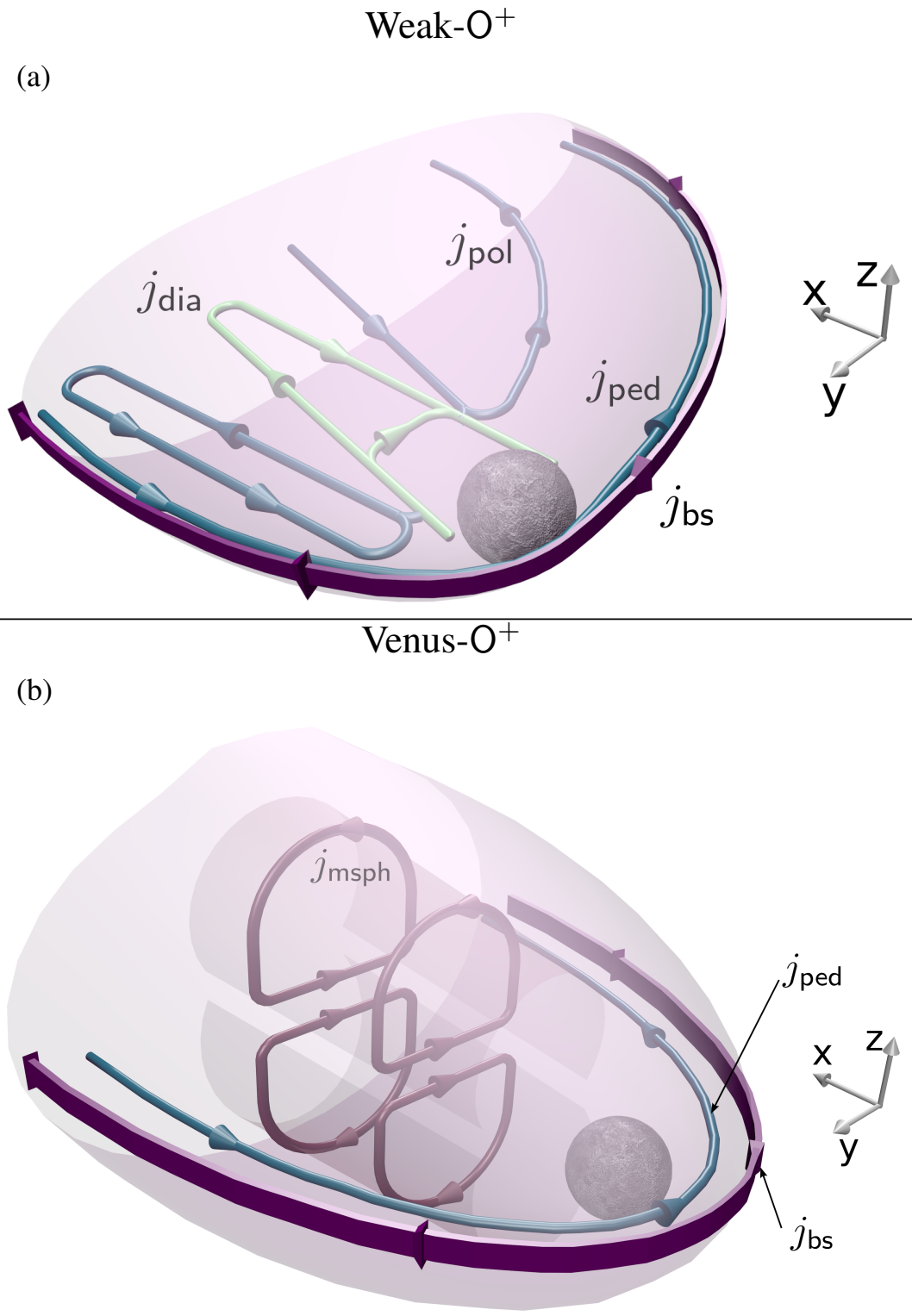

Figure 6.11: Three dimensional schematic representation of the Weak-O^+ (Panel (a)) and Venus-O^+ (Panel (b)) systems (see Table 6.2). Description same as Figure 6.3.

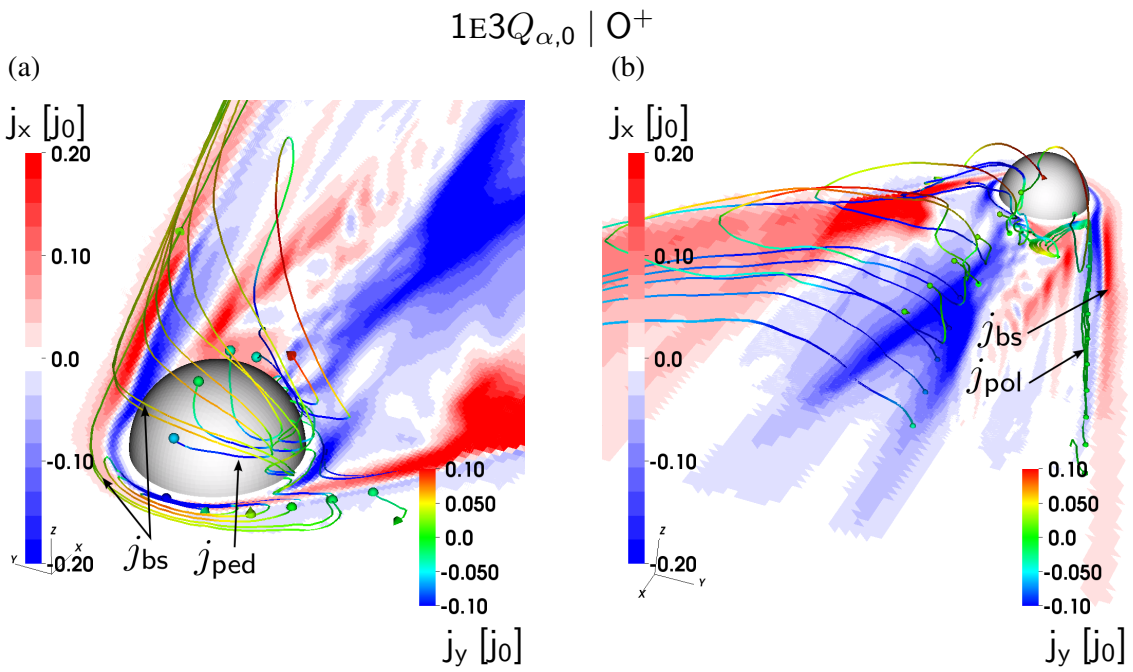

Figure 6.12: Front (a) and back (b) views of the X-component of the current density in the equatorial plane for a 1E3$Q_{\alpha,0}$ | O^+ interaction (see Table 6.2). Description same as Figure 6.2.

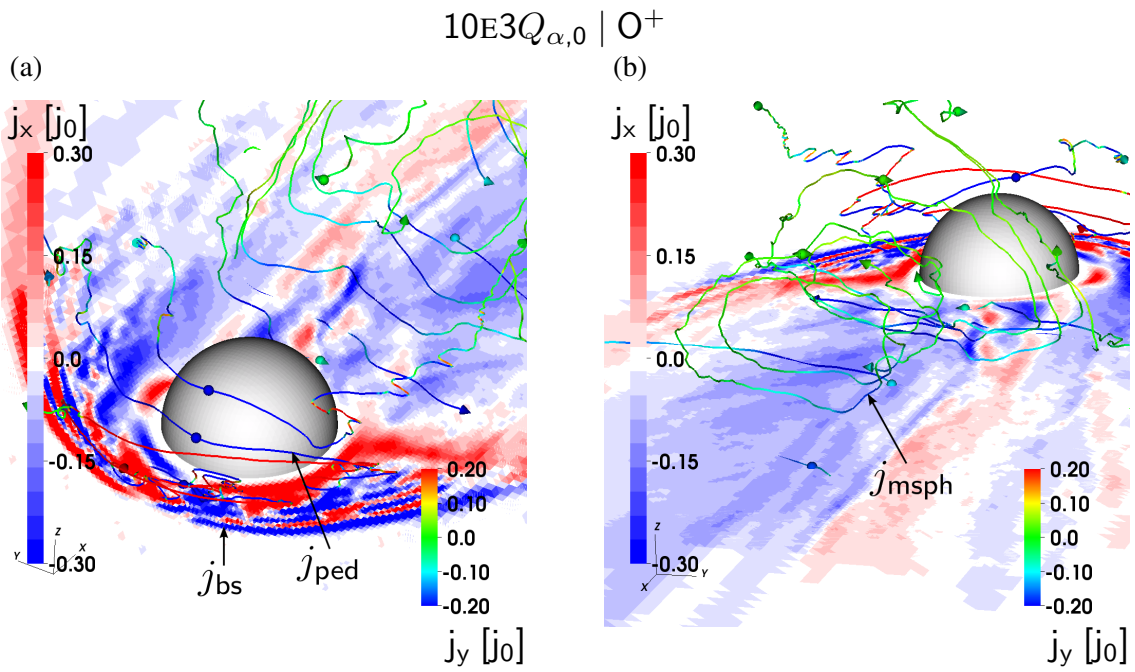

Figure 6.13: Front (a) and back (b) views of the 10E3$Q_{\alpha,0}$ | O^+ interaction system (parameters are given in Table 6.2). Description same as Figure 6.2.

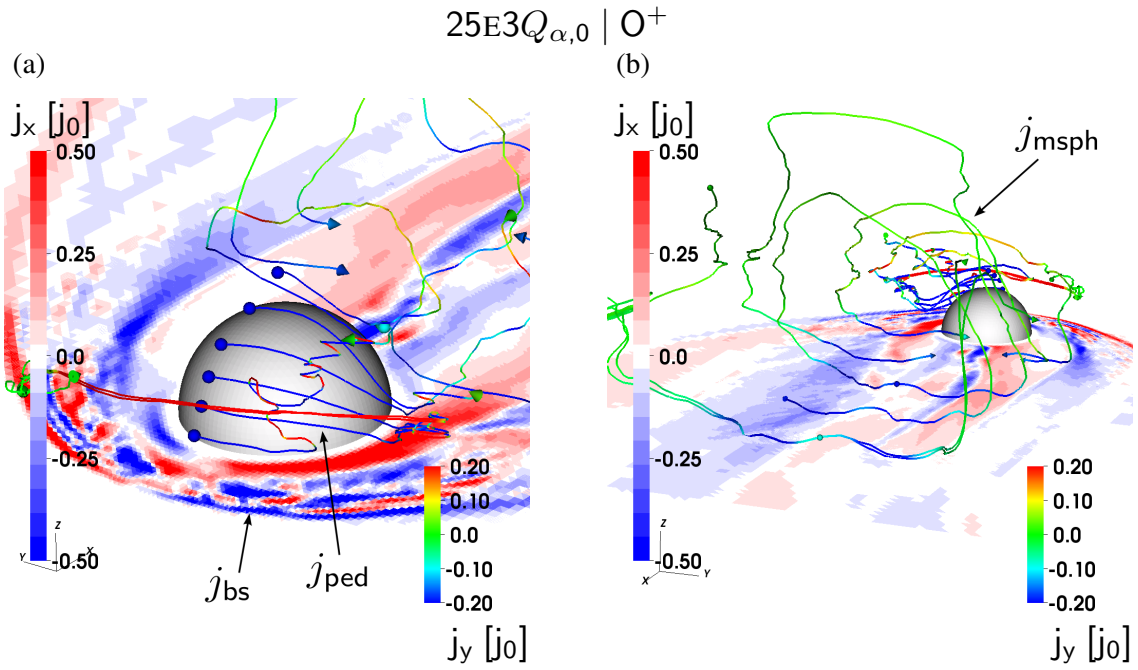

Figure 6.14: Front (a) and back (b) views of the 25E3$Q_{\alpha,0}$ | O^+ interaction type (see Table 6.2). Description same as Figure 6.2.

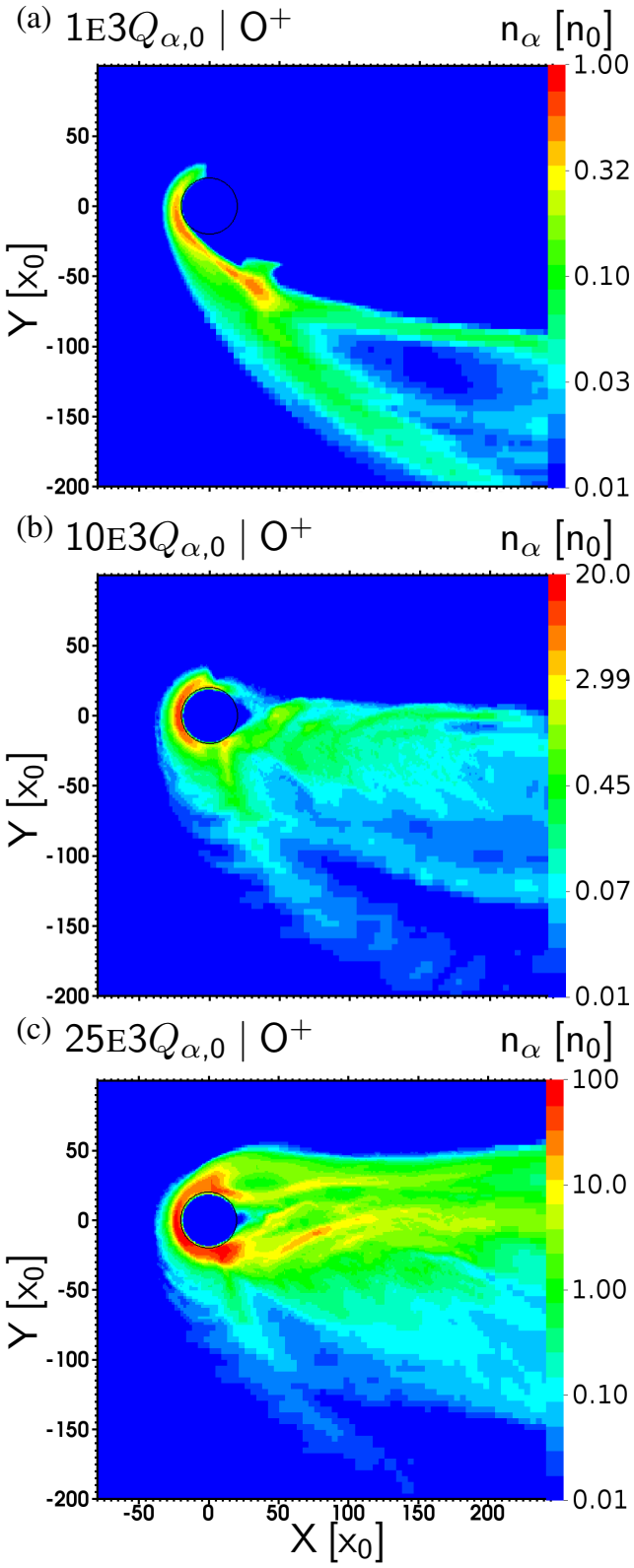

Figure 6.15: Ionospheric density in the equatorial plane for the 1E3$Q_{\alpha,0}$ | O^+, 10E3$Q_{\alpha,0}$ | O^+, and 25E3$Q_{\alpha,0}$ | O^+systems, in Panels (a), (b), and (c), respectively. Description same as Figure 6.1.

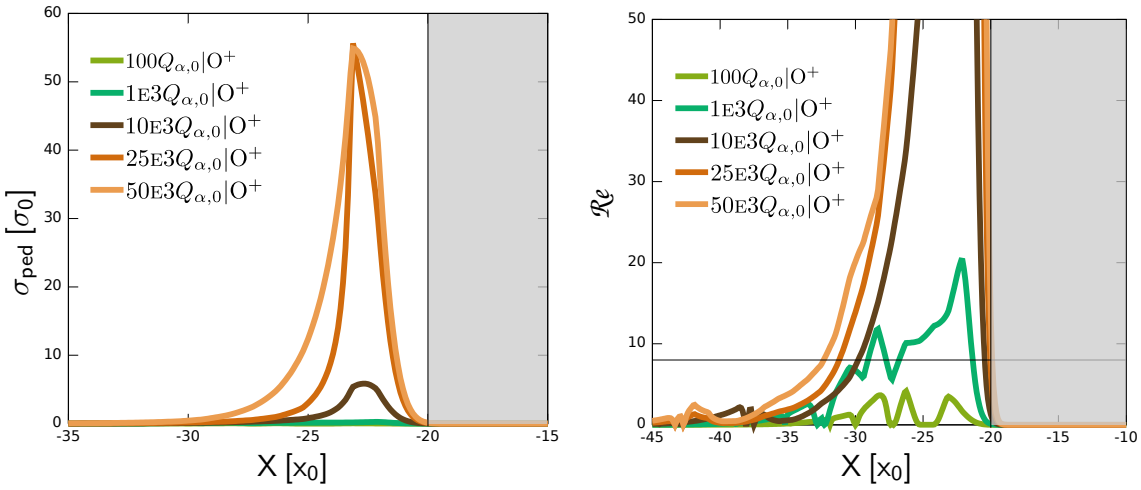

Figure 6.16: Pedersen conductivity (a) and Magnetic Reynolds number (b) for all cases treated in Section 6.3, i.e. O^+ generated ionospheres (see Table 6.2). Description same as Figure 6.8.

Figure 6.17: Three dimensional representation of the intermediate step appearing between the Weak-O^+ and Venus-O^+ systems, so called the 10E3$Q_{\alpha,0}$ | O^+ system (see Table 6.2). Description same as Figure 6.3.

6.4 Conclusions

Interactions of a super-Alfvénic stellar wind with obstacles possessing an ionosphere are investigated. The analysis is divided in three steps. The current structures around a Lunar-Type obstacle is first discussed. The interaction region consists in a wake in the nightside, which is dominated by a diamagnetic current, a polarization current and an Alfvénic current. From this starting point, the ionospheric ion production rate is increased. The first feature appearing is a Pedersen current which follows the paths of ionospheric ions (described by their gyration radius and thus their mass), through a pick-up process. The second step is the perturbation of the wake, due to ionospheric ions insertions, driven in this region by the pick-up process. Once the density inserted in the nightside of the obstacle by the dayside ions reaches steady state, streams instabilities are observed, and disturbance in the polarization and diamagnetic current are noticeable. With the next step of the transition, those currents totally disappear, the obstacle dayside is dominated by a Pedersen current, which includes production as a dynamo-like driving mechanism. At this stage, when the dynamo driven by the Pedersen current generates a magnetic pressure balancing the stellar wind, the magnetopause and the bow-shock are fully developed. This is seen in the case of a Venus-Type obstacle.

7 Conclusion

7.1 Summary

In this dissertation we describe the foundations of a global description of the interaction between a stellar wind and planetary bodies using a hybrid simulation code. The aim is to set up a consistent description of the plasma interaction processes in order to categorize the interaction types. The construction of a catalog of interactions starts with the development of the interaction between a Lunar-Type obstacle with a super-Alfvénic stellar wind. This interaction is present in our solar system with the case of our Moon. In our simulation, we only treat the case where the stellar wind magnetic field is perpendicular to the stellar wind flow velocity. We show in Section 3.3 that, in the parameters space, the angle between the flow velocity and the IMF is important to describe the plasma regime. Once the full development of the plasma structures configuration has been done, we take interest in the evolution of the interaction by modifying the velocity of the stellar wind, decreasing its value from $v_{sw} = 8v_{A,0}$ to a sub-Alfvénic value, $v_{sw} = 0.5v_{A,0}$. There are several examples of this regime in our solar system among the moons of Jupiter and Saturn. Therefore we call this regime the Rhea-Type. Then, we add a magnetic moment to the planet and increase its magnitude step by step. One should note that at this point that, the interaction parameters that bring enough information to fully describe the properties of the interaction region are not limited to the ratio between the stellar wind pressure and the planetary moment strength. Like in the case of an inert obstacle, the angle between the IMF and the stellar wind flow velocity plays a role, as well as the angle of the planetary magnetic moment with respect to the other parameters. First, we study the interaction in which the planetary magnetic moment is anti-parallel to the IMF, leading to a configuration where the planetary magnetic field and the IMF are parallel at the subsolar point. From this situation, we study four cornerstones, two in super-Alfvénic regime with $v_{sw} = 8v_{A,0}$: the Lunar-Upward, and the Mercury-Upward, and two in sub-Alfvénic regime with $v_{sw} = 0.5v_{A,0}$: the Rhea-Upward, and the Ganymede-Upward.

We continue with the description of the intermediate states between those cornerstones by studying the evolution of the plasma interaction when increasing the dipole strength between Lunar-Upward and Mercury-Upward obstacles. Three steps are identified, named $+10\text{E}3M_0\hat{z} \mid 8v_{A,0}$, $+20\text{E}3M_0\hat{z} \mid 8v_{A,0}$, and $+40\text{E}3M_0\hat{z} \mid 8v_{A,0}$ systems. Those steps refers to particular stage in the evolution of the surface magnetic field. At first the surface magnetic field is weaker than the IMF and one observes a Lunar-Type interaction, then the surface magnetic field reaches the order of magnitude of the IMF and we have a situation where the magnetospheric jump is exactly at the surface at the obstacle. The next step is reached when the surface magnetic field is stronger than the dynamic pressure of the

stellar wind. This is the Mercury-Upward interaction. In a second part, we study the intermediate situations between the Rhea-Upward and the Ganymede-Upward interactions, as well as the intermediate steps between the Mercury-Upward, and the Ganymede-Upward interactions. This fills out a two-dimensional parameter space containing the magnetic moment and the stellar wind velocity. The intermediate states are introduced so that no qualitative differences appears in between. The continuous changes in the plasma structures between two defined states lie in the connections between the velocity regimes and the MHD waves propagation velocities.
In the following part, we study the same type of interaction, but for a magnetic moment parallel to the stellar wind magnetic field, which means that the planetary field and the IMF are anti-parallel at the subsolar point. We define two cornerstones in super-Alfvénic regime: the Lunar-Downward and the Mercury-Downward interaction. From those two cornerstones, we introduce several intermediate regimes. Those intermediates regimes are identified as $-10\text{E}3M_0\hat{z}$, $-20\text{E}3M_0\hat{z}$, and the $-40\text{E}3M_0\hat{z}$. The logic of the evolution of the interaction regime is similar to the cases studied for the northward magnetic moment. Depending on the magnitude of the planetary magnetic field at the surface of the obstacle we identify three different regimes.
Although the identified regimes are similar for the northward magnetic moment and the southward magnetic moment, the interaction regions are topologically different. The major differences are driven by the vectorial property of the magnetic field and therefore the importance of the direction of the field in space. For example, the different configurations of magnetic moment leading to different interaction region are important for reconnection processes. While in the IMF configuration which is directed southward, the magnetic moment is directed northward, the reconnection process happens at the north and south polar regions of the obstacle. However, when the magnetic moment is directed southward, the reconnection happens at the subsolar point and the obstacle nightside.
In the last chapter we introduce interaction types between a stellar wind and a planetary obstacle possessing an ionosphere. For these interaction types, we set up four cornerstones in a super-Alfvénic regime: the Weak-H^+ with a production of hydrogen and Weak-O^+ with a production of oxygen, as well the Venus-H^+ and the Venus-O^+ interactions. between those parameters spaces points, we study the intermediate situation, leading to three intermediate steps, the $1\text{E}3Q_{\alpha,0}$ | H^+, $10\text{E}3Q_{\alpha,0}$ | H^+, and the $25\text{E}3Q_{\alpha,0}$ | H^+ for a production of hydrogen and $1\text{E}3Q_{\alpha,0}$ | O^+, $10\text{E}3Q_{\alpha,0}$ | O^+, and the $25\text{E}3Q_{\alpha,0}$ | O^+ for a production of oxygen. The intermediate steps are generated by modifying the value of the ion production of the atmosphere of the planets.

7.2 Outreach

The work developed in this thesis can be extended in several ways. Since its point is to develop a complete study of the parameters space, its extension straight forwardly follows the number of normalized plasma parameters, which are: the stellar wind velocity magnitude; the planetary magnetic moment magnitude; the angle between the upstream velocity, the IMF, and the planetary magnetic moment; the ion and electron plasma betas; the obstacle properties: shape, radius, conductivity of the obstacle, and presence and properties of an ionosphere. Those parameters are independent from each other and their

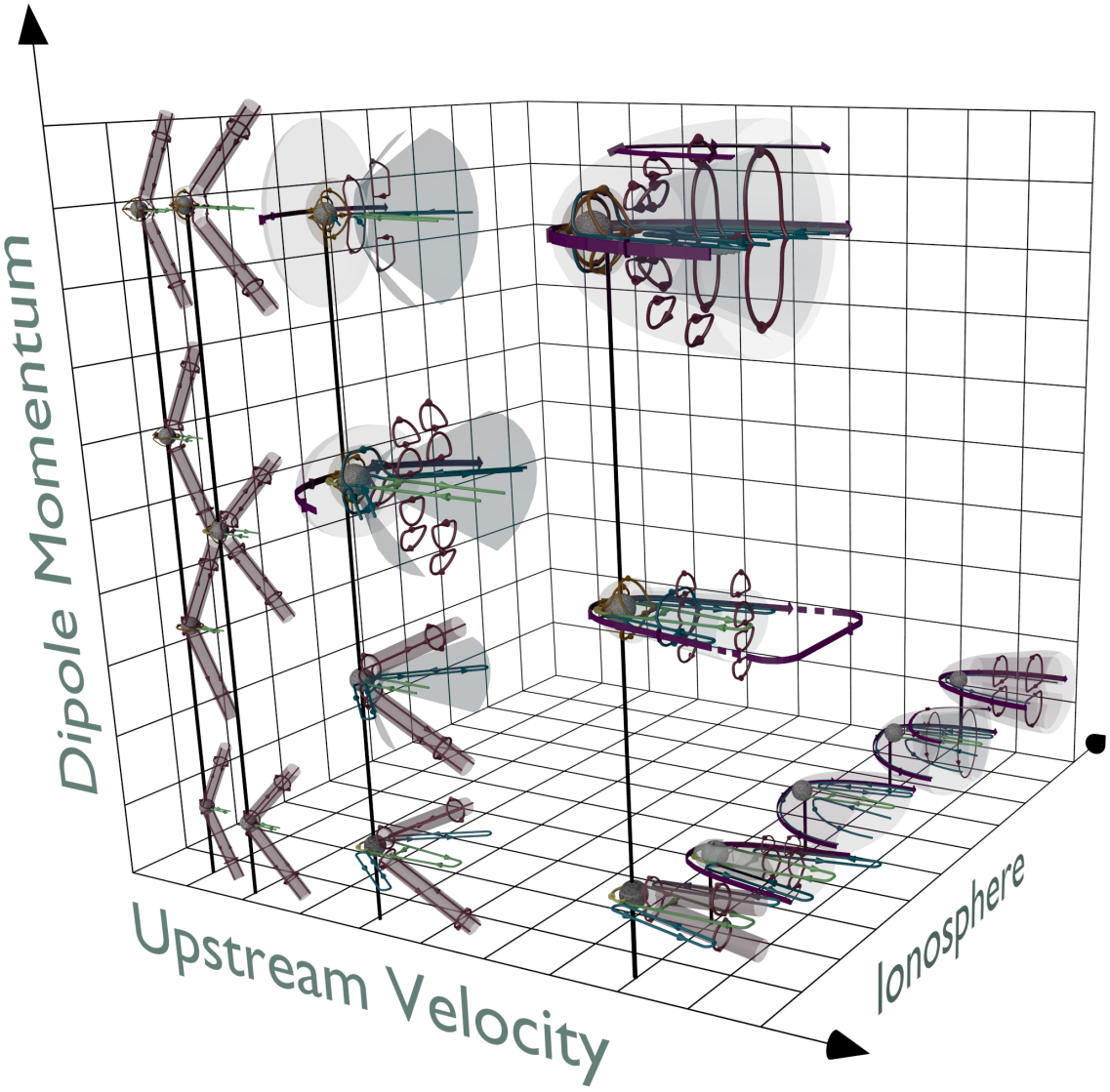

Figure 7.1: Summary of the diagrams presented in this dissertation. The diagrams on the upstream velocity axis with no ionosphere and no dipole momentum are described in Chapter 3. The diagrams of the plan made by the upstream velocity and the dipole momentum axis are described in Chapter 4. The results on the axis of the ionosphere with no dipole momentum are described in Chapter 6.

relative evolution could be studied in the whole parameter range. The parameter range is infinite, therefore a full description of every interaction with every parameter is impossible. However, our understanding of plasma interaction greatly improves by only considering the evolution of one parameter relative to one another. This is how this work has been done and how we wish to see it continued.

A Discussion about numerical effects

A.1 Obstacle boundary

As a high resistivity is used in order to decrease the pile-up effect due to the conductivity of the obstacle, numerical boundary effects arise due to the sharpness of the resistivity profile. A smoothing is applied to the resistivity profile in order to damp the boundary effects. Different resistivity profiles has been tried and are presented in Figure A.1a, with their respective impact on the magnetic field in Figure A.1b. The profiles chosen are those avoiding an unstable magnetic field at the interface between the obstacle and the stellar wind plasma. Profile 2 is used in Chapter 3 to study the Lunar-Type system. For the stellar wind velocity transition regimes, we use Profile 3. Using different sizes of the simulation domain for those two studies require adapting the resistivity profiles. An example of instability caused by a sharp profile is given through Profile 1.
In the case of the simulation of a magnetized obstacle (Chapters 4, and 5), another numerical effect has to be handled. This particular effect is an anomalous increase of the magnetic field magnitude at the surface of the obstacle. When using a highly resistive obstacle, a divergence in the equation of the field rises up. This can be emphasized by developing the curl of Equation (2.13), which corresponds to the time evolution of the magnetic field. Treating separately the resistive term yields:

$$\nabla \times (\mathbf{R} \cdot \frac{\nabla \times \boldsymbol{B}}{\mu_0}) = \mathbf{R}\nabla \times \frac{\nabla \times \boldsymbol{B}}{\mu_0} + \nabla \mathbf{R} \times \frac{\nabla \times \boldsymbol{B}}{\mu_0} \quad . \tag{A.1}$$

Therefore in the case of a current flowing perpendicular to the surface of the obstacle, an infinite value of the $\nabla \mathbf{R}$ term causes an infinite increase of the magnetic field with time. This issue has been observed in the simulations of an obstacle possessing a magnetic field confined within the obstacle on the dayside by the dynamic pressure of the stellar wind. Those cases have been introduced in Chapter 4 with the $+10\text{E}3 M_0\hat{z} \mid 8 v_{\text{A},0}$, $+20\text{E}3 M_0\hat{z} \mid 8 v_{\text{A},0}$, and $+40\text{E}3 M_0\hat{z} \mid 8 v_{\text{A},0}$ systems, and in Chapter 5 as the $-10\text{E}3 M_0\hat{z}$, $-20\text{E}3 M_0\hat{z}$, and $-40\text{E}3 M_0\hat{z}$ systems (parameters in Tables 4.2 and 5.2). It is important to note that, as soon as the planetary magnetization is high enough to counter the stellar wind total pressure, the magnetic field is no longer confined inside the obstacle, and the anomaly disappears. An illustration of this numerical issue is presented in Figure A.2b. At the subsolar point, the total magnetic field is decreasing, while at the north and south poles, there is an anomalous increase of the magnetic field magnitude. In a more general sense, this anomaly creates an anti-draping field pattern at the interface between the obstacles and the interplanetary medium. The same simulation has been run with two different resistivity profiles, plotted in Figure A.2a. The result of the simulation with the second profile is displayed in Figure

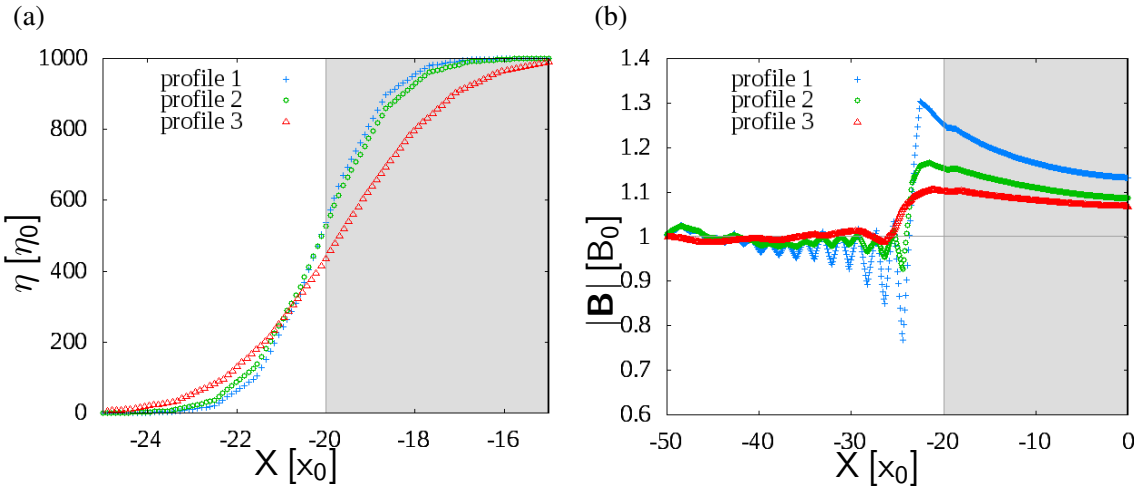

Figure A.1: (a): Three resistivity profiles along the line (Y=0, Z=0) from X=−25x_0 to X=−15x_0 used in a simulation of a Lunar-Type system. The resistivity is expressed in normalized units (see Table 2.1) (b): Normalized magnetic field magnitude along the line (Y=0, Z=0) from X=−50x_0 to the center of the obstacle X=0 resulting from each resistivity profile. The shaded region indicates the obstacle.

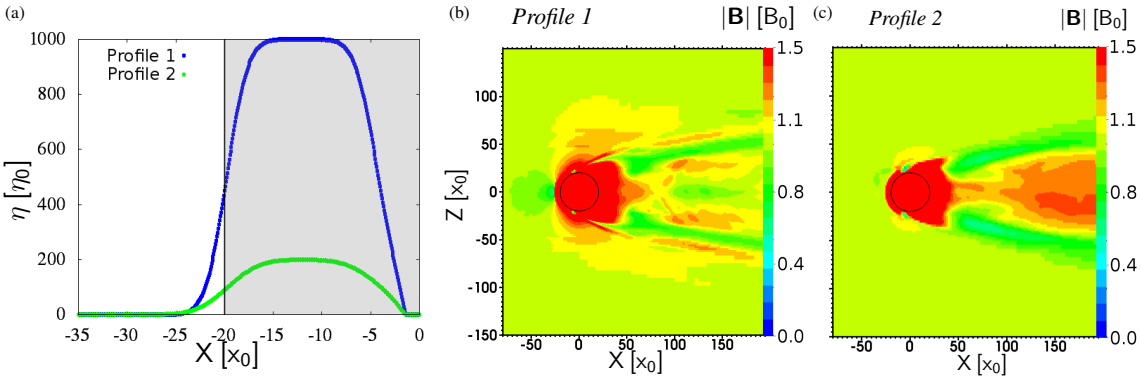

Figure A.2: (a): Two resistivity profiles along the line (Y=0, Z=0) from X=−35x_0 to X=0x_0. The resistivity is expressed in normalized units (see Table 2.1). The obstacle is represented by the shadowed region. (b) and (c): Normalized magnetic field magnitude in the meridional plane for a $+40\text{E}3M_0\hat{z} \mid 8v_{A,0}$ system, with the two resistivity profiles introduced in Panel (a). The obstacle is represented by a black circle.

A.2c, and shows that the anomaly has completely disappeared. By using Profile 2 instead of Profile 1, the behavior of the magnetic field at the dayside of the obstacle is comparable to the usual configuration of the magnetic field at a magnetospheric boundary (detailed in Chapter 4 and 5).

In order to understand the behavior of the simulation, we ran some tests, which are presented in Figure A.3. Those runs are non consistent simulations: the particles and the IMF have been deactivated, only the planetary field is advancing and subject to the stellar wind dynamic pressure. The density and velocity are constant in the entire simulation domain

and we only look at the magnetic field behavior. First, we identified which term in Equation (2.7) is responsible for the anomalous field. Deactivating each term one-by-one has shown that the resistive term alone is triggering the divergence. Figure A.3a presents an example of anomalous field. The resistivity of the obstacle is equal to $10\eta_0$ (normalization in Table 2.1) and the profile is not smoothed. The resistivity profile for this plot is shown in Figure A.3b and labeled "Not smoothed". Figure A.3c provides simulation results with the same resistivity profile (Not smoothed), except that the cleaning divergence procedure is turned off. The divergence cleaning procedure (Mueller 2011) is used to lower the magnetic divergence created by numerical inaccuracies. This plot shows that the anomaly seen in Figure A.3a is created by an erroneous solution created by the divergence cleaning procedure. However this procedure is necessary to keep the accuracy of the results, which require to maintain a divergence free magnetic field. Another test is performed using a perfectly conductive obstacle ($\eta = 0$), the result is provided in Figure A.3d. Conversely to the result presented in Figure A.3a, the anomaly has disappeared. This emphasizes the role of the resistivity in triggering the anomaly. The last test is performed with a simulation setup similar to the Figure A.3a, but using a smoothed resistivity profile, labeled "Smoothed" in Figure A.3e. Using a smoothed profile changes the resistivity gradient between the surface of the obstacle and the plasma. In this case the term $\nabla\mathbf{R}$ decreases, and this results in a disappearance of the magnetic field anomaly in front of the obstacle. These results show that a solution to suppress the magnetic anomaly in a self-consistent simulation is to reduce the resistivity gradient at the interface between the plasma and the obstacle.

A.2 Planetary core's boundary

The numerical effects due to the configuration of the planetary core in our simulation have been listed in order to discriminate physical effects and numerical effects when studying near surface features. In the AIKEF code, the core can be completely self-defined via setting the planetary resistivity profile. In the configuration used for the simulations presented in this thesis, we divide the obstacle in three regions: the numerical core, the physical core and the mantle. The numerical core is a boundary where no calculation is performed and which is necessary as soon as a magnetic moment is added to the obstacle. This boundary is necessary in order to prevent numerical removal of the magnetic moment when the simulation is running. The physical core is a region where we manually set the resistivity to zero. Unlike the numerical core, the electromagnetic field is calculated in this region. It permits the propagation of the magnetic field inside the obstacle. The mantle is the part of the profile, where we manually set the resistivity to the desired finite value. In this dissertation we use the highest possible resistivity in the mantle part.
The numerical effect following a wrong choice of parameters for the core of the obstacle are presented in Figure A.4. The result for an inert obstacle with an obstacle composed of twenty five percent of numerical core and seventy five percent of mantle (Profile 1) is present in Figure A.4b. The current appearing at the surface of the obstacle for such configuration is directed parallel to the electric field. This configuration is quite unexpected, as we expect an electric field parallel current inside the obstacle and an electric field anti-parallel current at the surface of the obstacle in the case of a conductive obstacle

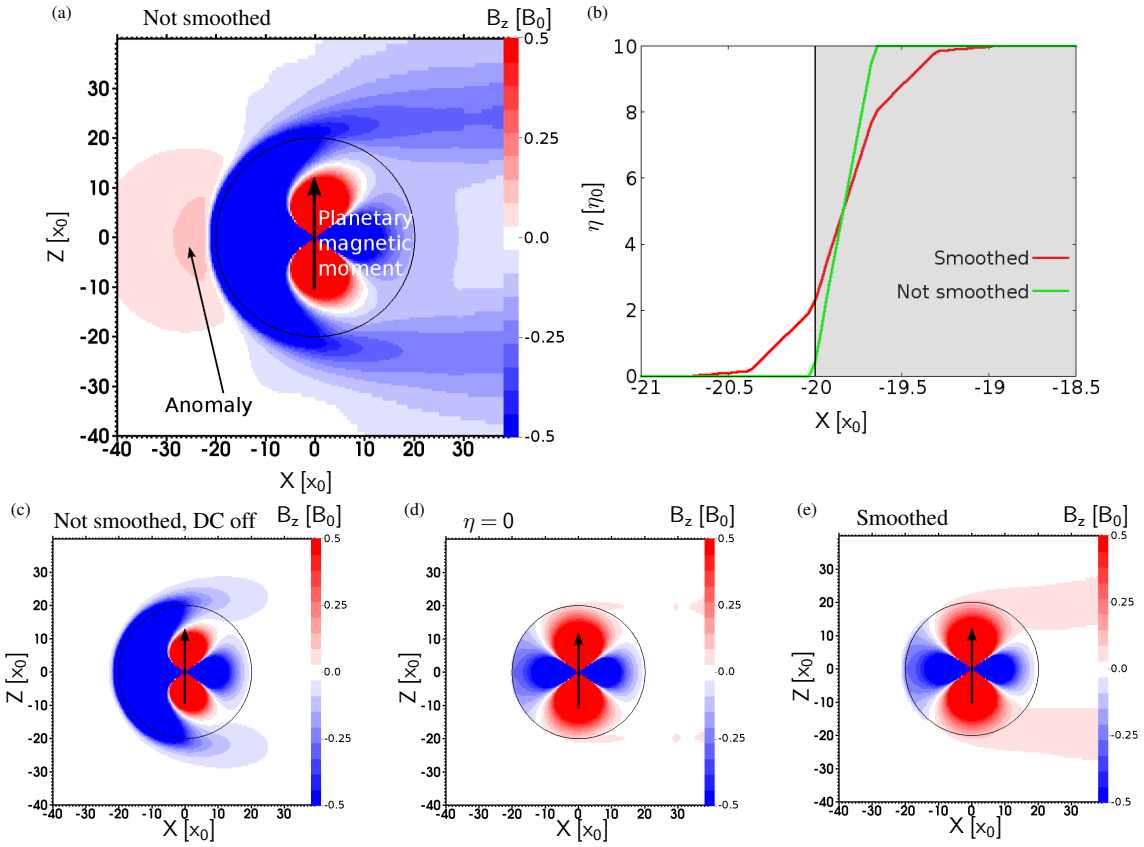

Figure A.3: Panels (a), (c), (d), (e), display the normalized magnetic field Z-component (B_z) in the meridional plane for simulations without IMF, a stellar wind velocity of $8v_{A,0}$, and a planetary magnetic moment M=1000M_0 directed northward. The normalization units are detailed in Table 2.1. Panel (b) shows the two resistivity profiles called "Not smoothed" and "Smoothed". The obstacle is represented by the shaded region. Panel (a) displays the result using the profile "Not smoothed". Panel (c) shows the results of the simulation when the divergence cleaning procedure (see text) is turned off (DC off). The results of the simulation with a perfectly conductive obstacle is shown in Panel (d) ($\eta = 0$). The result of the simulation using the profile "Smoothed" is given in Panel (e).

(see Chapter 3). The reason for the presence of a circular current around the core is purely numerical and due to the zero magnetic field in the numerical core. This creates a magnetic field gradient between the mantle (where the field is calculated) and the numerical core (where the field is set to zero). Therefore putting the numerical core directly into the mantle leads to a non physical behavior which must be avoided. Figure A.4c presents the results of the simulation of an inert obstacle where a physical core is set at the interface between the numerical core and the mantle (Profile 2). This creates a conductive region around the numerical core where the field is calculated. The presence of this region makes the numerical circular current to be present within the obstacle, conversely to Profile 1. Therefore the current flowing at the surface is not perturbed anymore by the numerical anomaly of the core and we can see that the induced current is present. Figure A.4d displays the result of a simulation in which the numerical core is replaced by an

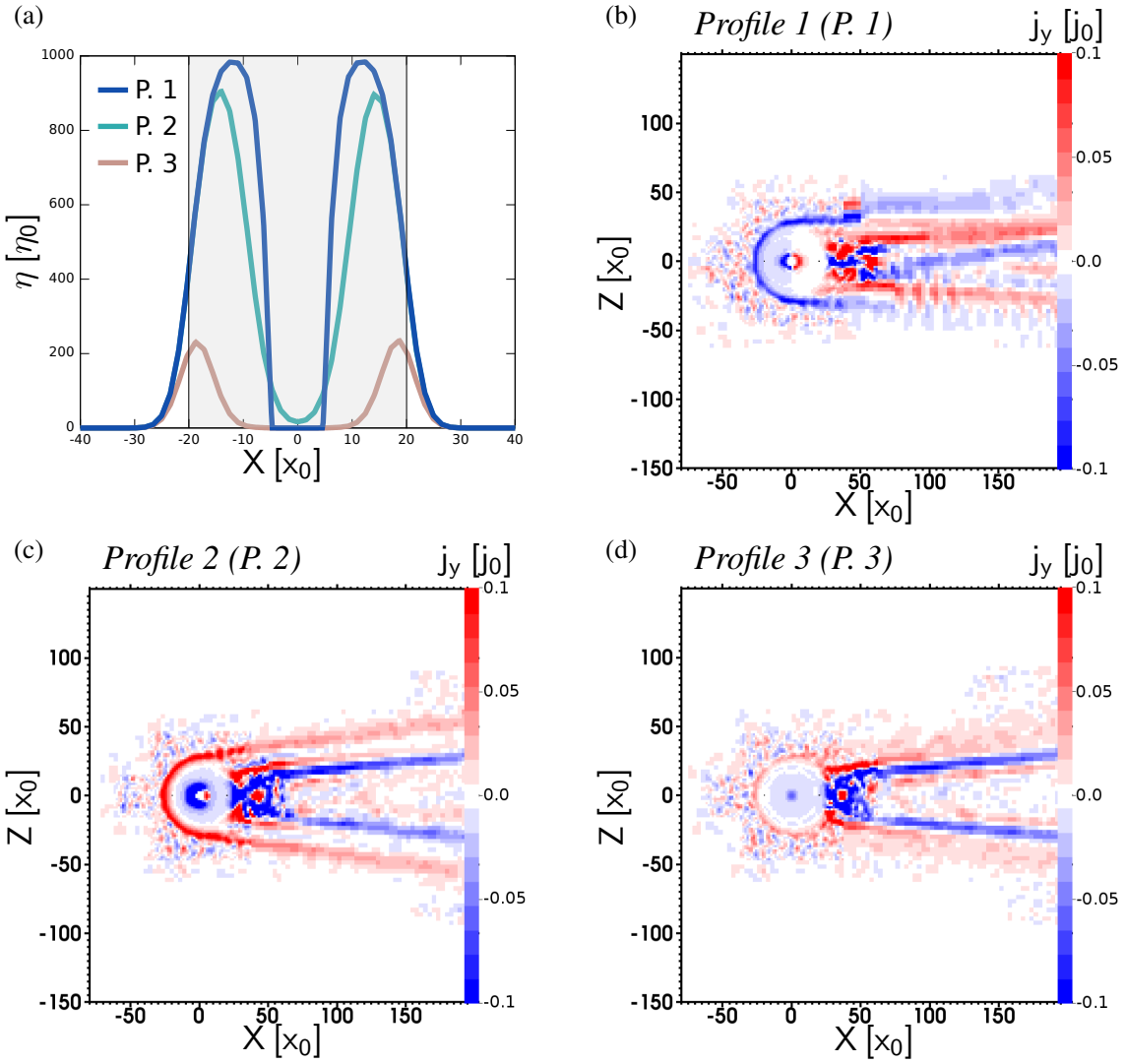

Figure A.4: (a): Three resistivity profile along the X-axis, derived from three different configurations of the planetary core. P. 1 states for Profile 1, P. 2 states for Profile 2, and P. 3 states for Profile 3. The obstacle is represented by the shaded region. (b), (c), and (d): Normalized Y-component of the current density in the meridional plane for the three different configurations of the planetary core introduced in Panel (a).

intermediary core. We see that the circular current is not present and the Ohmic current is significantly weaker. This emphasizes that, one has to keep in mind, when interpreting the results of simulations, that the Ohmic effect can be overestimated by the presence of a numerical core. In the simulations which uses a core, i.e. with magnetized obstacles, the inner obstacle is divided in three shells. The inner region represents 10% of the total volume of the obstacle and is the numerical core. The second shell, which extend up to $0.25R_{\rm p}$, encompasses the inner core. It is a region where the resistivity is manually set to zero. The last shell, which represents 75% of the obstacle, is the mantle where the resistivity applied in each simulation depends on the profile, considering others boundary effects (see Section A.1).

[!ht]

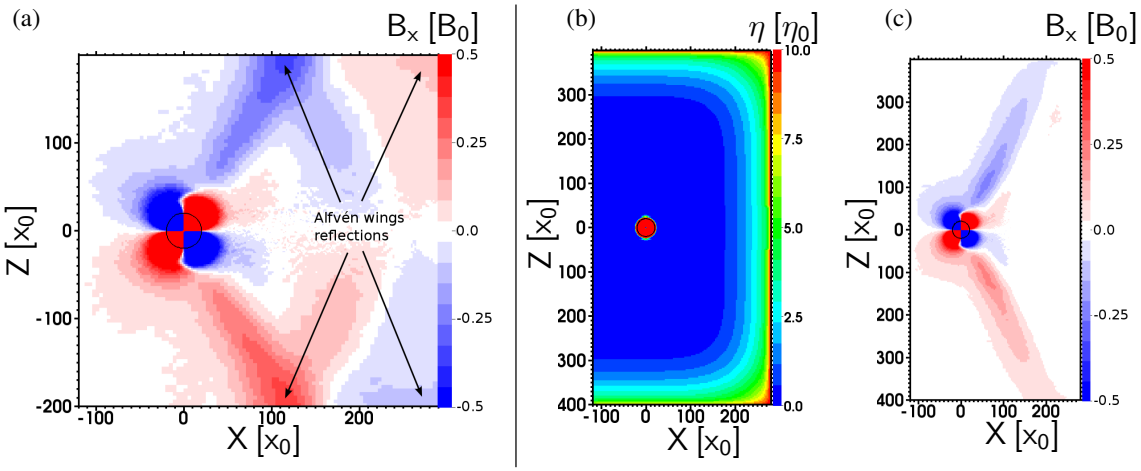

Figure A.5: (a): Normalized X-component of the magnetic field in the meridional plane (see normalization details in Table 2.1). The simulation parameters are those of a $+40\text{E}3M_0\hat{z} \mid 0.5v_{A,0}$ (also called Ganymede-Upward), which are available in Table 4.2. For this result, no particular resistivity profile has been applied to the simulation domain. Panels (b) and (c): simulation results with a modified simulation domain (compared to Panel (a)) and a particular resistivity profile, Panel (b) shows the resistivity profile. Panel (c) provides the normalized X-component of the magnetic field.

A.3 Reflections at the simulation domain boundaries

When simulating plasma interaction in a sub-Alfvénic regime, reflections at the boundaries of the box can become important and must be accounted for. An illustration of the problem is shown in Figure A.5a. The reflection is triggered at the top and bottom sides of the domain and at the boundary downstream of the obstacle. Due to the sub-Alfvénic nature of the flow, the MHD waves bounce on these boundaries and travel backward. A way to handle this issue is to use a particular resistivity profile along the simulation domain boundaries pictured in Figure A.5b. In conjunction with an extension of the simulation domain, the results obtained for this simulation are presented in Figure A.5c. The reflections are completely suppressed, and the boundary effects are no longer affecting the results. However, this solution gives results which are only valid in the area where no resistivity is applied (which should include the area of interest). This solution should be regarded as a compromise between the increase of the spatial domain (which increases the computational requirements) and the computational limit.

Another solution is to end the simulation before the magnetic field perturbations reach the downstream boundary of the box, i.e. before the time τ_{cross}, where τ_{cross} is the time needed to a particle traveling at the velocity of the upstream stellar wind to cross the entire simulation domain. This solution is applicable for simple objects like inert obstacles, or obstacles with a weak magnetic field. In the case of these particular objects, the steady state is achieved after the first stellar wind passage. However, for objects with a strong magnetic dipole momentum or an ionosphere, several times of crossing the simulation domain τ_{cross} are required to reach the steady state. In this case, stopping the simulation

prior to the perturbation reaching the downstream boundary of the simulation domain can lead to wrong interpretations.

B Derivation of the MHD mode group velocity

To derive the MHD modes, one needs to define the wave vector $\boldsymbol{k}$, which is separated between its parallel and perpendicular components (with respect to the magnetic field):

$$\boldsymbol{k} = \boldsymbol{k}_{\perp} + \boldsymbol{k}_{\parallel} \quad . \tag{B.1}$$

The derivation of the group velocity of the MHD waves begins with the equation of dispersion, which is:

$$\omega_{\mathrm{A}} = \pm k_{\parallel} v_{\mathrm{A}} \quad , \tag{B.2}$$

for the Alfvén waves, and:

$$\omega_{\mathrm{ms}}^2 = \frac{k^2}{2}\left(v_{\mathrm{A}}^2 + c_{\mathrm{s}}^2 \pm \sqrt{\left(v_{\mathrm{A}}^2 - c_{\mathrm{s}}^2\right)^2 + 4 v_{\mathrm{A}}^2 c_{\mathrm{s}}^2 \frac{k_{\perp}^2}{k^2}}\right) \quad , \tag{B.3}$$

for the fast ("+" sign in the equation) and slow ("−" sign) magnetosonic modes, which are usually simply called fast and slow modes. The phase velocity of the Alfvén waves is easily calculated:

$$v_{\mathrm{ph,A}} = \frac{k_{\parallel}}{k} v_{\mathrm{A}} = v_{\mathrm{A}} \cos\theta \quad , \tag{B.4}$$

with θ the angle between the wave vector direction and the magnetic field. The expressions of the magnetosonic modes phase velocity is:

$$v_{\mathrm{ph,ms}} = \sqrt{\frac{1}{2}\left(v_{\mathrm{A}}^2 + c_{\mathrm{s}}^2 \pm \sqrt{\left(v_{\mathrm{A}}^2 - c_{\mathrm{s}}^2\right)^2 + 4 v_{\mathrm{A}}^2 c_{\mathrm{s}}^2 \frac{k_{\perp}^2}{k^2}}\right)} \quad . \tag{B.5}$$

To derive the group velocity ($\boldsymbol{v_{gr}}$), one uses the gradient, along the vector $\boldsymbol{k}$, of the dispersion relation:

$$\boldsymbol{v_{gr}} = \nabla_{\boldsymbol{k}} \omega = \begin{pmatrix} \dfrac{\partial \omega}{\partial k_{\perp}} \\ \dfrac{\partial \omega}{\partial k_{\parallel}} \end{pmatrix} \quad . \tag{B.6}$$

The group velocity of the Alfvén mode is expressed as:

$$\boldsymbol{v}_{\mathbf{gr,A}} = \nabla_{\boldsymbol{k}}\omega_{\mathrm{A}} = \pm\begin{pmatrix} \partial_{k_\perp} k_\parallel v_{\mathrm{A}} \\ \partial_{k_\parallel} k_\parallel v_{\mathrm{A}} \end{pmatrix} = \pm\begin{pmatrix} 0 \\ v_{\mathrm{A}} \end{pmatrix} \quad , \tag{B.7}$$

since v_{A} is independent from $\boldsymbol{k}$. Deriving the group velocity of the magnetosonic modes uses the same approach, the full detail of the resulting expression for the fast mode is as follow:

$$\boldsymbol{v}_{\mathbf{gr,fast}} = \begin{pmatrix} k_\perp \dfrac{v_{\mathrm{A}}^2 + c_{\mathrm{s}}^2 + \sqrt{\left(v_{\mathrm{A}}^2 - c_{\mathrm{s}}^2\right)^2 + 4v_{\mathrm{A}}^2 c_{\mathrm{s}}^2 \dfrac{k_\perp^2}{k^2}} + \dfrac{2v_{\mathrm{A}}^2 c_{\mathrm{s}}^2 k_\parallel^2}{k^2\sqrt{\left(v_{\mathrm{A}}^2 - c_{\mathrm{s}}^2\right)^2 + 4v_{\mathrm{A}}^2 c_{\mathrm{s}}^2 \dfrac{k_\perp^2}{k^2}}}}{\sqrt{2k^2\left(v_{\mathrm{A}}^2 + c_{\mathrm{s}}^2 + \sqrt{\left(v_{\mathrm{A}}^2 - c_{\mathrm{s}}^2\right)^2 + 4v_{\mathrm{A}}^2 c_{\mathrm{s}}^2 \dfrac{k_\perp^2}{k^2}}\right)}} \\ k_\parallel \dfrac{v_{\mathrm{A}}^2 + c_{\mathrm{s}}^2 + \sqrt{\left(v_{\mathrm{A}}^2 - c_{\mathrm{s}}^2\right)^2 + 4v_{\mathrm{A}}^2 c_{\mathrm{s}}^2 \dfrac{k_\perp^2}{k^2}} - \dfrac{2v_{\mathrm{A}}^2 c_{\mathrm{s}}^2 k_\perp^2}{k^2\sqrt{\left(v_{\mathrm{A}}^2 - c_{\mathrm{s}}^2\right)^2 + 4v_{\mathrm{A}}^2 c_{\mathrm{s}}^2 \dfrac{k_\perp^2}{k^2}}}}{\sqrt{2k^2\left(v_{\mathrm{A}}^2 + c_{\mathrm{s}}^2 + \sqrt{\left(v_{\mathrm{A}}^2 - c_{\mathrm{s}}^2\right)^2 + 4v_{\mathrm{A}}^2 c_{\mathrm{s}}^2 \dfrac{k_\perp^2}{k^2}}\right)}} \end{pmatrix} , \tag{B.8}$$

and for the slow mode:

$$\boldsymbol{v}_{\mathbf{gr,slow}} = \begin{pmatrix} k_\perp \dfrac{v_{\mathrm{A}}^2 + c_{\mathrm{s}}^2 - \sqrt{\left(v_{\mathrm{A}}^2 - c_{\mathrm{s}}^2\right)^2 + 4v_{\mathrm{A}}^2 c_{\mathrm{s}}^2 \dfrac{k_\perp^2}{k^2}} - \dfrac{2v_{\mathrm{A}}^2 c_{\mathrm{s}}^2 k_\parallel^2}{k^2\sqrt{\left(v_{\mathrm{A}}^2 - c_{\mathrm{s}}^2\right)^2 + 4v_{\mathrm{A}}^2 c_{\mathrm{s}}^2 \dfrac{k_\perp^2}{k^2}}}}{\sqrt{2k^2\left(v_{\mathrm{A}}^2 + c_{\mathrm{s}}^2 - \sqrt{\left(v_{\mathrm{A}}^2 - c_{\mathrm{s}}^2\right)^2 + 4v_{\mathrm{A}}^2 c_{\mathrm{s}}^2 \dfrac{k_\perp^2}{k^2}}\right)}} \\ k_\parallel \dfrac{v_{\mathrm{A}}^2 + c_{\mathrm{s}}^2 - \sqrt{\left(v_{\mathrm{A}}^2 - c_{\mathrm{s}}^2\right)^2 + 4v_{\mathrm{A}}^2 c_{\mathrm{s}}^2 \dfrac{k_\perp^2}{k^2}} + \dfrac{2v_{\mathrm{A}}^2 c_{\mathrm{s}}^2 k_\perp^2}{k^2\sqrt{\left(v_{\mathrm{A}}^2 - c_{\mathrm{s}}^2\right)^2 + 4v_{\mathrm{A}}^2 c_{\mathrm{s}}^2 \dfrac{k_\perp^2}{k^2}}}}{\sqrt{2k^2\left(v_{\mathrm{A}}^2 + c_{\mathrm{s}}^2 - \sqrt{\left(v_{\mathrm{A}}^2 - c_{\mathrm{s}}^2\right)^2 + 4v_{\mathrm{A}}^2 c_{\mathrm{s}}^2 \dfrac{k_\perp^2}{k^2}}\right)}} \end{pmatrix} . \tag{B.9}$$

Those expressions can be expressed in a more convenient way by replacing the expression of the phase velocity (using Equation (B.5)), as well as:

$$\sqrt{\left(v_{\mathrm{A}}^2 - c_{\mathrm{s}}^2\right)^2 + 4v_{\mathrm{A}}^2 c_{\mathrm{s}}^2 \frac{k_\perp^2}{k^2}} = v_{\mathrm{A}}^2 + c_{\mathrm{s}}^2 - 2v_{\mathrm{ph,slow}}^2 = -v_{\mathrm{A}}^2 - c_{\mathrm{s}}^2 + 2v_{\mathrm{ph,fast}}^2 \quad . \tag{B.10}$$

The expression of the fast mode becomes:

$$\boldsymbol{v}_{\mathbf{gr,fast}} = \begin{pmatrix} 2v_{\mathrm{ph,fast}}^2 + \dfrac{2v_\mathrm{A}^2 c_\mathrm{s}^2 k_\parallel^2}{k^2\left(-v_\mathrm{A}^2 - c_\mathrm{s}^2 + 2v_{\mathrm{ph,fast}}^2\right)} \\ k_\perp \dfrac{}{2kv_{\mathrm{ph,fast}}} \\ 2v_{\mathrm{ph,fast}}^2 - \dfrac{2v_\mathrm{A}^2 c_\mathrm{s}^2 k_\perp^2}{k^2\left(-v_\mathrm{A}^2 - c_\mathrm{s}^2 + 2v_{\mathrm{ph,fast}}^2\right)} \\ k_\parallel \dfrac{}{2kv_{\mathrm{ph,fast}}} \end{pmatrix} = \begin{pmatrix} \dfrac{k_\perp}{|\boldsymbol{k}|}\dfrac{1}{v_{\mathrm{ph,fast}}}\left(v_{\mathrm{ph,fast}}^2 - \dfrac{k_\parallel^2}{k^2}\dfrac{c_\mathrm{s}^2 v_\mathrm{A}^2}{c_\mathrm{s}^2 + v_\mathrm{A}^2 - 2v_{\mathrm{ph,fast}}^2}\right) \\ \dfrac{k_\parallel}{|\boldsymbol{k}|}\dfrac{1}{v_{\mathrm{ph,fast}}}\left(v_{\mathrm{ph,fast}}^2 + \dfrac{k_\perp^2}{k^2}\dfrac{c_\mathrm{s}^2 v_\mathrm{A}^2}{c_\mathrm{s}^2 + v_\mathrm{A}^2 - 2v_{\mathrm{ph,fast}}^2}\right) \end{pmatrix} . \tag{B.11}$$

And the expression of the slow mode becomes:

$$\boldsymbol{v}_{\mathbf{gr,slow}} = \begin{pmatrix} 2v_{\mathrm{ph,slow}}^2 - \dfrac{2v_\mathrm{A}^2 c_\mathrm{s}^2 k_\parallel^2}{k^2\left(v_\mathrm{A}^2 + c_\mathrm{s}^2 - 2v_{\mathrm{ph,slow}}^2\right)} \\ k_\perp \dfrac{}{2kv_{\mathrm{ph,slow}}} \\ 2v_{\mathrm{ph,slow}}^2 - \dfrac{2v_\mathrm{A}^2 c_\mathrm{s}^2 k_\perp^2}{k^2\left(v_\mathrm{A}^2 + c_\mathrm{s}^2 - 2v_{\mathrm{ph,slow}}^2\right)} \\ k_\parallel \dfrac{}{2kv_{\mathrm{ph,slow}}} \end{pmatrix} = \begin{pmatrix} \dfrac{k_\perp}{|\boldsymbol{k}|}\dfrac{1}{v_{\mathrm{ph,slow}}}\left(v_{\mathrm{ph,slow}}^2 - \dfrac{k_\parallel^2}{k^2}\dfrac{c_\mathrm{s}^2 v_\mathrm{A}^2}{c_\mathrm{s}^2 + v_\mathrm{A}^2 - 2v_{\mathrm{ph,slow}}^2}\right) \\ \dfrac{k_\parallel}{|\boldsymbol{k}|}\dfrac{1}{v_{\mathrm{ph,slow}}}\left(v_{\mathrm{ph,slow}}^2 + \dfrac{k_\perp^2}{k^2}\dfrac{c_\mathrm{s}^2 v_\mathrm{A}^2}{c_\mathrm{s}^2 + v_\mathrm{A}^2 - 2v_{\mathrm{ph,slow}}^2}\right) \end{pmatrix} . \tag{B.12}$$

Finally, the expression of the group velocity can simply be expressed in term of the magnetosonic phase velocity given in Equation (B.5):

$$\boldsymbol{v}_{\mathbf{gr,ms}} = \begin{pmatrix} \dfrac{k_\perp}{|\boldsymbol{k}|}\dfrac{1}{v_{\mathrm{ph,ms}}}\left(v_{\mathrm{ph,ms}}^2 - \dfrac{k_\parallel^2}{k^2}\dfrac{c_\mathrm{s}^2 v_\mathrm{A}^2}{c_\mathrm{s}^2 + v_\mathrm{A}^2 - 2v_{\mathrm{ph,ms}}^2}\right) \\ \dfrac{k_\parallel}{|\boldsymbol{k}|}\dfrac{1}{v_{\mathrm{ph,ms}}}\left(v_{\mathrm{ph,ms}}^2 + \dfrac{k_\perp^2}{k^2}\dfrac{c_\mathrm{s}^2 v_\mathrm{A}^2}{c_\mathrm{s}^2 + v_\mathrm{A}^2 - 2v_{\mathrm{ph,ms}}^2}\right) \end{pmatrix} . \tag{B.13}$$

Bibliography

Alfvén, H., 1942, Existence of Electromagnetic-Hydrodynamic Waves, Nature, 150, 405–406

Bagdonat, T., 2004, Hybrid Simulation of Weak Comets, Ph.D. thesis, TU Braunschweig

Bagdonat, T., Motschmann, U., 2002a, From a weak to a strong comet - 3D global hybrid simulation studies, Earth Moon and Planets, 90, 305–321

Bagdonat, T., Motschmann, U., 2002b, 3D hybrid simulation code using curvilinear coordinates, Journal of Computational Physics, 183, 470–485

Bale, S. D., Owen, C. J., Bougeret, J.-L., Goetz, K., Kellogg, P. J., Lepping, R. P., Manning, R., Monson, S. J., 1997, Evidence of currents and unstable particle distributions in an extended region around the lunar plasma wake, Geophysical Research Letters, 24, 1427–1430

Baumjohann, W., Treumann, R. A., 1996, Basic space plasma physics, Imperial College Press, London, UK

Belmont, G., Chanteur, G., 1989, Advances in magnetopause Kelvin-Helmholtz instability studies, Physica Scripta, 40, 124–128

Birch, P. C., Chapman, S. C., 2001, Detailed structure and dynamics in particle-in-cell simulations of the lunar wake, Physics of Plasmas, 8, 4551–4559

Biver, N., Bockelée-Morvan, D., Colom, P., Crovisier, J., Germain, B., Lellouch, E., Davies, J. K., Dent, W. R. F., Moreno, R., Paubert, G., Wink, J., Despois, D., Lis, D. C., Mehringer, D., Benford, D., Gardner, M., Phillips, T. G., Gunnarsson, M., Rickman, H., Winnberg, A., Bergman, P., Johansson, L. E. B., Rauer, H., 1997, Long-term Evolution of the Outgassing of Comet Hale-Bopp From Radio Observations, Earth Moon and Planets, 78, 5–11

Boesswetter, A., Bagdonat, T., Motschmann, U., Sauer, K., 2004, Plasma boundaries at Mars: a 3-D simulation study, Annales Geophysicae, 22, 4363–4379

Boesswetter, A., Simon, S., Bagdonat, T., Motschmann, U., Fränz, M., Roussos, E., Krupp, N., Woch, J., Schüle, J., Barabash, S., Lundin, R., 2007, Comparison of plasma data from ASPERA-3/Mars-Express with a 3-D hybrid simulation, Annales Geophysicae, 25, 1851–1864

Boesswetter, A., Lammer, H., Kulikov, Y., Motschmann, U., Simon, S., 2010, Non-thermal water loss of the early Mars: 3D multi-ion hybrid simulations, Planetary and Space Science, 58, 2031–2043

Brace, L. H., Kliore, A. J., 1991, The structure of the Venus ionosphere, Space Science Reviews, 55, 81–163

Brain, D. A., Bagenal, F., Acuña, M. H., Connerney, J. E. P., 2003, Martian magnetic morphology: Contributions from the solar wind and crust, Journal of Geophysical Research, 108, 1424

Brecht, S. H., Ledvina, S. A., 2006, The Solar Wind Interaction With the Martian Ionosphere/Atmosphere, Space Science Reviews, 126, 15–38

Bryant, D. A., Cline, T. L., Desai, U. D., McDonald, F. B., 1962, Explorer 12 Observations of Solar Cosmic Rays and Energetic Storm Particles after the Solar Flare of September 28, 1961, Journal of Geophysical Research, 67, 4983–5000

Catto, P. J., 1974, A model for the steady interaction of the solar wind with the Moon, Astrophysics and Space Science, 26, 47–94

Chapman, S., Ferraro, V. C. A., 1930, A New Theory of Magnetic Storms., Nature, 126, 129–130

Chodura, R., Schlueter, A., 1981, A 3D code for MHD equilibrium and stability, Journal of Computational Physics, 41, 68–88

Colburn, D. S., Currie, R. G., Mihalov, J. D., Sonett, C. P., 1967, Diamagnetic Solar-Wind cavity discovered behind Moon, Science, 158, 1040–1042

Deca, J., Lapenta, G., Marchand, R., Markidis, S., 2013, Spacecraft charging analysis with the implicit particle-in-cell code iPic3D, Physics of Plasmas, 20, 102 902

Drell, S. D., Foley, H. M., Ruderman, M. A., 1965, Drag and Propulsion of Large Satellites in the Ionosphere: An Alfvén Propulsion Engine in Space, Journal of Geophysical Research, 70, 3131–3145

Dungey, J. W., 1961, Interplanetary Magnetic Field and the Auroral Zones, Physical Review Letters, 6, 47–48

Dyadechkin, S., Kallio, E., Jarvinen, R., 2013, A new 3-D spherical hybrid model for solar wind interaction studies, Journal of Geophysical Research, 118, 5157–5168

Eastman, T. E., Frank, L. A., Peterson, W. K., Lennartsson, W., 1984, The plasma sheet boundary layer, Journal of Geophysical Research, 89, 1553–1572

Fatemi, S., Holmström, M., Futaana, Y., Barabash, S., Lue, C., 2013, The lunar wake current systems, Geophysical Research Letters, 40, 17–21

Fermo, R. L., Drake, J. F., Swisdak, M., 2012, Secondary Magnetic Islands Generated by the Kelvin-Helmholtz Instability in a Reconnecting Current Sheet, Physical Review Letters, 108, 255005

Glassmeier, K.-H., 1997, The Hermean magnetosphere and its ionosphere-magnetosphere coupling, Planetary and Space Science, 45, 119–125

Glassmeier, K.-H., Auster, H.-U., Constantinescu, D., Fornaçon, K.-H., Narita, Y., Plaschke, F., Angelopoulos, V., Georgescu, E., Baumjohann, W., Magnes, W., Nakamura, R., Carlson, C. W., Frey, S., McFadden, J. P., Phan, T., Mann, I., Rae, I. J., Vogt, J., 2008, Magnetospheric quasi-static response to the dynamic magnetosheath: A THEMIS case study, Geophysical Research Letters, 35, L17S01

Gortsas, N., Motschmann, U., Kührt, E., Knollenberg, J., Simon, S., Boesswetter, A., 2009, Mapping of coma anisotropies to plasma structures of weak comets: a 3-D hybrid simulation study, Annales Geophysicae, 27, 1555–1572

Gortsas, N., Motschmann, U., Kührt, E., Glassmeier, K.-H., Hansen, K. C., Müller, J., Schmidt, A., 2010, Global plasma-parameter simulation of Comet 67P/Churyumov-Gerasimenko approaching the Sun, Astronomy and Astrophysics, 520, A92

Haider, S. A., Mahajan, K. K., Kallio, E., 2011, Mars ionosphere: A review of experimental results and modeling studies, Reviews of Geophysics, 49, RG4001

Halekas, J. S., Saito, Y., Delory, G. T., Farrell, W. M., 2011, New views of the lunar plasma environment, Planetary and Space Science, 59, 1681–1694

Hewett, D. W., 1985, Elimination of Electromagnetic Radiation in Plasma Simulation - the DARWIN or Magnetoinductive Approximation, Space Science Reviews, 42, 29–40

Holmström, M., Fatemi, S., Futaana, Y., Nilsson, H., 2012, The interaction between the Moon and the solar wind, Earth, Planets, and Space, 64, 237–245

Hood, L. L., Herbert, F., Sonett, C. P., 1982, The deep lunar electrical conductivity profile - Structural and thermal inferences, Journal of Geophysical Research, 87, 5311–5326

Iijima, T., Potemra, T. A., Zanetti, L. J., Bythrow, P. F., 1984, Large-scale Birkeland currents in the dayside polar region during strongly northward IMF - A new Birkeland current system, Journal of Geophysical Rkesearch, 89, 7441–7452

Jarvinen, R., Kallio, E., Janhunen, P., Barabash, S., Zhang, T. L., Pohjola, V., Sillanpää, I., 2009, Oxygen ion escape from Venus in a global hybrid simulation: role of the ionospheric O^+ ions, Annales Geophysicae, 27, 4333–4348

Jarvinen, R., Kallio, E., Dyadechkin, S., Janhunen, P., Sillanpää, I., 2010, Widely different characteristics of oxygen and hydrogen ion escape from Venus, Geophysical Research Letters, 37, L16201

Johansson, E. P. G., Bagdonat, T., Motschmann, U., 2009, Consequences of expanding exoplanetary atmospheres for magnetospheres, Astronomy and Astrophysics, 496, 869–877

Johansson, E. P. G., Mueller, J., Motschmann, U., 2011, Interplanetary magnetic field orientation and the magnetospheres of close-in exoplanets, Astronomy and Astrophysics, 525, A117

Kallio, E., 2005, Formation of the lunar wake in quasi-neutral hybrid model, Geophysical Research Letters, 32, L06107

Kallio, E., Barabash, S., Janhunen, P., Jarvinen, R., 2008, Magnetized Mars: Transformation of Earth-like magnetosphere to Venus-like induced magnetosphere, Planetary and Space Science, 56, 823–827

Kessel, R. L., Chen, S.-H., Green, J. L., Fung, S. F., Boardsen, S. A., Tan, L. C., Eastman, T. E., Craven, J. D., Frank, L. A., 1996, Evidence of high-latitude reconnecting during northward IMF: Hawkeye observations, Geophysical Research Letters, 23, 583–586

Khurana, K. K., Russell, C. T., Dougherty, M. K., 2008, Magnetic portraits of Tethys and Rhea, Icarus, 193, 465–474

Kivelson, M. G., Russell, C. T., 1995, Introduction to Space Physics, Cambridge University Press, Cambridge, UK

Kivelson, M. G., Khurana, K. K., Russell, C. T., Walker, R. J., Warnecke, J., Coroniti, F. V., Polanskey, C., Southwood, D. J., Schubert, G., 1996, Discovery of Ganymede's magnetic field by the Galileo spacecraft, Nature, 384, 537–541

Kivelson, M. G., Bagenal, F., Kurth, W. S., Neubauer, F. M., Paranicas, C., Saur, J., 2004, Jupiter. The planet, satellites and magnetosphere, vol. 1 of Cambridge planetary science, chap. Magnetospheric interactions with satellites, pp. 513–536, Cambridge University Press, Cambridge, UK

Koenders, C., Glassmeier, K.-H., Richter, I., Motschmann, U., Rubin, M., 2013, Revisiting cometary bow shock positions, Planetary and Space Science, 87, 85–95

Kriegel, H., 2014, The Plasma Environments of Saturn's Moons Enceladus and Rhea: Modeling of Cassini Magnetic Field Data, Ph.D. thesis, TU Braunschweig

Kriegel, H., Simon, S., Müller, J., Motschmann, U., Saur, J., Glassmeier, K.-H., Dougherty, M. K., 2009, The plasma interaction of Enceladus: 3D hybrid simulations and comparison with Cassini MAG data, Planetary and Space Science, 57, 2113–2122

Kriegel, H., Simon, S., Motschmann, U., Saur, J., Neubauer, F. M., Persoon, A. M., Dougherty, M. K., Gurnett, D. A., 2011, Influence of negatively charged plume grains on the structure of Enceladus' Alfvén wings: Hybrid simulations versus Cassini Magnetometer data, Journal of Geophysical Research, 116, A10223

Ledvina, S. A., Luhmann, J. G., Brecht, S. H., Cravens, T. E., 2004, Titan's induced magnetosphere, Advances in Space Research, 33, 2092–2102

Li, W., Raeder, J., Dorelli, J., Øieroset, M., Phan, T. D., 2005, Plasma sheet formation during long period of northward IMF, Geophysical Research Letters, 32, L12S08

Liemohn, M. W., Ganushkina, N. Y., Katus, R. M., de Zeeuw, D. L., Welling, D. T., 2013, The magnetospheric banana current, Journal of Geophysical Research, 118, 1009–1021

Lipatov, A. S., 2002, The hybrid multiscale simulation technology: an introduction with application to astrophysical and laboratory plasmas, Springer, New York, NY

Lipatov, A. S., Combi, M. R., 2006, Effects of kinetic processes in shaping Io's global plasma environment: A 3D hybrid model, Icarus, 180, 412–427

Lipatov, A. S., Motschmann, U., Bagdonat, T., Grießmeier, J.-M., 2005, The interaction of the stellar wind with an extrasolar planet - 3D hybrid and drift-kinetic simulations, Planetary and Space Science, 53, 423–432

Lipatov, A. S., Cooper, J. F., Sittler, Jr., E. C., Hartle, R. E., 2012, Effects of Na^+ and He^+ pickup ions on the lunar-like plasma environment: 3D hybrid modeling, Advances in Space Research, 50, 1583–1591

Liu, Z.-Q., Lu, J. Y., Kabin, K., Yang, Y. F., Zhao, M. X., Cao, X., 2012, Dipole tilt control of the magnetopause for southward IMF from global magnetohydrodynamic simulations, Journal of Geophysical Research, 117, A07207

Luhmann, J. G., Cravens, T. E., 1991, Magnetic fields in the ionosphere of Venus, Space Science Reviews, 55, 201–274

Maezawa, K., 1976, Magnetospheric convection induced by the positive and negative Z components of the interplanetary magnetic field - Quantitative analysis using polar cap magnetic records, Journal of Geophysical Research, 81, 2289–2303

Martinecz, C., Boesswetter, A., Fränz, M., Roussos, E., Woch, J., Krupp, N., Dubinin, E., Motschmann, U., Wiehle, S., Simon, S., Barabash, S., Lundin, R., Zhang, T. L., Lammer, H., Lichtenegger, H., Kulikov, Y., 2009, Plasma environment of Venus: Comparison of Venus Express ASPERA-4 measurements with 3-D hybrid simulations, Journal of Geophysical Research, 114, E00B30

Matthews, A. P., 1994, Current advance method and cyclic leapfrog for 2d multispecies hybrid plasma simulations, Journal of Computational Physics, 112, 102 – 116, ISSN 0021-9991

Meyer-Vernet, N., Issautier, K., 1998, Electron temperature in the solar wind: Generic radial variation from kinetic collisionless models, Journal of Geophysical Research, 103, 29 705–29 718

Modolo, R., Chanteur, G. M., 2008, A global hybrid model for Titan's interaction with the Kronian plasma: Application to the Cassini Ta flyby, Journal of Geophysical Research, 113, A01317

Moore, K. R., Thomas, V. A., McComas, D. J., 1991, Global hybrid simulation of the solar wind interaction with the dayside of Venus, Journal of Geophysical Research, 96, 7779–7791

Motschmann, U., Kührt, E., 2006, Interaction of the Solar Wind with Weak Obstacles: Hybrid Simulations for Weakly Active Comets and for Mars, Space Science Reviews, 122, 197–208

Motschmann, U., Sauer, K., Roatsch, T., McKenzie, J. F., 1991, Subcritical multiple-ion shocks, Journal of Geophysical Research, 96, 13 841

Mueller, J., 2011, A.I.K.E.F.: An Adaptive Hybrid Model with Application to Fossil Fields at Titan and Mercury's Double Magnetopause, Ph.D. thesis, TU Braunschweig

Mueller, J., Simon, S., Motschmann, U., Glassmeier, K.-H., Saur, J., Schüle, J., Pringle, G. J., 2010, Magnetic field fossilization and tail reconfiguration in Titan's plasma environment during a magnetopause passage: 3D adaptive hybrid code simulations, Planetary and Space Science, 58, 1526–1546

Mueller, J., Simon, S., Motschmann, U., Schüle, J., Glassmeier, K.-H., Pringle, G. J., 2011, A.I.K.E.F.: Adaptive hybrid model for space plasma simulations, Computer Physics Communications, 182, 946–966

Mueller, J., Simon, S., Wang, Y.-C., Motschmann, U., Heyner, D., Schüle, J., Ip, W.-H., Kleindienst, G., Pringle, G. J., 2012, Origin of Mercury's double magnetopause: 3D hybrid simulation study with A.I.K.E.F., Icarus, 218, 666–687

Muranaka, T., Ueda, H. O., Usui, H., Shinohara, I., 2009, Evaluation of Electric Field Probe Onboard Spacecraft Using a 3D Full PIC Simulation, Transactions of Space Technology Japan, 7, 219P

Najib, D., Nagy, A. F., Tóth, G., Ma, Y., 2011, Three-dimensional, multifluid, high spatial resolution MHD model studies of the solar wind interaction with Mars, Journal of Geophysical Research, 116, A05204

Ness, N. F., Behannon, K. W., Scearce, C. S., Cantarano, S. C., 1967, Early Results from the Magnetic Field Experiment on Lunar Explorer 35, Journal of Geophysics Research, 72, 5769

Ness, N. F., Behannon, K. W., Lepping, R. P., Whang, Y. C., Schatten, K. H., 1974, Magnetic Field Observations near Mercury: Preliminary Results from Mariner 10, Science, 185, 151–160

Neubauer, F. M., 1980, Nonlinear standing Alfven wave current system at Io - Theory, Journal of Geophysics Research, 85, 1171–1178

Neubauer, F. M., 1998, The sub-Alfvénic interaction of the Galilean satellites with the Jovian magnetosphere, Journal of Geophysics Research, 103, 19 843–19 866

Ogilvie, K. W., Scudder, J. D., Hartle, R. E., Siscoe, G. L., Bridge, H. S., Lazarus, A. J., Asbridge, J. R., Bame, S. J., Yeates, C. M., 1974, Observations at Mercury Encounter by the Plasma Science Experiment on Mariner 10, Science, 185, 145–151

Ogino, T., 1986, A three-dimensional MHD simulation of the interaction of the solar wind with the earth's magnetosphere - The generation of field-aligned currents, Journal of Geophysical Research, 91, 6791–6806

Ogino, T., Walker, R. J., 1984, A magnetohydrodynamic simulation of the bifurcation of tail lobes during intervals with a northward interplanetary magnetic field, Geophysical Research Letters, 11, 1018–1021

Omidi, N., Blanco-Cano, X., Russell, C. T., Karimabadi, H., 2004, Dipolar magnetospheres and their characterization as a function of magnetic moment, Advances in Space Research, 33, 1996–2003

Opp, A. G., 1980, Scientific results from the Pioneer Saturn encounter - Summary, Science, 207, 401–403

Owen, C. J., Lepping, R. P., Ogilvie, K. W., Slavin, J. A., Farrell, W. M., Byrnes, J. B., 1996, The lunar wake at 6.8 R_L: WIND magnetic field observations, Geophysical Research Letters, 23, 1263–1266

Parker, E. N., 1965, Dynamical Theory of the Solar Wind, Space Science Reviews, 4, 666–708

Piddington, J. H., 1979, The closed model of the Earth's magnetosphere, Journal of Geophysical Research, 84, 93–100

Pokhotelov, D., von Alfthan, S., Kempf, Y., Vainio, R., Koskinen, H. E. J., Palmroth, M., 2013, Ion distributions upstream and downstream of the Earth's bow shock: first results from Vlasiator, Annales Geophysicae, 31, 2207–2212

Potemra, T. A., 1979, Current systems in the Earth's magnetosphere - A review of U.S. progress for the 1975-1978 IUGG quadrennial report, Reviews of Geophysics and Space Physics, 17, 640–656

Richer, E., Modolo, R., Chanteur, G. M., Hess, S., Leblanc, F., 2012, A global hybrid model for Mercury's interaction with the solar wind: Case study of the dipole representation, Journal of Geophysical Research, 117, A10228

Ridley, A. J., 2007, Alfvén wings at Earth's magnetosphere under strong interplanetary magnetic fields, Annales Geophysicae, 25, 533–542

Riousset, J. A., Paty, C. S., Lillis, R. J., Fillingim, M. O., England, S. L., Withers, P. G., Hale, J. P. M., 2013, Three-dimensional multifluid modeling of atmospheric electrodynamics in Mars' dynamo region, Journal of Geophysical Research, 118, 3647–3659

Riousset, J. A., Paty, C. S., Lillis, R. J., Fillingim, M. O., England, S. L., Withers, P. G., Hale, J. P. M., 2014, Electrodynamics of the Martian dynamo region near magnetic cusps and loops, Geophysical Research Letters, 41, 1119–1125

Roussos, E., Müller, J., Simon, S., Bößwetter, A., Motschmann, U., Krupp, N., Fränz, M., Woch, J., Khurana, K. K., Dougherty, M. K., 2008, Plasma and fields in the wake of Rhea: 3-D hybrid simulation and comparison with Cassini data, Annales Geophysicae, 26, 619–637

Russell, C. T., 1972, The Configuration of the Magnetosphere, in Critical Problems of Magnetospheric Physics, (Ed.) E. R. Dyer, p. 1

Samir, U., Wright, Jr., K. H., Stone, N. H., 1983, The expansion of a plasma into a vacuum: basic phenomena and processes and applications to space plasma physics., Reviews of Geophysics and Space Physics, 21, 1631–1646

Saur, J., Grambusch, T., Duling, S., Neubauer, F. M., Simon, S., 2013, Magnetic energy fluxes in sub-Alfvénic planet star and moon planet interactions, Astronomy and Astrophysics, 552, A119

Schunk, R. W., Nagy, A. F., 2004, Ionospheres: Physics, Plasma Physics, and Chemistry, Cambridge Atmospheric and Space Science, Cambridge University Press, Cambridge, UK

Simon, S., 2007, Titan's highly variable plasma environment: A 3D hybrid simulation study, Ph.D. thesis, TU Braunschweig

Simon, S., Boesswetter, A., Bagdonat, T., Motschmann, U., Glassmeier, K.-H., 2006, Plasma environment of Titan: a 3-D hybrid simulation study, Annales Geophysicae, 24, 1113–1135

Simon, S., Saur, J., Neubauer, F. M., Motschmann, U., Dougherty, M. K., 2009, Plasma wake of Tethys: Hybrid simulations versus Cassini MAG data, Geophysical Research Letters, 36, L04108

Simon, S., Kriegel, H., Saur, J., Wennmacher, A., Neubauer, F. M., Roussos, E., Motschmann, U., Dougherty, M. K., 2012, Analysis of Cassini magnetic field observations over the poles of Rhea, Journal of Geophysical Research, 117, A07211

Smith, E. J., Davis, Jr., L., Coleman, Jr., P. J., Sonett, C. P., 1963, Magnetic Field, Science, 139, 909–910

Smith, E. J., Davis, Jr., L., Jones, D. E., Coleman, Jr., P. J., Colburn, D. S., Dyal, P., Sonett, C. P., Frandsen, A. M. A., 1974, The planetary magnetic field and magnetosphere of Jupiter: Pioneer 10, Journal of Geophysical Research, 79, 3501

Sonett, C. P., 1963, A Summary Review of the Scientific Findings of the Mariner Venus Mission, Space Science Reviews, 2, 751–777

Sonett, C. P., Colburn, D. S., 1967, Establishment of a lunar unipolar generator and associated shock and wake by the solar wind, Nature, 216, 340–343

Takeda, M., Araki, T., 1985, Electric conductivity of the ionosphere and nocturnal currents, Journal of Atmospheric and Terrestrial Physics, 47, 601–609

Tanaka, T., Saito, Y., Yokota, S., Asamura, K., Nishino, M. N., Tsunakawa, H., Shibuya, H., Matsushima, M., Shimizu, H., Takahashi, F., Fujimoto, M., Mukai, T., Terasawa, T., 2009, First in situ observation of the Moon-originating ions in the Earth's Magnetosphere by MAP-PACE on SELENE (KAGUYA), Geophysical Research Letters, 36, L22106

Trávníček, P., Hellinger, P., Schriver, D., Bale, S. D., 2005, Structure of the lunar wake: Two-dimensional global hybrid simulations, Geophysical Research Letters, 32, L06102

Wang, Y.-C., Mueller, J., Motschmann, U., Ip, W.-H., 2010, A hybrid simulation of Mercury's magnetosphere for the MESSENGER encounters in year 2008, Icarus, 209, 46–52

Wang, Y.-C., Mueller, J., Ip, W.-H., Motschmann, U., 2011, A 3D hybrid simulation study of the electromagnetic field distributions in the lunar wake, Icarus, 216, 415–425

Whang, Y. C., 1968a, Interaction of the magnetized solar wind with the Moon, Physics of Fluids, 11, 969–975

Whang, Y. C., 1968b, Theoretical study of the magnetic field in the lunar wake, Physics of Fluids, 11, 1713–1719

Wiehle, S., Plaschke, F., Motschmann, U., Glassmeier, K.-H., Auster, H. U., Angelopoulos, V., Mueller, J., Kriegel, H., Georgescu, E., Halekas, J., Sibeck, D. G., McFadden, J. P., 2011, First lunar wake passage of ARTEMIS: Discrimination of wake effects and solar wind fluctuations by 3D hybrid simulations, Planetary and Space Science, 59, 661–671

Winglee, R. M., 1998, Multi-fluid simulations of the magnetosphere: The identification of the geopause and its variation with IMF, Geophysical Research Letters, 25, 4441–4444

Wu, C. C., 1985, The effects of northward IMF on the structure of the magnetosphere, Geophysical Research Letters, 12, 839–842

Wurz, P., Rohner, U., Whitby, J. A., Kolb, C., Lammer, H., Dobnikar, P., Martín-Fernández, J. A., 2007, The lunar exosphere: The sputtering contribution, Icarus, 191, 486–496

Zhang, H., Khurana, K. K., Zong, Q.-G., Kivelson, M. G., Hsu, T.-S., Wan, W. X., Pu, Z. Y., Angelopoulos, V., Cao, X., Wang, Y. F., Shi, Q. Q., Liu, W. L., Tian, A. M., Tang, C. L., 2012, Outward expansion of the lunar wake: ARTEMIS observations, Geophysical Research Letters, 39, L18104

Zhang, M. H. G., Luhmann, J. G., Nagy, A. F., Spreiter, J. R., Stahara, S. S., 1993, Oxygen ionization rates at Mars and Venus - Relative contributions of impact ionization and charge exchange, Journal of Geophysical Research, 98, 3311–3318

Acknowledgements

I would like to thank my two supervisors Prof. Dr. Uwe Motschmann and Prof. Dr. Karl-Heinz Glassmeier, for introducing me to the topic of plasma physics applied to planetary-star interactions. This has become the ground on which this dissertation is constructed. I am particularly grateful for their trust from the moment they hired me, till the submission of this work. They quickly understood my work methods giving me freedom in the decision about how to approach specific problems, yet they provide supports and scientific insight and understanding during fruitful discussions to set me on the right tracks. I would like to thank the Max Planck Institute for Solar System Research at Göttingen for funding this doctoral work.
Unfortunately I cannot name all the people who accompanied me on this journey without forgetting anyone. However, I want to express my most sincere gratitude to some of them that I cannot possibly left unnamed. First, I want to thank the "Source": Joachim Müller, who wrote the AIKEF code and was never found unable to answer a question. A quality only challenged by Hendrik Kriegel, whose knowledge of AIKEF is only surpassed by his understanding of the physics of Alfvén wings. I want to thanks Stefan Wiehle, which supports inside the institute was at least as valuable as his help outside (could not have moved without you, dude), and in translating all the weird letters from the German administration. I would also like to recognize Sven Simon, whose point of view was always enlightening during our discussions and who was always able to spark new ideas in my mind, improving the content of this work.
I am also indebted to Jeremy Riousset for correcting this dissertation. I hope his knowledge in the language of Noam Chomsky (whose expertise in languages makes him a more relevant reference than Shakespeare in the present context) made this work more readable to an average English reader, and particularly to my jury and anyone interested about it.
I want to express special thanks to Julie Brisset for driving the IGEP bus to Katlenburg-Lindau (I assure you, even when you passed those trucks with two inches of free space, I was not scared). I wish to extend my thanks to Emilien for introducing me to the French group at Braunschweig, for many opportunities to unwind, when I needed to. Besides, I want to acknowledge Johannes, Ismael, and Hendrik for the training at the Tae Kwon Do club, which helped relaxing body and soul. In addition, I am truly grateful to Eric for always providing me some opportunities to enjoy my (short) vacations back in Nizza.
I cannot write this acknowledgment without mentioning my parents who were always here in time of needs, and my brothers because they are my brothers and I love them.
Some needs to pray, I only need music, It gives me strength and I could not work without it, this work would have never been done without music.

Yoann Vernisse

This is my dissertation. There are many like this but his one is mine.
My dissertation is my best friend. It is my life.
I must master it as I must master my life. Without me, my dissertation is useless.
Without my dissertation I am useless. I must write my dissertation true.
I must do science better than my competitor, who is trying to surpass me. I must publish before he publishes. I will.
Before Prometheus I swear this creed: my dissertation and myself are defenders of science, we are the masters of physics, we are the saviors of my life.
So be it, until there is no competitor, but peace.
QED. [1]

[1] Adapted from *Full Metal Jacket* (1987), Stanley Kubrick, Warner Bros.